N°d'ordre NNT : 2021LYSEI055

THESE de DOCTORAT DE L'UNIVERSITE DE LYON
opérée au sein de
L'Institut National des Sciences Appliquées de Lyon

Ecole Doctorale N° 162
Mécanique, Energétique, Génie civil, Acoustique (MEGA)

Spécialité/discipline de doctorat :
Génie Mécanique

Soutenue publiquement le 21/09/2021, par :

Chiara Balbinot

Étude tridimensionnelle des phénomènes d'imprégnation de renforts fibreux biosourcés pour matériaux composites

Devant le jury composé de :

Protière Suzie	Chargée de recherche, HDR (CNRS)	Rapporteure
Comas-Cardona Sébastien	Professeur (École Centrale Nantes)	Rapporteur
Park Chung Hae	Professeur (IMT Lille Douai)	Président
Dumont Pierre	Professeur (INSA Lyon)	Directeur de thèse
Martoïa Florian	Maitre de conférences (INSA Lyon)	Co-encadrant de thèse
Orgéas Laurent	Directeur de recherche (CNRS)	Co-directeur de thèse

Département FEDORA – INSA Lyon - Ecoles Doctorales

SIGLE	ECOLE DOCTORALE	NOM ET COORDONNEES DU RESPONSABLE
CHIMIE	**CHIMIE DE LYON** **https://www.edchimie-lyon.fr** Sec. : Renée EL MELHEM Bât. Blaise PASCAL, 3e étage secretariat@edchimie-lyon.fr	**M. Stéphane DANIELE** C2P2-CPE LYON-UMR 5265 Bâtiment F308, BP 2077 43 Boulevard du 11 novembre 1918 69616 Villeurbanne **directeur@edchimie-lyon.fr**
E.E.A.	**ÉLECTRONIQUE, ÉLECTROTECHNIQUE, AUTOMATIQUE** **https://edeea.universite-lyon.fr** Sec. : Stéphanie CAUVIN Bâtiment Direction INSA Lyon Tél : 04.72.43.71.70 secretariat.edeea@insa-lyon.fr	**M. Philippe DELACHARTRE** INSA LYON Laboratoire CREATIS Bâtiment Blaise Pascal, 7 avenue Jean Capelle 69621 Villeurbanne CEDEX Tél : 04.72.43.88.63 **philippe.delachartre@insa-lyon.fr**
E2M2	**ÉVOLUTION, ÉCOSYSTÈME, MICROBIOLOGIE, MODÉLISATION** **http://e2m2.universite-lyon.fr** Sec. : Sylvie ROBERJOT Bât. Atrium, UCB Lyon 1 Tél : 04.72.44.83.62 secretariat.e2m2@univ-lyon1.fr	**M. Philippe NORMAND** Université Claude Bernard Lyon 1 UMR 5557 Lab. d'Ecologie Microbienne Bâtiment Mendel 43, boulevard du 11 Novembre 1918 69 622 Villeurbanne CEDEX **philippe.normand@univ-lyon1.fr**
EDISS	**INTERDISCIPLINAIRE SCIENCES-SANTÉ** **http://ediss.universite-lyon.fr** Sec. : Sylvie ROBERJOT Bât. Atrium, UCB Lyon 1 Tél : 04.72.44.83.62 secretariat.ediss@univ-lyon1.fr	**Mme Sylvie RICARD-BLUM** Institut de Chimie et Biochimie Moléculaires et Supramoléculaires (ICBMS) - UMR 5246 CNRS - Université Lyon 1 Bâtiment Raulin - 2ème étage Nord 43 Boulevard du 11 novembre 1918 69622 Villeurbanne Cedex Tél : +33(0)4 72 44 82 32 **sylvie.ricard-blum@univ-lyon1.fr**
INFOMATHS	**INFORMATIQUE ET MATHÉMATIQUES** **http://edinfomaths.universite-lyon.fr** Sec. : Renée EL MELHEM Bât. Blaise PASCAL, 3e étage Tél : 04.72.43.80.46 infomaths@univ-lyon1.fr	**M. Hamamache KHEDDOUCI** Université Claude Bernard Lyon 1 Bât. Nautibus 43, Boulevard du 11 novembre 1918 69 622 Villeurbanne Cedex France Tél : 04.72.44.83.69 **hamamache.kheddouci@univ-lyon1.fr**
Matériaux	**MATÉRIAUX DE LYON** **http://ed34.universite-lyon.fr** Sec. : Yann DE ORDENANA Tél : 04.72.18.62.44 yann.de-ordenana@ec-lyon.fr	**M. Stéphane BENAYOUN** Ecole Centrale de Lyon Laboratoire LTDS 36 avenue Guy de Collongue 69134 Ecully CEDEX Tél : 04.72.18.64.37 **stephane.benayoun@ec-lyon.fr**
MEGA	**MÉCANIQUE, ÉNERGÉTIQUE, GÉNIE CIVIL, ACOUSTIQUE** **http://edmega.universite-lyon.fr** Sec. : Stéphanie CAUVIN Tél : 04.72.43.71.70 Bâtiment Direction INSA Lyon mega@insa-lyon.fr	**M. Jocelyn BONJOUR** INSA Lyon Laboratoire CETHIL Bâtiment Sadi-Carnot 9, rue de la Physique 69621 Villeurbanne CEDEX **jocelyn.bonjour@insa-lyon.fr**
ScSo	**ScSo*** **https://edsciencessociales.universite-lyon.fr** Sec. : Mélina FAVETON INSA : J.Y. TOUSSAINT Tél : 04.78.69.77.79 melina.faveton@univ-lyon2.fr	**M. Christian MONTES** Université Lumière Lyon 2 86 Rue Pasteur 69365 Lyon CEDEX 07 **christian.montes@univ-lyon2.fr**

*ScSo : Histoire, Géographie, Aménagement, Urbanisme, Archéologie, Science politique, Sociologie, Anthropologie

Acknowledgements

Je voudrais remercier toutes les personnes qui ont partagé avec moi ma vie professionnelle et privé et qui, de différentes manières, m'ont aidé à atteindre cet objectif.

Je tiens à exprimer ma plus profonde gratitude et mes sincères remerciements à mes superviseurs, *Pierre Dumont, Florian Martoïa* et *Laurent Orgéas*. Merci d'avoir cru en moi il y a quatre ans, de m'avoir fait confiance et de m'avoir donné l'opportunité de travailler avec vous dans ce projet en collaboration entre les laboratoires LaMCoS et 3SR. Merci pour votre patience, votre temps et votre soutien scientifique et dans la vie quotidienne pendant ce défi difficile mais passionnant qu'est le doctorat.

Je tiens à exprimer ma gratitude pour le jury, *Dr. Suzie Protière, Prof. Sébastien Comas-Cardona* et *Prof. Chung-Hae Park* d'avoir accepté de faire partie de mon comité de thèse, pour les suggestions et commentaires donnés sur mon travail et pour les discussions que nous avons eues et qui ont permis d'améliorer ce travail et les suivants.

Je voudrais remercier tous les collègues qui ont collaboré pour ce projet et pour avoir partagé avec moi leur expertise : *Tarek, Nils, Frédéric Flin* et *Sabine Rolland Du Roscoat*.

A toutes mes collègues rencontrés sur le site de plasturgie de l'INSA à Oyonnax un grand merci de m'avoir accueilli, pour votre soutien, aide et amitié pendant les années passées ensemble: *Jean-Yves, Isabelle, Hayet, Murat, Hervé, Anne, Sam, Pierre, Renaud, Claire, Mohamed et M'hamed*.

Je tiens à remercie tous les doctorants et amis rencontrés à Oyonnax et à Grenoble pendant ces années en France, pour toutes les bons moments partagé ensemble : *Celeste, Raúl, Ivan, Federico, Ibtissam, Javier, José Luis, Xavi, Shubham, Habib, Alex, Alberto, François, Marta, Ritesh, Ankit*, *Thanos, Clara, Antoine*…

Merci à *Geraldine, Pierre, Grecia, Jacqueline* et *Jordan* pour votre amitié et pour être ma famille à Oyonnax.

Un remerciement tout particulier à mes chers amies *Floriana* et *Maria* pour votre amitié, pour avoir partagé nos vies pendant la thèse, comme une famille et pour être toujours là pour moi surtout pendant les moments difficiles que on a passé.

Enfin je voudrais remercie tout ma famille pour leur soutien, leurs encouragements, pour m'avoir toujours poussé à croire un peu plus en moi et aussi pour avoir toujours compris, sans juger, mes choix de vie.

Merci à tous. Thank you all.

Abstract

Most of composite manufacturing processes require an impregnation phase of the fibrous reinforcement by a polymer matrix. The optimization of this phase is crucial to avoid defects such as porosity that can compromise the end-use properties of the parts. This is even more difficult with biosourced fibrous reinforcements. Hence, it is crucial to determine the permeability of the fibre reinforcements as a function of the process-induced evolution of their microstructure, and to control the propagation of the flow front of the polymer matrix.

Thus, we investigated experimentally and numerically the evolution of several key descriptors of the microstructure of flax fibre reinforcement materials as a function of their compaction, using 3D X-ray microtomography images. These descriptors were used in a modified Kozeny-Carman anisotropic permeability model whose predictions were in good agreement with CFD simulation results performed on the 3D images. However, one remaining unknown flow-microstructure coupling parameter needs to be identified by a numerical method. Then, a new full analytical tensorial permeability model was built using the homogenisation with multiple scale asymptotic expansions. Its originality is that it accounts for variations in the fibre orientation distributions. Its relevance was assessed using permeability results obtained numerically on various virtual fibre networks as well as real fibrous materials.

3D images were also used to investigate the phenomena that occur during the propagation of a flow front in a model fibre network. For that, in situ impregnation experiments were performed using ultrafast and high resolution synchrotron X-ray microtomography and a specially developed device. The variations in the fluid-air interface curvatures, triple line lengths, and local contact angles were quantified using advanced image analysis procedures. Hence, local capillary forces and capillary pressure were estimated during the flow front propagation. These original results will allow theoretical and numerical impregnation models to be improved.

Keywords: Biosourced composite materials, impregnation, permeability, capillary effects, synchrotron X-ray microtomography, numerical simulations, analytical models.

Résumé

La plupart des procédés de mise en forme des matériaux composites nécessitent une phase d'imprégnation du renfort fibreux par une matrice polymère. L'optimisation de cette phase est cruciale pour éviter l'apparition de défauts tels que la porosité qui peuvent compromettre les propriétés d'utilisation finale des pièces. Celle-ci est encore plus difficile avec des renforts fibreux biosourcés. Il est donc crucial de déterminer la perméabilité des renforts fibreux en fonction de l'évolution de leur microstructure induite par les procédés de mise en forme et de contrôler la propagation du front d'écoulement de la matrice polymère en leur sein.

Nous avons ainsi étudié expérimentalement et numériquement l'évolution de plusieurs descripteurs clés de la microstructure de matériaux à base de fibres de lin au cours de leur compaction, en utilisant des images 3D obtenues par microtomographie à rayons X. Ces descripteurs ont été utilisés dans un modèle anisotrope de perméabilité de type Kozeny-Carman modifié. Les prédictions de ce modèle sont en accord avec des résultats de simulations numériques d'écoulements réalisées sur les images 3D. Cependant, dans ce modèle, un paramètre de couplage entre écoulement et microstructure est inconnu et doit être identifié par méthode numérique. Un nouveau modèle tensoriel de perméabilité complètement analytique a ensuite été construit en utilisant pour cela la méthode d'homogénéisation multi-échelles à développement asymptotique. Son originalité est qu'il tient compte des variations de distributions d'orientation des fibres. Sa pertinence a été évaluée à l'aide de résultats de perméabilité obtenus numériquement sur différents réseaux de fibres virtuels ainsi que sur des milieux fibreux réels.

Des images 3D ont également été utilisées pour étudier les phénomènes qui se produisent lors de la propagation d'un front d'écoulement de fluide au sein d'un réseau modèle constitué de fibres parallèles. Pour cela, des expériences d'imprégnation in situ ont été réalisées à l'aide de la technique ultra-rapide et à haute résolution de microtomographie à rayonnement synchrotron et d'un dispositif d'imprégnation spécialement développé. Les variations des courbures de l'interface fluide-air, des longueurs des lignes triples et des angles de contact locaux ont été quantifiées à l'aide de procédures d'analyse d'image avancées. Les forces capillaires locales et la pression capillaire ont ainsi été mesurées pendant la propagation du front d'écoulement. Ces résultats originaux permettront d'améliorer des modèles d'imprégnation théoriques et numériques dédiés aux milieux fibreux.

Mots clés: Matériaux composites biosourcés, imprégnation, perméabilité, phénomènes capillaires, microtomographie à rayons X, simulations numériques, modèles théoriques

Résumé étendu

Les matériaux composites à matrice polymère sont de plus en plus utilisés dans différents domaines tels que les transports, l'aéronautique, les industries de l'énergie ou pour la fabrication de pièces ou d'objets pour les sports et loisirs. Ces matériaux sont utilisés comme pièces semi-structurelles ou structurelles pour des applications spécifiques en raison de leurs excellentes propriétés mécaniques et de leur faible densité. Les matériaux composites classiques sont généralement renforcés par des fibres synthétiques (verre, carbone, aramide). Pour limiter l'impact environnemental de ces matériaux, l'intérêt pour l'utilisation de fibres naturelles utilisées comme renforts dans des biocomposites performants s'est accru au cours des dernières années. Cependant, ces fibres sont encore peu utilisées dans des applications industrielles, en raison de la plus grande variabilité de leurs propriétés et de problèmes spécifiques liés à leur processus d'extraction et d'utilisation dans les processus de fabrication de matériaux composites.

Les matériaux composites peuvent être fabriqués par divers procédés de mise en forme, par voie humide, tels que les procédés de la famille « Liquid Composite Moulding » (LCM), ou les procédés de mise en forme par voie sèche tels que le moulage par compression de renforts fibreux pré-imprégnés. Ces procédés impliquent la déformation du renfort fibreux et son imprégnation par une matrice polymère fluide pour obtenir la pièce finale. La maîtrise de la phase d'imprégnation est essentielle pour limiter la formation de défauts comme par exemple l'apparition de porosités ou des mécanismes de déformation hétérogènes et non maîtrisés induisant par exemple des plissements ou la séparation de mèches de fibres. Ces phénomènes, qui jouent un rôle important pendant la phase d'imprégnation, ont fait l'objet de nombreuses études.

L'écoulement d'un fluide dans la zone saturée à l'arrière du front d'imprégnation est généralement décrit par la loi de Darcy qui relie la vitesse du fluide au gradient de pression par le biais du tenseur de perméabilité $\boldsymbol{K}$. La perméabilité d'un renfort fibreux et son évolution au cours des procédés de mise en forme sont des paramètres importants pour la modélisation de la phase d'imprégnation car ils affectent le temps et le déroulement du remplissage du moule. Plusieurs études expérimentales et numériques ont eu pour objectif de simuler l'écoulement d'un fluide à travers des renforts fibreux présentant des géométries plus ou moins complexes pour comprendre le lien entre les paramètres de microstructure et la perméabilité. La plupart des expressions analytiques proposées pour l'estimation de la perméabilité sont valables pour des milieux fibreux dont la géométrie est simple (fibres à section régulière, bien réparties dans l'espace et parallèles les unes aux autres). Peu d'études ont été conduites pour des réseaux de fibres anisotropes plus complexes.

L'écoulement d'un fluide dans un renfort fibreux est également contrôlé par les effets capillaires. Les effets capillaires sont connus pour jouer un rôle central dans la propagation du front à l'intérieur et entre les mèches de fibres qui constituent en général les renforts

fibreux. La géométrie du front d'imprégnation est souvent complexe. Au cours de sa propagation, des défauts peuvent apparaître tels que des formations de porosité. Les effets capillaires sont liés à plusieurs paramètres de mouillabilité propres aux renforts fibreux et aux fluides mouillants (matrice polymère à l'état fluide) et non-mouillants (p. ex. air) en présence. Au cours des dernières années, le développement de techniques d'imagerie tridimensionnelle à haute résolution comme la microtomographie à rayons X a permis d'étudier les phénomènes d'imprégnation à des échelles microscopiques.

Dans ce contexte, les principaux objectifs de cette thèse sont de mieux comprendre, caractériser et modéliser les phénomènes d'imprégnation qui se produisent pendant la mise en forme des matériaux composites au niveau front d'écoulement et loin de celui-ci. Pour ce faire, les travaux menés s'appuient sur des approches expérimentales, théoriques et numériques. Les travaux décrits dans ce manuscrit s'articulent de la manière suivante :

- Les trois premiers chapitres du manuscrit donnent un aperçu général des matériaux composites et un état de l'art sur la perméabilité et les effets capillaires au sein des milieux fibreux.
  - Le chapitre 1 donne une vue générale du domaine des composites : types de composites, procédés de fabrication et principaux défauts associés.
  - Le chapitre 2 présente les lois qui régissent l'écoulement et les différentes techniques expérimentales, numériques ainsi que les modèles qui peuvent être utilisés pour la prédiction des propriétés de perméabilité dans les milieux fibreux saturés.
  - Le chapitre 3 se concentre sur les phénomènes capillaires. Les lois gouvernant l'équilibre de l'interface fluide-air et l'équilibre de la ligne triple air-fluide-solide sont présentées. Une description des méthodes théoriques, expérimentales et numériques de la littérature pour étudier ces phénomènes est fournie.
- Le chapitre 4 présente les principaux objectifs de ce travail de thèse.
- Les trois chapitres suivants donnent une description de la méthodologie et des résultats qui ont été obtenus. Le dernier chapitre donne la conclusion générale de ce travail et dresse quelques perspectives de poursuite de ces travaux.

Chapitre 1. Aperçu des matériaux composites et des procédés de fabrication

Ce chapitre a comme objectif de fournir une vue générale des principaux types de matériaux composites et de leurs procédés de fabrication. Un matériau composite est un matériau multiphasé constitué d'une matrice et d'un renfort fibreux. Dans le cadre de cette thèse nous faisons référence aux matériaux composites à matrice polymère (thermoplastique ou thermodurcissable) renforcée par des fibres. La nature des fibres (verre, carbone aramide ou fibres naturelles) ainsi que leur géométrie (fibre courtes ou fibres longues) peuvent varier en fonction des propriétés recherchées pour les pièces composites. Les fibres peuvent être assemblées de différentes manières pour obtenir des renforts fibreux avec des

structures unidirectionnelles, 2D ou 3D. Les procèdes de fabrication varient en fonction du type de matrice polymère, de l'architecture de renforts et des caractéristiques, notamment géométriques, des pièces à produire. Ce chapitre se focalise plus particulièrement sur quelques procédés pour lesquels la phase d'imprégnation du renfort fibreux par la matrice polymère joue un rôle majeur. On peut distinguer les procédés en voie sèche des procédés en voie liquide. Dans le premier groupe, on retrouve par exemple les procédés de mise en forme par compression de renforts préimprégnés. Dans le deuxième, on retrouve les procédés de la famille « Liquid Composite Moulding » (LCM) ou la pultrusion. Un mauvais contrôle de la phase d'imprégnation peut conduire à la formation de différents types des défauts comme à l'apparition de vides ou de déformations incontôlées des renforts néfastes à la qualité des pièces composites produites.

Chapitre 2. Écoulement de fluides dans des milieux fibreux poreux saturés

Dans ce chapitre, les lois permettant de décrire l'écoulement d'un fluide newtonien au sein d'un milieu poreux sont présentées. Généralement, l'écoulement d'un fluide dans un milieu poreux est décrit à l'échelle microscopique par les équations de Navier-Stokes. À l'échelle macroscopique, dans le cas de fluides newtoniens incompressibles, l'écoulement est décrit par la loi de Darcy :

$$\overline{\boldsymbol{v}} = -\frac{1}{\mu}\boldsymbol{K}\cdot\boldsymbol{\nabla}P \qquad (1)$$

qui relie la vitesse macroscopique de l'écoulement avec le gradient de pression à travers le tenseur de perméabilité $\boldsymbol{K}$. La perméabilité est définie comme la facilité d'un fluide à s'écouler à travers un milieu poreux. Elle correspond donc à une mesure inverse de la résistance opposée par le milieu poreux à l'écoulement du fluide. La mesure de ce paramètre est donc fondamentale pour prédire et simuler numériquement les phénomènes d'écoulement se produisant lors de la phase d'imprégnation des renforts fibreux par les matrices polymères dans les procédés de mise en forme des composites.

Les principales méthodes expérimentales, numériques et analytiques développées pour mesurer et estimer la perméabilité de milieux fibreux et poreux sont ainsi présentées dans ce chapitre. Les techniques numériques utilisées pour déterminer la perméabilité de milieux fibreux sont de plus en plus sophistiquées. Elles peuvent faire appel à l'utilisation d'images 3D de milieux virtuels générés numériquement ou de milieux imagés par microtomographie à rayons X. Les résultats expérimentaux et numériques montrent que la perméabilité des milieux fibreux dépend fortement du taux et du rayon des fibres, ainsi que de leur orientation. Sur le plan théorique, plusieurs modèles ont été développés pour prédire la perméabilité de milieux fibreux simples, constitués notamment de fibres de longueur infinie et parallèles les unes aux autres. En revanche, ces modèles théoriques ne sont pas capables de prédire la perméabilité de milieux fibreux à architecture désordonnée.

Chapitre 3. Phénomènes capillaires dans les milieux fibreux

Ce chapitre a comme objective de décrire les phénomènes capillaires se produisant au front d'écoulement où trois différents phases coexistent : le fluide, le solide et l'air. La surface qui sépare les phases liquide et l'air est appelée interface. A travers l'interface, une discontinuité de la pression peut apparaître: la pression capillaire. Dans certains cas le phénomène capillaire ne sont pas tenues en compte pour décrire l'imprégnation des matériaux fibreux car la pression externe appliqué est superiore. Par contre l'écoulement à l'échelle microscopique (écoulement à l'intérieur d'un faisceau de fibres) est contrôlé surtout par les effets capillaires qui dépendent de paramètres de mouillabilité et cela peut conduire à une propagation hétérogène du fluide et à la formation de vides. Les équations tensorielles qui régissent l'équilibre de l'interface air-fluide ainsi que l'équilibre de ligne triple sont proposé. Les paramètres de mouillabilité qui régulent l'équilibre sont l'angle de contact entre la phase solide et liquide et les tensions de surfaces. Trois cas simple pour décrire les paramètres de mouillabilité sont aussi développées : le cas de la goutté posé sur une surface, la remonté capillaire à l'intérieur d'un tube (loi de Jurin) et la formation d'un ménisque à l'extérieur d'un tube. Dans la littérature différents autours ont proposé de méthodes à la fois expérimental ou numériques pour suivre et reproduire la complexité de la propagation du front d'imprégnation. Toujours grâce au développement de la méthode d'imagerie par microtomographie à rayonne X l'études de phénomènes capillaire à l'échelle de pores ont commencé à être réalisées dans le domaine des géosciences. Les autours proposent de techniques avancées d'analyse d'images pour mesurer et estimer les paramètres locaux à partir d'images 3D (pression capillaire à partir de courbures de l'interface du front d'imprégnation, angles de contacts). Dans la dernière année certains études en utilisant ces techniques d'imagerie ont aussi été menés pour suivre la propagation d'un front fluide, la formation et le transport des vides et les phénomènes de réarrangement des fibres lors de l'imprégnation des mèches de fibres.

Chapitre 4. Objectifs de la thèse

L'étude bibliographique présentée dans les chapitres précédents a mis en évidence la complexité des procédés de fabrication des matériaux composites, plus particulièrement ceux renforcés par des fibres naturelles. Il a été montré que l'étape d'imprégnation des renforts fibreux par les matrices polymères est cruciale pour obtenir des matériaux composites avec des microstructures contrôlées et des propriétés d'usage optimisées. Pour mieux contrôler cette étape, il faut évaluer les propriétés de perméabilité des renforts fibreux en fonction de leurs caractéristiques microstructurales. Il est également nécessaire de mieux comprendre le rôle des effets capillaires sur l'imprégnation car ils peuvent conduire à des phénomènes de propagation incontrôlée du front de matière polymère à l'état fluide.

Dans ce contexte, les objectifs de cette étude sont :

- (i) de proposer un modèle de Kozeny-Carman directionnel pour la prédiction des propriétés de perméabilité des milieux fibreux à architecture désordonnée,

(ii) une méthodologie pour identifier les paramètres de microstructure des milieux fibreux/poreux apparaissant dans ce modèle, en analysant pour cela des images 3D de réseaux fibreux réels de fibres de lin, et (iii) de vérifier la validité de ce modèle par rapport à des calculs « CFD » à l'échelle des fibres réalisés directement sur ces images 3D. Les résultats de cette étude sont présentés dans le chapitre 5.

- (i) de proposer un modèle analytique et tensoriel simple pour l'estimation des composantes du tenseur de perméabilité $\boldsymbol{K}$ pour des milieux fibreux désordonnés avec des fibres discontinues qui présentent différents états d'orientation, (ii) de mesurer la pertinence de la prédiction de ce modèle par rapport à des simulations CFD réalisées sur un grand nombre de réseaux fibreux virtuels, générés numériquement, ou de réseaux fibreux réels, imagés par microtomographie à rayons X. Les résultats obtenus sont présentés dans le chapitre 6.
- (i) d'étudier en 3D par microtomographie à rayons X la propagation et la géométrie d'un front de fluide au sein de réseaux fibreux modèles sous forme de réseaux des fibres parallèles au cours d'expériences d'imprégnation et de « désimprégnation », (ii) développer ou adapter des procédures d'analyse d'images 3D afin de mesurer les paramètres locaux liés aux phénomènes de capillarité, (iii) proposer une méthodologie pour déterminer les forces et pressions capillaires locales, (iv) vérifier la pertinence des modèles mésoscopiques d'imprégnation qui sont utilisés dans le domaine des composites. Les résultats obtenus sont présentés dans le chapitre 7.

Enfin, le chapitre 8 présente les conclusions de ce travail et quelques perspectives.

Chapitre 5. Perméabilité de mats de lin: prédictions numérique et théorique à partir d'images 3D de microtomographie à rayons X

Les objectifs de ce chapitre est d'étudier la microstructure d'un mat de lin et son évolution au cours d'un essai de compression afin de reproduire les phénomènes de compaction qui se produisent dans de nombreux procédés de mise en forme des composites. Dans ce but, des expériences de compression in situ ont été réalisées en utilisant la microtomographie à rayons X. Les expériences d'imagerie ont été réalisées sur la ligne ID19 de l'ESRF à Grenoble. L'analyse des images tridimensionnelles a permis de quantifier l'évolution de plusieurs descripteurs clés de la microstructure des mats pendant leur compaction : le rayon moyen des fibres $\bar{r}_s$, la porosité $\bar{\phi}_p$, le taux des fibres $\bar{\phi}_s$, la surface spécifique S_v et la tortuosité directionnelle τ_i. Les résultats montrent que la porosité diminue pendant la compaction, le diamètre des fibres reste inchangé, la surface spécifique augmente ainsi que la tortuosité directionnelle. Ensuite, les images 3D ont été importées dans un code de simulation d'écoulement de fluides en milieux poreux. Les composantes du tenseur de perméabilité $\boldsymbol{K}$ ont ainsi pu été estimées pour les différentes étapes de compression. Les résultats de perméabilité confirment le comportement isotrope transverse du mat de lin et montrent une décroissance non-linéaire de la perméabilité au cours de la compaction.

Les paramètres de microstructure obtenus à partir des images 3D ont aussi été utilisés comme paramètres d'entrée d'un modèle de type Kozeny-Carman « directionnel ». Ce modèle s'écrit selon l'équation suivante :

$$K_i^* = \frac{(1-\bar{\phi}_s)^3}{2c_i S_v^2 {\tau_i}^2} \frac{1}{\bar{r}_s^2} \tag{2}$$

Les valeurs du paramètre directionnel c_i ont été identifiées par une méthode inverse à partir de calculs de perméabilité de réseaux 3D de fibres générés numériquement mimant la microstructure des mats de lin. Cette approche a permis d'identifier les paramètres c_i dans le plan et hors du plan en fonction de la fraction volumique de fibres. Les valeurs de perméabilité obtenues par ce modèle sont proches de celles obtenues par simulation numérique.

Chapitre 6. Modèle de perméabilité analytique pour des réseaux à architecture fibreuse désordonnée

Dans ce chapitre, nous proposons un modèle analytique tensoriel pour la prédiction des propriétés de perméabilité de réseaux fibreux présentant différentes distributions d'orientation de fibres, c'est-à-dire des réseaux de fibres alignées ou légèrement désalignées, des réseaux à orientation de fibres plane et aléatoire ou présentant une orientation privilégiée des fibres dans un plan ainsi que des réseaux 3D à orientation de fibres isotrope. Le modèle tensoriel proposé a été construit en s'appuyant sur une méthode d'homogénéisation multi-échelle par développements asymptotiques et en utilisant des hypothèses simplificatrices pour la microstructure fibreuse et les forces hydrodynamiques visqueuses locales exercées par le fluide newtonien en écoulement sur les segments de fibres. Après simplification le modèle tensoriel de perméabilité s'écrit de la manière suivante pour un réseau fibreux homogène constitué de fibres élancées à section circulaire :

$$\boldsymbol{K}^{-1} = \frac{1}{k_L}\boldsymbol{A} + \frac{1}{k_T}(\boldsymbol{I} - \boldsymbol{A}) \tag{3}$$

où $\boldsymbol{A}$ est le tenseur d'orientation d'ordre 2 des segments de fibres et k_L et k_T sont les perméabilités longitudinale et transverse.

Dans ce chapitre, les coefficients k_L et k_T ont été choisis à partir de deux modèles analytiques de la littérature : le modèle dit hybride pour le coefficient transversal et un modèle proposé par Drummond et Tahir pour le coefficient longitudinal. Les prédictions du modèle proposé ont été comparées aux résultats de perméabilité obtenus par simulation numérique en utilisant des images 3D de réseaux fibreux virtuels générées numériquement ou des images 3D de réseaux fibreux réels obtenues par microtomographie à rayons X. Cette comparaison montre que le modèle analytique est capable de prédire la dépendance des propriétés de perméabilité des réseaux avec l'orientation fibreuse. Plus particulièrement, le modèle donne une bonne prédiction des propriétés de perméabilité pour des réseaux fibreux concentrés et/ou présentant des distributions spatiales de fibres

homogènes. En revanche, des écarts entre les prédictions du modèle et les données de perméabilités numériques ont été observés pour des réseaux fibreux virtuels hétérogènes ainsi que pour des réseaux fibreux réels (mats et UD à base de fibres de lin) constitués de fibres biosourcées ayant une géométrie complexe (fibres présentant des distributions de taille polydisperses et des géométries de sections droites complexes).

Chapitre 7. Observations 3D in situ des phénomènes d'imprégnation se produisant dans des arrangements parallèles de fibres rigides

Ce chapitre vise à étudier les phénomènes d'imprégnation se produisant dans des réseaux de fibres rigides alignées. Pour ce faire, des expériences d'imprégnation in situ couplées à des observations 3D par microtomographie à rayonnement synchrotron ont été réalisées. Ces expériences ont consisté à imprégner ou « désimprégner » progressivement un réseau de fibres alignées par un fluide mouillant en utilisant un dispositif d'imprégnation spécialement conçu et réalisé pour cela. Deux fluides mouillants au comportement newtonien ont été utilisés pour réaliser les expériences d'imprégnation : de l'eau déminéralisée et de l'huile silicone. Le dispositif d'imprégnation constitué d'un réservoir rempli de fluide et d'un système de maintien du réseau de fibres a été installé sur le microtomographe à haute résolution de la ligne ID19 de l'ESRF. Ces expériences originales nous ont permis d'acquérir des images 3D du réseau de fibres alignées pour différentes étapes d'imprégnation et de désimprégnation. À partir de ces images, il a été possible de suivre en 3D la propagation et la géométrie du front de fluide au sein du réseau fibreux. Les images 3D obtenues ont été trinarisées afin de séparer les trois phases fluide, fibres et air. Une procédure numérique d'analyse des images 3D trinarisées a ensuite été spécifiquement développée afin de mesurer les longueurs des lignes triples que le fluide forme autour de chaque fibre du réseau et les angles de contact fluide-fibre le long des lignes triples. Une procédure numérique a également été utilisée pour mesurer la courbure moyenne locale de l'interface air-fluide. Les résultats obtenus ont révélé que la valeur de l'angle de contact varie de manière significative le long des lignes triples et que la valeur moyenne de l'angle de contact tend à augmenter au cours des étapes d'imprégnation par trempage et à diminuer au cours des étapes de désimprégnation. À partir des mesures de courbures moyennes locales de l'interface air-fluide, de longueurs de lignes triples et d'angles de contact, il a été possible d'estimer la pression capillaire locale et les forces capillaires transverses et longitudinales locales exercées par le fluide sur chaque fibre constituant le réseau fibreux. Ces mesures originales ont notamment permis de mettre en évidence le fait que lors de l'imprégnation longitudinale d'un réseau de fibres rigides alignées, les forces capillaires transversales exercées par le fluide sur les fibres situées à l'extérieur du réseau sont du même ordre de grandeur que les forces capillaires longitudinales. Ces mesures de forces capillaires locales sont intéressantes car elles peuvent permettre de mieux appréhender les phénomènes de réorganisation et de déformation des renforts fibreux constitués de fibres déformables qui sont susceptibles de se produire au cours de leur imprégnation par des matrices polymères.

Chapitre 8. Conclusion générale et perspectives

De manière générale, ce travail visait à mieux comprendre, caractériser et modéliser les phénomènes d'imprégnation se produisant au cours de la mise en forme des matériaux composites à renforts biosourcés. Ainsi, dans le chapitre 5, les objectifs étaient d'étudier l'évolution de la microstructure et des propriétés de perméabilité d'un mat de fibres de lin soumis à un essai de compression hors plan. Pour ce faire, nous avons réalisé des expériences de compression in situ en utilisant une micro-presse installée sur le microtomographe haute résolution de la ligne ID19 de l'ESRF. Ces expériences nous ont permis d'obtenir des images 3D du mat de fibres de lin et de suivre l'évolution de plusieurs descripteurs de la microstructure au cours de la compression du mat comme la porosité, le diamètre des fibres, la surface spécifique et la tortuosité directionnelle. Les images 3D obtenues par microtomographie à rayons X ont également été importées dans un code de simulation numérique d'écoulement de fluide. Grâce à ces simulations, nous avons pu quantifier l'évolution des composantes du tenseur de perméabilité au cours de la compaction du mat. Les perméabilités obtenues numériquement ont été comparées avec celles prédites analytiquement en utilisant un modèle « directionnel » de Kozeny-Carman modifié dont les principaux paramètres de microstructure comme la porosité, surface spécifique et tortuosité ont été mesurés à partir des images 3D. Il serait intéressant de tester le modèle directionnel de Kozeny-Carman sur un plus grand nombre de milieux fibreux isotropes transverses soumis à divers modes de déformations thermo-hygromécaniques.

L'approche développée dans le chapitre 5 montre qu'un modèle simple de type Kozeny-Carman modifié peut être utilisé pour prédire les propriétés de perméabilité de milieux fibreux à architecture désordonnée. Cependant, ce modèle requiert la connaissance d'un paramètre de couplage entre la microstructure poreuse/fibreuse et l'écoulement qui ne peut pas être identifié facilement. En effet, nous avons montré dans le chapitre 5 que ce paramètre de couplage peut être identifié par méthode inverse à partir de simulations numériques réalisées sur des réseaux fibreux virtuels générés numériquement. Ainsi, dans le chapitre 6, nous avons proposé un modèle de perméabilité analytique pour les milieux fibreux à architecture désordonnée. Dans ce modèle, le tenseur de perméabilité $\boldsymbol{K}$ dépend de deux coefficients de perméabilité pondérés par le tenseur d'orientation du second ordre des segments de fibres. Les deux coefficients de perméabilité intervenant dans ce modèle peuvent être obtenus en utilisant des modèles analytiques de la littérature. Les résultats obtenus dans ce chapitre ont montré que le modèle est performant pour prédire les propriétés de perméabilité de milieux fibreux concentrés et/ou de milieux fibreux constitués de fibres élancées et présentant une répartition spatiale des fibres homogène. Ce modèle pourrait être enrichi en prenant en compte la longueur finie des fibres (effet des extrémités des fibres).

Dans le chapitre 7, nous avons étudié, en utilisant une approche expérimentale originale, les phénomènes d'imprégnation se produisant dans des réseaux de fibres rigides alignées dont l'architecture se rapproche de celle des mèches de fibres utilisées dans les renforts de matériaux composites. L'approche expérimentale développée dans ce chapitre a consisté à

observer en 3D la propagation et la géométrie d'un front de fluide au sein d'un réseau fibreux en utilisant pour cela la microtomographie haute résolution à rayonnement synchrotron au cours d'expériences d'imprégnation et de désimprégnation. Grâce à l'analyse des images 3D obtenues nous avons pu mesurer les pressions capillaires ainsi que les forces capillaires transverses et longitudinales exercées par le fluide sur chaque fibre du réseau fibreux. Cette approche pourrait être étendue à l'étude des phénomènes capillaires se produisant au cours de l'imprégnation de réseaux de fibres plus complexes, par exemple constitués de fibres déformables. Il serait également intéressant de poursuivre ce travail sur des réseaux de fibres biosourcées ce qui nous permettrait de mieux appréhender les phénomènes couplés d'écoulement du fluide et de gonflement des fibres qui interviennent au cours de l'imprégnation des milieux biosourcés.

Table of contents

General introduction

Polymer matrix composites are increasingly used in different domains such as transportation, aeronautic, energy industries or for sport manufacturing. These materials are used as semi-structural or structural parts for specific applications due to their excellent mechanical properties and low density. The main elements of a composite material are the polymer matrices and the reinforcing materials that are often fibrous media. Classical composite materials are reinforced with synthetic fibres (glass, carbon, aramid). Because of environmental and sustainability issues, the interest in using natural fibres to obtain high-performance biocomposites has been increasing worldwide. However, there are still poorly used in industrial applications, owing to the greater variability of their properties and the specific issues related to their manufacturing processes. Composite materials can be fabricated using various processes, depending on the nature of the matrix (thermoplastic or thermoset matrix) and the fibrous reinforcement (continuous or discontinuous fibre reinforcements). Several families of manufacturing processes can be identified, e.g. (i) wet forming processes such as Liquid composite Moulding (LCM) or pultrusion processes or (ii)dry forming processes such as compression moulding of preimpregnated fibre reinforcements. These processes involve the deformation of the fibrous reinforcement and its impregnation by a fluid polymer matrix to obtain the final parts.

The composite parts that are fabricated using these processes often exhibit multiscale defects that are detrimental for their end-use properties. The formation of voids or pores between or inside the fibre bundles or yarns that constitute the fibre reinforcement is one of the most frequent defects. As well wrinkling of the reinforcement, buckling of fibre bundles/yarns or separation phenomena of fibre bundles/yarns can appear during the various process phases and more particularly during the impregnation phase. Therefore, several studies were carried out to investigate all the mechanisms that play a role during the impregnation phase.

When a fluid starts to impregnate a fibrous reinforcement, three principal zones can be identified in the fibre reinforcement: (i) the saturated zone where the fluid completely impregnates the fibrous network, (ii) the unsaturated zone behind the fluid front where there is still the presence of air, and (iii) the fluid front. The flow of the fluid in the saturated zone is usually described by Darcy's law which relates the fluid velocity to the pressure gradient through the permeability tensor $\boldsymbol{K}$. The permeability of a fibrous reinforcement is thus one of the most important input parameter for the modelling of the impregnation phase since it governs, for instance, the mould filling time and resin flow patterns.

Many studies have been conducted and are still ongoing with the aim of (i) reproducing experimentally or with numerical simulations the flow of fluids through fibrous reinforcements and (ii) understanding the effect of microstructural descriptors on

permeability properties. It was demonstrated that permeability strongly depends on the fibre volume fraction, geometry, spatial distribution, architectures and orientation. Many authors proposed theoretical expressions to determine permeability, knowing microstructural descriptors. While a huge number of studies were conducted on simple fibrous networks, e.g. fibres with regular cross sections that were well distributed in space and with a unidirectional orientation, few theoretical studies focused on more complex anisotropic fibre networks. The determination of microstructure descriptors and the formulation of theoretical expressions that are able to take into account the complexity of real fibrous networks still constitute a challenge. This is even more true for fibrous reinforcements made of natural fibres. These points deserve to be further investigated to improve impregnation models for composite manufacturing processes.

The flow of a fluid through a fibre reinforcement is also controlled by the capillary effects that act at the fluid front. While from a macroscopic point of view the fluid front can often be simplified as a sharp interface that moves through the fibrous network during the impregnation, the shape of the fluid front is really complex at the fibre scale. The complexity of the geometry of this interface can be one of the major sources of void entrapments during the impregnation phase. For these reasons, it is of great interest to better describe and model the propagation of the fluid front and the complex evolution of its geometry. Capillary effects are known to play a central role on the front propagation. These effects depend on several parameters related to the fluid, fibres and fibrous networks (contact angles, fluid tension surface, fibre surface energy, etc.).

Synchrotron X-ray microtomography imaging has been increasingly used to study the microstructure of composites and fibrous materials in various situations. More recently, thanks to the improvement in scanning time, image resolution and image analysis methods, this imaging technique was used to investigate transient phenomena such as the evolution of porosity or fibre orientation, fibre deformation, fibre-matrix segregation that occur during composite processing because of thermomechanical loadings. Advanced use of this technique has also allowed recent progress in the study of capillarity-related phenomena in geomaterials. More recently, the advantage of this technique has been showed for the study of the impregnation of fibre reinforcement in composite materials.

In this context, the main objectives of this PhD thesis is to better understand, characterise and model the impregnation phenomena that occur within fibre reinforcement materials, and in particular those made of plant-based fibres, at the flow front and far from it. This was done by performing original in situ impregnation experiments coupled with X-ray microtomography imaging and fibre scale fluid flow numerical simulations on model and real fibrous materials combined with theoretical modelling.
The manuscript is organised as follows:

- The first three chapters of the manuscript give a general overview of composite materials and a state of the art on permeability and capillary phenomena in fibrous media.

  - Chapter 1 provides a general view of the composite domain: type of composites, fabrication procedures and typical defects that can occur during the manufacturing processes.
  - Chapter 2 briefly presents the laws that govern the fluid flow in a fibre and porous material in saturated conditions. The different numerical approaches and models that can be used for the determination or the prediction of the permeability of fibrous media are presented.
  - Chapter 3 focuses on capillary phenomena in fibrous media. Governing laws for the fluid-air interface and triple line equilibrium are presented. A description of the experimental, numerical and theoretical methods that are used in the literature to investigate these phenomena is provided.
- Chapter 4 gives the main objectives of this work.
- The last three chapters give a description of the methodology and the results that have been obtained.
  - Chapter 5 focuses on the determinations of microstructure descriptors from 3D images obtained during in situ compression experiment performed on a flax fibre mats. These parameters are then used to feed a modified Kozeny-Carman model for anisotropic fibrous networks. Finally the predictions of this model were compared with fibre scale CFD simulation results.
  - In Chapter 6 an analytical tensorial model is proposed for the permeability estimate of complex fibrous networks that exhibit varying fibre orientations. The robustness of this model was assessed with respect to permeability results obtained from fibre scale CFD simulations on a large number of virtual and real fibrous networks.
  - Chapter 7 is dedicated to the 3D characterisation of the propagation of a flow front through a model fibre network, using synchrotron X-ray microtomography 3D images. Several original results such as measurements of local contact angles, triple line lengths, fluid interface curvatures and local capillary pressures are shown and discussed.

Chapter 1

Review of composite materials and main fabrication processes

1.1 Introduction to composite materials

A composite material is a multi-phase system composed of a matrix material and a reinforcement material.
The main interest of combining two materials with different physical and chemical properties is to obtain a new material with "improved" end-use properties (lightweight, strength, stiffness, corrosion resistance, thermal and acoustic insulation) specific for a given application. Composite materials are widely used as structural or multi-functional parts in many engineering domains such as aeronautic, automotive, construction and energy (Figure 1.1).

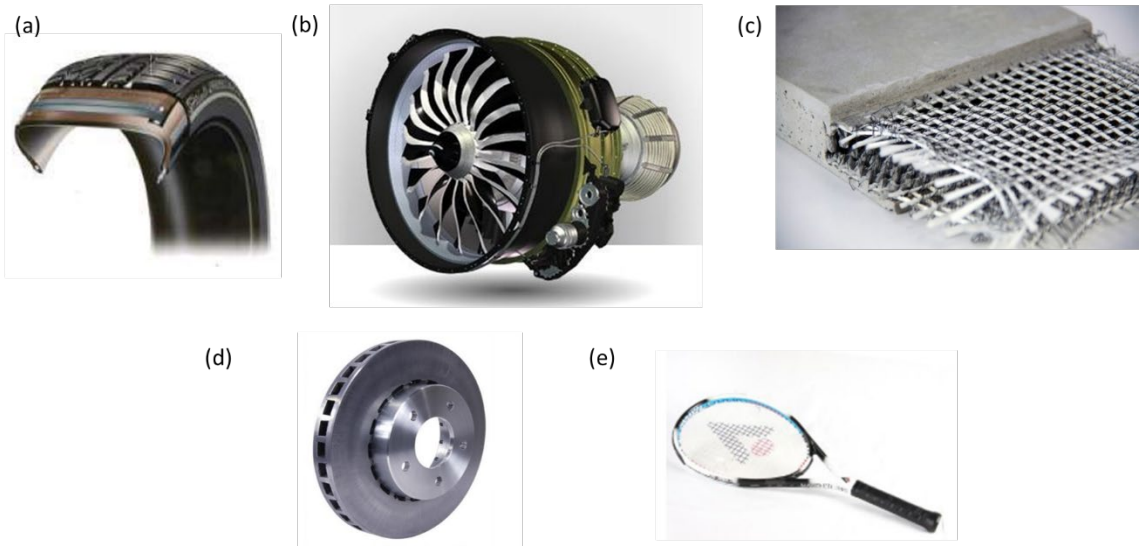

Figure 1.1. Examples of different composite materials used in various engineering applications: (a) car tires made of polymer matrix composites (PMCs), (b) ceramic matrix composite (CMC) used in a turbofan engine, (c) fibre-reinforced concrete used in civil engineering, (d) aluminium metal matrix composite (MMC) used in automotive car brake, (d) sport equipment (tennis racket) reinforced with carbon fibres.

There are many ways to classify composite materials, depending on the viewpoint.

1- Classification in accordance with the type of matrix:
   a. Metal matrix composites (MMC's), used especially in the aerospace domain but also for bicycles, electronic substrates or automobiles;
   b. Inorganic non-metallic matrix composite materials such as ceramic matrix composites (CMC's) used for applications in extreme conditions (high temperatures), e.g. components for gas turbine, burners, heat shield system for aerospace;
   c. Polymer matrix composites (PMC's), thermosetting or thermoplastic resin-based composites.
2- Classification in accordance with the nature of reinforcing fibres:
   a. Carbon fibre composite materials;
   b. Glass fibre composite materials;

c. Biocomposites;
d. Organic fibre composite materials;
e. Boron fibre or silicon carbide fibre composite materials;
f. Hybrid fibre composite materials.

3- Classification in accordance with the type of reinforcement:
a. Fibre-reinforced composite materials that can be continuous or discontinuous (short) fibre reinforced composite materials;
b. Structural composite materials: laminate or sandwich panels;
c. Particle reinforced composite materials.

In the following sections polymer matrix composites will be presented in detail, considering biocomposites, i.e., reinforced materials composed of plant-derived or plant-extracted or animal-derived or animal-extracted fibres or matrices.

1.1.1 Fibre-reinforced polymer matrix (FRP) composites

1.1.1.1 Types of polymer matrices

A polymer matrix material is a continuous phase. Its main functions are:
- to bond fibres together and ensure the force transmission between the fibres;
- to maintain the orientation of fibres and prevent the fibres from buckling and wearing;
- to protect fibres from the environment.

Many properties of composite materials such as heat-resistance, corrosion resistance, flame retardance, solvent resistance and low moisture absorption are mainly determined by the matrix.
The polymer matrices of commercial PMC's can have petrosourced or biosourced origins. Polymer matrices are mainly made of thermoset or thermoplastic polymers or elastomers.

Table 1.1. Mechanical properties of common thermoplastic and thermoset polymers used to fabricate composite materials.

	Density	**Young's modulus**	**Maximum strength**	**Elongation to break**	**Use temperature**
	ρ (g/cm^3)	E (GPa)	σ_r (MPa)	ε (%)	T (°C)
Epoxy (TS)	1.1-1.4	3-4	70-90	4	150
Polyester (TS)	1.1-1.5	2.8-4.5	20-70	5	80
Polypropylene (TP)	0.9	1.1-1.6	30-40	100-600	260
Polyamide (TP)	1.14	1-3.5	50-80	45	260-400
PLA	1.2	0.35-1.4	20-30	2.5-6	150
PHA	1.3	2.7-3.4	20-100	2-1000	60-150

Thermosetting polymers harden/solidify by an irreversible chemical reaction of two components: the monomer or pre-polymer and the hardener or catalyst to form chemical bridges. This reaction called curing crosslinks the polymer chains and thus connects the entire matrix together in a three-dimensional network. Once fully cured, these materials cannot be reshaped upon heating. This type of polymers includes unsaturated polyesters (UPR), vinylesters, epoxies, bismaleimides. Thermosets, because of their three-dimensional crosslinked structure, tend to have high dimensional stability, high-temperature resistance, good resistance to solvents and hydrocarbons and high mechanical properties usually higher than thermoplastic polymers (Table 1.1). In their uncured state, the viscosity of the resin systems ranges from 0.1 to 1 Pa s, i.e. 2 or 3 orders of magnitude higher than that of water at room temperature. The processing temperature of these resins typically ranges from room temperature to about 200°C.
Thermosetting unsaturated polyester resins are the most common matrices used in fibre reinforced composites because of their low prices with respect to epoxy resins, and ease of use. These matrices can be cured in a mould at room temperature and at atmospheric pressure. Epoxy resins are also used for PMC's since the 1930's: the advantage of using epoxy matrices is given by their high mechanical strength (Table 1.1) and good chemical corrosion resistance.

Amorphous or semi-crystalline thermoplastic polymers consist of long macromolecular chains that form a viscous liquid at the processing temperature (that ranges from ca. 120°C to 400°C). After processing, these matrices are cooled and form an amorphous or semi-crystalline solid. The degree of crystallinity has a strong effect on the final properties of thermoplastic matrices. Thermoplastic polymers are considered to be solid when cold (below the glass transition temperature T_g) and plastified/melted for temperatures well above T_g. This is in this range of temperature that the TP polymers are usually used. Unlike the curing process of thermosetting resins, the processing of thermoplastics is reversible, and, in principle, by simply reheating to the process temperature the TP polymers can be formed into another shape, if desired. Thermoplastic polymers, also called sometimes engineering plastics, include some polyesters, poly-etherimide, polyamide (PA), polyphenylene sulphide (PP), polyether-etherketone (PEEK), and liquid crystal polymers.
Thermoplastic matrices are usually less dense than thermosets making them a viable alternative for weight critical applications. Moreover, they are more resistant to cracking and impact damage and can be easily stored. The negative aspects of this type of polymers is that they are sensitive to organic solvents.

Elastomers are usually thermosets but may also be thermoplastics, depending on whether they are subjected or not to a post-curing stage. Indeed, various chemical processes such as, for example, sulphur vulcanisation, can be used to cross-link the long polymer chains. Several elastomers such as natural rubber (NR), butadiene rubber (BR), isoprene rubber (IR), chloroprene rubber (CR), isobutylene–isoprene rubber (IIR), acrylonitrile–butadiene rubber (NBR), and styrene–butadiene rubber (SBR) are the most commonly used rubber

types (N. Dishovsky & M. Mihaylov, 2018). The main remarkable characteristic of elastomers is their elastic deformation higher than 200%.

These types of matrices are produced with raw materials from oil industry. In the last years, petrosourced thermoset and thermoplastic resins began to be replaced with biosourced polymers derived from renewable raw materials (plants, wood). The most used **biopolymers** are the PHA (polyhydroxyalkanoate) and the PLA (polylactic acid) derived from agricultural resources through bioconversion and polymerization. Biosourced matrices are not largely used in industrial applications, mainly because of their cost (2 to 10 times higher than that of oil-sourced matrices), their poorer mechanical characteristics and their low thermal stability. These biopolymers have, due to their oxygen-rich chemical structure, a sensitivity to moisture, which can considerably complicate their use (problem of degassing, degradation of the degree of polymerisation by hydrolysis). Thus, it is often necessary to modify biopolymers because of the difficulties encountered during their forming processes and their poor mechanical properties.

1.1.1.2 Fibre reinforcements

The second constituent that forms a composite material is the reinforcement material whose main function is to improve mechanical properties.
The reinforcement material can have more or less complex geometry and usually consists of an assembly of individual filaments or fibres, as referred to in the textile literature, with a diameter of the order of 5-20 μm. The most common fibres used for composite materials are synthetic fibres (carbon, glass, aramid) or natural fibres (wood, flax, hemp, cotton…). Nowadays even if the use of synthetic fibres for the production of composite materials is still considerably higher (87% of total production, cf. Figure 1.2) than that of natural fibres, because of the increasing of environmental concerns, the development of biocomposites has become an emerging area of interest for several applications. As shown in Figure 1.2, in the last decay, plant, cotton fibre and wood plastic composites represented ≈13% of 2.4 million tonne EU FRP market.

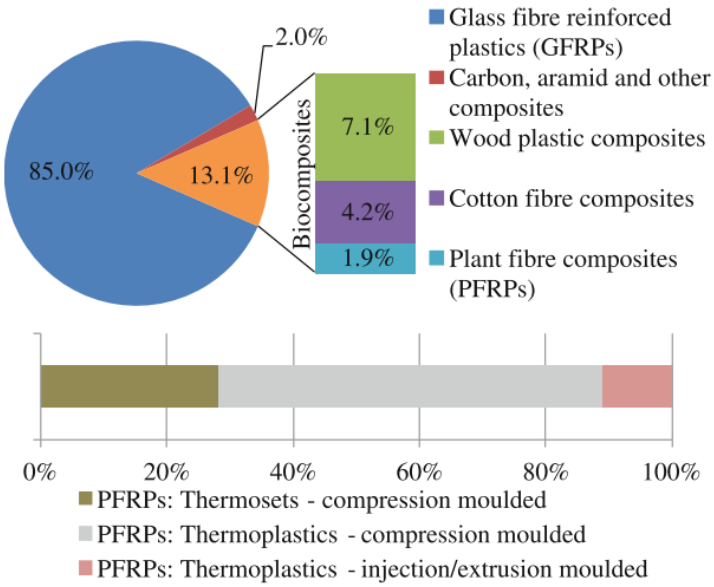

Figure 1.2. Natural fibre reinforced composite materials account for 13% of the 2.4 million tonne EU FRP market in 2010 (Shah, 2013).

1.1.1.2.1 Synthetic fibres

Glass, carbon and aramid fibres are the most common synthetic fibres used as reinforcement materials in composite materials (Figure 1.3).

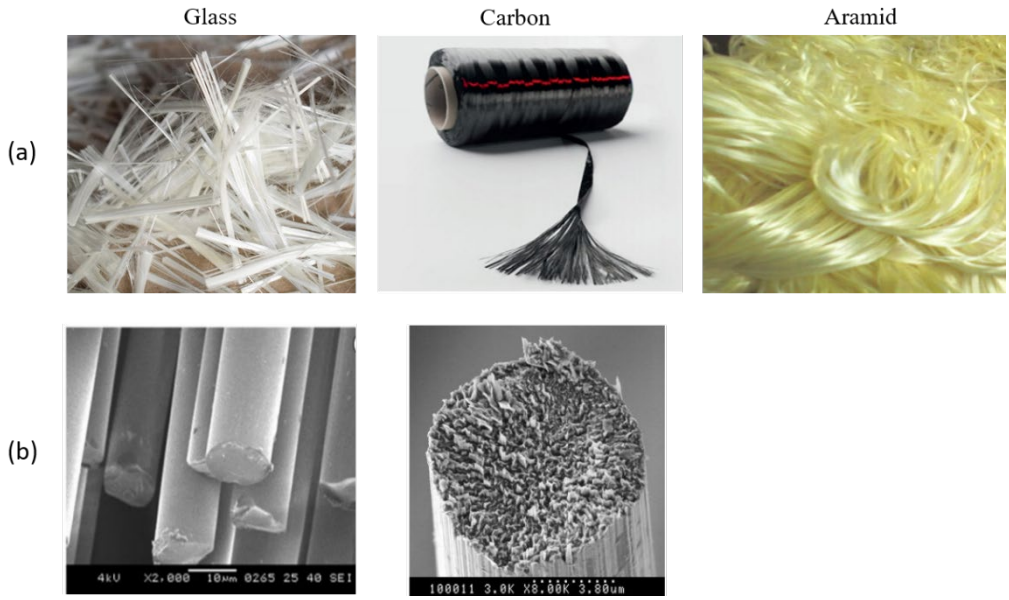

Figure 1.3. (a) Photographs of synthetic fibre bundles: glass fibres, carbon fibres, and aramid fibres. (b) SEM micrographs showing the geometry of cross sections and microstructure of glass and carbon fibres.

Glass fibres have a diameter that ranges between 5 µm and 25 µm. These fibres are available in a variety of shapes and forms and find applications in different domains such

as in automotive, marine industries, in civil constructions but also for the production of sporting goods.

Carbon fibres which diameter ranges between 5 µm and 8 µm are commonly used in aerospace industries due to their high strength, high stiffness and low density (Table 1.2).

Aramid fibres have a diameter of about 12 µm. They are characterized by high specific strength and heat-resistance. **Kevlar** is a well-known aramid fibre developed by Kwolek at DuPont in 1965. These fibres are mainly used for safety or sport clothes or in the aeronautic industry due to the lightweight, high fatigue and abrasion resistance, high tensile strength-to-weight ratio and high thermal stability.

Table 1.2. Mechanical properties of glass, carbon and Kevlar fibres (Latil, 2012)

	Density	**Young's modulus**	**Maximum strength**	**Elongation to break**
	ρ (g/cm^3)	E (GPa)	σ_r (MPa)	ε (%)
E-glass	2.6	73	3400	2.5
R-glass	2.53	86	4400	5.4
HM carbon	1.95	500	2300	0.5
HT carbon	1.85	230	4000	1.4
Kevlar	1.44	120	3100	3.5

1.1.1.2.2 Natural fibres

Natural fibres (Figure 1.4) used for composite materials can be classified according to their origin:

- Bast fibres (flax, hemp, jute, kenaf, ramie, bamboo);
- Leaf fibres (sisal, henequen, pineapple, abaca);
- Seed or fruit fibres (cotton, coconut, coir and oil palm);
- Others (wood and roots).

The advantages of natural fibres are their low cost of production (1.5-2 €/kg for flax fibres, less than 1 €/kg for bleached wood fibres), low density ($\rho \approx 1200\text{-}1400$ kg.m^{-3}), acceptable strength and stiffness ($E \approx 10\text{-}60$ GPa, $\sigma \approx 400\text{-}700$ MPa). The most important interest for the industry is the ecological aspect since they come from renewable resources and they are recyclable so they might be a sustainable alternative to the traditional E-glass fibres (Martoïa, 2015).

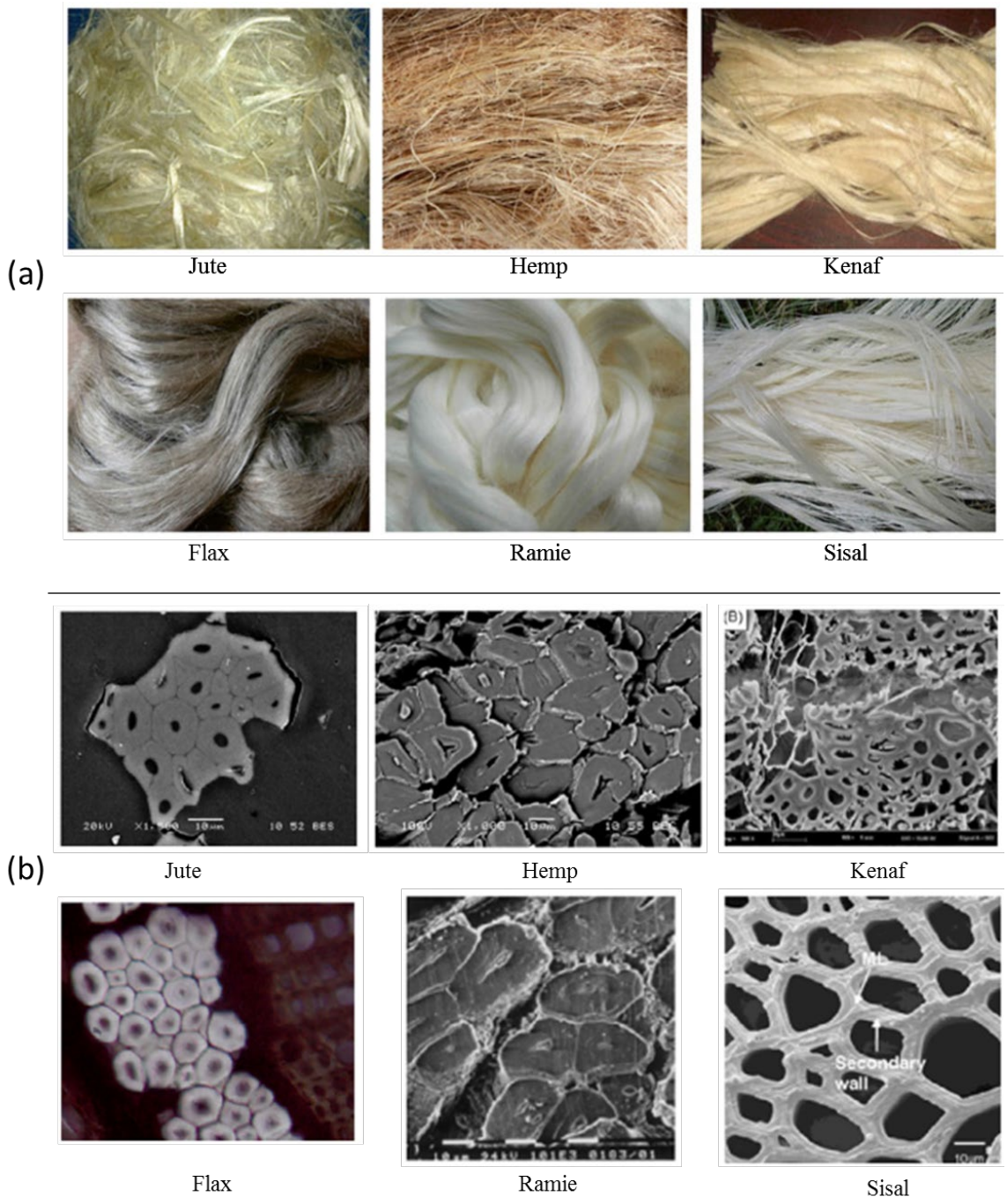

Figure 1.4. (a) Photographs of different types of plant fibre bundles used as reinforcement materials in biocomposite materials (Dumont et al. 2016) (b) SEM images of the respective plant fibre cross sections (Bourmaud et al., 2018).

The major constituents of natural fibres are microfibrils of cellulose (≈40%), hemi-celluloses (≈30%) and lignin (≈30%): the content of cellulose can vary according to the species and the age of the plants. The structure of an elementary natural fibre is illustrated in Figure 1.5. The plant fibres are constituted by cell walls (P, S_1, S_2, S_3) surrounding a central lumen. The cell wall is constituted of several layers: the first layer, deposited during the cell growth, where the microfibrils (0.5 µm of diameter) have a disordered

orientation, and the secondary cell wall composed of three layers. Between the different layers (S_1, S_2, S_3), the arrangement of microfibrils can change considerably. At smaller scale, cellulose microfibrils are composed of bundles of cellulose nanofibrils (diameter 10-100 nm) made of elementary fibrils (diameter 3.5-5 nm). The cellulose nanofibrils are referred to in literature as CNFs. The outer cell wall of plant and wood fibres is porous and contains most of the non-cellulose compounds, proteins, inorganic salts that determine the wettability and absorption properties of the fibre. The lumen also contributes to the water absorption typical of plant fibres. The diameter of an elementary plant fibre is around 10 to 50 µm and their typical length is around 10 to 250 mm (the average length for industrial applications is 80 mm).

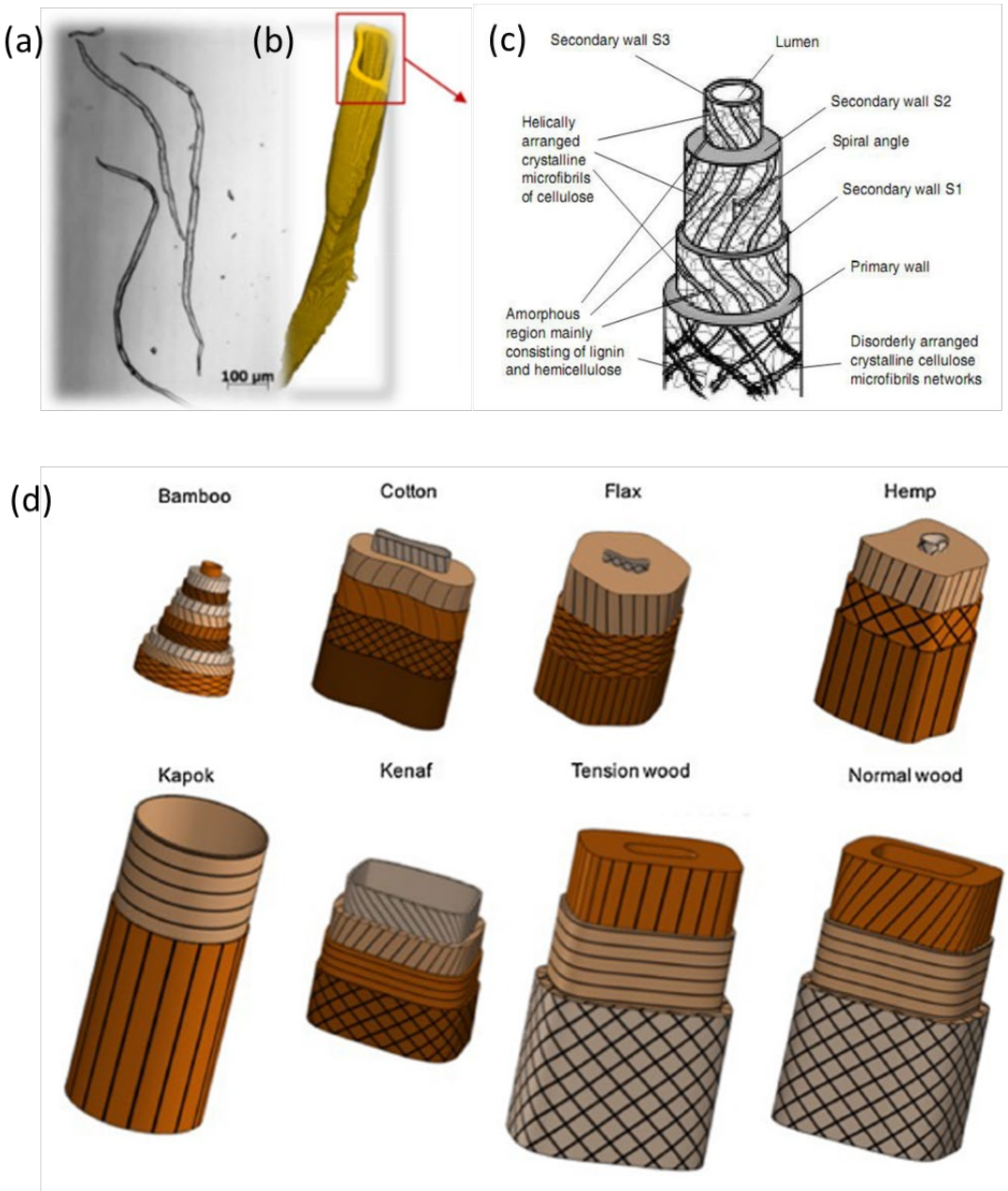

Figure 1.5. (a) Micrograph of eucalyptus wood fibres obtained by optical microscopy showing three elementary fibres. (b) 3D X-ray microtomography image of a softwood fibre (Toungara et al., 2015). (c) Scheme of the elementary structure of a natural

fibre (Nguyen, 2014). (d) Schematic representation of the structure of several plant and wood fibres (Bourmaud et al., 2018).

A comparison of the mechanical properties of various natural and synthetic fibres is presented in Table 1.3. It is observed that several plant fibres, including flax, hemp, and jute, have better specific (longitudinal) tensile stiffness than E-glass fibres. Moreover, the advantages of plant fibres with respect to synthetic fibres are their lower density, reduced abrasion to processing machinery, and CO_2 neutrality. On the other hand, the specific tensile strength of plant fibres is consistently lower than that of synthetic fibres (Nguyen, 2014; Shah, 2013). The main drawbacks of the natural fibres are the large dispersion of their morphology and intrinsic mechanical properties compared to synthetic fibres (Charlet et al., 2010), their poor interfacial adhesion and poor dispersion in most of hydrophobic thermoplastic matrices (Eichhorn et al., 2001). For this reason, natural fibres undergo chemical or physical treatments to modify their physico-chemical properties.

Table 1.3. Mechanical properties of some plant and wood fibres

	Diameter range	**Density**	**Young's modulus**	**Maximum strength**	**Elongation to break**
	D (mm)	ρ (g/cm^3)	E (GPa)	σ_r (MPa)	ε (%)
Cotton	12-38	1.5	5-13	287-597	7-8
Jute	10-25	1.3	25-55	393-773	1.5-1.8
Flax	5-38	1.5	28-100	345-1035	2.7-3.2
Hemp	10-51	1.4	32-60	285-690	0.8-1.6
Sisal	8-41	1.5	9-28	511-635	2-2.5
Coir	-	1.2	4-6	175-340	15-45
Bamboo	-	0.8	11-30	391-1000	-
Pineapple	-	1.6	34.5-82.5	413-1267	0.8-1.6
Softwood	-	1.5	15-40	550-1000	-
Ramie	11-80	1.5	34.5-82.5	400-938	3.6-3.8

1.1.1.2.3 Regenerated cellulose fibres

The use of cellulose regenerated fibres as reinforcement materials in composites has been the subject of a lot of research studies (Bledzki & Gassan, 1999; Faruk et al., 2012; Satyanarayana et al., 2009) and nanocomposites (Berglund, 2005). Different types of regenerated fibres have been obtained by dissolving cellulose pulp in a suitable solvent and subsequently spinning the ensuing solution. The most widely regenerated fibres available in the market are: viscose, modal and Lyocell fibres (Figure 1.6).

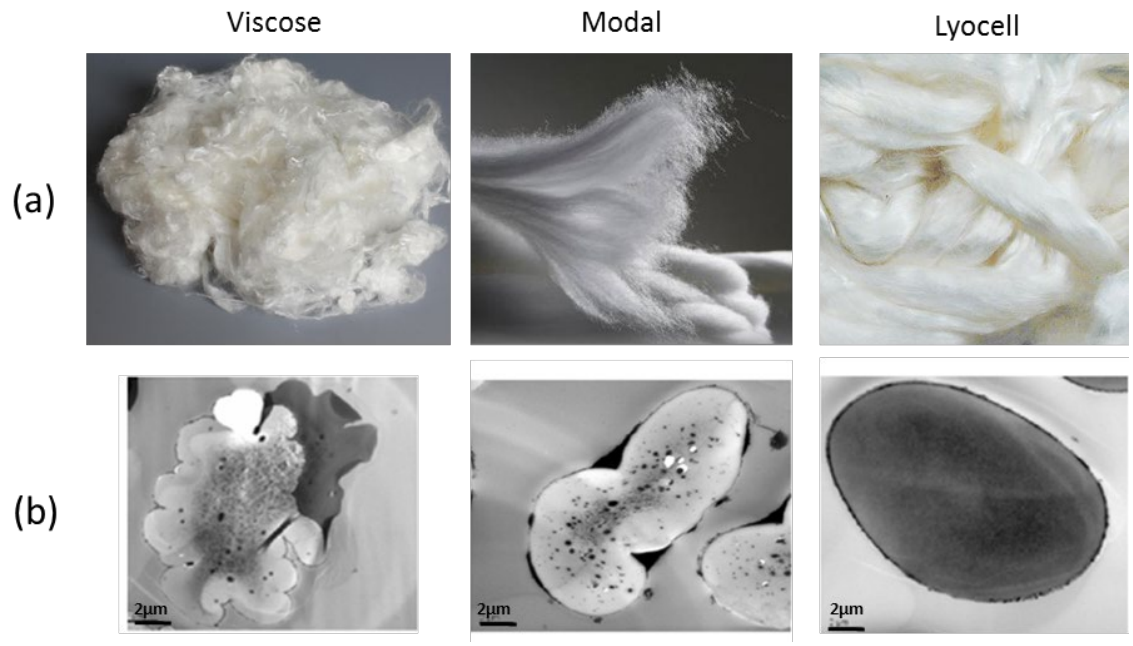

Figure 1.6. (a) Photograps of different types of fibre bundles made of regenerated cellulose. (b) SEM micrographs of the regenerated fibres shown in (a). The dark areas show water absorbed into the internal structure of fibres (Lenzing AG company).

Viscose is a type of rayon and is obtained by combining cellulose with carbon bisulphide. Modal fibres were developed by the Lenzing AG company. It is a wood pulp based cellulosic fibre, made up of pure wooden chips from beech tree. While viscose and rayon can be obtained from the pulp from various fibre sources, modal uses only beech wood fibres. Thus, modal fibres are essentially a variety of viscose that have high tensile toughness and high elastic modulus.

Lyocell fibres are produced from a solution of non-derivative cellulose using a solvent spinning process. The aforementioned solution is obtained by dissolving directly the cellulose fibres in an organic solvent, namely the N-methylmorpholine-Noxide (NMMO) (Loubinoux & Chaunis, 1987). This process offers a viable environmentally friendly alternative to the conventional viscose production process, because no derivatization of cellulose chains is required.

The diameters of regenerated fibres vary from 12.8 µm for Lyocell fibres to 14.2 µm for modal and viscose fibres while their lengths are usually 40 mm for all of them. The mechanical properties of regenerated fibres are summarised in Table 1.4. Lyocell fibres unlike viscose and modal fibres offer good mechanical properties such as high modulus and tensile toughness comparable to those of flax fibres.

Table 1.4. Average tensile properties of regenerated cellulose fibres (Adusumali et al., 2006).

	Linear Density	**Young's modulus**	**Maximum strength**	**Elongation to break**
	T (dtex)	E (GPa)	σ_r (MPa)	ε (%)
Viscose	1.70-2	8.3-12.8	270-410	13.2-17.6
Modal	1.50-2	11-15.4	360-500	8.8-12.2
Lyocell	1.52-2.10	20-28.3	480-620	6.3-8.3

1.1.1.2.4 Architectures of fibre reinforcements

Synthetic, natural and regenerated fibres, as described above, can be used for the reinforcement of composite materials in a large variety of industrial fields. While the geometry of synthetic fibres is usually simple with well-defined shapes, namely regular cross-sections (Figure 1.3) and sizes, plant and regenerated fibres have a more complex one. As described in section 1.1.1.2.2, plant and wood fibres are made of different scale elements such as meso- or nanofibrils. In the following, we will not consider nanoscale elements. Elementary plant and wood fibres will be typically defined as shown in Figure 1.5.

As illustrated in Figure 1.7, starting from single elementary fibres it is possible to fabricate several types of fibre reinforcements with more or less complex geometries.

Single synthetic fibres and extracted biosourced fibres (schematically represented in Figure 1.7a) can be simply used as reinforcement by mixing them with the polymer matrix and processed for instance by injection moulding to obtain short fibre reinforced composites.

Single fibres can also be assembled together in the form of yarns or bundles. Yarns or bundles exhibit unidirectional architecture. They can be formed by an assembly of parallel continuous fibres or by an assembly of spun fibres (Figure 1.7b). Using textile processes, yarns can be combined together to form more or less complex, ordered or disordered two-dimensional structures: mats with random planar fibre orientation, woven fabrics where the yarns are woven in two perpendicular directions, unidirectional or non-crimp fabrics, knits, braids, as illustrated in Figure 1.7. Woven fabrics and fibre mats often exhibit a more "isotropic" in-plane mechanical behaviour.

In addition, fibres can also be arranged in the third dimension using specific textile processes such as weaving, braiding and knitting, in order to create 3D fibrous preforms.

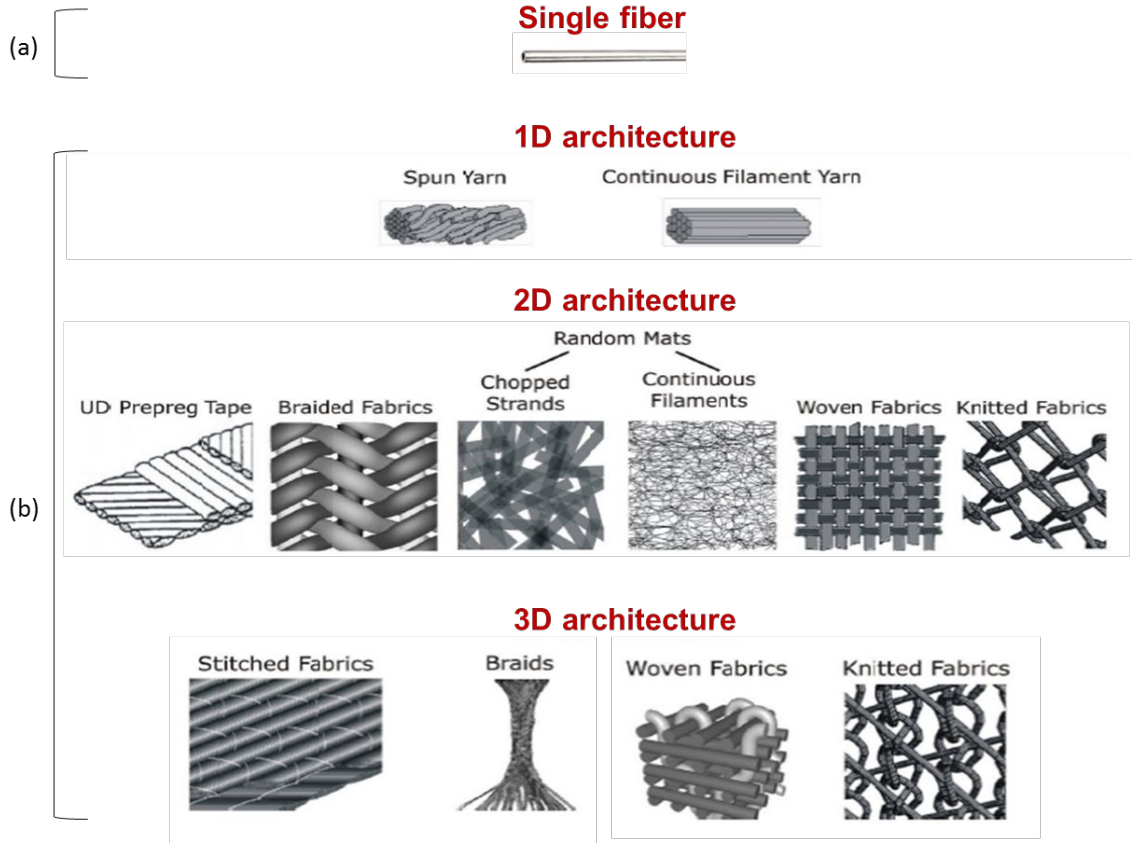

Figure 1.7. Different types of fibre reinforcements encountered in composite materials (Harper, 2006).

Due to the complexity of fibre reinforcements, it is necessary to well define the various scales that can be considered to describe their structure and mechanics (see Figure 1.8).

a) **Microscopic fibre scale**: scale of a single fibre or a contact between neighbouring fibres (Figure 1.8a). At this scale, each fibre/contact is considered/seen as a single element for which several geometry and deformation parameters such as position, orientation, strain or curvature can be defined. A fibre can be mechanically described as a (complex) beam (Latil, 2006). In the case of the contact between a fibre and a liquid, various parameters can also be defined: local contact angle, length of triple line or surface energy (Pucci, 2016);
b) **Mesoscopic yarn or bundle scale**: scale of an assembly of fibres (Figure 1.8b). At this scale, a single yarn or bundle is seen as a continuous material. At this scale, there are different levels of complexity, depending on the structure of the fibre assembly: single yarn (1D structure) or assembly of yarns with different geometries (2D or 3D structure), as mentioned above. As for the single fibres, it is possible to define the geometry and mechanical properties of this continuum (Badel et al., 2008; Charmetant et al., 2011; Gatouillat, 2011; Pucci, 2016).
c) **Macroscopic reinforcement or composite part scale:** scale of the reinforcement or scale of the composite part. At this scale, the fibre reinforcement is considered as a continuum. The details of the internal structure (e.g. woven, mat, unidirectional or random fibres) are not considered anymore. The mechanical behaviour can be

seen as those of a plate or a shell, i.e., a structure with a thickness smaller than the others dimensions, with more or less complex kinematics.

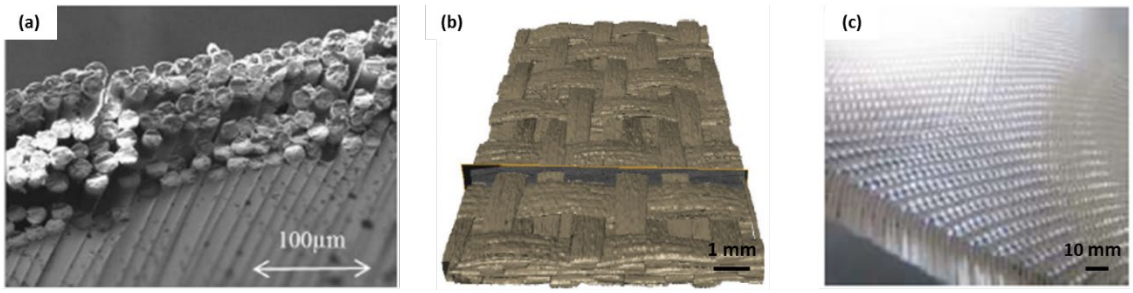

Figure 1.8. Different scales of fibre reinforced composite materials: (a) fibre scale, (b) mesoscopic (yarn/bundle) scale (Badel et al., 2008), and (c) reinforcement scale.

1.2 Composite manufacturing processes

The different manufacturing processes used to fabricate polymer matrix composites have been developed to satisfy different needs: shape and dimensions of the final part, type of reinforcement e.g., short or continuous fibres, type of polymer matrix (thermoset or thermoplastic). The main manufacturing processes for PMC's include injection moulding, compression moulding, thermostamping, liquid composite moulding, pultrusion, autoclave processes and all their variants. The majority of the aforementioned composite fabrication methods involve the impregnation of fibre reinforcements with a liquid polymer matrix. Impregnation can be defined as the flow of the polymer matrix through fibre reinforcements with more or less complex fibrous architectures.

There are different ways to classify composite forming processes that require an impregnation phase. One of these classifications defines two groups of processes:

- the wet forming processes (e.g. LMC and pultrusion, fabrication of prepregs)
- the dry forming processes (e.g. compression moulding of preimpregnated materials).

A typical flow chart related to wet and dry moulding composite processes is shown in Figure 1.9. It shows the principle steps of wet and dry composite forming processes. The two types of processes differ essentially for the impregnation phase. In the wet method a dry fibre reinforcement is placed in the mould, preformed and then impregnated with the polymer. In contrast, in the dry method a pre-impregnated material (prepreg) is placed and formed in the mould. Thus, the dry method requires the fabrication of a pre-impregnated material (sheet of fibres impregnated with a polymer) so that the impregnation phase occurs mainly during the fabrication of the prepreg. This process will be discussed in detail in section 1.2.2. After the forming of the prepreg in the case of the dry processes or the impregnation of the dry fibre reinforcement with the polymer matrix in the case of wet processes, a curing phase (in the case of the thermoset matrices) or solidification phase (in the case of thermoplastic polymers) takes place. Then, the composite part is solidified and can be demoulded.

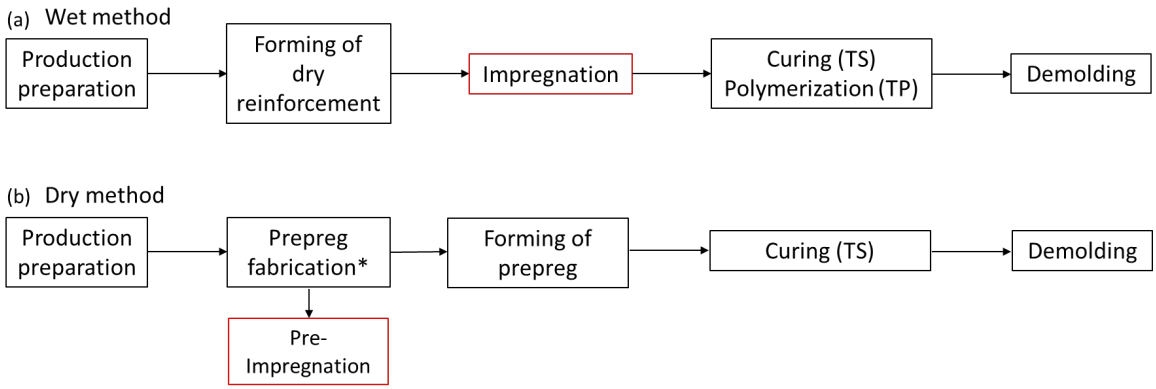

Figure 1.9. Typical flow chart of the wet and dry moulding composite processes. (a) For the wet method the fibre reinforcement is impregnated by the polymer matrix after being placed and formed in the mould. (b) For the dry method, a pre-impregnated material is formed and then compressed in the mould. (*) The impregnation phase occurs during the fabrication of the prepreg with a possible pre-curing phase (thermoset polymer) or pre-polymerization (thermoplastic polymer).

In the following sections, a particular focus will be made on the impregnation phase that occurs in two different wet forming processes, i.e., LCM and pultrusion processes, and in the fabrication of prepregs, i.e., the so-called sheet moulding compounds.

1.2.1 Wet forming processes

1.2.1.1 Liquid Composite moulding

Liquid Composite Moulding (LCM) is a cost-effective process. It is commonly used for the manufacturing of large composites parts in the transport industry. In LCM processes, a dry or partially impregnated fibrous preform is placed in a closed mould cavity. Then, the empty spaces between the fibres are filled with a polymer resin (Figure 1.10) by transferring the liquid resin from a reservoir under positive pressure or by drawing the resin into the mould by subjecting the mould to vacuum.

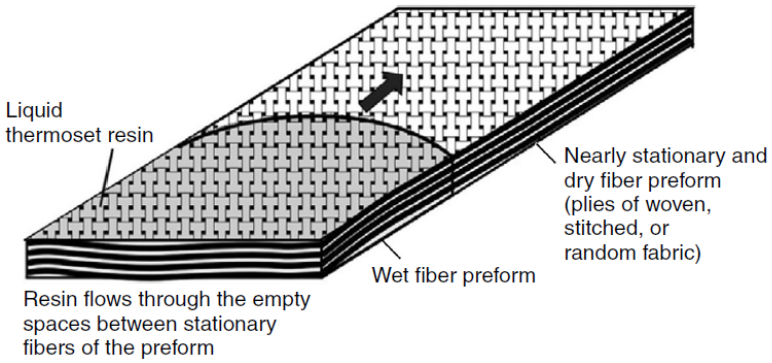

Figure 1.10. Schematic representation of the resin flow through a fibrous reinforcement (impregnation phase) (Sozer et al., 2012)

To obtain a good impregnation of the fibre preform, a thermoset resin system with a low viscosity (typically 0.1 - 0.5 Pa s) is used. The mould filling must be completed before the reticulation of thermoset resin occurs (Sozer et al., 2012). The thermoset resins can be heated to reduce their viscosity and thus ease their infiltration through the fibrous reinforcement. However, an increase of the temperature may also initiate cross-linking of polymer chains leading to a significant increase of the resin viscosity and uncontrolled impregnation conditions. The use of thermoplastic resins is still a subject of ongoing research works because of their high viscosity (10^2 - 10^6 Pa s) that would require a very high injection pressure. To circumvent this difficulty, some studies investigated the possibility to induce in situ the polymerization of the thermoplastic matrices during the impregnation phase. However, the quality of the as-obtained thermoplastic matrices is still an issue.
There are several types of LCM processes. Two of them are very common: the resin transfer moulding (RTM), and the liquid resin infusion (LRI).

1.2.1.2 Resin Transfer Moulding (RTM) process

The sequence of the various stages of the RTM process is schematically illustrated in Figure 1.11.

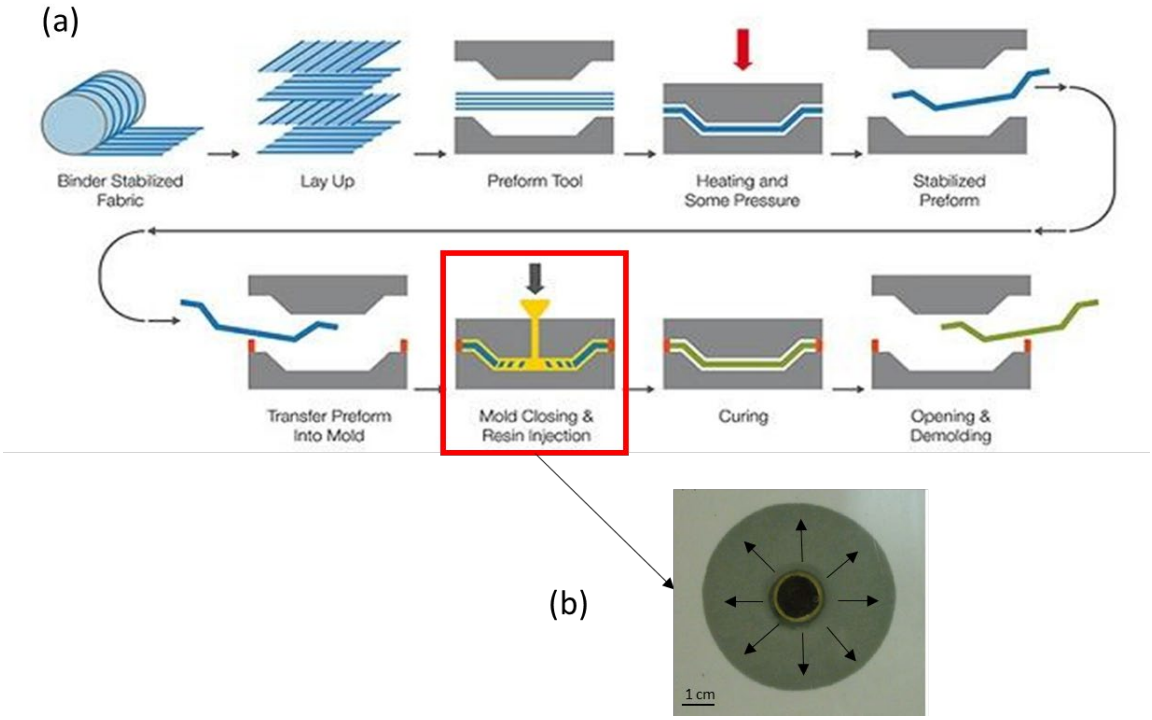

Figure 1.11. (a) Schematic representation of the RTM process with a zoom (b) on the in-plane radial flow of the matrix that occurs from the injection nozzle through the fibrous reinforcement during the impregnation phase (highlighted in the red box).

The RTM is a closed mould process where the polymer matrix is injected in the fibre reinforcement with a pressure higher than the atmospheric one (typically around 1-10 bar).

This process allows manufacturing high-performance composite parts with simple or complex shapes, and with small or large dimensions (a few meters). During a cycle of the RTM process, the mould is first heated (up to a maximum temperature of 230°C) and the dry or partially impregnated fibrous preform is placed in the cavity of the lower half part of the mould. The upper half part of the mould is then closed, deforming and compacting the fibrous reinforcement (draping phase). Then the liquid polymer is injected through one or more gates until the mould is filled. The matrix flows through the fibrous reinforcement thanks to the pressure gradient between the location of the injection inlet and the flow front position. The polymer matrix is then cross-linked (curing phase). Finally, the finished part is removed from the mould. The main issue with this process is the mould design (injection point placement, vent location, etc.), the control of the homogeneity of the fibrous reinforcement in the finished part after its deformation, the displacement or the deformation of the fibre reinforcement during the injection phase, the quality of the impregnation (residual voids) and the control of the curing (curing time, homogeneity).

1.2.1.3 Liquid Resin Infusion (LRI) process

The LRI process (Figure 1.12) is an evolution of the RTM process described in the previous section.

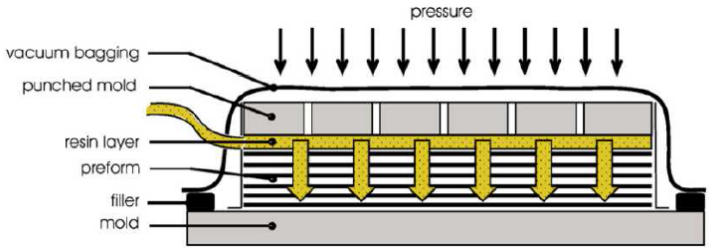

Figure 1.12: Schematic representation of the LRI process (Celle et al., 2008).

In this process the polymer resin impregnates the initially dry fibrous preform with a pressure lower than the atmospheric one (vacuum). More precisely, the preform is draped over a mould and covered with a draining fabric with high permeability to promote the flow of the resin, first on the surface and then in the thickness of the preform. The assembly is then covered by a flexible bag that seals the mould and induces the compaction of the preform during the impregnation by drawing a vacuum. A vacuum pump provides suction and the pressure gradient between the resin inlet, placed at the level of the draining tissue, and the vent, located at the base of the preform, allows the infusion of the resin through the porous reinforcement. This process is becoming increasingly popular owing to its ability to produce high quality parts with relatively low residual porosity and the low cost of tooling (only a half mould is needed).

1.2.1.4 Pultrusion

Pultrusion is a fully automated process that allows continuous manufacturing of composite parts with more or less complex shapes of their cross sections. The pultrusion process (Figure 1.13a) consists in pulling the reinforcement (usually continuous either in the form of rovings or rolls of fabrics, mats or veils) from a series of creels. The dry reinforcement is then fed continuously through a guideline system into a resin bath to get impregnated (Figure 1.13b) before it enters into a forming die.
There are three types of impregnation systems currently used for thermoset matrices: dip bath, straight through bath and resin injection system. The most common type of impregnation method is constituted by an open resin-filled bath in which the reinforcement is guided over and under rolls located under the resin surface. The impregnation is mainly due to capillary forces. The advantages of this method are the simplicity and the goodness of the results, while the disadvantage is related to volatile organic compound emissions. In a straight-through resin bath, the reinforcement is not guided down in the resin but enters and exits the bath remaining always horizontally positioned. This method is used to produce hollow pultruded composite parts. The injection method is quite innovative and consists in the injection of the resin into the dry preform just before it enters into the die. A combination of the resin injection pressure and pulling velocity of the reinforcement into the die generates enough pressure to force the resin to flow through the fibrous reinforcement and to well impregnate it. In the case of thermoplastic matrices, the impregnation takes place in the pultrusion die due to temperature and the pressure applied. After the impregnation, the impregnated reinforcement is shaped with a constant cross section through a heated die. A pultrusion die is machined from tool steel and it has a length of 600 - 1500 mm. Most of the dies are heated. Die temperatures are in the range of 100-160°C for unsatured polyester and vinylester resins and about 300°C for epoxy resins. At the end of the pultrusion machine, the profiled material is cut to the desired length.
Pultrusion allows the production of composite parts with high fibre contents (up to 85%) that exhibit superior strength and stiffness in longitudinal direction (Mitschang and Christmann, 2012). Composite parts fabricated using pultrusion processes can be found in many industrial domains: window, door frame, marine constructions, railway carriage and stairways.

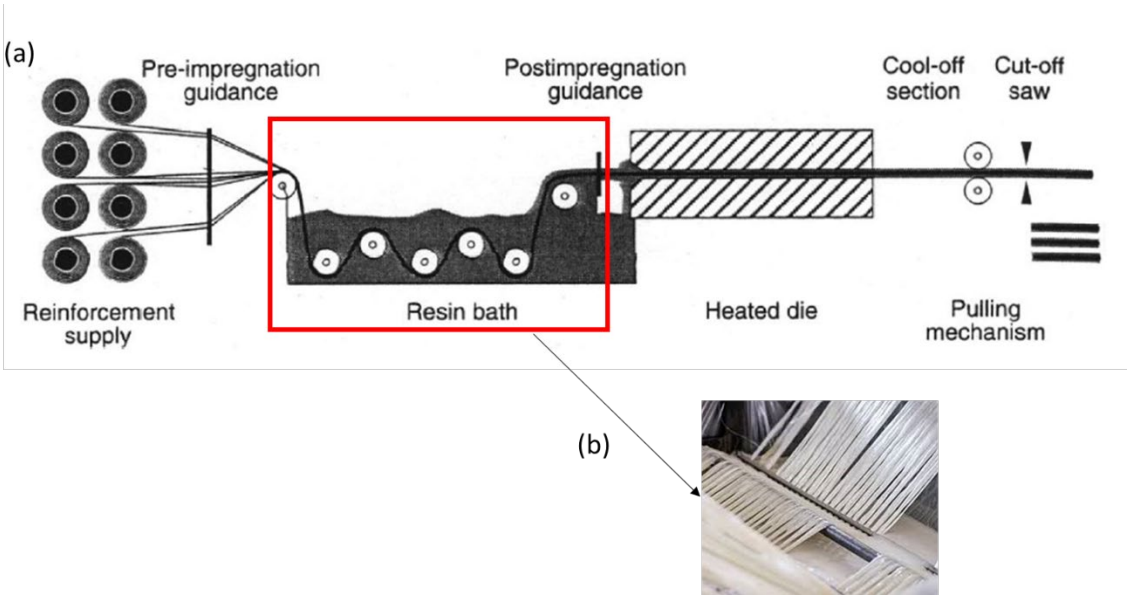

Figure 1.13. Schematic representation of the pultrusion process with a zoom on the impregnation phase (the illustrated impregnation method is the open resin-filled bath) (Vergani, 2005).

1.2.2 Dry forming processes

Contrary to the aforementioned composite forming processes, dry forming processes require the use of semi-finished products or prepregs. The impregnation phase takes place during the fabrication of the pre-impregnated materials. A prepreg is a reinforced material (usually made of short synthetic or natural fibre bundles) that is pre-impregnated with a thermoset or thermoplastic polymer (Figure 1.14). The most common prepregs with thermoset resins and discontinuous fibre reinforcements are the Sheet Moulding Compounds (SMCs). SMCs are pre-impregnated materials in the form of a sheet composed of a thermoset matrix reinforced with fibre bundles (around 20-40 mm in length). Different types of thermoset matrices can be used (polyester, vinylester, epoxy), mixed with fillers ($CaCO_3$, Al_2O_3, glass beads, etc.), and fibres (glass, carbon or biosourced) depending on the final functions of the composite part.

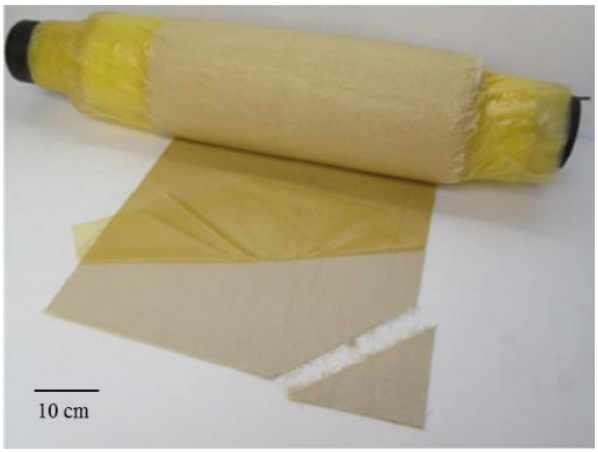

Figure 1.14. Photograph of a roll of glass-fibre SMC prepreg (Ferré Sentis, 2017).

1.2.2.1 Fabrication of prepregs

The fabrication of prepregs is the first step for the production of composites through dry forming processes (e.g. compression moulding). This stage includes an impregnation phase that needs to be well controlled to obtain a final part with good end-use properties. The prepreg fabrication for SMCs (Figure 1.15) is divided into three phases:

1- Mixing of the polymer matrix/paste: in the first mixer all the components of the matrix (i.e., the thermoset resin) except the fillers and thickening agent are mechanically stirred. Then the mixture enters in the second mixer where fillers and additives are added. Then, at the outlet of the second mixer, the matrix is divided into two paths. Finally, the polymer matrix is transported on polyethylene (PE) films to the impregnation system of the SMC machine.
2- Impregnation of the reinforcement: the fibre bundles are cut above a layer of PE film and matrix and then covered by another layer of PE film and matrix to form a sandwich structure. Then, this sandwich material goes through a calendaring system that promotes the impregnation of the layers of fibre reinforcement by the matrix and allows a constant thickness (1-3 mm) to be obtained. The as-obtained sheet is a "stiff" impregnated mat which, after peeling off the release film, is cut into blanks for compression moulding.
3- Curing/storage: the sheet is then stored in the form of a roll of SMC in a room at a controlled temperature of approx. 26°C for some days to start the curing phase and then at 15°C to inhibit it.

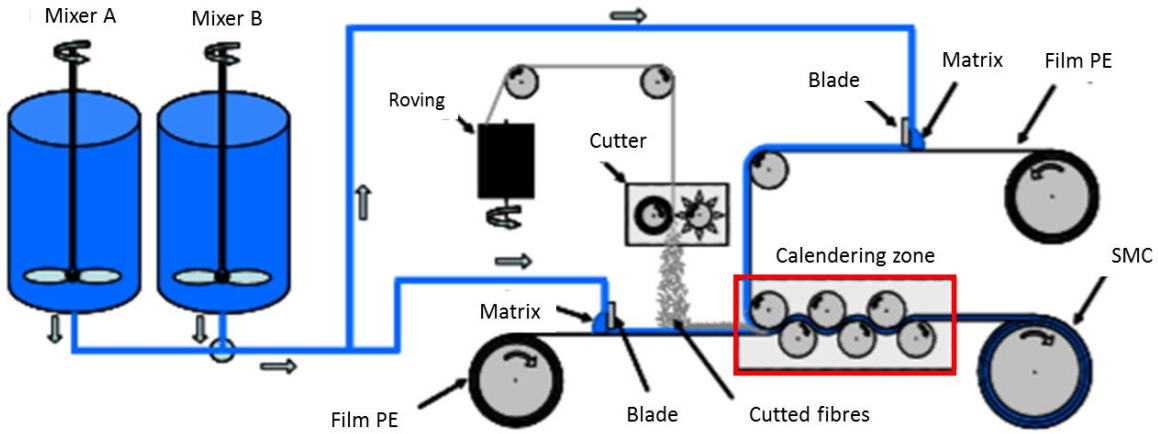

Figure 1.15. Scheme of a manufacturing line of SMC prepregs. The calendaring zone where the impregnation phase takes place is highlighted in red.

1.2.2.2 Manufacturing process of SMCs

Once the pre-impregnated material in form of sheet (SMC) is prepared, the composite part can be manufactured using a compression moulding process (Figure 1.16).

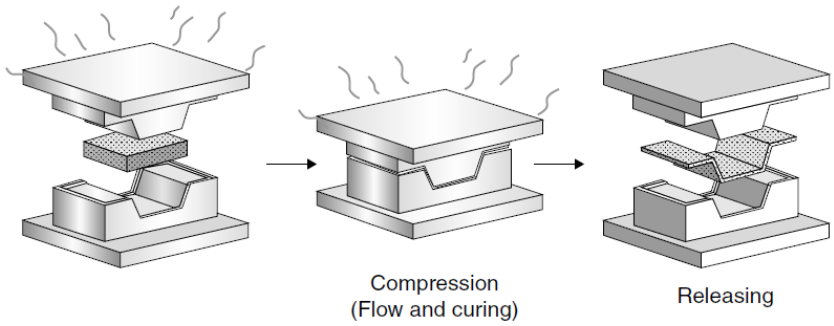

Figure 1.16: Schematic view of the different stages of a compression moulding process (Park et al., 2012).

In this process, the moulding material, also called the charge, is placed in the hot mould. Once placed the upper mould moves down and compresses the charge. The latter flows and fills the mould cavity. The air escapes through the shear edges or air vents. Once the mould is filled the compression stress is maintained and the resin cures and consolidates. The velocity of the mould closing and temperature are some of the relevant parameters that must be controlled to obtain high quality homogenous composite parts.

1.3 Defects and deformation mechanisms during composite processing

The fabrication processes of composite materials are complex and include different stages (e.g. placement of the reinforcement, impregnation, curing or polymerization) that have to be well controlled to avoid the formation of defects that can compromise the quality and mechanical properties of the final composite parts. The formation of defects during the manufacturing of composite parts can have several origins according to the types of processes, reinforcements and matrices. All the forming stages are crucial for the determination of the microstructure (porosity, orientation and spatial distribution of fibres/yarns/bundles) of the composites, the dimensional defects and end-use properties of the composite parts. In the following sections, some typical defects that commonly appear at different scales during the manufacturing of composite parts are briefly described.

1.3.1 Defects due to deformation mechanisms of fibre reinforcements

In the case of continuous fibre reinforcements the placement of the fibre preform on the mould during the forming process can be at the origin of several defects such as ply cracking, wrinkles (Figure 1.17a), fibre buckling (Figure 1.17b) or other local fibre deformation (Figure 1.17c). These defects are induced by deformation mechanisms that the fibre reinforcement undergoes during the forming process. For instance, during the draping phase, the fibrous reinforcement is constrained to follow the more or less complex shape

of the mould, which results in bending, shear or tensile heterogeneous deformation mechanisms. Then, the structural heterogeneities (e.g. variation in the fibre content and orientation) that result from these deformation mechanisms largely affect the impregnation phase.

The deformation mechanisms of fibre reinforcements have been studied by several authors (Badel et al., 2008; Gatouillat, 2011; Charmetant et al., 2011; Boisse et al., 2011) at the yarn/bundle scale using numerical approach. In many of these approches the deformation of the yarns are modelled by considering that these elements can be seen as a continuum. The mechanisms of deformation at the yarn scale are influenced by the microstructure and the micromechanics of each single fibre that compose the yarns/bundles (Latil, 2012). Thus it is important to study how the phenomena visible at a upper scale are linked with the deformation mechanisms and variations in the geometry as well as mechanical properties of a single fibre.

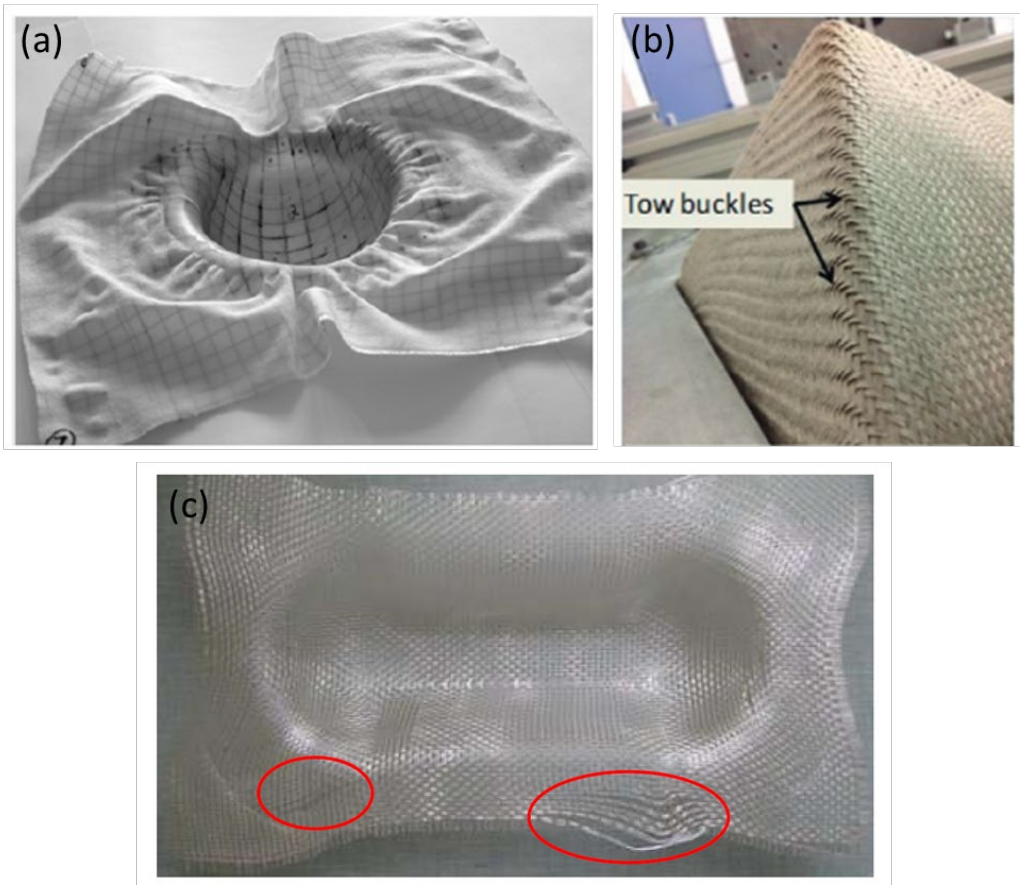

Figure 1.17. Photographs showing examples of defects that can appear during the forming process of a composite reinforcement material: (a) wrinkling of the reinforcement (Boisse et al., 2011), (b) fibre tow buckling (Capelle et al., 2014), (c) local deformation due to separation of fibre yarns (Gatouillat, 2011).

It is also important to notice that some deformation mechanisms are typical of the natural fibre reinforcements. Natural fibres unlike synthetic fibres can absorb/desorb liquids (typically water) when they are wetted/dried. This can cause the swelling or shrinking of

the natural fibres: fibres deform increasing their diameter and shrink when the liquid content decreases (for instance by evaporation) (Figure 1.18). Moreover, the hydroabsorption can cause the opening of the lumen of some natural fibres that can induce cracks in the fibre wall. Residual liquid within the fibre microstructure can influence not only the quality of the composite parts but also the composite processes.

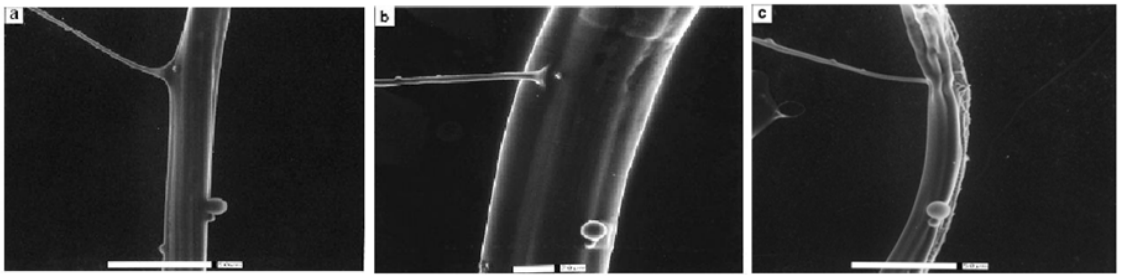

Figure 1.18. E-SEM micrographs showing the moisture induced swelling and shrinkage of a natural fibre. (a) dry fibre; (b) fully swollen fibre; (c) fully shrunk fibre (Nguyen, 2014).

1.3.2 Defects due to the formation of voids

The most important manufacturing defect that is likely to occur is “porosity”, i.e. voids inside the composite part. The impregnation of fibre reinforcements has to be well controlled to avoid the formation of voids that can compromise the mechanical properties of the composite parts. Several authors reported that strength can decrease up to 30% in bending, 3% in tension, 9% in torsional shear with every 1% increase in the void content (Hamidi et al., 2004). The study of the mechanisms that induce the formation of voids is still an ongoing research study in the field of composite forming processes. Voids can appear at different scales inside the composite parts, depending on the architecture of the reinforcement (single scale of porosity in the case of random mat or unidirectional yarn, double scale of porosity in the case of woven, braided or knitted fabrics). Voids can have dimensions ranging from some millimetres to some micrometres. Generally, small voids are classified as ‘inter-yarn’ voids (Figure 1.19) when they form between the fibres tows (also called yarns or bundles) and as ‘intra-yarn’ voids when they form inside the fibre tows.

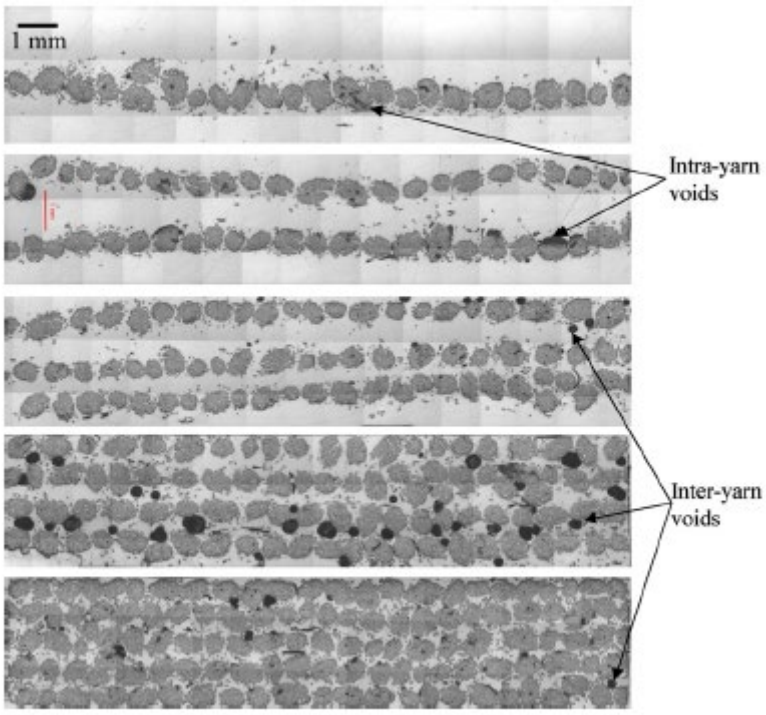

Figure 1.19. SEM images of the cross section of a biocomposite showing the different types of voids that can be observed in a composite part (Shah et al., 2012).

There are several origins of voids. Their nature depends often on the manufacturing process. In the case of LCM processes, voids are created by various mechanisms such as air entrapment, volatilization of dissolved gases in the resin, nucleation, leakage, cavitation, partial evaporation of mould releasing agent into the preform or initial air bubbles in the resin. Voids can form dry regions known as dry spots in the preform if the resin flow front reaches the vents before impregnating completely the reinforcement (owing to the so called race tracking effect, Figure 1.20). In addition, the formation of dry spots can be caused by a premature gelling of the resin, or air entrapment due to the merging of multiple flow fronts or even by heterogeneous preform permeability properties.

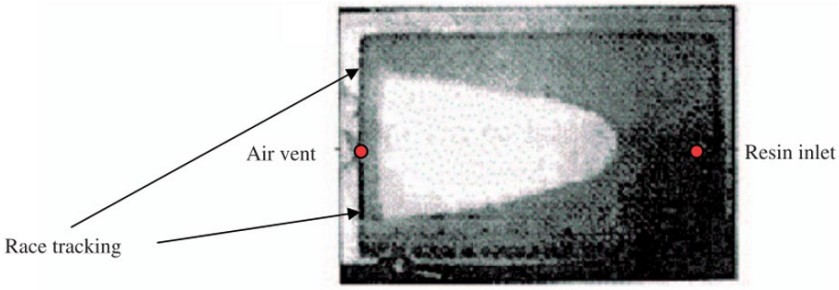

Figure 1.20. Example of a typical void defect (Park & Lee, 2011).

At the yarn or fibre scales, a possible origin of voids is the local deformation of the fluid front (Figure 1.21). Voids can be entrapped just behind the fluid front. This shows that the

complex architecture of fibre reinforcements and the heterogeneity of their microstructure also play an important role in the formation of voids.

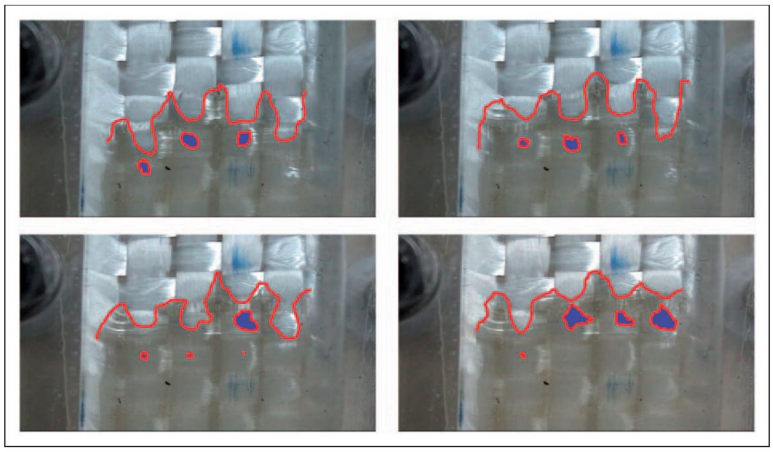

Figure 1.21. Local deformation of the fluid front (red line) and resulting voids (blue spots) that are formed behind it (Park & Lee, 2011).

The objective of several experimental and numerical studies was to predict the formation mechanisms of voids during the fabrication of pre-impregnated material or the mould filling stages (Patel & Lee, 1996; Park & Lee, 2011; Devalve et al., 2013). The control of the impregnation phase of prepregs is crucial to obtain high quality composite parts. For instance, in the case of SMCs, the majority of air bubbles form during (i) the mixing of the polymer paste, (ii) the compounding needed for the prepreg manufacturing, or (iii) during the moulding process (degassing phenomena).

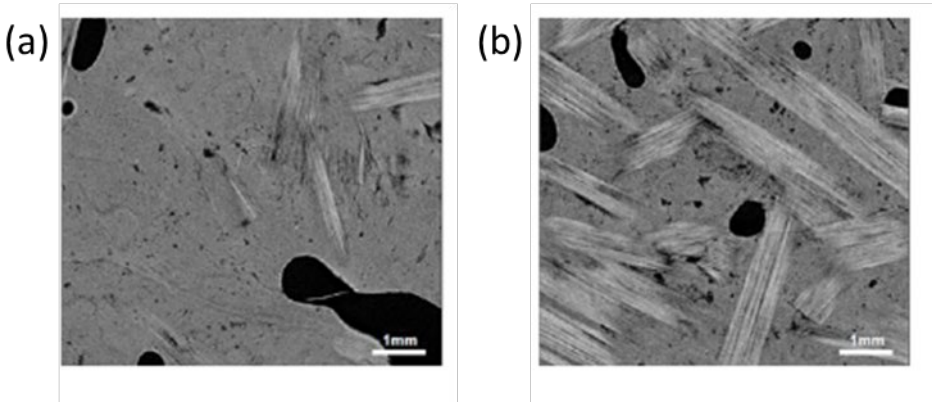

Figure 1.22. Cross sections of 3D microtomography images of a sample of a SMC prepreg as obtained after its manufacturing. From these images, it is possible to distinguish the presence of voids in black colour (Le et al., 2008).

3D images obtained using X-ray microtomography can be used to study the morphology of voids within SMC specimens before their moulding (Le et al., 2008; Ferré Sentis et al., 2017). Figure 1.22 shows the presence of voids in a prepreg. These voids were entrapped during the impregnation phase of the studied SMC prepreg. Figure 1.23 shows the evolution of the porosity of a SMC specimen from its initial state through different compression stages. During the subsequent compression phase, initial pores can be transported. Their

dimensions can decrease. Some voids can completely disappear. However, it is also worth noting that numerous voids can also remain entrapped after compression as shown in Figure 1.23g-h.

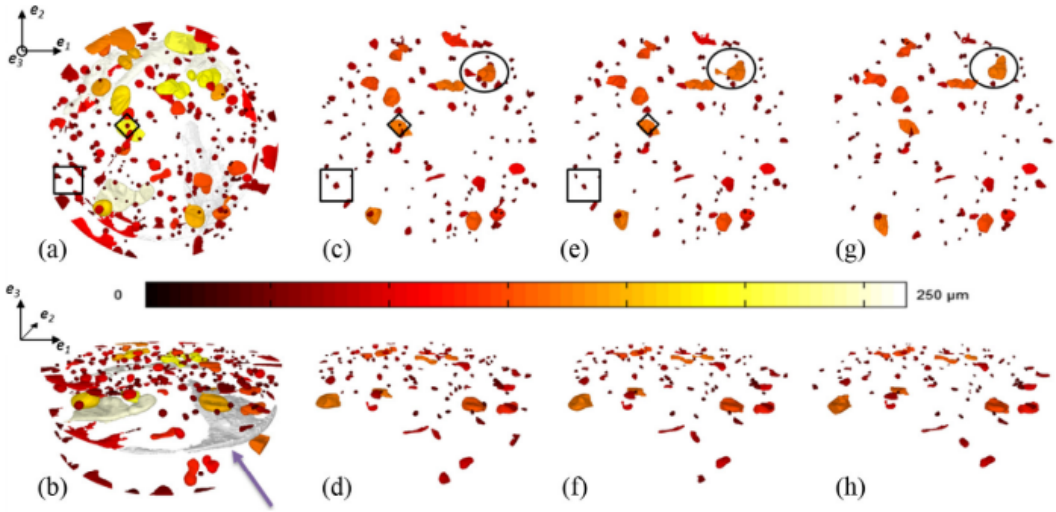

Figure 1.23. 3D X-ray microtomography images showing the in situ evolution of pores in a SMC prepreg for various compression stages corresponding to logarithmic compression strains that were equal to (a,b) 0, (c,d) 0.11, (e,f) 0.14, (g,h), respectively (Ferré Sentis et al., 2017).

In the case of biocomposites reinforced with natural fibres the water that may be present in the lumens of fibres can evaporate during the forming process because of process-induced temperature variations, resulting in the formation of voids due to degassing phenomena.

1.4 Impregnation mechanisms

In the previous sections, different types of composite materials have been presented as well as the different forming processes used to fabricate them. Regardless of the composite processing routes, an impregnation phase of the composite fibre reinforcement is usually required. The impregnation of a fibre reinforcement can be defined as the flow of a complex fluid in an anisotropic, deformable and multiscale porous medium.

The characterization and modelling of fluid flow through an anisotropic porous/fibrous medium have been the subject of a huge amount of studies (Singh et al., 2019; Zhou et al., 2008; Bréard et al., 2003; Lawrence et al., 2009; Michaud & Mortensen, 2001; Charpentier et al., 2020) that are still ongoing. The complexity of the impregnation phase of a fibre reinforcement is mainly due to the complex and anisotropic architecture of the fibre reinforcements and the complex rheological properties of the polymer matrices. A poor control of the impregnation mechanisms may lead the onset of several defects in the composite parts, as reported in the previous section. These defects can compromise the end-use mechanical properties of the parts. To decrease the number of defects and also to decrease the mould filling time (for LCM processes), it is important to properly control and

optimize the impregnation phase. The control of the impregnation phase can be significantly improve by knowing and controlling all the parameters that affect the resin flow and the propagation of the flow front of the polymer matrices through the fibre reinforcements.

Many experimental and numerical studies were done on saturated and unsaturated fluid flows through porous media with the aim of quantifying the governing parameters (Pillai, 2002; Michaud, 2016; Bréard et al., 2003). When a fluid impregnates a porous medium, three phases coexist: the solid structure, i.e. the dry fibrous reinforcement, the liquid and the air phases. In the literature, it has been reported that the non uniform advancement of the flow front of the matrix is due to the heterogeneus nature of fibrous reinforcement. During the impregnation, the interface between the dry reinforcement and the liquid is not sharp and it is rather difficult to clearly identify the flow front location as shown by Park and Lee (Park & Lee, 2011) (Figure 1.24).

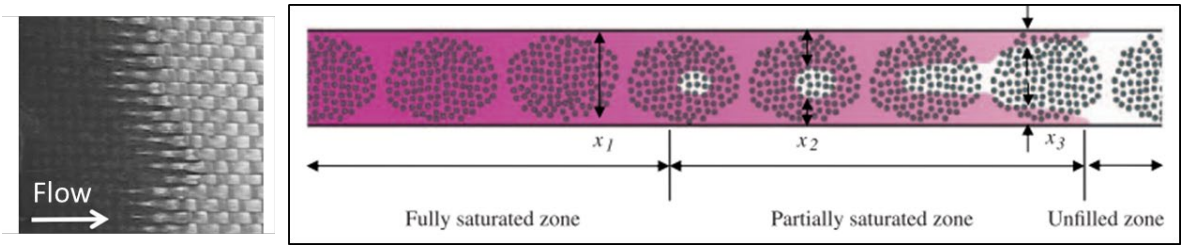

Figure 1.24. Right hand side: scheme of the different characteristic zones that are commonly observed during the unidirectional impregnation of a fibrous reinforcement with the LCM process. Left hand side: the three zones are clearly visible in the photograph taken during the impregnation of woven reinforcement fabric (Park & Lee, 2011).

Considering the results of simple experiments consisting in the radial or unidirectional in plane flow impregnation, it is possible to distinguish three characteristic zones during the filling of a fibrous reinforcement: a saturated zone, an unsaturated zone well behind the flow front and an unfilled zone (dry preform) after the flow front. The length or the onset of each characteristic zone depends on several parameters. For instance, if the mould is not sufficiently long the fibrous preform close to/at the fluid inlet never becomes fully saturated when the flow front reaches the end of the mould. It is also important to distinguish the two different flow conditions, i.e., saturated or unsaturated flow conditions, when studying the impregnation mechanisms of a fibre reinforcement. The flow of a polymer matrix through a fibrous reinforcement is mainly affected by the permeability of the preform that depends on the degree of saturation, as well as on the capillary phenomena that occur at the matrix air and matrix fibre-interfaces. Capillary phenomena have a central role on the impregnation phenomena since they govern the local deformation phenomena of the fibres that occur at the flow front and the flow propagation itself. At the interface between two fluids, i.e. the polymer matrix and the air, the discontinuity in the hydrodynamic pressure due to the surface tension is called the capillary pressure. Capillary pressure depends on the wetting properties of the liquid and the wettability of the fibre surface (surface tension, contact angle) as well as on geometrical factors related to the architecture of the fibrous

reinforcements (Ahn et al., 1997; Pillai & Advani, 1996; Singh et al., 2019). Capillary pressure and hydrodynamic forces can promote or not the advancement of the fluid, i.e., the fluid front propagation within the fibre reinforcement and as well as its deformation.

References

Adusumali, R., Reifferscheid, M., Weber, H., Roeder, T., Sixta, H., & Gindl, W. (2006). Mechanical Properties of Regenerated Cellulose Fibres for Composites. *Macromolecular Symposia*, *244*(1), 119–125. https://doi.org/10.1002/masy.200651211

Ahn, K., Seferis, J., & Berg, J. C. (1997). Simultaneous Measurements of Permeability and Capillary. *Polymer Composites*, *12*(3), 146–152.

Badel, P., Vidal-Sallé, E., Maire, E., & Boisse, P. (2008). Simulation and tomography analysis of textile composite reinforcement deformation at the mesoscopic scale. *Composites Science and Technology*, *68*(12), 2433–2440. https://doi.org/10.1016/j.compscitech.2008.04.038

Bledzki, A. K., & Gassan, J. (1999). Composites reinforced with cellulose based fibres. *Progress in Polymer Science*, *24*, 221–274.

Boisse, P., Hamila, N., Vidal-Sallé, E., & Dumont, F. (2011). Simulation of wrinkling during textile composite reinforcement forming. Influence of tensile, in-plane shear and bending stiffnesses. *Composites Science and Technology*, *71*(5), 683–692. https://doi.org/10.1016/j.compscitech.2011.01.011

Bourmaud, A., Beaugrand, J., Shah, D. U., Placet, V., & Baley, C. (2018). Towards the design of high-performance plant fi bre composites. *Progress in Materials Science*, *97*, 347–408. https://doi.org/10.1016/j.pmatsci.2018.05.005

Bréard, J., Henzel, Y., Trochu, F., & Gauvin, R. (2003). Analysis of dynamic flows through porous media. Part II: Deformation of a double-scale fibrous reinforcement. *Polymer Composites*, *24*(3), 409–421. https://doi.org/10.1002/pc.10039

Capelle, E., Ouagne, P., Soulat, D., & Duriatti, D. (2014). Complex shape forming of flax woven fabrics: Design of specific blank-holder shapes to prevent defects. *Composites Part B: Engineering*, *62*, 29–36. https://doi.org/10.1016/j.compositesb.2014.02.007

Celle, P., Drapier, S., & Bergheau, J. M. (2008). Numerical modelling of liquid infusion into fibrous media undergoing compaction. *European Journal of Mechanics, A/Solids*, *27*(4), 647–661. https://doi.org/10.1016/j.euromechsol.2007.11.002

Charlet, K., Jernot, J. P., Gomina, M., Bizet, L., & Bréard, J. (2010). Mechanical properties of flax fibers and of the derived unidirectional composites. *Journal of Composite Materials*, *44*(24), 2887–2896. https://doi.org/10.1177/0021998310369579

Charmetant, A., Vidal-Sallé, E., & Boisse, P. (2011). Hyperelastic modelling for mesoscopic analyses of composite reinforcements. *Composites Science and Technology*, *71*(14), 1623–1631. https://doi.org/10.1016/j.compscitech.2011.07.004

Charpentier, J. B., Brändle de Motta, J. C., & Ménard, T. (2020). Capillary phenomena in assemblies of parallel cylindrical fibers: From statics to dynamics. *International Journal of Multiphase Flow*, *129*, 103304. https://doi.org/10.1016/j.ijmultiphaseflow.2020.103304

Devalve, C., & Pitchumani, R. (2013). Simulation of void formation in liquid composite molding processes. *Composites Part A: Applied Science and Manufacturing*, *51*, 22–32. https://doi.org/10.1016/j.compositesa.2013.03.016

Dishovsky, N., & Mihaylov, M. (2018). Elastomer-based composite materials. In *Journal of Chemical Information and Modeling* (Vol. 01, Issue 01).

Dumont P.J.J., Orgéas L., Martoïa F., Budtova T., Vincent, M., 5 Mise en œuvre des composites à fibres lignocellulosiques. In: Composites polymères et fibres lignocellulosiques. Ed. Berzin F., Lavoisier, Paris, 2016.

Eichhorn, S. J., Baillie, C. A., Zafeiropoulos, N., Mwaikambo, L. Y., Ansell, M. P., Dufresne, A., Entwistle, K. M., Herrera-Franco, P. J., Escamilla, G. C., Groom, L., Hughes, M., Hill, C., Rials, T. G., & Wild, P. M. (2001). Current international research into cellulosic fibres and composites. *Journal of Materials Science*, *36*(9), 2107–2131. https://doi.org/10.1023/A:1017512029696

Faruk, O., Bledzki, A. K., Fink, H. P., & Sain, M. (2012). Biocomposites reinforced with natural fibers: 2000-2010. In *Progress in Polymer Science* (Vol. 37, Issue 11, pp. 1552–1596). https://doi.org/10.1016/j.progpolymsci.2012.04.003

Ferré Sentis, D., Orgéas, L., Dumont, P. J. J., Rolland du Roscoat, S., Sager, M., & Latil, P. (2017). 3D in situ observations of the compressibility and pore transport in Sheet Moulding Compounds during the early stages of compression moulding. *Composites Part A: Applied Science and Manufacturing*, *92*, 51–61. https://doi.org/10.1016/j.compositesa.2016.10.031

Ferré Sentis, Dimitri. (2017). Rhéologie et microstructures des Sheet Moulding Compounds hautes performances au cours de leur mise en forme par compression. *PhD Thesis, Université Grenoble Alpes*.

Gatouillat, S. (2011). Approche mésoscopique pour la mise en forme des renforts tissés de composites. *Comptes-Rendus Des 17èmes Journées Nationales Sur Les Composites (JNC17)*, 71. http://hal.archives-ouvertes.fr/hal-00597986

Hamidi, Y. K., Aktas, L., & Altan, M. C. (2004). Formation of microscopic voids in resin transfer molded composites. *Journal of Engineering Materials and Technology, Transactions of the ASME*, *126*(4), 420–426. https://doi.org/10.1115/1.1789958

Harper, L. T. (2006). Discontinuous Carbon Fibre Composites for Automotive Applications. *PhD Thesis*, *August*, 1–335.

Latil, P. (2012). Micro-mécanismes de déformation de mèches de fibres saturées. *PhD Thesis, Université Grenoble Alpes*.

Lawrence, J. M., Neacsu, V., & Advani, S. G. (2009). Modeling the impact of capillary pressure and air entrapment on fiber tow saturation during resin infusion in LCM. *Composites Part A: Applied Science and Manufacturing*, *40*(8), 1053–1064. https://doi.org/10.1016/j.compositesa.2009.04.013

Le, T. H., Dumont, P. J. J., Orgéas, L., Favier, D., Salvo, L., & Boller, E. (2008). X-ray phase contrast microtomography for the analysis of the fibrous microstructure of SMC composites. *Composites Part A: Applied Science and Manufacturing*, *39*(1), 91–103. https://doi.org/10.1016/j.compositesa.2007.08.027

Loubinoux, D., & Chaunis, S. (1987). An experimental approach to spinning new cellulose fibers with N-methylmorpholine-oxide as a solvent. *Textile Research Journal*, *57*(2), 61–65.

Martoïa, F. (2015). Nanocomposites et mousses à base de nanofibrilles de cellulose : rhéologie au cours de leur mise en forme et propriétés mécaniques. *PhD Thesis, Université Grenoble Alpes*.

Michaud, V., & Mortensen, A. (2001). Infiltration processing of fibre reinforced composites: Governing phenomena. *Composites - Part A: Applied Science and Manufacturing*, *32*(8), 981–996. https://doi.org/10.1016/S1359-835X(01)00015-X

Michaud, Véronique. (2016). A Review of Non-saturated Resin Flow in Liquid Composite Moulding processes. *Transport in Porous Media*, *115*(3), 581–601. https://doi.org/10.1007/s11242-016-0629-7

Mitschang, P., & Christmann, M. (2012). Continuous fiber reinforced profiles in polymer matrix composites. In *Manufacturing techniques for polymer matrix composites (PMCs)*. Woodhead Publishing Limited. https://doi.org/10.1533/9780857096258.2.209

Nguyen, V. (2014). Characterization and Modeling of Flax Fiber Reinforced Composites Manufacturing by Resin Transfer Molding process. *PhD Thesis*, *072, université de Lille*.

Park, C. H., & Lee, W. I. (2012). Compression molding in polymer matrix composites. In *Manufacturing techniques for polymer matrix composites (PMCs)*. Woodhead Publishing Limited. https://doi.org/10.1533/9780857096258.1.47

Park, Chung Hae, & Lee, W. (2011). Modeling void formation and unsaturated flow in liquid composite molding processes: A survey and review. *Journal of Reinforced Plastics and Composites*, *30*(11), 957–977. https://doi.org/10.1177/0731684411411338

Patel, N., & Lee, L. J. (1996). Modeling of void formation and removal in liquid composite molding. Part I: wettability analysis. *Polymer Composites*, *17*(1), 96–103. https://doi.org/10.5194/gmdd-8-6669-2015

Pillai, K. M. (2002). Governing equations for unsaturated flow through woven fiber mats. Part 1. Isothermal flows. *Composites - Part A: Applied Science and Manufacturing*, *33*(7), 1007–1019. https://doi.org/10.1016/S1359-835X(02)00034-9

Pillai, K. M., & Advani, S. G. (1996). Wicking across a Fiber-Bank. *Journal of Colloid and Interface Science*, *110*, 100–110.

Pucci, M. F. (2016). Elaboration de composites bio-sourcés par procédés d'élaboration directe : Etude et modification des interfaces lors de l'imprégnation . *PhD Thesis, Ecole Des Mines de Saint-Etienne*.

Satyanarayana, K. G., Arizaga, G. G. C., & Wypych, F. (2009). Biodegradable composites based on lignocellulosic fibers-An overview. *Progress in Polymer Science (Oxford)*, *34*(9), 982–1021. https://doi.org/10.1016/j.progpolymsci.2008.12.002

Shah, D. U. (2013). Developing plant fibre composites for structural applications by optimising composite parameters: A critical review. *Journal of Materials Science*, *48*(18), 6083–6107. https://doi.org/10.1007/s10853-013-7458-7

Shah, D. U., Schubel, P. J., Licence, P., & Clifford, M. J. (2012). Determining the minimum, critical and maximum fibre content for twisted yarn reinforced plant fibre composites. *Composites Science and Technology*, *72*(15), 1909–1917. https://doi.org/10.1016/j.compscitech.2012.08.005

Singh, K., Jung, M., Brinkmann, M., & Seemann, R. (2019). Capillary-Dominated Fluid

Displacement in Porous Media. *Annual Review of Fluid MechanicsFluid Mechanics*, *51*, 429–449.

Sozer, E. M., Simacek, P., & Advani, S. G. (2012). Resin transfer molding (RTM) in polymer matrix composites. In *Manufacturing Techniques for Polymer Matrix Composites (PMCs)*. Woodhead Publishing Limited. https://doi.org/10.1533/9780857096258.3.243

Vergani, L. (2005). Damage mechanisms in pultruded unidirectional fiber reinforced composites under static and fatigue loads. *Fracture and Damage of Composites*, *21*, 49–72. https://doi.org/10.2495/978-1-85312-669-7/03

Zhou, F., Alms, J., & Advani, S. G. (2008). A closed form solution for flow in dual scale fibrous porous media under constant injection pressure conditions. *Composites Science and Technology*, *68*(3–4), 699–708. https://doi.org/10.1016/j.compscitech.2007.09.010

Chapter 2

Fluid flow in saturated porous fibrous media

2.1 Introduction

The flows of incompressible Newtonian fluids through saturated porous media have been studied extensively using experimental, theoretical and numerical approaches. These studies have shown that fluid flow through porous media is affected by a large number of parameters including the physical characteristics of the fluid (e.g., fluid density and viscosity), the microstructure of the porous media as well as thermomechanical variables (e.g., flow rate, pressure and temperature). The objectives of this chapter are (i) to describe the physics at the pore scale that governs the laminar flow of a Newtonian fluid through a saturated porous media, and (ii) to give a brief overview of the experimental, numerical and theoretical studies that are dedicated to the determination of the permeability properties of fibrous media.

2.2 Microscopic description of fluid flows through porous media

Let us consider the flow through a porous medium (Figure 2.1) occupying a domain Ω of volume V. As illustrated in Figure 2.1, the porous medium is supposed to be made of a connected solid phase saturated by a connected fluid phase. The solid phase (resp. fluid phase) occupies the domain Ω_s of volume V_s (resp. the domain Ω_p of volume V_p) and the fluid-solid interface is defined by Γ. The solid volume fraction of the considered porous media is $\phi_s = V_s/V$ and its porosity is $\phi_p = V_p/V$. The solid phase of the porous media is assumed to be rigid and the liquid is viewed as an incompressible Newtonian fluid.

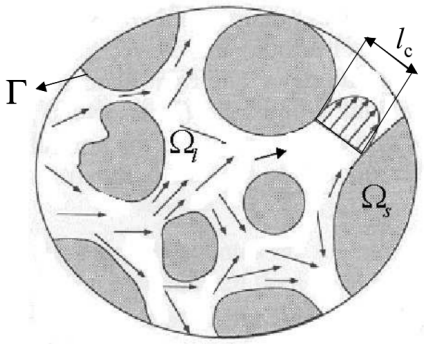

Figure 2.1. Schematic view of the fluid flow at microscopic scale through a porous medium (Idris et al., 2004).

At the pore scale, the fluid flow can be described by the Navier-Stokes equations:

$$\rho\left(\frac{\partial \boldsymbol{v}}{\partial t} + \boldsymbol{v}\cdot\boldsymbol{\nabla}\boldsymbol{v}\right) = -\boldsymbol{\nabla}p + \mu\,\boldsymbol{\nabla}^2\boldsymbol{v} + \boldsymbol{f} \quad in\ \Omega_p \tag{2.1}$$

where ρ is the fluid density, p is the fluid pressure, μ the dynamic fluid viscosity and $\boldsymbol{v}$ is the velocity of the fluid at the pore scale. The terms $\rho(\boldsymbol{v}\cdot\boldsymbol{\nabla})v$, $\mu\boldsymbol{\nabla}^2\boldsymbol{v}$ and $\boldsymbol{f}$ shown in

equation 2.1 are the convective inertia term, the viscous term and the body forces, respectively. Note that if the body forces are only due to gravity, $\boldsymbol{f} = \rho \boldsymbol{g}$.

The Navier-Stokes equations satisfy the momentum balance equation and the continuity equation given hereafter:

$$\frac{\partial \rho}{\partial t} = -\boldsymbol{v} \cdot \boldsymbol{\nabla} \rho - \rho \boldsymbol{\nabla} \cdot \boldsymbol{v} \tag{2.2}$$

In addition, accounting for the fluid incompressibility condition and the no-slip boundary condition on Γ:

$$\boldsymbol{\nabla} \cdot \boldsymbol{v} = 0 \ \ in\, \Omega_p \tag{2.3}$$

and

$$\boldsymbol{v} = \boldsymbol{0} \qquad on\, \Gamma \tag{2.4}$$

The Navier-Stokes equations (2.1) can be written in a dimensionless form to gauge the importance of each of its terms. For that purpose, the following dimensionless variables must be defined:

$$\boldsymbol{X}^* = \frac{1}{l_c}\boldsymbol{X},\ \boldsymbol{\nabla}^* = l_c \boldsymbol{\nabla},\quad \boldsymbol{v}^* = \frac{1}{v_c}\boldsymbol{v},\ p^* = \frac{1}{\Delta p_c} p,\ t^* = \frac{t}{t_c},\ \boldsymbol{g}^* = \frac{1}{g_c}\boldsymbol{g} \tag{2.5}$$

where the subscripts "c" and "*" denote the characteristic and dimensionless variables. Introducing into equation 2.1 the dimensionless variables 2.5 and multiplying both sides of equation 2.1 by $l_c/\rho v_c^2$, the dimensionless form of the Navier-Stokes equation is:

$$St\ \frac{\partial \boldsymbol{v}^*}{\partial t^*} + \boldsymbol{v}^* \cdot \boldsymbol{\nabla}^* \boldsymbol{v}^* = -Eu\ \boldsymbol{\nabla}^* p^* + \frac{1}{Re}\ \boldsymbol{\nabla}^{*2} \boldsymbol{v}^* + \frac{1}{Fr^2}\ \boldsymbol{g}^* \quad in\, \Omega_p \tag{2.6}$$

where *St, Eu, Re* and *Fr* are dimensionless numbers:

- *St* is the Strouhal number which describes oscillating flow mechanisms:

$$St = \frac{l_c}{v_c t_c} \tag{2.7}$$

- *Eu* is the Euler number that represents the ratio of the inertia effects to the pressure drop:

$$Eu = \frac{Pressure}{Inertia} = \frac{\Delta p_c}{\rho v_c^2} \tag{2.8}$$

- *Fr* is the Froude number that represents the ratio of the inertia forces to gravity:

$$Fr = \frac{Inertia}{Gravity} = \sqrt{\frac{v_c^2}{g_c l_c}} \tag{2.9}$$

- Re is the Reynolds number that represents the ratio of the inertia effects to the viscous effects:

$$Re = \frac{Inertia}{Viscosity} = \frac{\rho v_c l_c}{\mu} \tag{2.10}$$

Hence, at the pore scale, considering isothermal and steady state conditions and neglecting body forces, the laminar flow of a Newtonian fluid through a porous medium reduces to the Stokes flow problem:

$$\boldsymbol{\nabla} p = \mu \, \boldsymbol{\nabla}^2 \boldsymbol{v} \quad in \, \Omega_p \tag{2.11}$$

Note that flow situations at high Reynolds numbers ($Re > 10$) are not considered in this chapter.

2.3 Macroscopic description of flows through porous media: Darcy's law

To study the laminar flow of a Newtonian fluid through a porous granular material made of sand, Darcy used the apparatus schematised in Figure 2.2. This apparatus was made of a vertical sand-filled column of height H equipped with two U-tube manometers that indicated the pressures p_1 and p_2 at the top and bottom extremities of the column. The vertical column was filled with siliceous sand of Saône that had a porosity ϕ_p of 0.38. The higher part of the column received water thanks to a reservoir and the lower part of the column had outlet on a gauging basin. The reservoir and outlet had valves that enabled the flow rate of water Q to be properly controlled. Using this experimental setup, Darcy observed that Q was proportional to the pressure gradient. In addition, the constant of proportionality was found to depend on the studied porous materials and the fluid properties. This constitutes the so-called Darcy's law that can be written (neglecting body forces) as:

$$\bar{v}_1 = \frac{Q}{A} = -\frac{k}{\mu}\frac{p_2 - p_1}{H} \tag{2.12}$$

where $\bar{v}_1$ [m.s^{-1}] is the superficial velocity at the macroscopic scale, k [m^2] is the permeability of the porous material, $A = \frac{\pi D^2}{4}$ [m^2] is the column section and D is the diameter of the column.

This empirical law (Darcy, 1856) was then proved theoretically using different upscaling techniques (Auriault, 1991). Darcy's law (Eq. 2.12) can be extended to three-dimensional flows and for any anisotropic porous media as:

$$\bar{\boldsymbol{v}} = -\frac{1}{\mu}\boldsymbol{K} \cdot \boldsymbol{\nabla} P \tag{2.13}$$

where $\overline{\boldsymbol{v}}$ is the Darcy's velocity (macroscopic velocity) defined as $\overline{\boldsymbol{v}} = \frac{1}{\Omega}\int_{\Omega_f} \boldsymbol{v}\, d\Omega$ and $\boldsymbol{K}$ is the permeability tensor of the porous medium. $\boldsymbol{K}$ is a second order tensor defined positive and symmetric. Note that the equation 2.13 can be modified to account for the gravity effects as follows:

$$\overline{\boldsymbol{v}} = -\frac{1}{\mu}\boldsymbol{K} \cdot (\boldsymbol{\nabla} P - \rho \boldsymbol{g}) \tag{2.14}$$

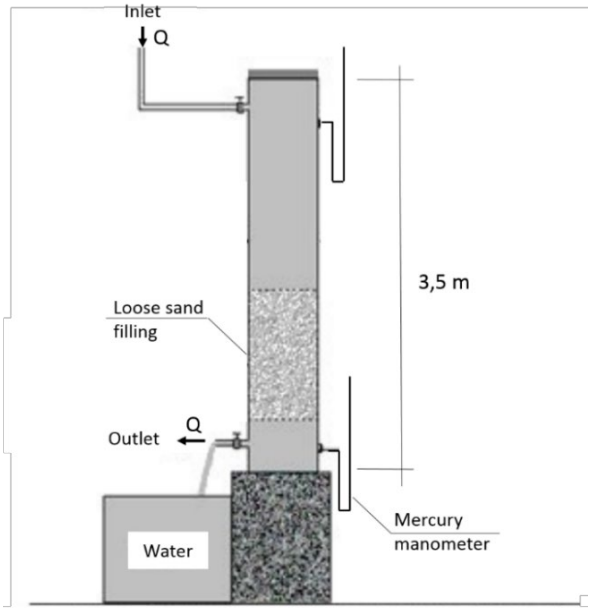

Figure 2.2. Schematic representation of the apparatus used by Darcy to investigate the flow of a Newtonian fluid through saturated sands (Darcy, 1856).

It is worth noting that for flows at high local Reynolds numbers (i.e. $Re > 10$) Darcy's law is no more valid. Some authors such as Forchheimer, (1901), Ergun, (1952), Mei & Auriault, (1991) have proposed a modified expression for the Darcy's law that become non-linear to describe the flow in porous media at higher Reynolds numbers.

2.4 Permeability of fibrous media

Permeability is defined as the ease of a fluid to flow through a porous medium, and therefore it is an inverse measure of the flow resistance (Long, 2005). The determination and quantitative prediction of the permeability of fibrous porous media is a longstanding but still challenging engineering problem. Many research efforts were conducted to determine the components of the permeability tensor $\boldsymbol{K}$ of fibrous media, including fibre reinforcement materials that are used in composite materials. The permeability of fibrous materials was found to depend on several key microstructure descriptors such as the fibre volume fraction (or conversely the porosity), fibre geometry, fibre arrangement and orientation. In the following section, we recall briefly the main experimental, numerical

and theoretical approaches that were proposed to determine the permeability of fibrous materials.

2.4.1 Permeability measurements

2.4.1.1 Experimental approaches

Several experimental studies are devoted to the determination of the components of the permeability tensor $\boldsymbol{K}$ of fibrous materials. Two types of experimental techniques are commonly used to determine the in-plane components of the permeability tensor: (i) in-plane radial flow experiments and (ii) in-plane channel flow experiments. Both types of experiments can be conducted using either a constant injection pressure or a constant injection flow rate. The fluids used in these experiments are model fluids with a Newtonian behaviour. Experimental devices that are used to perform in-plane radial and channel flow experiments are composed of a mould with fluid inlet and outlet, the positions of which depend on the type of experiment considered. In addition, the mould is equipped with several rotameters and pressure sensors that allow measuring the flow rate and the pressure gradient during fluid flow, respectively (Sharma, 2010). Experiments are often carried out in saturated flow conditions. In this case, the mould with the fibre reinforcement is entirely filled by the fluid. Once steady state flow conditions are reached, the resulting flow rate and pressure gradient are measured, thus enabling the permeability to be deduced from the Darcy's law.

The in-plane radial flow method (Figure2.3a-b) was used in a large number of experiments. In this type of experiments, a fluid inlet is placed at the centre of the porous medium leading to an in-plane radial fluid flow. In addition, this impregnation device is often equipped with an optical visualisation system. This system enables following the propagation of the fluid flow front during impregnation. This experimental method enables measuring the two principal in-plane components of the permeability tensor in unsaturated conditions from a single impregnation experiment.

The in-plane channel flow method is illustrated in Figure 2.3c-d. In this type of experiments, the fluid inlet is placed at one extremity of the mould leading to an in-plane directional fluid flow towards the outlet of the impregnation device that is placed on the opposite side of the mould. Using this method, it is possible to perform permeability measurements either in unsaturated or saturated conditions. To obtain the in-plane components of the permeability tensor $\boldsymbol{K}$, at least two independent impregnation experiments must be performed. However, it is important to note that it is difficult to control properly the flow conditions using this impregnation setup. Pronounced irregularities of the flow front characterized by the appearance of race-tracking zones along the edges of the mould often occur during impregnation experiments. To perform permeability measurements in unsaturated conditions, the experimental setup must be equipped with an optical visualisation system enabling the propagation of the fluid to be tracked as a function of time.

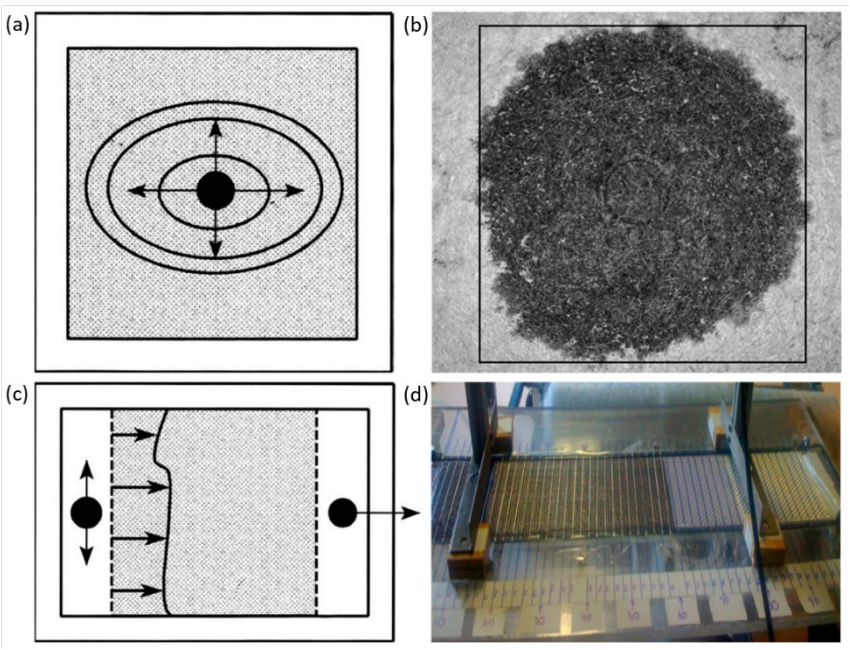

Figure 2.3. Scheme of the two experimental techniques that are classically used to determine the in-plane components of the permeability tensor of fibrous materials: (a-b) in-plane radial flow method (Xue et al., 2011) and (c-d) in-plane channel flow method (Parnas et al., 1995). Both types of setups were equipped with an optical visualisation system, enabling the propagation of the fluid front to be tracked during impregnation.

Out-of-plane measurements of the permeability – Several studies were devoted to the measurements of the out-of-plane permeability of fibrous materials in saturated flow conditions (Trevino, 1991; Drapier et al., 2002; Merhi, 2006). In this approach, a porous fibrous material is placed into the cavity of a mould equipped with mobile parts. The thickness of the mould cavity can be adjusted by applying an out-of-plane compaction stress on the upper and lower surfaces of the mould. This enables controlling the fibre volume content (or conversely the porosity) of the studied fibrous material. After compaction, the fluid is injected through the thickness of the fibrous material. Out-of-plane flow experiments can be performed using a constant injection pressure or a constant injection flow rate. Then from the measurements of the flow rate and pressure gradient, it is possible to determine the out-of-plane permeability of the fibrous material using the Darcy's law. More recently, "continuous techniques" were developed for the measurements of the in-plane and out-of-plane permeability (Comas-Cardona et al., 2007; Ouagne & Bréard, 2010; Liotier et al., 2015). These "continuous" techniques allow measuring the in-plane (Buntain & Bickerton, 2003) or the out-of-plane permeability components while compacting continuously the saturated fibre reinforcement. These methods are really efficient since the evolution of the permeability as a function of the fibre content (or conversely the porosity) can be obtained from a single impregnation experiment.

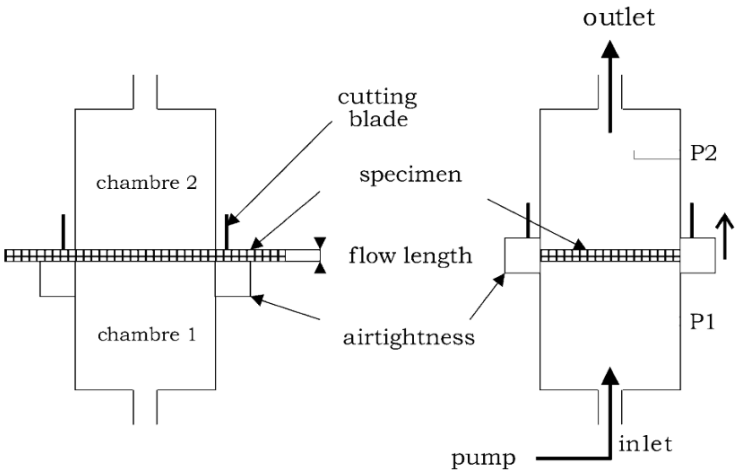

Figure 2.4. Scheme of an apparatus designed to measure the out-of-plane permeability of fibrous materials (Drapier et al., 2002).

The lack of standardization in the realisation of permeability measurements still constitutes a major problem in the composite domain (Parnas et al., 1995; Lundström et al., 2000). To identify the sources of errors and their effects on the permeability measurements, several institutions worldwide worked together to carried out a permeability benchmark exercise for the experimental determination of the permeability of fibre reinforcements. In the first study (Arbter et al., 2011), 11 different institutions were involved to measure the in-plane permeability of two different fibre reinforcements, namely a 2×2 twill weave made of an assembly of carbon fibre bundles and a 2×2 twill weave made of an assembly of glass fibre bundles. The procedures used to measure the permeability were not imposed and can be summarized as follows: 9 in-plane channel flow experiments, 7 in-plane radial flow experiments, 12 experiments performed with a constant injection pressure, 3 experiments carried out with a constant injection flow rate, 9 experiments conducted in saturated flow conditions and 7 experiments performed using unsaturated flow conditions.

The results of the benchmark exercise showed that the permeability measurements were very scattered with permeability variations up to one order of magnitude (Figure 2.5). The scattering of the data was supposed to be mainly related to several human factors. In a second permeability benchmark exercise (Vernet et al., 2014), the involved participants were asked to use the same values for parameters such as the fibre volume fraction, the injection pressure and the fluid viscosity to minimize the sources of scattering in the determination of the permeability. In addition, all the impregnation tests were performed using in-plane channel flow experiments with the fluid injected with a constant pressure. In this study, adopting a common procedure and standardised experimental parameters, the variation in the permeability measurements (for a fibre reinforcement with a given fibre volume fraction) was reduced to 25%. These results highlighted the difficulty in measuring the permeability of fibrous materials using experimental approaches and also the necessity of using standardised and well-controlled experimental procedures.

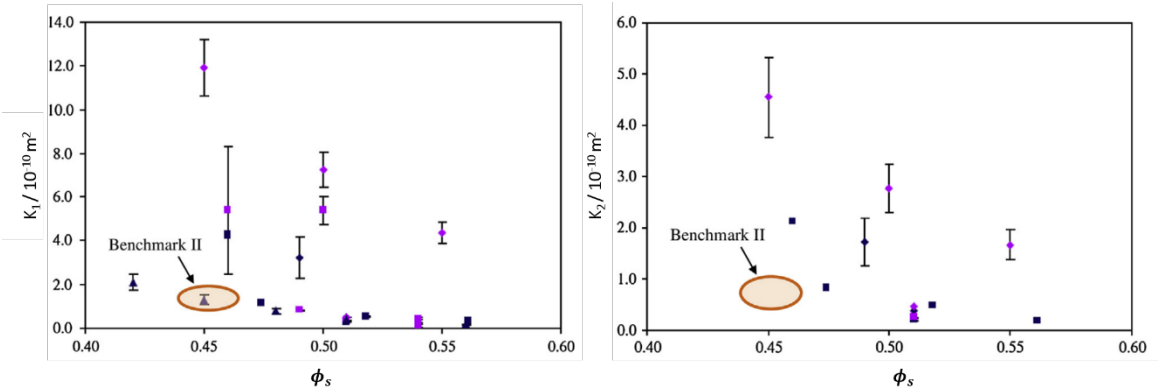

Figure 2.5. In-plane components K_1 and K_2 of the permeability tensor obtained for a 2×2 twill weave made of an assembly of carbon fibre bundles and for different fibre volume fractions. Black diamonds: in-plane radial flow experiments in unsaturated flow conditions, purple diamonds: in-plane radial flow experiments in saturated conditions, black squares: in-plane channel flow experiments in unsaturated flow conditions, purple squares: in-plane channel flow experiments in saturated flow conditions. These data were obtained during the two permeability benchmark exercises (Vernet et al., 2014).

2.4.1.2 Numerical methods

Several studies were devoted to the determination of the permeability of fibrous materials using fibre scale CFD simulations. Most of the CFD simulations were performed on virtual fibrous networks that were generated using different numerical generator procedures (Figures 2.6 and 2.7). This numerical approach enables investigating the permeability of a wide diversity of fibrous materials by varying several microstructure descriptors such as the fibre volume content, geometry and arrangement.

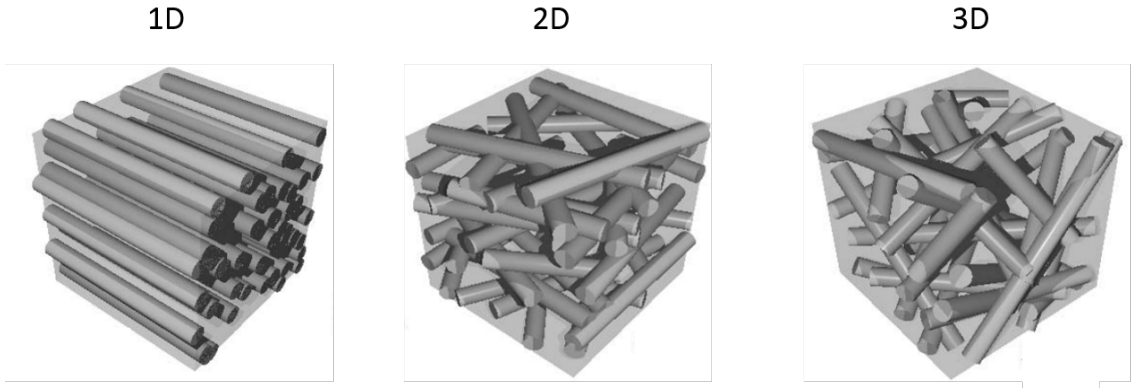

Figure 2.6. Numerically generated virtual fibrous networks with (i) aligned fibres in one direction (ii) 2D random and (iii) 3D random fibre orientations (Tomadakis et al., 2005).

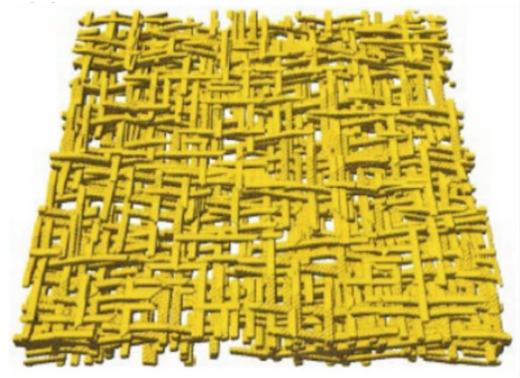

Figure 2.7. Numerically generated virtual fibrous network mimicking the fibre structure of a low-density paper (porosity of 0.83) (Koponen et al., 1998).

In addition, the current development of 3D imaging techniques such as laboratory X-ray microtomography or synchrotron X-ray microtomography allows obtaining high-resolution 3D images of fibrous media with complex fibre bundle/fibre architectures. From these 3D images, several microstructure descriptors of fibrous materials such as the fibre volume fraction (conversely the porosity), specific surface area, tortuosity and fibre orientation can be quantitatively measured using image processing techniques (Delisée et al., 2010; Joffre et al., 2015; Rolland du Roscoat et al., 2007; Viguié et al., 2011). In addition, an increasing number of current studies have performed CFD simulations on 3D images acquired using the aforementioned imaging techniques to obtain relevant permeability measurements of fibrous materials with complex fibre architectures (Jaganathan et al., 2008; Delisée et al., 2010; Koivu et al., 2010; Soltani et al., 2014; Naresh et al., 2020). Figure 2.8 shows an example of binarised 3D images of fibre mats obtained using X-ray microtomography. These binarised 3D images were then used as input numerical images for fibre scale CFD simulations.

Figure 2.8. Examples of 3D microtomography images of fibre mats that exhibit different fibre orientations (Soltani et al., 2014b)

From a numerical viewpoint, various strategies were used to numerically solve the Stokes flow problem at the pore scale (equation 2.11). For instance, Gebart (1992), Berdichevsky, (1993) and Bruschke & Advani (1993) used a numerical method that was based on the finite element method to solve the velocity-pressure fluid flow problem related to the impregnation of numerically generated fibrous networks with fibre arrangements similar to

those shown in Figure 2.6. In contrast, Succi et al., (1989), Koponen et al., (1998), Belov et al., (2003), Vidal et al., (2009) used a lattice-Boltzman numerical method (LBM). These authors claimed that the LBM model was particularly well adapted to the resolution of fluid flow problems occurring in complex geometries such as the porous structures encountered in fibrous media (Figures 2.7, 2.8). More currently, fibre scale CFD simulations were carried out using finite volume methods on 3D X-ray microtomography images that were meshed using a voxel-based discretization technique. The boundary conditions adopted in these calculations are generally of periodic type, zero shear stress (Happel, 1959) or zero vorticity (Kuwabara, 1959)

2.4.2 Effect of microstructure descriptors of fibre networks on their permeability

A large number of studies deals with the experimental and numerical investigation of the fluid flow through porous fibrous media. In the following sections, some important results that highlight the key role of some microstructures descriptors on the permeability of fibrous materials are briefly recalled.

2.4.2.1 Effect of fibre volume fractions and fibre arrangements

In their review, Jackson & James, (1986) gathered a large set of experimental data concerning the filtration of Newtonian fluids through various fibrous media. In their review, 25 different fibrous media were considered: filter mats and industrial fibres (Chen, 1955), wires of stainless steel (Carman, 1938), of copper (Wiggins et al., 1939) or of Cr-Ni fibres (Kostornov & Shevchuk, 1977), wool or glass cylinders (Wiggins et al., 1939; Brown, 1950), nylon fibres (Ingmanson, 1959;Labrecque, 1968), regular arrangements of heat exchanger tubes (Bergelin et al., 1950) or of fibres (Kirsch & Fuchs, 1967), gel or polymer solutions (White, 1960; Jackson and James, 1982) and collagen membranes (Viswanadham et al., 1978). Most of the aforementioned studies were done on disordered fibrous media made of long or short flexible fibres. The fibre volume fractions of the studied fibrous materials varied from $3 \times 10^{-4} \leq \phi_s \leq 0.71$ and the range of the equivalent fibre radius ranged between 10^{-6} mm and 10 mm. The data collected by the authors are shown in Figure 2.9 where the evolution of the dimensionless permeability K^* ($K^* = K/r^2$ where r is the equivalent fibre radius) is plotted as a function of the fibre volume fraction ϕ_s (see black markers in Figure 2.9). It can be shown from this figure that all the experimental data gathered in this study practically followed the same tendency, regardless of the fibre arrangement: the permeability of fibrous media depended non-linearly on the fibre volume fraction ϕ_s. This trend clearly highlights the main role of the fibre volume fraction ϕ_s on the permeability of fibrous media. At the same time, this figure underlines the role of the fibre arrangement. Indeed, for the same fibre volume fraction, the variation of the dimensionless permeability ranges within a decade.

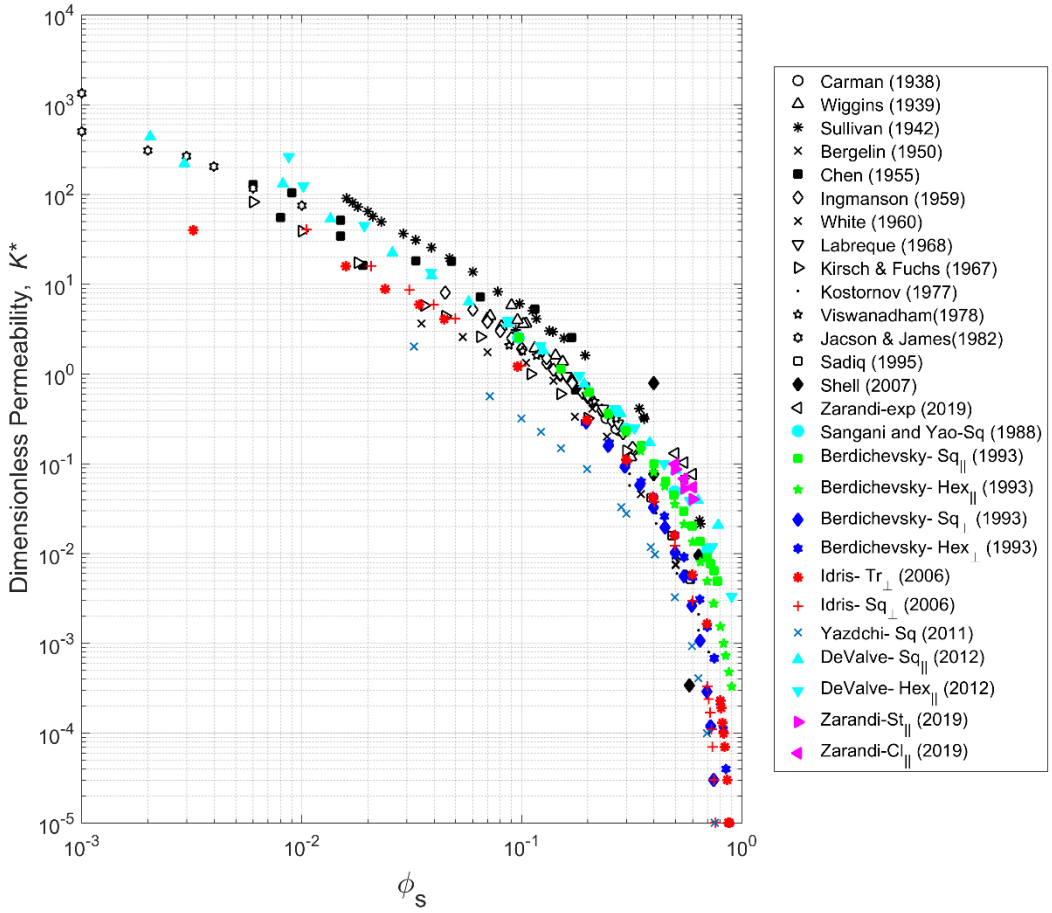

Figure 2.9. Evolution of the dimensionless permeability K^* ($K^* = K/r^2$ where r is the equivalent fibre radius) of various types of fibrous media as a function of their fibre volume fraction ϕ_s. Black markers correspond to experimental data reported in the review by Jackson & James (1986) and coloured markers correspond to numerical permeability results obtained for arrays made of different arrangements of aligned fibres.

2.4.2.2 Effect of fibre arrangements and flow directions

Several authors carried out experiments using well-defined and perfectly periodic fibrous media to study the impact of the microstructure on the permeability. Bergelin et al. (1950) studied fluid flow normal to triangular, square and staggered square arrays of parallel fibres that exhibited medium and low porosities. Kirsch & Fuchs (1967) studied different arrangements of rows of parallel fibres normal to the flow: square arrays, “staggered” arrays from which alternate rows where shifted to make a diamond pattern, and “fan” arrays from which each row was turned through an angle in its own plane (Figure 2.10).

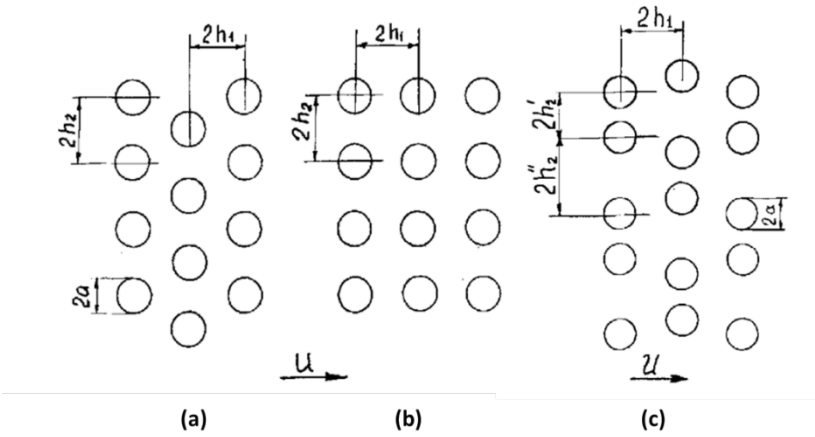

Figure 2.10. Model arrays made of different arrangements of parallel cylinders: (a) "staggered", (b) square and (c) non-uniform (Kirsch & Fuchs, 1967) arrays.

Their experimental results revealed that, if the distance between the rows was sufficiently large, i.e., equal or greater than the distance between fibres, then the permeability of the different arrays was practically the same. This tends to show that the transverse permeability of fibrous media does not depend significantly on the fibre arrangement when the porosity is important (or conversely the fibre volume fraction ϕ_s is small). As the distance between the rows was reduced, the "fan" array displayed a lowest permeability than the rectangular array, and the "staggered" array of fibres exhibited the lowest permeability. Besides, Sadiq et al. (1995) studied experimentally the flow of viscous fluids across square arrays of circular cylinders for fibre volume fractions that ranged between 0.38 and 0.61. The comparison of the results gathered in these different experimental studies carried out on defined fibrous media were in good agreement.

To better assess the effects of the fibre arrangement on the permeability of fibrous media, experimental data were largely completed with numerical permeability results. Many CFD simulations were performed on a wide diversity of model arrays made of different arrangements of parallel fibres and varying the fibre volume fractions (Berdichevsky & Cai, 1993; Yazdchi et al., 2011; Sangani & Yao, 1988; Cortis & Smeulders, 2001; Devalve & Pitchumani, 2012; Zarandi et al., 2019). The numerical permeability results shown in Figure 2.9 clearly emphasise the effect of the flow direction with respect to the fibre arrangement. The permeability measured for fluid flows oriented along the fibres (i.e., longitudinal permeability) is higher than the permeability measured for flows oriented perpendicular to the fibres (transverse permeability). Bechtold & Ye (2003), investigated the effects of variations in the spatial fibre distribution on the permeability of arrays of parallel fibres. The authors found that fibre networks with a more "regular" fibre arrangement exhibited higher transverse permeability than fibre networks with random spatial fibre distributions. At the same time the appearance of large flow channels due to fibres cluster could increase the permeability.

The number of numerical studies dealing with the determination of the permeability of fibrous materials with more complex fibre architectures is less important. Tsay &

Weinbaum (1991) were the first to investigate using CFD simulations the effect of the in-plane fibre orientation on the transverse permeability of fibrous media. Higdon & Ford (1996) investigated the flows of Newtonian fluids through various 3D porous structures such as cubic (SC), body-centred cubic (BCC), and face-centred cubic (FCC) structures for a wide range of fibre volume fractions. The permeability of 2D and 3D fibre networks was investigated by several authors (Tomadakis et al., 2005; Nabovati et al., 2009). Nabovati (2009) found that the fibre curvature had a negligible effect on the permeability of fibre networks. These studies also highlighted the important role of fibre orientation on the permeability of fibre networks. This point will be further discussed in the next section.

More recently, several studies performed using CFD simulations on realistic 3D images of fibrous materials with complex fibre architectures such as fibre mats and papers (Jaganathan et al., 2008; Delisée et al., 2010; Soltani et al., 2017). The permeability results obtained using CFD simulations on realistic 3D images of different types of fibrous materials are shown in Figure 2.11. For comparison purpose, experimental permeability measurements are also plotted in Figure 2.11.

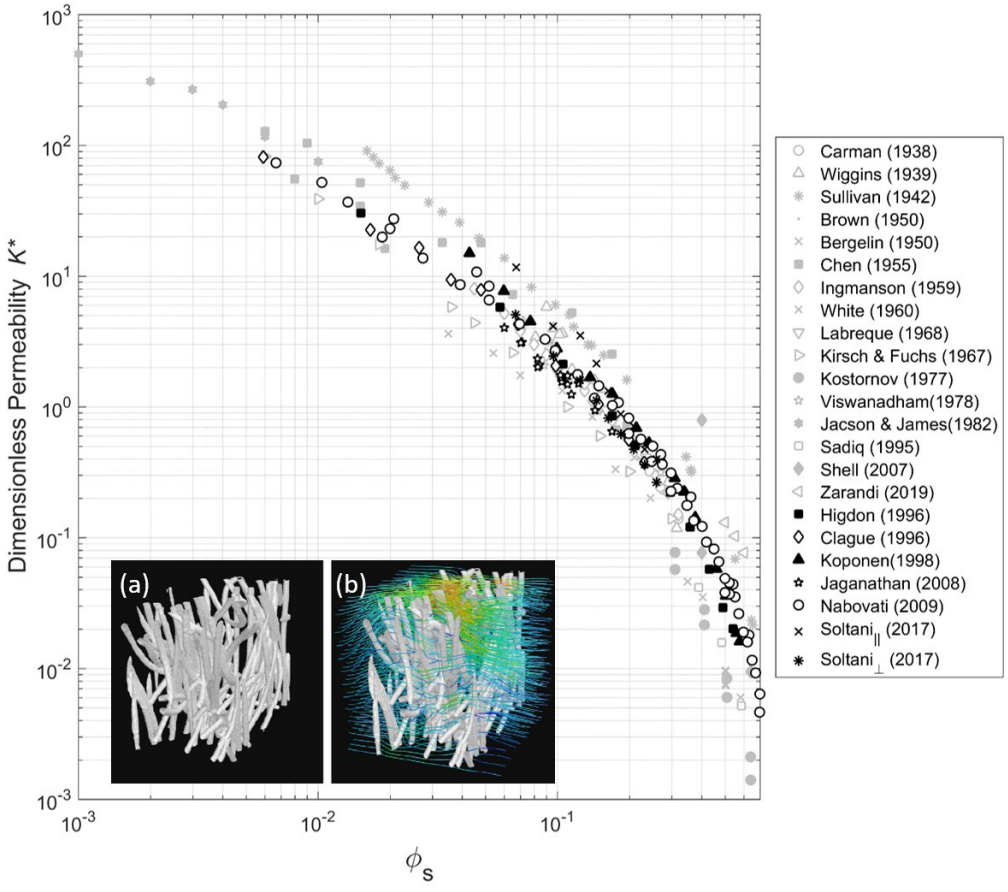

Figure 2.11. Dimensionless permeability of various types of fibrous materials obtained using (i) CFD simulations on realistic 3D images (black markers) and (ii) experimental approaches (grey markers). The inset images show the results of a fibre scale CFD simulation that was performed on hydro-entangled nonwoven materials (Jaganathan et al., 2008)

The numerical permeability results obtained for a wide range of fibre volume fractions, i.e., $0.1 \leq \phi_s \leq 0.7$, are in accordance with experimental measurements. This shows that the developed numerical strategies enable the permeability of fibrous materials with complex microstructures to be properly determined. Note also that the figure emphasises once again the predominant effect of the fibre volume fraction on the permeability of fibrous materials.

2.4.2.3 Effect of fibre orientations

Several studies aimed a better understanding of the effect of fibre orientations on the permeability of fibrous media. Using CFD simulations, Stylianopoulos et al. (2008) investigated the effect of fibre misalignments on the longitudinal and transverse permeability of numerically generated 3D networks with varying degrees of orientation. The authors observed that the highly aligned fibre networks had higher longitudinal and transverse permeability components than the moderately aligned fibre networks (Figure 2.12). They also reported that the transverse and longitudinal permeability of moderately aligned fibre networks was higher than that of fibre networks with random fibre orientations (Figure 2.12). Moreover transverse permeability is lower than longitudinal one. More recently Soltani et al. (Soltani et al., 2014b) performed fibre scale CFD simulations on 3D X-ray microtomography images of fibre mats that exhibited different fibre orientations (Figure 2.8). Their simulation results revealed that the in-plane permeability components of the fibre mats followed the same trends than those reported by Stylianopoulos et al. (2008) on numerically generated fibre networks: fibre mats with pronounced fibre alignment had higher longitudinal permeability than the mats with moderate fibre alignment but the transverse permeability for layered structures is lower. In addition, fibre mats with a random fibre orientation had lower permeability than fibre mats with moderate fibre alignment. Similar results were found by Pradhan (2012) who compute permeability solving Stokes equation in three dimensional structures obtained by varying the degree of anisotropy of 3D fibre orientation.

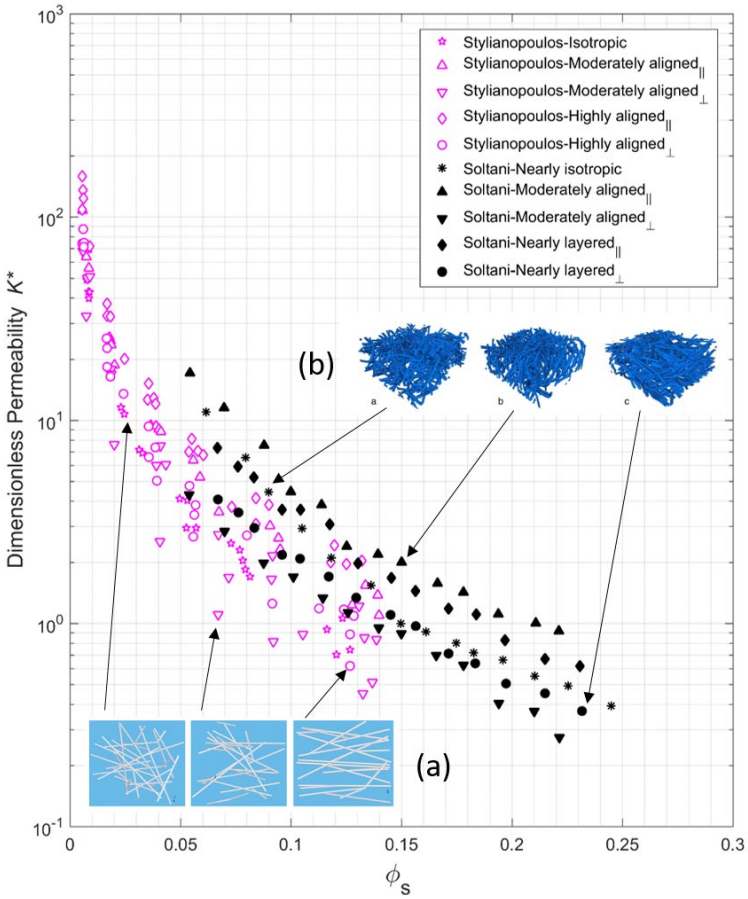

Figure 2.12. Dimensionless longitudinal and transverse permeability components obtained for numerically generated (Stylianopoulos et al., 2008) (a) and realistic (Soltani et al., 2014b) (b) fibre networks that exhibit different fibre volume fractions and orientations.

2.4.3 Analytical models for the prediction of the permeability of fibrous media

Based on the numerous experimental and numerical permeability data, several authors proposed analytical models for the prediction of the permeability of fibrous media. In the following sections, we provide a brief overview of the most frequently used permeability models.

2.4.3.1 Capillary models

A first strategy that is widely used to estimate the permeability of porous materials consists in using permeability models based on a capillary approach (Blake, 1922; Kozeny, 1927; (Carman, 1938; Carman, 1956). One of the most used capillary model is the Kozeny-Carman permeability model that writes:

$$K^* = \frac{\phi_p^3}{2c_0 S_v^2 \tau^2} \frac{1}{r^2} \tag{2.15}$$

where ϕ_p is the volume fraction of pores, S_v is the specific surface area, τ is the tortuosity (defined as the ratio between the mean flow path length and a characteristic length of the porous media). The Kozeny-Carman permeability model was initially developed by assuming that the porous medium was equivalent to an assembly of parallel tortuous capillaries with equal length L_o and diameter $2R$ and circular cross sections A_o, as shown in Figure 2.13. The assembly of capillaries has the same equivalent porosity ϕ_p and specific surface area S_v as the considered porous medium. The parameter c_0 can be seen as a corrective term to extend the model to cylinders with any cross section geometry.

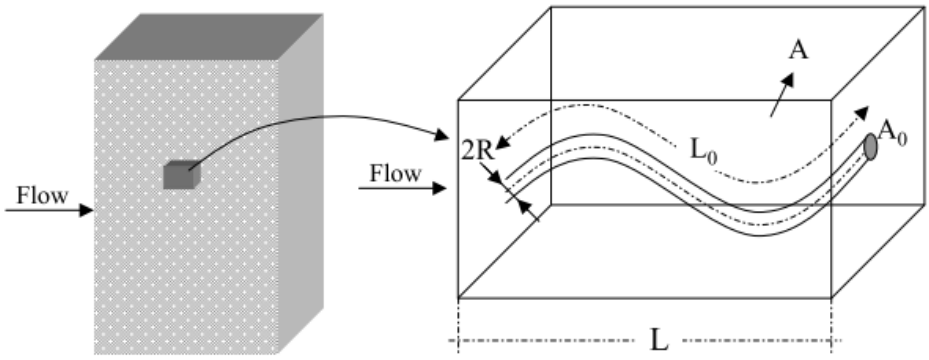

Figure 2.13. Schematic representation of the capillary model considered in the approach proposed by Kozeny and Carman.

The Kozeny-Carman model has been widely used to determine the longitudinal permeability of fibrous media of aligned fibre beds. Several authors (Skartsis et al., 1992; Bruschke & Advani, 1993, Mostaghimi et al., 2013) showed that the Kozeny-Carman expression was valid for slow Newtonian flow through porous media over limited porosity ranges. However, the predictions of the Kozeny-Carman model for transverse flow across fibrous media of aligned fibre beds were found to be inaccurate. For example, the study by Bruschke (1993) revealed that the transverse permeability results obtained using CFD simulations on several arrays made of square and triangular fibre arrangements were not in accordance with the permeability predictions given by the Kozeny-Carman model.
Note also that an improvement on the Kozeny-Carman model was proposed by Gutowski (Gutowski et al., 1987). To improve the accuracy of the Kozeny-Carman for the prediction of the longitudinal and transverse permeability of fibrous media of aligned fibre beds, Gutowski (1987) proposed different values for the parameter c_0 of the Kozeny-Carman model with respect to the considered flow direction. Similarly, Koponen et al. (1998) also proposed exmpirical expressions for the parameter c_0 of the Kozeny-Carman to better predict the out-of-plane permeability of fibre mats and papers. In their approach, the parameter c_0 was identified by inverse method using numerical permeability results

obtained by CFD simulations on numerically generated fibrous networks. They found that the parameter c_0 was a non-linear function of the fibre volume fraction.

2.4.3.2 Lubrication models

Several permeability models for fibrous media are based on the lubrication theory (Keller, 1964; Gebart, 1992; Bruschke & Advani, 1993). In this approach, the fibrous medium is seen as an assembly of parallel cylinders with triangular, square or hexagonal periodic arrangements (Figure 2.14). In these arrays, it is possible to define a "unit cell" (Elementary Representative Volume) where the flow is the same as in all other cells of the fibrous medium. Hence, the problem reduces in solving Stokes equations, with zero velocity at the cylinder surface and with periodic boundary conditions at the edges of the considered unit cell. Analytical expressions for the flow of the fluid between adjacent fibres can be obtained using the approximations given by the lubrication theory. Note that this approach can be used for flows that are oriented parallel or perpendicular to the fibre arrays. However, the lubrication approach is valid when the fibres are closely spaced, i.e., for fibre networks with high fibre contents.

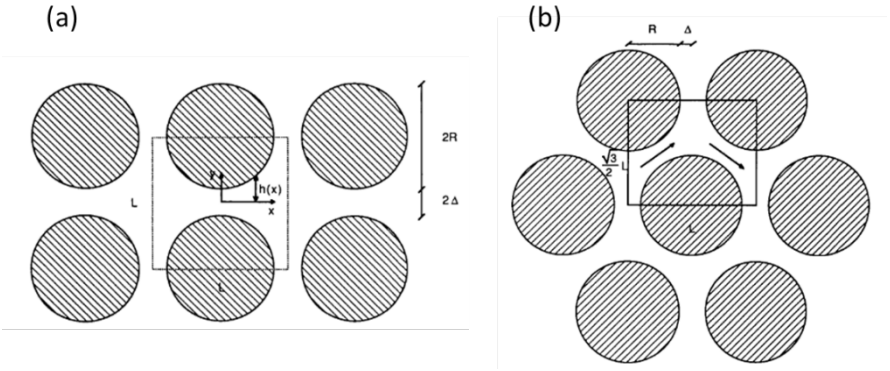

Figure 2.14. Schematic representation of arrays of parallel cylinders with square (a) and hexagonal (b) fibre arrangements. The black box shows the periodic "unit cell" within which the Stokes flow problem can be solved theoretically using (i) the approximations given by the lubrication theory and (ii) periodic boundary conditions at its edges (Gebart, 1992).

The aforementioned lubrication approach was used by Gebart (Gebart, 1992). Using this approach the author proposed an analytical permeability model for the flows oriented parallel and perpendicular to arrays of cylinders with square and hexagonal fibre arrangements (Figure 2.14). The dimensionless longitudinal and transverse permeability components write:

$$K_{\parallel}^{*} = \frac{8}{\beta}\frac{(1-\phi_s)^3}{{\phi_s}^2} \tag{2.16}$$

$$K_{\perp}^{*} = C_1 \left(\sqrt{\frac{c_{max}}{\phi_s}} - 1 \right)^{5/2}$$

where C_1, c_{max} and β are parameters that depend on the fibre arrangement (Table 2.1). The values of the aforementioned parameters are given in Table 2.1 for both types of fibre arrangements.

Table 2.1. Theoretical values used in the analytical model proposed by Gebart for flows parallel and perpendicular to the cylinder axis.

Fibre arrangement	C_1	C_{max}	β
Square	$\frac{16}{9\pi\sqrt{2}}$	$\frac{\pi}{4}$	57
Hexagonal	$\frac{16}{9\pi\sqrt{6}}$	$\frac{\pi}{2\sqrt{3}}$	53

2.4.3.3 Cell models

Several permeability models were specifically developed for fibre arrays made of widely spaced parallel fibres, i.e., for fibrous media of aligned fibres with low fibre contents (Happel, 1959; Kuwabara, 1959) These permeability models are based on a cell model idealisation. This approach assumes that the fibres are spaced far enough apart that the fibrous medium can be divided into independent cells. As shown in Figure 2.15, in this approach a cell is made of two concentric cylinders: an inner cylinder that represents a fibre of radius R_i and another cylinder that represents the fluid domain between adjacent cylinders. Hence, by applying a proper set of boundary conditions on the external surface of the REV, it is possible to solve the Stokes flow problem. However, it is important to note that the transverse flow does not depend on the fibre arrangement owing to the important spacing between the fibres.

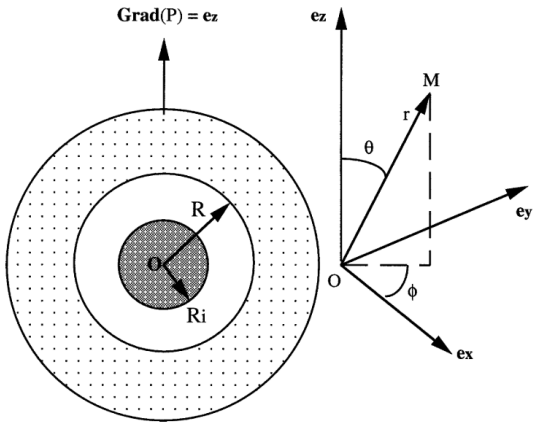

Figure 2.15. Scheme of a cell model idealisation.

2.4.3.4 Hybrid models

Lubrication and cell models allow obtaining good prediction for the permeability of fibrous media made of aligned fibres with high and low fibre volume fractions, respectively. However, both types of models are not able to give relevant permeability predictions over a wide range of fibre volume fractions. For that purpose, Bruschke & Advani, (1993), proposed an hybrid model that is a phenomenological combination of the analytical cell model k_{cell} known to give good predictions within the low fibre volume fraction range, and the analytical lubrication model k_{lub} much more accurate at higher fibre volume fractions. The expressions of the dimensionless transverse permeability proposed by Bruschke & Advani (1993) writes:

$$k_T^* = \frac{k_T}{r^2} = \xi_1 k_{lub}^* + \xi_2 k_{cell}^* \tag{2.17}$$

with

$$k_{lub}^* = \frac{k_{lub}}{r^2} = \frac{1}{3\sqrt{3}} \frac{(1-\Phi)}{\Phi^{3/2}} \left(\sqrt[3]{\Phi \frac{\tan^{-1}\left(\frac{1+\sqrt{\Phi}}{1-\sqrt{\Phi}}\right)}{\sqrt{1-\Phi}} + \frac{\Phi}{2} + 1} \right)^{-1} \tag{2.18}$$

and

$$k_{cell}^* = \frac{k_{cell}}{r^2} = \frac{1}{8\phi_s} \left(-\ln \phi_s - \frac{3}{2} + 2\phi_s - \frac{\phi_s^2}{2} \right) \tag{2.19}$$

where $\xi_1 = 1 - e^{\alpha\left(\frac{\Phi}{\Phi-1}\right)}$, $\xi_2 = 1 - e^{\alpha((\Phi-1)/\Phi)}$, $\alpha = 0.528$ and $\Phi = \pi\phi_s/(2\sqrt{3})$.

As shown in Figure 2.16, the hybrid model gives good predictions for a wide range of fibre volume fractions, i.e., $0 < \phi_s \leq 0.8$.

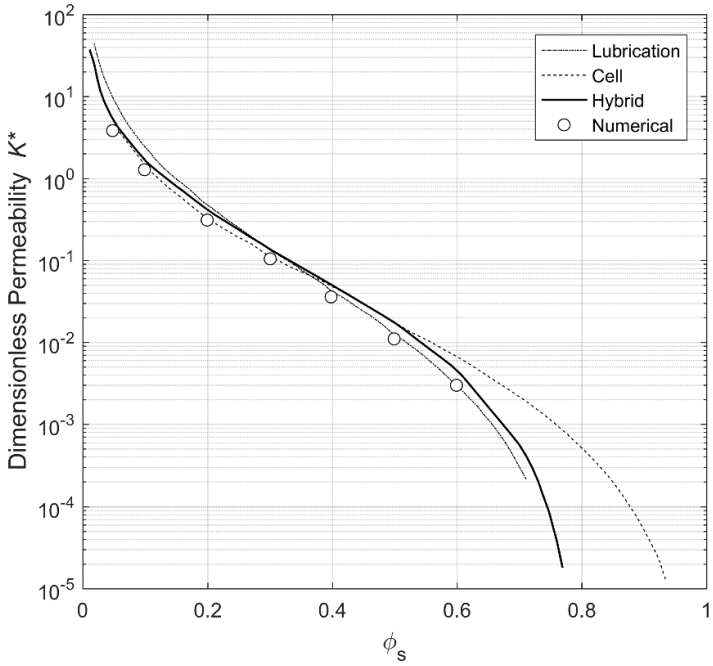

Figure 2.16. Predictions of the dimensionless transverse permeability of square arrays of circular cylinders as a function of their fibre volume fraction obtained using the lubrication, the cell and the hybrid models. To gauge the relevance of the hybrid models, numerical permeability results are also plotted in the graph (Bruschke & Advani, 1993).

2.4.4 Predictions of permeability models for fibre networks made of aligned fibres

In this section, the analytical expressions of several permeability models based on the lubrication theory, the cell model idealisation (Happel, 1959; Sparrow & Loeffler, 1959; Sangani & Acrivos, 1982) or on both types of approaches (hybrid models) (Bruschke & Advani, 1993) are given in Table 2.2. Happel (1959) was the first author to propose an analytical solution for the flows oriented parallel or perpendicular to arrays of cylinders with undefined fibre arrangement. To obtain an analytical expression, the author used a circular cell and a zero shear stress condition at the surface of the cylinder.Sangani & Acrivos (1982b) solved the problem of normal flows through square and hexagonal arrays following the methodology of Sparrow & Loeffler (1959). Drummond & Tahir (1983), proposed analytical models for the flows oriented parallel and perpendicular to arrays of cylinders with square, triangular and hexagonal fibre arrangements. Young (1996) derived an expression for the prediction of the transverse permeability of arrays of parallel cylinders. Using both homogenisation of periodic media and self-consistent methods, Boutin (2000) established, for kinematic and static conditions, analytical expressions for flows oriented parallel and perpendicular to arrays of cylinders (with random fibre arrangement). Shou et al. (2015) proposed a simple analytical model for the prediction of the longitudinal permeability for arrays of parallel cylinders with square, hexagonal and

random fibre arrangements. The analytical expressions of the aforementioned permeability models are given in Table 2.2.

Table 2.2. Permeability models developed for flows parallel and perpendicular to arrays of cylinders with different fibre arrangements.

Authors	Fibre Arrange-ment	$\boldsymbol{K}_{\parallel}^{*}$	$\boldsymbol{K}_{\perp}^{*}$
Happel (1959)	-	$\frac{1}{4\phi_s}\left(-\ln(\phi_s)-\frac{3}{2}+2\phi_s-\frac{{\phi_s}^2}{2}\right)$	$\frac{1}{8\phi_s}\left(-\ln(\phi_s)+\frac{{\phi_s}^2-1}{{\phi_s}^2+1}\right)$
Drummond and Tahir (1959)	Square	$\frac{1}{4\phi_s}\left(-\ln(c\phi_s)-1.476+2\phi_s-\frac{{\phi_s}^2}{2}+O({\phi_s}^4)\right)$	$\frac{1}{8\phi_s}\left(-\ln(\phi_s)-1.476+2\phi_s-1.77{\phi_s}^2+O({\phi_s}^3)\right)$
	Triangular	$\frac{1}{4\phi_s}\left(-\ln(\phi_s)-1.498+2\phi_s-\frac{{\phi_s}^2}{2}+O({\phi_s}^6)\right)$	$\frac{1}{8\phi_s}\left(-\ln(\phi_s)-1.497+2\phi_s-\frac{{\phi_s}^2}{2}-0.739{\phi_s}^4+O(\phi_s)\right)$
	Hexagonal	$\frac{1}{4\phi_s}\left(-\ln(\phi_s)-1.354+2\phi_s-\frac{{\phi_s}^2}{2}+O({\phi_s}^4)\right)$	$\frac{1}{8\phi_s}\left(-\ln(\phi_s)-1.476+2\phi_s-\frac{{\phi_s}^2}{2}+O({\phi_s}^4)\right)$
Sangani and Acrivos (1982)	Square		$\frac{1}{8\phi_s}\left(-\ln(\phi_s)-1.476+2\phi_s-1.77{\phi_s}^2+4.07{\phi_s}^3+O({\phi_s}^4)\right)$
	Hexagonal		$\frac{1}{8\phi_s}\left(-\ln(\phi_s)-1.49+2\phi_s-\frac{{\phi_s}^2}{2}+O({\phi_s}^4)\right)$
Berdichevsky (1993)	-	$\frac{1}{8\phi_s}\left(\ln\left(\frac{1}{{\phi_s}^2}\right)-(3-\phi_s)(1-\phi_s)\right)$	$\frac{1}{8\phi_s}\left(\ln\left(\frac{1}{\phi_s}\right)-\frac{(1-{\phi_s}^2)}{(1+{\phi_s}^2)}\right)$
Young (1996)	-		$\frac{1}{0.8}\left(\sqrt{\frac{0.82}{\phi_s}}-1\right)^3\left(\frac{0.82}{\phi_s}-1\right)^{-1}$
Boutin (2000) Kinematic	Random	$\frac{1}{4\phi_s}\left(-\ln(\phi_s)-\frac{2(1-\phi_s)}{(1+\phi_s)}\right)$	$\frac{1}{8\phi_s}\left(-\ln(\phi_s)-\frac{2(1-\phi_s)}{(1+\phi_s)}\right)$
Boutin (2000) Static	Random	$\frac{1}{4\phi_s}\left(-\ln(\phi_s)-\frac{(1-\phi_s)(3-\phi_s)}{2}\right)$	$\frac{1}{8\phi_s}\left(-\ln(\phi_s)-\frac{(1-{\phi_s}^2)}{(1+{\phi_s}^2)}\right)$
Shou (2015)	Square	$0.65\frac{(1-0.8{\phi_s}^{0.5})^4}{\phi_s}$	
	Triangular	$0.9\frac{(1-0.9{\phi_s}^{0.5})^4}{\phi_s}$	

Figures 2.17a,b show the theoretical and numerical results of the dimensionless permeability for flows oriented parallel ($K_{\parallel}^{*}$) and perpendicular ($K_{\perp}^{*}$) to the fibres. This figure shows that, in the case of flows oriented parallel to the fibres, and at low fibre volume fractions, the predictions of practically all the analytical permeability models (except the model proposed by Gebart) are coincident. Gebart's model tends to overpredict the permeability of highly porous fibre networks. At higher fibre volume fractions, Figure 2.17a clearly emphasizes the effect of the fibre arrangement on the longitudinal permeability. In the case of a square array, we can observe that numerical results obtained by Berdichevsky & Cai (1993), and Sangani & Yao (1988) are in good agreement with the prediction of Drummond & Tahir (1983) model for $\phi_s < 0.8$. Besides, in their study Tahir & Vahedi Tafreshi (2009) showed that, in the case of a triangular array, numerical results from Sparrow and Loeffler (1959) and Berdichevsky and Cai (1993) and theoretical predictions of the model proposed by Drummond and Tahir (1984) are very close. Finally, it worth noting that the predictions of the models proposed by Happel, Boutin (for the static bound) and Berdichevsky are very close.

In the case of flows oriented perpendicular to the arrays of parallel cylinders (Figure 2.17b) several important remarks can be drawn. First, similarly to what was observed previously for longitudinal flows for low fibre volume fractions ($\phi_s < 0.3$), we can observe that the predictions of the different permeability models agree well with each other. Note also that the permeability predictions of the model proposed by Gebart (1992) and Boutin (2000) for the static bound are similar over the entire range of fibre volume fractions. In addition, theoretical predictions were in agreement with the numerical permeability results obtained for low fibre volume fractions ($\phi_s < 0.3$). In contrast, for higher fibre volume fractions ($\phi_s > 0.3$), we can observe that the transverse permeability of fibre networks strongly depends on the fibre arrangement. For fibre volume fractions higher than 0.4, Figure 2.17b reveals that the theoretical predictions of Sangani and Acrivos (1982) and Drummond and Tahir (hexagonal arrays) are unrealistic. The model of Sangani and Acrivos (resp. Drummond and Tahir model) predicts an increase (resp. a nearly constant evolution) of the transverse permeability with increasing the fibre volume fraction. These predictions are not in accordance with experimental and numerical permeability results. In contrast, the hybrid model of Bruschke and Advani (1993) for triangular arrays agrees well with the numerical permeability results of Berdichevsky and Cai (1993). The theoretical model of Happel (1959) does not fit well with numerical data in the case of flow perpendicular to the fibre orientation.

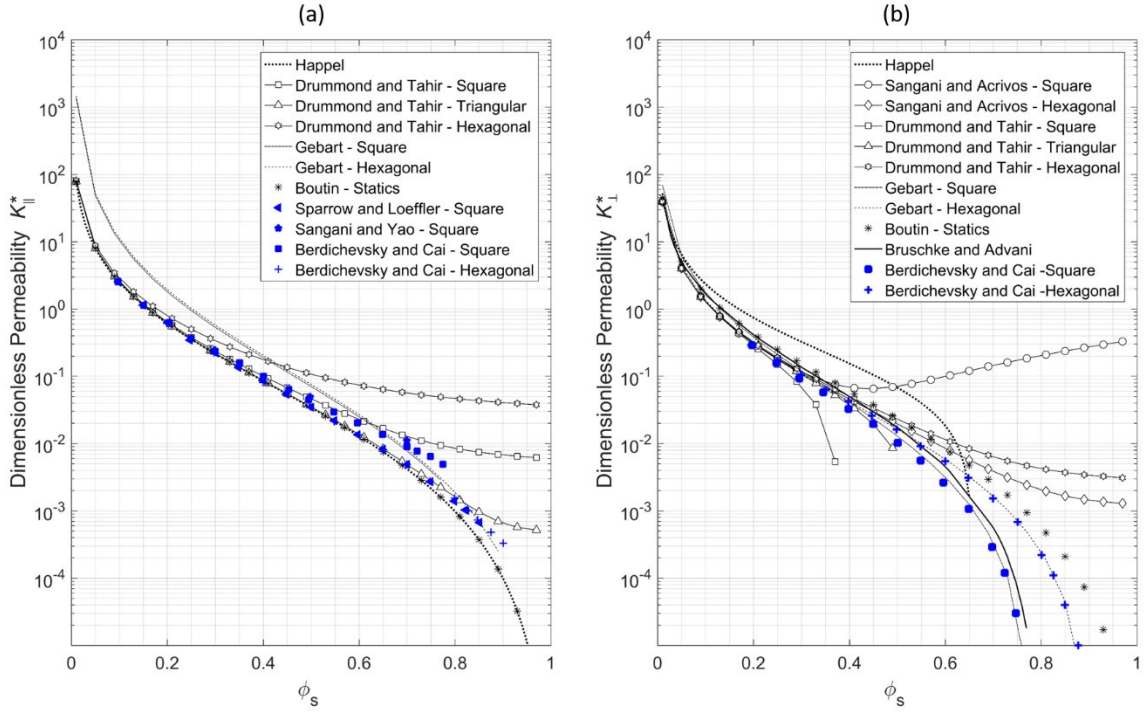

Figure 2.17. Curves with black symbols: predictions of the dimensionless longitudinal (a) and transverse (b) permeability for arrays of parallel cylinders with different fibre arrangements. Curves with blue symbols: dimensionless longitudinal and transverse permeability results obtained using CFD simulations on the same arrays.

The previous permeability models were developed for fibre networks made of perfectly ordered and aligned fibres. Few permeability models were proposed for 2D or 3D model fibre networks. For instance, Spielman & Goren (1968) used a self-consistent method to determine the permeability of 3D networks with random fibre orientations (Table 2.3). Using a similar approach, the same authors proposed an analytical model for the prediction of the out-of-plane permeability of 2D networks with random fibre orientation. Jackson & James (1986) proposed a permeability model for cubic lattice structures (Table 2.3). In their approach, the permeability was determined by considering that the total flow resistance in any direction of the lattice structure is equal to the sum of the flow resistance of cylinders (constituting the lattice structure) oriented perpendicular to the considered flow direction and the flow resistance of cylinders oriented parallel to this flow direction.

Table 2.3. Analytical expressions of permeability models for flows through 3D fibre structures. Note that k_1 and k_2 are modified Bessel functions (Spielman and Goren 1968).

Authors	K^*
Spielman and Goren (1968)	$\frac{1}{4\phi_s} = \frac{1}{3} + \frac{5}{6}\frac{\sqrt{k}}{r}\frac{k_1\,(r/\sqrt{k})}{k_2\,(r/\sqrt{k})}$
Jackson and James (1982)	$\frac{3}{20\phi_s}(-\ln(\phi_s) - 0.931)$

The predictions of the permeability models proposed by Spielman and Goren (1968) and Jackson and James (1982) were found to be in good agreement with the numerical permeability results obtained by Higdon & Ford (1996) for simple cubic (SC), body-centered cubic (BCC) and faced centred cubic (FCC) arrangements of fibres for low fibre volume fractions $\phi_s < 0.3$ (Figure 2.18). In addition, Clague & Phillips (1997) calculated the permeability of periodic and 3D random fibre networks. Results from spatially periodic systems exhibit good agreement with the theories proposed by Spielman and Goren (1968) and Jackson and James (1982) up to fibre volume fractions of 0.25 (Figure 2.18).

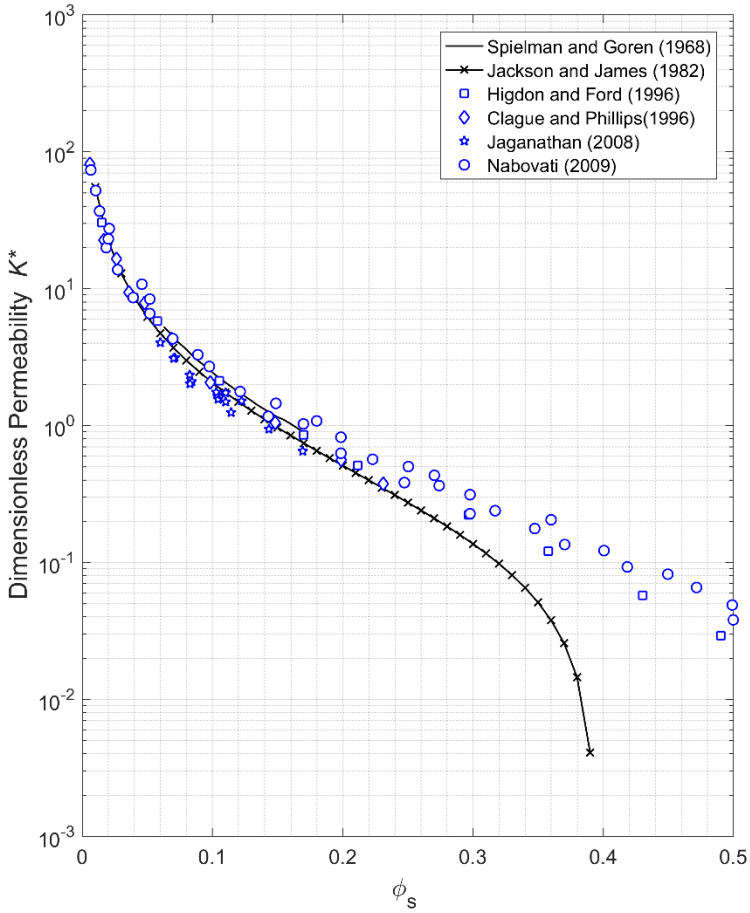

Figure 2.18. Black curves: Analytical predictions given by models developed for flows through 3D fibrous media. Blue symbols: numerical permeability results obtained for flows through 3D fibre media.

References

Arbter, R., Beraud, J. M., Binetruy, C., Bizet, L., Bréard, J., Comas-cardona, S., Demaria, C., Endruweit, A., Long, A., Michaud, V., Morren, G., Ruiz, E., Sol, H., Trochu, F., Verleye, B., Wietgrefe, M., Wu, W., & Ziegmann, G. (2011). Experimental determination of the permeability of textiles : A benchmark exercise. *Composites : Part A*, *42*, 1157–1168. https://doi.org/10.1016/j.compositesa.2011.04.021

Auriault, J. L. (1991). Heterogeneous medium. Is an equivalent macroscopic description possible? *International Journal of Engineering Science*, *29*(7), 785–795. https://doi.org/10.1016/0020-7225(91)90001-J

Bechtold, G., & Ye, L. (2003). Influence of fibre distribution on the transverse flow permeability in fibre bundles. *Composites Science and Technology*, *63*(14), 2069–2079. https://doi.org/10.1016/S0266-3538(03)00112-X

Belov, P. A., Marqués, R., Maslovski, S. I., Nefedov, I. S., Silveirinha, M., Simovski, C. R., & Tretyakov, S. A. (2003). Strong spatial dispersion in wire media in the very large wavelength limit. *Physical Review B - Condensed Matter and Materials Physics*, *67*(11), 4. https://doi.org/10.1103/PhysRevB.67.113103

Berdichevsky, A. L., & Cai, Z. (1993). Preform Permeability Predictions by Self-

Consistent Method and Finite Element Simulation. *Polymer Composites*, *14*(2), 132–143.

Bergelin, O. P., Brown, G. A., Hull, H. L., & Sullivan, F. W. (1950). Heat transfer and fluid friction during viscous flow across banks of tubes: III--a study of tube spacing and tube size. *ASME Transactions*, *72*, 881–888.

Blake, F. C. (1922). The resistance of packing to fluid flow. *Transactions of the American Institute of Chemical Engineers*, *14*(415–421), 3.

Boutin, C. (2000). Study of permeability by periodic and self-consistent homogenisation. *European Journal of Mechanics-A/Solids*, *19*, 603–632.

Brown, J. C. (1950). Determination of the exposed specific surface of pulp fibers from air permeability measurements. *Tappi*, *33*(3), 130–137.

Bruschke, M. V, & Advani, S. G. (1993). Flow of generalized Newtonian fluids across a periodic array of cylinders. *Journal of Rheology*, *37*(3), 479–498. https://doi.org/10.1122/1.550455

Buntain, M. J., & Bickerton, S. (2003). Compression flow permeability measurement : a continuous technique. *Composites - Part A: Applied Science and Manufacturing*, *34*, 445–457. https://doi.org/10.1016/S1359-835X(03)00090-3

Cai, Z., & Berdichevsky, A. L. (1993). An improved self-consistent method for estimating the permeability of a fiber assembly. *Polymer composites* 14.4 314-323.

Carman, P. C. (1938). Determination of the specific surface of powders I. Transactions. *J. Soc. Chemical Industries.*, *57*, 225–234.

Carman, P. C. (1956). *Flow of gases through porous media*.

Chen, C. Y. (1955). Filtration of aerosols by fibrous media. *Chemical Reviews*, *55*(3), 595–623.

Clague, D. S., & Phillips, R. J. (1997). A numerical calculation of the hydraulic permeability of three-dimensional disordered fibrous media. *Physics of Fluids*, *9*(6), 1562–1572. https://doi.org/10.1063/1.869278

Comas-Cardona, S., Binetruy, C., & Krawczak P. (2007). Unidirectional compression of fibre reinforcements. Part 2 : A continuous permeability tensor measurement. *Composites Science and Technology*, *67*, 638–645. https://doi.org/10.1016/j.compscitech.2006.07.020

Cortis, A., & Smeulders, D. M. J. (2001). On the viscous length scale of wedge-shaped porous media. *International Journal of Engineering Science*, *39*(8), 951–962.

Darcy, H. (1856). *Les fontaines publiques de la ville de Dijon: exposition et application des principes à suivre et des formules à employer dans les questions de distribution d'eau*. Victor Dalmont.

Delisée, C., Lux, J., & Malvestio, J. (2010). 3D Morphology and permeability of highly porous cellulosic fibrous material. *Transport in Porous Media*, *83*(3), 623–636. https://doi.org/10.1007/s11242-009-9464-4

Devalve, C., & Pitchumani, R. (2012). An analytical model for the longitudinal permeability of aligned fibrous media. *Composites Science and Technology*, *72*(13), 1500–1507. https://doi.org/10.1016/j.compscitech.2012.04.019

Drapier, S., Pagot, A., Vautrin, A., & Henrat, P. (2002). Influence of the stitching density on the transverse permeability of non-crimped new concept (NC2) multiaxial

reinforcements : measurements and predictions. *Composites Science and Technology*, *62*, 1979–1991.

Drummond, J. ., & Tahir, M. I. (1983). Laminar viscous flow through regular arrays of parallel solid cylinders. *International Journal of Multiphase Flow*, *10*(5), 515–540.

Ergun, S. (1952). Fluid flow through packed columns. *Chem. Eng. Prog.*, *48*, 89–94.

Forchheimer, P. (1901). Wasserbewegung durch boden. *Z. Ver. Deutsch, Ing.*, *45*, 1782–1788.

Gebart, B. R. (1992). Permeability of Unidirectional Reinforcements for RTM. *Journal of Composite Materials*, *26*(8), 1100–1133. https://doi.org/10.1177/002199839202600802

Gutowski, T. G., Cai, Z., Bauer, S., Boucher, D., Kingery, J., & Wineman, S. (1987). Consolidation Experiments for laminate composites. *Journal of Composite Materials*, 650–669. https://doi.org/10.1177/002199838702100705

Happel, J. (1959). Viscous Flow Relative to Arrays of Cylinders. *A.1.Ch.E. Journal 5.2*, 174–177.

Higdon, J. J. ., & Ford, G. D. (1996). Permeability of three-dimensional models of fibrous porous media. *Journal of Fluid Mechanics*, *308*, 341–361.

Idris, Z., Orgéas, L., Geindreau, C., Bloch, J. F., & Auriault, J. L. (2004). Microstructural effects on the flow law of power-law fluids through fibrous media. *Modelling and Simulation in Materials Science and Engineering*, *12*(5), 995–1015. https://doi.org/10.1088/0965-0393/12/5/016

Ingmanson, W. L. (1959). Internal pressure distribution in compressible mats under fluid stress. *TAPP1*, *42*, 840–849.

Jackson, & James. (1986). The permeability of fibrous porous media. *The Canadian Journal of Chemical Engineering*, *64.3*, 364–374.

Jaganathan, S., Vahedi Tafreshi, H., & Pourdeyhimi, B. (2008). A realistic approach for modeling permeability of fibrous media: 3-D imaging coupled with CFD simulation. *Chemical Engineering Science*, *63*(1), 244–252. https://doi.org/10.1016/j.ces.2007.09.020

Joffre, T., Girlanda, O., Forsberg, F., Sahlén, F., Sjödahl, M., & Gamstedt, E. K. (2015). A 3D in-situ investigation of the deformation in compressive loading in the thickness direction of cellulose fiber mats. *Cellulose*, *22*(5), 2993–3001. https://doi.org/10.1007/s10570-015-0727-7

Keller, J. B. (1964). A theorem on the conductivity of a composite medium. *Journal of Mathematical Physics*, *5*(4), 548–549.

Kirsch, A. A., & Fuchs, N. A. (1967). Studies on fibrous aerosol filters—II. Pressure drops in systems of parallel cylinders. *Annals of Occupational Hygiene*, *10*(4), 23–30. https://doi.org/10.1093/annhyg/11.4.299

Koivu, V., Decain, M., Geindreau, C., Mattila, K., Bloch, J., & Kataja, M. (2010). Transport properties of heterogeneous materials . Combining computerised X-ray micro-tomography and direct numerical simulations. *International Journal of Computational Fluid Dynamics*, *23*(10), 713–721. https://doi.org/10.1080/10618561003727512

Koponen, A., Kandhai, D., Hellén, E., Alava, M., Hoekstra, A., Kataja, M., Niskanen, K.,

Sloot, P., & Timonen, J. (1998). Permeability of Three-Dimensional Random Fiber Webs. *Physical Review Letters*, *80*(4), 716.

Kostornov, A. G., & Shevchuk, M. S. (1977). Hydraulic characteristics and structure of porous metal fiber materials. *Soviet Powder Metallurgy and Metal Ceramics*, *16*(9), 694–699.

Kozeny, J. (1927). Uber kapillare leitung der wasser in boden. *Royal Academy of Science, Vienna, Proc. Class I*, *136*, 271–306.

Kuwabara, S. (1959). The forces experienced by randomly distributed parallel circular cylinders or spheres in a viscous flow at small Reynolds numbers. *Journal of the Physical Society of Japan*, *14*(4), 527–532.

Labrecque, R. P. (1968). Effects of fiber cross-sectional shape on resistance to flow of fluids through fiber mats. *Tappi*, *51*(1).

Liotier, P., Govignon, Q., Swery, E., Drapier, S., Liotier, P., Govignon, Q., Swery, E., Drapier, S., Char-, S. B., Liotier, P., Govignon, Q., Swery, E. (2015). Characterisation of woven flax fibres reinforcements : Effect of the shear on the in-plane permeability. *Journal of Composite Materials*, *49*(27), 3415–3430.

Long, A. C. (2005). *Design and manufacture of textile composites*. Elsevier.

Lundström, T. S., Stenberg, R., Bergström, R., Partanen, H., & Birkeland, P. A. (2000). In-plane permeability measurements: a nordic round-robin study. *Composites Part A: Applied Science and Manufacturing*, *31*(1), 29–43. https://doi.org/10.1016/S1359-835X(99)00058-5

Mei, C. C., & Auriault, J.-L. (1991). The effect of weak inertia on flow through a porous medium. *Journal of Fluid Mechanics*, *222*, 647–663. https://doi.org/10.1017/S0022112091001258

Merhi, D. (2006). Transverse permeability of chopped fibre bundle beds. *Composites Part A: Applied Science and Manufacturing*, *38*(3), 739–746. https://doi.org/10.1016/j.compositesa.2006.09.006

Mostaghimi, P., Blunt, M. J., & Bijeljic, B. (2013). Computations of Absolute Permeability on Micro-CT Images. *Mathematical Geosciences*, *45*(1), 103–125. https://doi.org/10.1007/s11004-012-9431-4

Nabovati, A., Llewellin, E. W., & Sousa, A. C. M. (2009). A general model for the permeability of fibrous porous media based on fluid flow simulations using the lattice Boltzmann method. *Composites Part A*, *40*(6–7), 860–869. https://doi.org/10.1016/j.compositesa.2009.04.009

Naresh, K., Khan, K. A., Umer, R., & Cantwell, W. J. (2020). The use of X-ray computed tomography for design and process modeling of aerospace composites : A review. *Materials & Design*, *190*, 108553. https://doi.org/10.1016/j.matdes.2020.108553

Ouagne, P., & Bréard, J. (2010). Continuous transverse permeability of fibrous media. *Composites Part A: Applied Science and Manufacturing*, *41*(1), 22–28. https://doi.org/10.1016/j.compositesa.2009.07.008

Parnas, R. S., Howard, J. G., Luce, T. L., & Advani, S. G. (1995). Permeability Characterization. Part 1 : A Proposed Standard Reference Fabric for Permeability. *Polymer Composites*, *16*(6), 429–445.

Pradhan. (2012). Effect of 3D fi ber orientation distribution on transverse air permeability of fi brous porous media. *Powder Technology*, *221*, 101–104.

https://doi.org/10.1016/j.powtec.2011.12.027

Rolland du Roscoat, S., Decain, M., Thibault, X., Geindreau, C., & Bloch, J. F. (2007). Estimation of microstructural properties from synchrotron X-ray microtomography and determination of the REV in paper materials. *Acta Materialia*, *55*(8), 2841–2850. https://doi.org/10.1016/j.actamat.2006.11.050

Sadiq, T. A. K., Advani, S. G., & Parnas, R. S. (1995). Experimental investigation of transverse flow through aligned cylinders. *International Journal of Multiphase Flow*, *21*(5), 755–774.

Sangani, A., & Acrivos, A. (1982a). Slow flow past periodic arrays of cylinders with application to heat transfer. *International Journal of Multiphase Flow*, *8*(3), 193–206.

Sangani, A., & Acrivos, A. (1982b). Slow flow through a periodic array of spheres. *International Journal of Multiphase Flow*, *8*(4), 343–360.

Sangani, A. S., & Yao, C. (1988). Transport processes in random arrays of cylinders. II. Viscous flow. *The Physics of Fluids*, *31*(9), 2435–2444.

Sharma, S., & Siginer, D. A. (2010). Permeability measurement methods in porous media of fiber reinforced composites. *Applied Mechanics Reviews*, *63*(2), 1–19. https://doi.org/10.1115/1.4001047

Shou, D., Ye, L., & Fan, J. (2015). On the longitudinal permeability of aligned fiber arrays. *Journal of Composite Materials*, *49*(14), 1753–1763. https://doi.org/10.1177/0021998314540192

Skartsis, L., Kardos, J. L., & Khomami, B. (1992). Resin flow through fiber beds during composite manufacturing processes. Part I: Review of newtonian flow through fiber beds. *Polymer Engineering & Science*, *32*(4), 221–230. https://doi.org/10.1002/pen.760320402

Soltani, P., Johari, M. S., & Zarrebini, M. (2014a). Tomography-based determination of transverse permeability in fibrous porous media. *Journal of Industrial Textiles*, *44*(5), 738–756. https://doi.org/10.1177/1528083713512357

Soltani, P., Johari, M., & Zarrebini, M. (2014b). Effect of 3D fiber orientation on permeability of realistic fi brous porous networks. *Powder Technology*, *254*, 44–56. https://doi.org/10.1016/j.powtec.2014.01.001

Soltani, P., Zarrebini, M., Laghaei, R., & Hassanpour, A. (2017). Prediction of permeability of realistic and virtual layered nonwovens using combined application of X-ray MCT and computer simulation. *Chemical Engineering Research and Design*, *124*, 299–312. https://doi.org/10.1016/j.cherd.2017.06.035

Sparrow, E. M., & Loeffler, A. L. (1959). Longitudinal laminar flow between cylinders arranged in regular array. *AIChE Journal*, *5*(3), 325–330.

Spielman, L., & Goren, S. L. (1968). Model for predicting pressure drop and filtration efficiency in fibrous media. *Environmental Science & Technology*, *2*(4), 279–287.

Stylianopoulos, T., Yeckel, A., Derby, J. J., Luo, X., Shephard, M. S., Shephard, M. S., Sander, E. A., & Barocas, V. H. (2008). Permeability calculations in three-dimensional isotropic and oriented fiber networks. *Physics of Fluids*, *20*(12), 123601. https://doi.org/10.1063/1.3021477

Succi, S., Foti, E., & Higuera, F. (1989). Three-dimensional flows in complex geometries with the lattice boltzmann method. *Epl*, *10*(5), 433–438. https://doi.org/10.1209/0295-5075/10/5/008

Tahir, M. A., & Vahedi Tafreshi, H. (2009). Influence of fiber orientation on the transverse permeability of fibrous media. *Physics of Fluids*, *21*(8). https://doi.org/10.1063/1.3211192

Tomadakis, M., M, M., & Robertson, T. J. (2005). Viscous Permeability of Random Fiber Structures: Comparison of Electrical and Diffusional Estimates with Experimental and Analytical Results. *Ournal of Composite Materials*, *39*(2), 163–188. https://doi.org/10.1177/0021998305046438

Trevino, L. (1991). Analysis of Resin Injection Molding in Molds With Paeplaced Fiber Mats. I: Permeability and Compressibility Measurements. *Polymer Composites*, *12*(1), 20–29.

Tsay, B. R., & Weinbaum. (1991). Viscous flow in a channel with periodic cross-bridging fibres: exact solutions and Brinkman approximation. *Journal of Fluid Mechanics*, *226*, 125–148.

Vernet, N., Ruiz, E., Advani, S., Alms, J. B., Aubert, M., Barburski, M., Barari, B., Beraud, J. M., Berg, D. C., Correia, N., Danzi, M., Delavière, T., Dickert, M., Fratta, C. Di, Endruweit, A., Ermanni, P., Francucci, G., Garcia, J. A., George, A., … Ziegmann, G. (2014). Experimental determination of the permeability of engineering textiles: Benchmark II. *Composites Part A: Applied Science and Manufacturing*, *61*, 172–184. https://doi.org/10.1016/j.compositesa.2014.02.010

Vidal, D., Ridgway, C., Pianet, G., Schoelkopf, J., Roy, R., & Bertrand, F. (2009). Effect of particle size distribution and packing compression on fluid permeability as predicted by lattice-Boltzmann simulations. *Computers & Chemical Engineering*, *33*(1), 256–266.

Viguié, J., Dumont, P. J. J., Mauret, É., Du Roscoat, S. R., Vacher, P., Desloges, I., & Bloch, J. F. (2011). Analysis of the hygroexpansion of a lignocellulosic fibrous material by digital correlation of images obtained by X-ray synchrotron microtomography: Application to a folding box board. *Journal of Materials Science*, *46*(14), 4756–4769. https://doi.org/10.1007/s10853-011-5386-y

Viswanadham, R., Agrawal, D. C., & Kramer, E. J. (1978). Water transport through reconstituted collagen hollow-fiber membranes. *Journal of Applied Polymer Science*, *22*(6), 1655–1663.

White, M. L. (1960). The permeability of an acrylamide polymer gel. *The Journal of Physical Chemistry*, *64*(10), 1563–1565.

Wiggins, E. J., Campbell, W. B., & Maass, O. (1939). Determination of the specific surface of fibrous materials. *Canadian Journal of Research*, *17*(10), 318–324.

Xue, D., Miao, M., & Hu, H. (2011). Permeability anisotropy of flax nonwoven mats in vacuum-assisted resin transfer molding. *Journal of the Textile Institute*, *102*(7), 612–620. https://doi.org/10.1080/00405000.2010.504566

Yazdchi, K., Srivastava, S., & Luding, S. (2011). Microstructural effects on the permeability of periodic fibrous porous media. *International Journal of Multiphase Flow*, *37*(8), 956–966. https://doi.org/10.1016/j.ijmultiphaseflow.2011.05.003

Zarandi, M. A. F., Arroyo, S., & Pillai, K. M. (2019). Longitudinal and transverse flows in fiber tows: Evaluation of theoretical permeability models through numerical predictions and experimental measurements. *Composites Part A: Applied Science and Manufacturing*, *119*, 73–87. https://doi.org/10.1016/j.compositesa.2018.12.032

Chapter 3

Capillary phenomena in fibrous media

3.1 Introduction

In this chapter the attention will be focused on the description of the phenomena occurring at the flow front where three phases coexist: liquid (wetting fluid), air (non wetting fluid) and fibres (solid phase). The surface that separates the liquid and air phases is called the interface. Across the interface, a discontinuity in the pressure can appear (Bear & Braester, 1972). At the junction (triple) line of the three phases, capillary forces are present. The capillary pressure and the capillary forces can promote or not the advancement of the fluid (Michaud, 2016). They depend on the wettability properties (fluid-air surface tension, fluid-solid and air-solid surface energies or conversely contact angles) and microstructure features of the porous and fibrous materials.

Capillary pressure is significantly lower than the injection pressure in pressure-assisted composite processing routes. Thus, the capillary effects have often been neglected in the modelling of these processes. For instance, for LCM processes, capillary pressure drops are in the range of 50-100 kPa (Michaud, 2016) compared to about 700 kPa for the injection pressure. Thus, neglecting the capillary pressure can lead to a wrong estimate of the filling time and can have an impact on the impregnation "dynamics". Besides, in the case of dual scale fabrics, i.e. fabrics made of an assembly of fibre bundles, tows or yarns, capillary effects can induce a velocity of the liquid inside the fibre bundles/tows/yarns that is different from the liquid velocity between these elements. This can lead to a heterogeneous propagation of the fluid and the formation of voids (Park & Lee, 2011)

3.2 Governing equations for multiphase flow in porous media

The flow of the liquid polymer inside a fibre reinforcement can be modelled as a multiphase flow in a porous media including the presence of interfaces between the fluid phases, i.e. the polymer liquid and the air. A description of the governing equations of these flows is given, following the general framework proposed by Deemer & Slattery (1978), Hassanizadeh & Gray (1993a) and Starnoni & Pokrajac (2020).

3.2.1 Balance equations

A system as the one schematised in Figure 3.1 is composed of three different phases: the solid s, a wetting phase w and a non-wetting phase n. For composites, w would correspond to the polymer liquid and n to the displaced air. The interface Γ_{nw} that separates the wetting and non wetting phases can be seen as a sort of membrane. Two other interfaces complete the system: the interface between the wetting phase and the solid phase Γ_{sw} and the interface between the non-wetting phase and the solid Γ_{sn}. In addition Γ_{nws} is the so called triple line where the three phases intersect. Boundary conditions at the Γ_{nw} interface and at the triple line will be considered in the two next sections.

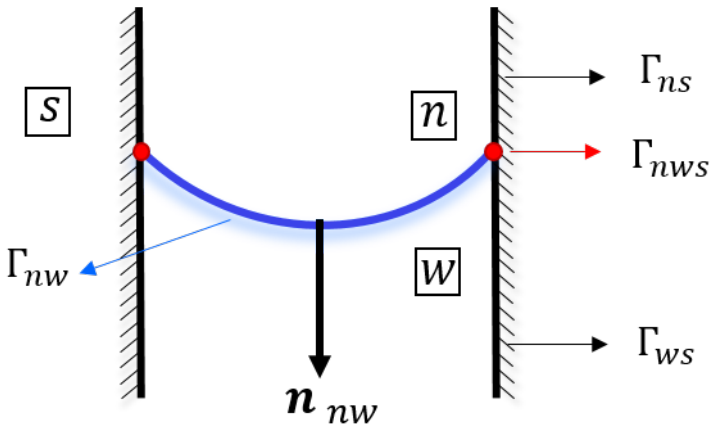

Figure 3.1. Schematic representation of a solid-liquid-liquid system. n corresponds to the non-wetting liquid, w to the wetting liquid and s is the solid phase. The interfaces between the different phases Γ_{sw}, Γ_{sn}, Γ_{nw} as well as the triple line Γ_{nws} are indicated.

3.2.1.1 Interface balance equations

The momentum balance of an interface Γ_{nw} between two bulk phases n and w is governed by the balance of the forces exerted by the two phases on the interface and the forces present within the interface. The momentum balance equation for this interface can be written as follows:

$$\frac{\partial}{\partial t}(\rho_{wn}\boldsymbol{v}_{wn}) + \boldsymbol{\nabla}^{\Gamma}\cdot(\rho\boldsymbol{v}_{wn}\otimes\boldsymbol{v}_{wn}) - \boldsymbol{\nabla}^{\Gamma}\cdot\boldsymbol{T}_{wn} - \rho_{wn}\boldsymbol{g} + [\![\rho\boldsymbol{v}\otimes(\boldsymbol{v}-\boldsymbol{v}_{wn})\cdot\boldsymbol{n} - \boldsymbol{T}\cdot\boldsymbol{n}]\!]_{w}^{n} = \boldsymbol{0} \tag{3.1}$$

where:

ρ_{wn} is the interface density with unit of mass per unit area;
$\boldsymbol{v}$ is the velocity in the bulk phase and $\boldsymbol{v}_{wn}$ the interface velocity;
$\boldsymbol{\nabla}^{\Gamma}$ is the surficial component of the operator $\boldsymbol{\nabla}$, $\boldsymbol{\nabla}^{\Gamma} = \boldsymbol{\nabla} - \boldsymbol{n}\otimes\boldsymbol{n}\cdot\boldsymbol{\nabla}$;
$\boldsymbol{T}$ and $\boldsymbol{T}_{wn}$ are the stress tensors for the bulk (units FL^{-2}) and the interface (units FL^{-1}) respectively;
$[\![\mathbf{B}\cdot\boldsymbol{n}]\!]_{\alpha}^{\beta} = \boldsymbol{B}_{\alpha}\cdot\boldsymbol{n}_{\alpha\beta} + \boldsymbol{B}_{\beta}\cdot\boldsymbol{n}_{\beta\alpha}$ is the jump condition across the interface where $\boldsymbol{n}_{\alpha\beta}$ is the unit normal vector pointing from the α phase into the β phase.

The microscopic mass conservation equation of the interface is given by:

$$\frac{\partial\rho_{wn}}{\partial t} + \boldsymbol{\nabla}^{\Gamma}\cdot(\rho_{wn}\boldsymbol{v}_{wn}) + [\![\rho(\boldsymbol{v}-\boldsymbol{v}_{wn})\cdot\boldsymbol{n}]\!]_{w}^{n} = 0 \tag{3.2}$$

Combining equations 3.1 with 3.2 the momentum equation is rearranged as:

$$\rho_{wn}\frac{D_{\Gamma}\boldsymbol{v}_{wn}}{Dt} - \boldsymbol{\nabla}^{\Gamma}\cdot\boldsymbol{T}_{wn} - \rho_{wn}\boldsymbol{g} + [\![\rho(\boldsymbol{v}-\boldsymbol{v}_{wn})\otimes(\boldsymbol{v}-\boldsymbol{v}_{wn})\cdot\boldsymbol{n} - \boldsymbol{T}\cdot\boldsymbol{n}]\!]_{w}^{n} = \boldsymbol{0} \tag{3.3}$$

The constitutive relations for the stress tensors for the bulk phases and the interface take the forms:

$$\boldsymbol{T} = -p\boldsymbol{I} + \mu\,[\boldsymbol{\nabla v} + (\boldsymbol{\nabla v})^T] = -p\boldsymbol{I} + \boldsymbol{\tau} \tag{3.4}$$

$$\boldsymbol{T_s} = -\gamma_{wn}\boldsymbol{I}^\Gamma + \mu\,[\boldsymbol{\nabla v}_{wn} + (\boldsymbol{\nabla v}_{wn})^T] = -\gamma_{wn}\boldsymbol{I}^\Gamma + \boldsymbol{\tau}_{wn} \tag{3.5}$$

where:
μ is the viscosity of the bulk phase
p is the pressure;
$\boldsymbol{\tau}$ and $\boldsymbol{\tau}_{wn}$ are the viscous stress tensor for the bulk phase and for the interface, respectively;
$\boldsymbol{I}$ is the identity tensor;
$\boldsymbol{I}^\Gamma$ is the surficial identity tensor, $\boldsymbol{I}^\Gamma = \boldsymbol{I} - \boldsymbol{n} \otimes \boldsymbol{n} \cdot \boldsymbol{I}$;
γ_{wn} the surface tension between the w and n phases.

Substituting Equations 3.4 and 3.5 into 3.3, the momentum balance for the interface becomes:

$$\begin{gathered}\rho_{wn}\tfrac{D_\Gamma \boldsymbol{v}_{wn}}{Dt} - \boldsymbol{\nabla}^\Gamma\gamma_{wn} - \gamma_{wn}\left(\boldsymbol{\nabla}^\Gamma \cdot \boldsymbol{n}\right) - \boldsymbol{\nabla}^\Gamma \cdot \boldsymbol{\tau}_{wn} - \rho_{wn}\boldsymbol{g} + (p_n - p_w)\boldsymbol{n} - \\ (\boldsymbol{\tau}_n - \boldsymbol{\tau}_w)\cdot\boldsymbol{n} + [\rho_n(\boldsymbol{v}_n - \boldsymbol{v}_{wn}) \otimes (\boldsymbol{v}_n - \boldsymbol{v}_{wn}) - \rho_w(\boldsymbol{v}_w - \boldsymbol{v}_{wn}) \otimes \\ (\boldsymbol{v}_w - \boldsymbol{v}_{wn})]\cdot\boldsymbol{n} = \boldsymbol{0}\end{gathered} \tag{3.6}$$

The term $\boldsymbol{\nabla}^\Gamma \cdot \boldsymbol{n}$ in this equation corresponds to the mean curvature κ of the surface (Aris, 1962).

The tangential and the normal components of the momentum balance are, respectively:

$$\begin{gathered}\boldsymbol{\nabla}^\Gamma\gamma_{nw} = \rho_{wn}\boldsymbol{I}^\Gamma \cdot \tfrac{D_\Gamma \boldsymbol{v}_{wn}}{Dt} - \boldsymbol{I}^\Gamma \cdot (\boldsymbol{\nabla}^\Gamma \cdot \boldsymbol{\tau}_{wn}) - \rho_{wn}\boldsymbol{I}^\Gamma \cdot \boldsymbol{g} - \boldsymbol{I}^\Gamma \cdot (\boldsymbol{\tau}_n - \boldsymbol{\tau}_w)\cdot\boldsymbol{n} + \\ \boldsymbol{I}^\Gamma \cdot [\rho_n(\boldsymbol{v}_n - \boldsymbol{v}_{wn}) \otimes (\boldsymbol{v}_n - \boldsymbol{v}_{wn}) - \rho_w(\boldsymbol{v}_w - \boldsymbol{v}_{wn}) \otimes (\boldsymbol{v}_w - \boldsymbol{v}_{wn})]\cdot\boldsymbol{n}\end{gathered} \tag{3.7}$$

$$\begin{gathered}p_n - p_w = -\rho_{wn}\tfrac{D_s \boldsymbol{v}_{nw}}{Dt}\cdot\boldsymbol{n} + \gamma_{wn}\kappa - \left(\boldsymbol{\nabla}^\Gamma \cdot \boldsymbol{\tau}_{wn}\right)\cdot\boldsymbol{n} - \rho_{wn}\boldsymbol{g}\cdot\boldsymbol{n} + \boldsymbol{n}\cdot(\boldsymbol{\tau}_n - \boldsymbol{\tau}_w)\cdot \\ \boldsymbol{n} - \boldsymbol{n}\cdot[\rho_n(\boldsymbol{v}_n - \boldsymbol{v}_{wn}) \otimes (\boldsymbol{v}_n - \boldsymbol{v}_{wn}) - \rho_w(\boldsymbol{v}_w - \boldsymbol{v}_{wn}) \otimes (\boldsymbol{v}_w - \boldsymbol{v}_{wn})]\cdot\boldsymbol{n}\end{gathered} \tag{3.8}$$

Equations 3.7 and 3.8 have to be considered always valid since they are independent from the nature of the flow or from the properties of the fluids.
The normal component of the momentum balance can also be written as:

$$p_n - p_w = \gamma_{wn}\kappa + \boldsymbol{\lambda}_s \cdot \boldsymbol{n} \tag{3.9}$$

where $\boldsymbol{\lambda}_s$ is a sum of several terms $\boldsymbol{\lambda}_s = \boldsymbol{\lambda}_\rho + \boldsymbol{\lambda}_{\tau_s} + \boldsymbol{\lambda}_g + \boldsymbol{\lambda}_\tau + \boldsymbol{\lambda}_{v_s}$ with:

$$\begin{gathered}\boldsymbol{\lambda}_\rho = \rho_{wn}\frac{D_\Gamma \boldsymbol{v}_{wn}}{Dt}, \qquad \boldsymbol{\lambda}_{\tau_s} = \left(\boldsymbol{\nabla}^\Gamma \cdot \boldsymbol{\tau}_{wn}\right), \\ \boldsymbol{\lambda}_g = \rho\boldsymbol{g}, \qquad \boldsymbol{\lambda}_\tau = (\boldsymbol{\tau}_n - \boldsymbol{\tau}_w)\cdot\boldsymbol{n}, \\ \boldsymbol{\lambda}_{v_s} = -[\rho_n(\boldsymbol{v}_n - \boldsymbol{v}_{wn}) \otimes (\boldsymbol{v}_n - \boldsymbol{v}_{wn}) - \rho_w(\boldsymbol{v}_w - \boldsymbol{v}_{wn}) \otimes (\boldsymbol{v}_w - \boldsymbol{v}_{wn})]\cdot\boldsymbol{n}\end{gathered} \tag{3.10}$$

If the inertia and body forces terms are negligible, $\boldsymbol{\lambda_\rho} = \boldsymbol{\lambda_g} = \mathbf{0}$. Assuming no fluid exchange between the interface and the surroundings, $\boldsymbol{\lambda_{v_s}} = \mathbf{0}$. Neglecting the viscous part of the interface stress tensor, $\boldsymbol{\lambda_{\tau_s}} = \mathbf{0}$. Then, equation 3.7 reduces to $\boldsymbol{\nabla}^\Gamma \gamma_{nw} = \mathbf{0}$. Under these assumptions, the normal component of momentum balance simplifies to:

$$p_n - p_w = P_c = \gamma_{wn}\, \boldsymbol{\nabla}^\Gamma \cdot \boldsymbol{n} = \gamma_{wn}\kappa \tag{3.11}$$

This equation is known as the Young-Laplace equation. It shows the relationship between the surface tension, the mean interface curvature κ and the pressure jump across any curved interface. The pressure difference at the interface between two immiscible fluids is defined as the capillary pressure P_c.

3.2.1.2 Triple line balance equations

The momentum balance of the triple line can be written as follows:

$$\begin{aligned}\rho^* \frac{D_c \boldsymbol{u}^*}{Dt} - \boldsymbol{\nabla}^c \cdot \boldsymbol{C} - \rho^* \boldsymbol{g} \\ + [\![\rho^*(\boldsymbol{u}^* - \boldsymbol{v}_{wn}) \otimes (\boldsymbol{u}^* - \boldsymbol{v}_{wn}) \cdot \boldsymbol{n}^* - \boldsymbol{T_s} \otimes \boldsymbol{n}^*]\!]_{edges} = 0\end{aligned} \tag{3.12}$$

where:

ρ^* is the excess mass of the contact line (with units of mass per unit length);
$\boldsymbol{u}^*$ is the velocity of the contact line;
$\boldsymbol{\nabla}^c$ is the curvilinear divergence operator, $\boldsymbol{\nabla}^c = \boldsymbol{t}^* \otimes \boldsymbol{t}^* \cdot \boldsymbol{\nabla}$;
$\boldsymbol{t}^*$is the unit vector tangent to the contact line;
$\boldsymbol{C}$ is the stress tensor for the contact line;
$\boldsymbol{n}^*$ is the unit vector normal to the contact line pointing outward to surfaces interacting with the triple line along its edges.

The constitutive relation for the stress tensor $\boldsymbol{C}$ is:

$$\boldsymbol{C} = -\gamma_{wns} \boldsymbol{t}^* \otimes \boldsymbol{t}^* \tag{3.13}$$

where γ_{wns} is the contact curve compression.

Substituting equation 3.13, under the hypotheses of negligible inertia and body forces, assuming no fluid exchanges and neglecting the viscous part of the interface stress tensor, the momentum balance (Eq. 3.12) for the triple line becomes:

$$\boldsymbol{\nabla}^c \cdot (\gamma_{wns} \boldsymbol{t}^* \otimes \boldsymbol{t}^*) - \boldsymbol{n}^*_{wn}\gamma_{wn} - \boldsymbol{n}^*_{ws}\gamma_{ws} - \boldsymbol{n}^*_{ns}\gamma_{ns} - \boldsymbol{F} = \mathbf{0} \tag{3.14}$$

The vector $\boldsymbol{F}$ accounts for the elastic deformation of the solid-fluid surfaces as a result of the pull of the meniscus on the contact line (Hassanizadeh & Gray, 1993b).

The tangential and the normal components of the momentum balance equations are respectively:

$$\boldsymbol{t}^* \cdot \boldsymbol{\nabla}^c \gamma_{wns} = \boldsymbol{t}^* \cdot \boldsymbol{F} \tag{3.15}$$

$$\gamma_{wns} \boldsymbol{t}^* \cdot \boldsymbol{\nabla}^c \otimes \boldsymbol{t}^* - \boldsymbol{n}^*_{wn} \gamma_{wn} - \boldsymbol{n}^*_{ws} \gamma_{ws} - \boldsymbol{n}^*_{ns} \gamma_{ns} = (\boldsymbol{I} - \boldsymbol{t}^* \otimes \boldsymbol{t}^*) \cdot \boldsymbol{F} \tag{3.16}$$

For a common case of a vertical tube in which the triple line is a circle γ_{nws} is a constant property of the triple line because of the symmetry so $\boldsymbol{\nabla}^c \gamma_{wns} = \boldsymbol{0}$ and the force exerted by the solid has no tangent component. Under this condition, the momentum balance of the triple line is:

$$\boldsymbol{n}^*_{wn} \gamma_{wn} + \boldsymbol{n}^*_{ws} \gamma_{ws} + \boldsymbol{n}^*_{ns} \gamma_{ns} = \boldsymbol{0} \tag{3.17}$$

This equation is known as the Young-Dupré equation that describes the tangential equilibrium of the tension surfaces in the triple point.

3.2.2 Stress conditions and dimensionless numbers

Performing scaling operations with dimensionless variables for the previous equations described above (Eqs 3.7 and 3.8), it is possible to obtain three important dimensionless numbers that gauge the effects of the surface tension γ_{wn} in quasi-static or dynamic flow conditions. From the normal component of the momentum balance equation it is possible to obtain:

- the Bond number Bo that represents the balancing between forces induced by gravity and surface tension:

$$Bo = \frac{Gravity}{Tension\ surf.} = \frac{l^2 \rho g}{\gamma_{wn}} \tag{3.18}$$

- the Weber number We that gauges the relative magnitude of inertia forces and surface tension:

$$We = \frac{Inertia}{Tension\ surf.} = \frac{\rho v^2 l}{\gamma_{wn}} \tag{3.19}$$

- the capillary number Ca that represents the ratio between viscous forces and surface tension:

$$Ca = \frac{Viscosity}{Tension\ surf.} = \frac{\mu v}{\gamma_{wn}} \tag{3.20}$$

The Bond number is also related to the so called capillary length λ_c. This characteristic dimension is defined as:

$$\lambda_c = \sqrt{\frac{\gamma_{wn}}{\rho g}} \tag{3.21}$$

and corresponds to the situation when the effects induced by the surface tension and the gravity are comparable (e.g. Bo =1). The length λ_c is generally of the order of few millimetres, e.g. about 2.7 mm for water at room temperature. If the radius of the system (e.g. radius of a fibre or tube immersed in a liquid, radius of a laying drop) is smaller than λ_c the effects of the capillary forces prevail and the effects of gravity are negligible. The opposite case, i.e., $r > \lambda_c$ is referred to as the "gravity" regime.

By scaling the tangential components of the momentum balance equation 3.7, the Marangoni number that compares the effects of surface gradient of the surface tension $\boldsymbol{\nabla}^{\Gamma}\gamma_{wn}$ with the fluid shear stress τ is obtained:

$$Ma = \frac{Marangoni\ stress}{Viscosity} = \frac{\Delta\gamma_{wn}}{\mu v} \tag{3.22}$$

The Marangoni effect is known as a flow of a liquid that is induced because of gradients in the surface tension of the liquid.

3.3 Applications of governing equations for capillary phenomena to simple 2D axisymmetric cases

In the section 3.2, the governing equations for multiphase flow in porous media were described. In this section, we apply the established tensorial laws to simple 2D case studies: (i) a drop deposited onto a horizontal surface, (ii) capillary rise in a tube and (iii) rise of a fluid meniscus on a vertical cylinder. These examples enable a better understanding of the underlying physics of capillary and wetting phenomena that are described by the tensorial laws in section 3.2.

Note that in the examples treated below the surface tension of the gas-fluid interface, the energy surface of the solid-gas and solid-liquid interfaces are denoted γ_{lv}, γ_{sv}, and γ_{ls}, respectively. In the previous section they were denoted γ_{wn}, γ_{sn}, and γ_{ws}. The subscripts "l" and "v" must be replaced by "w" and "n".

3.3.1 Case study I: drop deposited onto a horizontal surface

One of the most typical 2D case study that is used to illustrate capillary and wetting phenomena is the example of a drop of liquid deposed onto a surface (Figure 3.2). The shape of the drop at the equilibrium depends on several parameters such as the radius of the drop r_0, the surface tension of the gas-fluid interface γ_{lv}, the energy surface of the solid-

gas γ_{sv}, and solid-liquid γ_{sl} interfaces. The size of the drop determines the order of magnitude of the gravity effects with respect to the capillary effects. If $r_0 < \lambda_c$ (where λ_c is the capillary length), the effects induced by the surface tension are predominant on the gravity effects. In this situation the drop exhibits a spherical shape which means that the curvature of the gas-fluid interface is constant (Figure 3.2a). On the contrary if $r_0 > \lambda_c$, the gravity effects are predominant on the effects induced by the fluid surface tension. In this situation, the drop tends to flatten under the effects of the gravity (Figure 3.2b).

In addition, the surface tension of the gas-fluid interface γ_{lv}, the energy surface of the solid-gas γ_{sv}, and solid-liquid γ_{ls} interfaces determine the equilibrium contact angle θ_e that is defined as the angle between the solid surface plane and the tangent to the liquid-gas interface at the triple point. A detailed description of the concept of contact angle is done in paragraph 3.3.4.

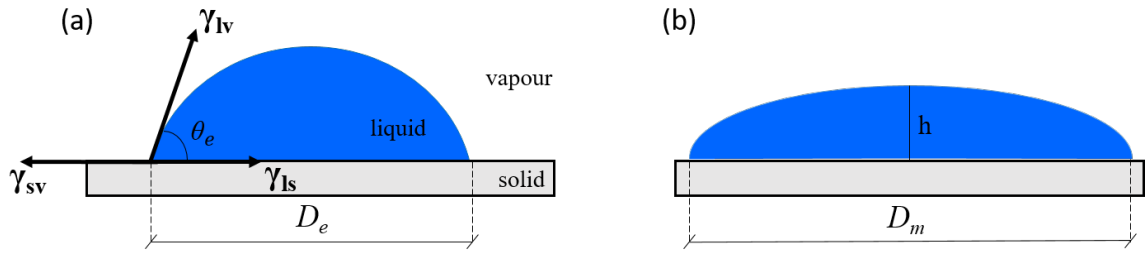

Figure 3.2. Schematic representations of two drops deposited onto a surface. In image (a) the radius of the drop was less than the capillary length ($r_0 < \lambda_c$). The effects induced by tension surface are predominant on gravity effects. Hence the drop has a spherical shape. In image (b) $r_0 > \lambda_c$, gravity effects are predominant on tension surface effects. The drop has a flattened shape with thickness h.

Three wetting states exist for a liquid in contact with a solid surface. The wetting state can be described by a spreading parameter S defined as:

$$S = \gamma_{sv} - (\gamma_{sl} + \gamma_{lv}) \tag{3.23}$$

and substituting the horizontal projection of γ_{lv} into equation 3.23 yields:

$$S = \gamma_{lv}(\cos\theta_e - 1) \tag{3.24}$$

The wetting state that corresponds to a situation where S is close to 0 is defined as “total wetting”. In this condition, the liquid spreads completely onto the surface of the solid phase to lower its surface energy. In contrast, when $-\gamma_{lv} \leq S < 0$ the liquid does not spread completely onto the surface, wetting is partial. Finally, the state that corresponds to a situation where $-2\gamma_{lv} \leq S < -\gamma_{lv}$, is defined as “non-wetting” (Figure 3.3).

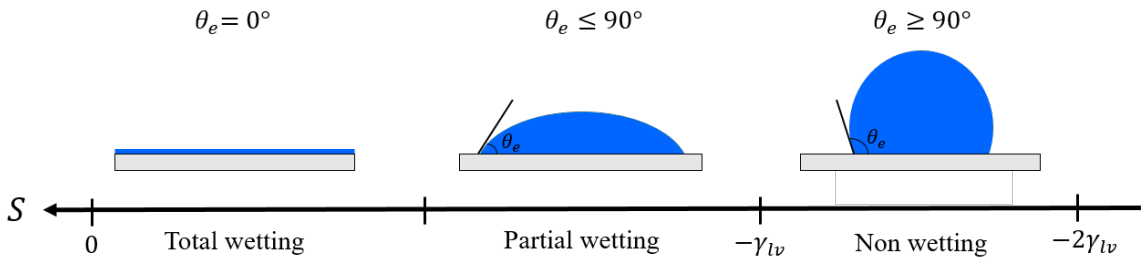

Figure 3.3. Wetting states as a function of the spreading parameter S.

In the case of a small drop (i.e., $r_0 < \lambda_c$) deposited on a horizontal surface, the fluid-gas interface Young-Laplace balance equation stated in equation 3.11 writes:

$$p_v - p_l = P_c = \gamma_{lv}\kappa = \frac{2\gamma_{lv}}{r_o} \tag{3.25}$$

For this problem, the triple line Young-Dupré balance equation 3.17 can be written as follows:

$$\gamma_{sv} = \gamma_{sl} + \gamma_{lv}\cos\theta_e \tag{3.26}$$

Young's equations is valid only for ideal solid surface (Young, 1805). There are other key equations that correlate the equilibrium contact angle θ_e of the system with solid surface energy γ_{sv}: Wenzel equation (Wenzel, 1936) that takes into account the surface roughness, the Cassie equation (Cassie, 1948) that describes the case of a liquid in contact with a heterogeneous solid surface and the Cassie-Baxter equation (Cassie, 1948) for a liquid sitting on the top a textured solid with air trapped underneath.

3.3.2 Case study II: Capillary rise in a tube

The second case study corresponds to the case of a capillary tube immersed in a fluid. When a narrow tube of radius r_0 enters in contact with a wetting liquid the equilibrium is disturbed and the liquid starts to rise inside the tube (Figure 3.4). An interface Γ_{sl} forms inside the tube as well as a triple line Γ_{lsv}. The triple line tends to move upward and the interface/meniscus Γ_{lv} becomes concave, forming an angle with the tube that is equal to θ_e. At the equilibrium position the meniscus adopts the shape of a spherical dome with a radius $R_1 = r_0/\cos\theta_e$. In the point A, immediately underneath the meniscus the pressure is given by Young-Laplace equation. At the same time the pressure must also conform to hydrostatics. Then the pressure in point A can be written:

$$p_A = p_v - \frac{2\gamma_{lv}\cos\theta_e}{r_0} = p_v - \rho g H \tag{3.27}$$

with p_v the gas pressure (atmospheric pressure in the case of air). From this expression it is possible to derive the law of capillary rise, known as Jurin's law. This gives the maximum height H of the fluid reached inside the tube:

$$H = \frac{2\gamma_{lv}\cos\theta_e}{\rho g r_0} \tag{3.28}$$

From this relation it turns out that the height H reached is in inverse proportion to the radius of the tube.

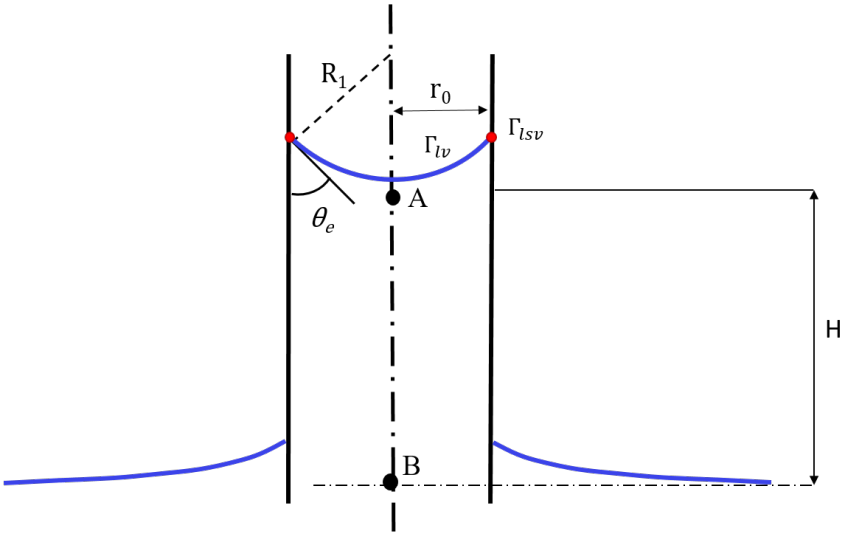

Figure 3.4. Scheme showing the capillary rise of a fluid in a tube. H denotes the height difference between point A that is located underneath the fluid surface and point B that corresponds to the position of a flat fluid-gas interface Γ_{lv} located far from the tube.

3.3.3 Case study III: Rise of a fluid meniscus on a vertical cylinder

When a circular cylinder is plunged inside a wetting fluid, a fluid meniscus starts rising up around the cylinder until it reaches an equilibrium position (Figure 3.5). At the equilibrium, the fluid forms an angle equal to θ_e with the cylinder surface. At a certain distance from the tube, of the same order as the capillary length λ_c, the fluid gas interface is horizontal as it is not affected by the presence of the cylinder. (James, 1974) proposed an approximate analytical solution to determine the shape of the meniscus that forms outside of the circular cylinder. The shape of the meniscus and the expression to compute the maximum height H' are given by the two following equations, respectively:

$$z(r,\varepsilon) = -c\ln\varepsilon + c(2\ln 2 - \Upsilon) - c\ln r + (r^2 - c^2)^{1/2} \tag{3.29}$$

$$H' = z(r=1) = c\left[\ln\left(\frac{4}{\varepsilon(1+\sin\theta_e)}\right) - \Upsilon\right] \tag{3.30}$$

where $z = y/r_0$, $r = x/r_0$, $\varepsilon = r_0/\lambda_c$, $c = \cos\theta_e$ and $\Upsilon = 0.57721\ldots$ corresponds to Euler's constant. The expression is valid for $\theta_e < \frac{\pi}{2}$ and for $r \ll \lambda_c$.

Note that the equilibrium at the triple line is governed by the Young–Dupré equation (Eq. 3.26).

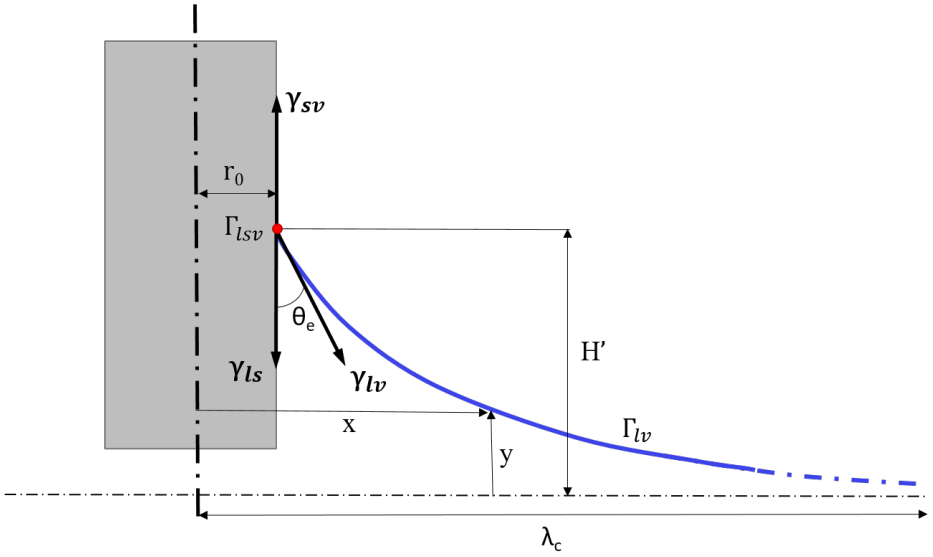

Figure 3.5. Scheme showing a fluid meniscus that is formed on a circular vertical cylinder.

3.3.4 Concept of contact angle

In their reviews Drelich (2019) and Marmur et al. (2017) proposed a specific terminology to distinguish the different contact angles that appear in the literature.
The so-called apparent contact angle is the angle that is commonly measured using various experimental techniques (Gennes et al., 2013). This apparent contact angle is assumed to be constant along the triple line. The apparent contact angle can differ from the local contact angle as it is measured at the micro- or nanometric scales at any point along the triple line. Its variations might be caused by roughness or heterogeneities of the solid surface (Figure 3.6a).

The equilibrium contact angle θ_e or most stable contact angle is associated to a thermodynamic state, i.e., the lowest state of Gibbs free energy for the three-phase system (Figure 3.6b).

Contact angles on real surfaces can vary between a maximum value, i.e., the advancing contact angle θ_a, and a minimum value, i.e., the receding contact angle θ_r. The advancing contact angle θ_a is the highest metastable apparent contact angle that can be measured and θ_r the lowest. The difference between the advancing and receding contact angles is called the contact angle hysteresis:

$$\Delta\theta = \theta_a - \theta_r \tag{3.31}$$

Advancing and receding contact angles are sometimes mistakenly considered as dynamic angles. Even if the transition between metastable contact angles is indeed a dynamic process, these contact angles represent thermodynamic equilibrium states (Figure 3.6b).

The dynamic contact angle θ_d is the angle measured under dynamic flow conditions. It is affected by viscous effects.

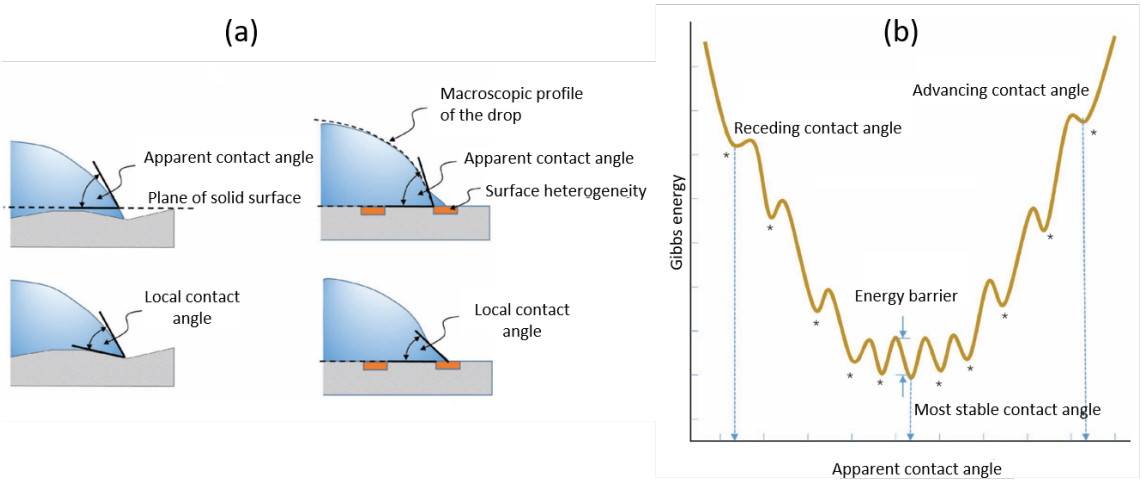

Figure 3.6. (a) Schemes showing apparent and local contact angles when measured on rough or heterogeneous surfaces (b) Schematic evolution of the Gibbs free energy as a function of the apparent contact angle (Marmur et al., 2017).

3.4 Capillary phenomena in fibrous media

3.4.1 Experimental observations of capillary phenomena in fibrous media

3.4.1.1 Impregnation of fibre reinforcements

Several authors investigated the influence of capillary effects on impregnation phenomena of fibre reinforcements, using different types of experimental approaches. For instance, some authors placed a fibre reinforcement in a mould equipped with a visualisation system (Figure 3.7). The advancement of the fluid front and the formation of voids was studied with a video-enhanced microscope or a high-magnification video camera (Chen et al., 1995; Patel & Lee, 1995; Rohatgi et al., 1996; Kuentzer et al., 2006). During the experiments, the resin was injected at constant pressure or constant flow rate in the fibre reinforcements. Then, it was possible to observe the flow of the fluid through the fibrous reinforcement. The analysis of the phenomena that occurred during the impregnation were mainly qualitative. This enabled a better understanding of the formation of voids and air entrapment during the impregnation of fibre reinforcements. Using this approach, the authors attempted to explain the influence of injection parameters (injection pressure, injection flow rate) and capillary pressure on the formation, development and displacement of voids in the vicinity of the flow front (Figure 3.7).

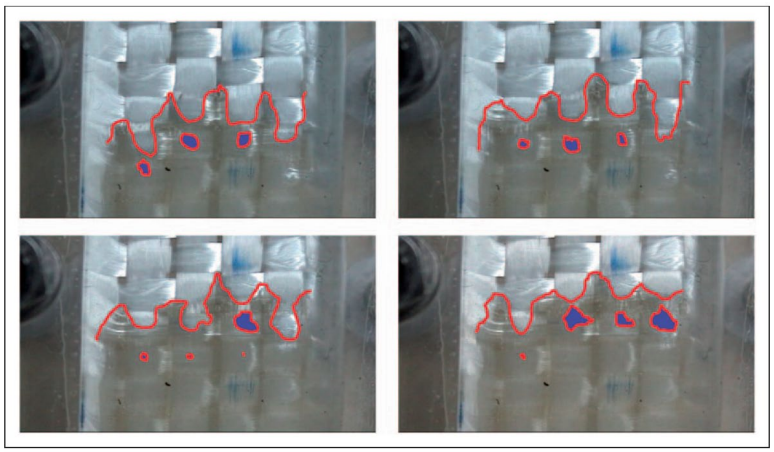

Figure 3.7. Local deformation of the fluid front (red line) and resulting voids (blue spots) that are formed behind it during the impregnation of a reinforcement fabric (Park & Lee, 2011).

These experiments demonstrated that there was a combined effect of the injection parameters and the wettability properties of the fibre reinforcements on the flow phenomena that occurred between or within the fibre bundles (Rohatgi et al., 1996; Patel & Lee, 1995; Hamidi et al., 2004). The competition between the viscous and capillary effects during the impregnation of a fibre reinforcement governs the formation of voids. For large flow velocity, i.e., large capillary numbers ($Ca > 10^{-2}$) estimated using the average flow front velocity, the viscous effects are dominant and the flow of the fluid occurs preferentially between the fibre bundles, which leads to the formation of voids within the bundles. On the contrary, for low capillary numbers ($Ca < 10^{-3}$), capillary effects are dominant; the fluid flow is faster inside the bundle of fibres, causing the formation of voids between the bundles. Park et al. (2011) showed that a minimum void content can be reached for an optimum range of capillary numbers ($10^{-3} < Ca < 10^{-2}$).

Thus, these experiments revealed that the propagation of the fluid flow front through a fibre reinforcement made of an assembly of fibre bundles/yarns is dependent on the capillary-driven flow that occurs within fibre bundles/yarns. This is the reason why, an important number of studies were focused on the investigation of capillary phenomena in fibre bundles or arrays of parallel fibres, using experimental, numerical and theoretical approaches.

3.4.1.2 Impregnation of fibre bundles

The study of the impregnation of fibre bundles was the subject of many research efforts (Princen, 1969a; Washburn, 1921 Neacsu et al., 2007; Neacsu et al., 2006; Yeager et al., 2017; Vilà et al., 2015; Larson et al., 2019; Castro et al., 2020). Several experiments based on the classical Wilhelmy method were performed to study longitudinal and transverse capillary driven flows within fibre bundles. These experiments were performed by dipping a real fibre bundle or a model one in the form of an array of parallel fibres into a reservoir

filled with a liquid (Chwastiak, 1973; Pillai & Advani, 1996; Patel & Lee, 1996; Ahn et al., 1991). Once the fibres and the liquid were in contact a capillary-driven flow was observed. The evolution of the weight of the bundle or the flow front position were recorded. Accounting for the buoyancy effect, the capillary force F_c exerted by the fluid on the fibre bundle can be estimated as follows:

$$F_c = \mathcal{P}\,\gamma_{lv} cos\theta \tag{3.32}$$

where $\mathcal{P}$ is the wetted perimeter of the fibre bundle that mainly depends on the number of fibres in the bundle, θ is the apparent contact angle. This approach allows validating impregnation models for bundles based either on modified Wahburn's law or Darcy's law (Pillai & Advani, 1996; Pucci et al., 2015). However, the observations made using this approach do not allow a fine description of the flow mechanisms that occur within the bundles.

Several studies have used advanced imaging techniques to further investigate the impregnation phenomena at the fibre scale. For instance, the fluid propagation in fibre bundles was studied using magnetic resonance imaging (MRI) measurements (Neacsu et al., 2007). This technique enabled detecting variations in fluid concentration and thus the formation of voids/pores (Endruweit et al., 2011). X-ray radiography was also used to track fluid propagation within fibre bundles (Bréard et al., 1999). These techniques give a 2D information on the impregnation phenomena.

More recently, 3D observation techniques such high resolution X-ray microtomography have been used to track the propagation of a fluid front and the formation and the transport of voids and the fibre rearrangement phenomena during the impregnation of fibre bundles (Vilà et al. 2015) (Figure 3.8). Using such types of 3D images, Larson & Zok (2018b) Castro et al. (2020) measured local contact angles only in particular zones. No distribution of contact angles along the triple lines were given.

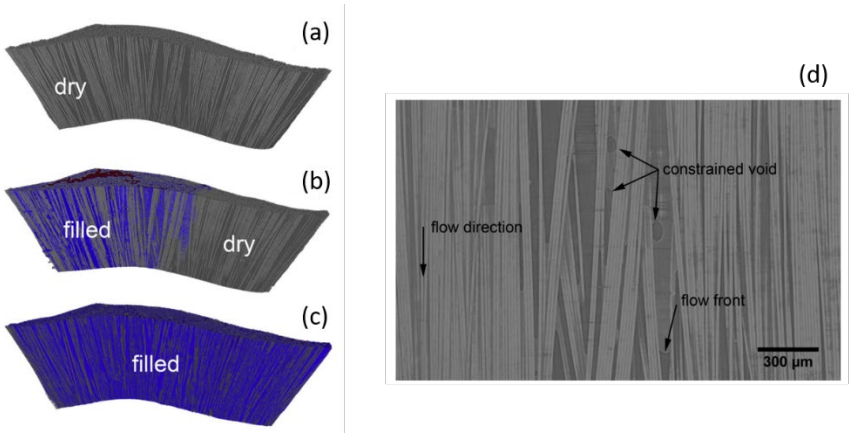

Figure 3.8. 3D images of three impregnation steps (a) dry fibre bundle, (b) partially impregnated fibre bundle (fluid in blue, fibres in grey), (c) longitudinal cross section of a grey scale 3D image of an impregnated bundle where voids and the fluid front can be distinguished (Vilà et al., 2015).

Recently, the use of X-ray microtomography technique saw a great development in the field of geosciences for the study of capillary phenomena that occur in various porous granular materials. Significant enhancements of image analysis techniques allowed measuring several pore scale parameters related to capillary phenomena. A pioneer work on local contact angle measurements from 3D images was carried out by Andrew et al. (2014), using 3D X-ray microtomography images of partially impregnated CO_2/brine/carbonate systems. For that purpose, Andrew et al. (2014) used 2D cross sections of 3D images oriented perpendicular to the triple line to measure manually the local contact angles along the triple line. Klise et al. (2016) and Scanziani et al. (2017) proposed algorithms to make automated mesurements of local contact angles in 3D images using the same approach (Figure 3.9). More recently, Alratrout et al. (2017) and Ibekwe et al. (2020) have further enhanced these procedures. Hence, the authors could show that large distribution of local angles can occur during imbibition or drainage experiments of the investigated geomaterials.

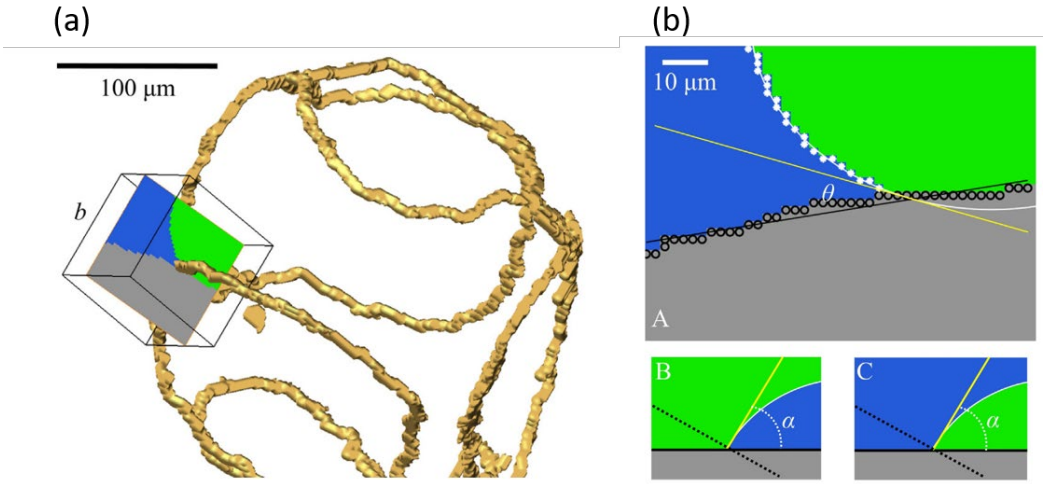

Figure 3.9. (a) 3D representation of a triple line (in yellow) obtained from a 3D X-ray microtomography image of a partially impregnated geomaterial. The solid phase appears in grey, the two fluid phases appear in blue and green in the 2D segmented cross section of this material that is represented in this 3D image. This cross section is normal to a tangent vector to the triple line. (b) Same 2D cross section showing the local contact angle θ measured between the grey phase and the green phase (Scanziani et al., 2017).

The authors also developed advanced image analysis procedures to measure the capillary pressure at the pore scale from X-ray microtomography 3D images, measuring for that local curvatures of the fluid-fluid interfaces that were extracted from segmented 3D images (Armstrong et al., 2012; Andrew et al., 2015; Singh, 2016; Alratrout et al., 2017; Herring et al., 2017; Li et al., 2017; Lin et al., 2018). The capillary pressure was then calculated using the Young-Laplace equations (Eq. 3.11). This method was originally described by Armstrong et al. (2012) who compared the capillary pressure obtained from interfacial curvatures measured from computed X-ray microtomography images with those measured experimentally with a transducer during imbibition and drainage experiments.

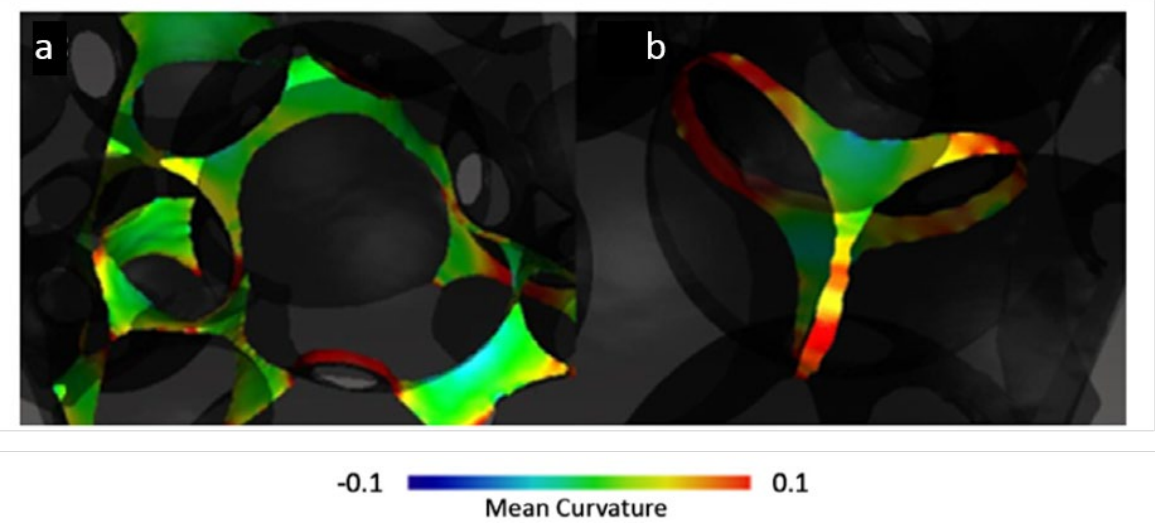

Figure 3.10. Examples of curvature maps across an oil/brin interface through a porous medium. The authors performed drainage and imbibition experiments using soda-lime glass beads to simulate the flow of oil and gas in reservoir rocks (Armstrong et al., 2012).

3.4.2 Numerical fibre scale simulations of capillary rise in arrays of parallel fibres

Several authors performed numerical studies to investigate capillary-driven flow phenomena in parallel assemblies of fibre bundles (Neacsu et al., 2006; Dimitrovova & Advani, 2002; Vennat et al., 2010; Chevalier et al., 2018; Charpentier et al., 2020). Few numerical models were formulated at the fibre scale for arrays of parallel cylinders, considering parallel or transverse flow situations with respect to the main fibre orientation.

Vennat et al. (2010) performed finite element simulations of the longitudinal capillary-driven rise of a liquid within an assembly of parallel fibres. The authors showed the influence of the interfibrillar/fibre space and various constant contact angles on the capillary rise (Figure3.11a,b). Charpentier et al. (2020) investigated the effects of dynamics flow conditions on the longitudinal capillary rise in a periodic array of parallel fibres. The authors investigated the influence of fibre spacing, inertia, viscosity and density ratios of the fluid and demonstrated more particularly that the static equilibrium height reached by the liquid-gas meniscus is in quantitative agreements with the predictions of Princen's equations (Princen, 1969a), see also below. Chevalier et al. (2018) performed quite similar finite element simulation of the capillary-driven rise of a liquid through a network of parallel fibres. Contrary to the simulations of Vennat et al. (2010) and Charpentier et al. (2020), the contact angle was not fixed. Instead, they employed an original approach to compute the mechanical equilibrium of the triple line, i.e., by incorporating into the weak formulation of the problem the Young-Dupré equation (Eq. 3.17) that accounts for the equilibrium of the surface tensions (Figure 3.11c).

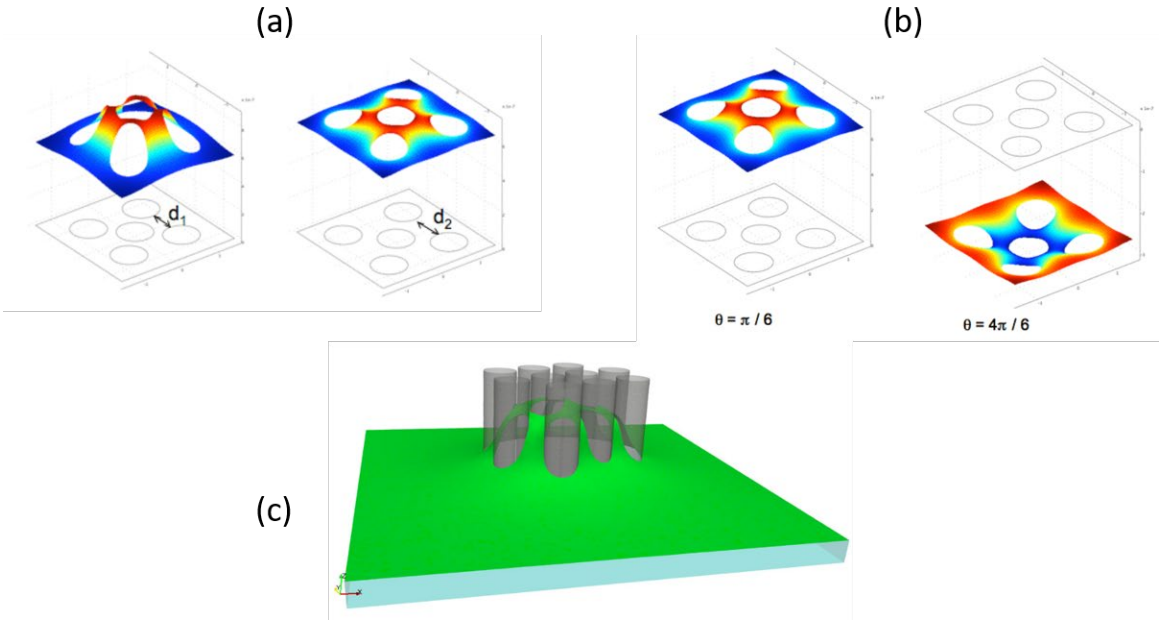

Figure 3.11. (a,b) Maps showing the altitude variations of the fluid-air interface in an array of parallel cylinders obtained by finite element simulation as a function of the cylinder distances d_1 and d_2 and the contact angle θ (Vennat et al., 2010). (c) Simulation of the equilibrium position of a fluid front (green surface) in an array of 10 parallel cylinders (Chevalier et al., 2018).

For transverse flow situations to arrays of parallel cylindrical fibres, Dimitrovova & Advani (2002) performed 2D simulations of the unsaturated flow of a viscous fluid taking into account capillary effects. They demonstrated the importance of the capillary number on the flow front propagation and also tested the effect of varying the contact angle. Their results allow identifying macroscopic capillary pressure and a so-called relative permeability that appear in a modified Darcy's law for unsaturated flow situations.

Neacsu et al., (2006) investigated radial flow situations in arrays of parallel fibres arranged in a quasi-hexagonal pattern. The authors treated the important problem of the radial fluid front propagation in a fibre bundle, where gas entrapment or dissolution is possible. For the modelling of the fluid propagation, they used a modified Darcy's law in which they incorporated an averaged capillary pressure. The average capillary depends on the fibre arrangement, the fibre content and radius as well the contact angle and the advancing and receding contact angles. Interestingly, they tested the effect of local variations of the fibre volume fraction on the fluid propagation.

3.4.3 Analytical models for the prediction of capillary rise in arrays of parallel fibres

Some analytical formulations have been proposed to estimate the capillary-driven rise of a fluid through periodic arrays of parallel and cylindrical fibres as well as to estimate the

capillary pressure at the fluid-air interface in these systems. Longitudinal and transverse flow situations were modelled.

Princen (1969) developed several models for these flow situations. In a first article, (Princen, 1969a), developed a model for the longitudinal capillary rise of a fluid between pairs of cylinders. His approach allows predicting the conditions for the existence of capillary bridges between pairs of cylinders. He proposed an analytical expression to estimate the rise of a liquid between two closely space cylinders (Figure 3.12) as a function of the distance of separation of the cylinders and the contact angle. His approach is based on an equilibrium of the forces that act on the fluid column. The considered forces are the weight of the liquid column (the horizontal cross section of the liquid column is shown in Figure 3.12), the upward capillary forces which exert on the triple line (arcs AC and BD in Figure 3.12). He also considered downward forces which tend to pull down the liquid column. These forces exert on the free vertical liquid surfaces and result from surface tension effects of the fluid-air interface (arcs AB and CD in Figure 3.12).

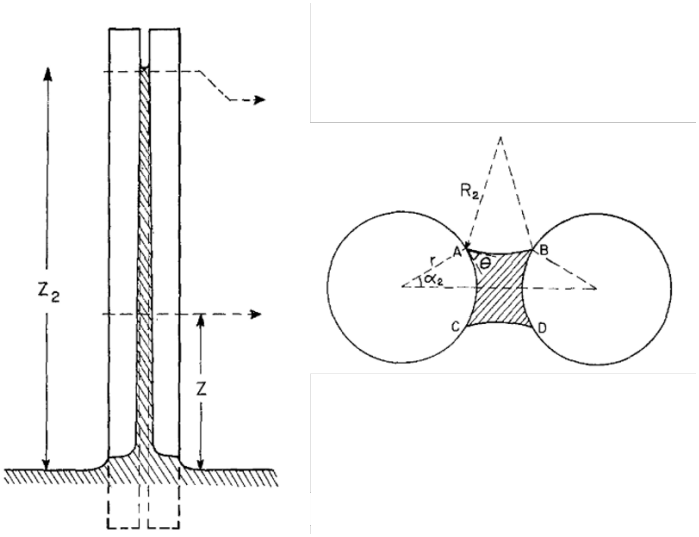

Figure 3.12. Capillary rise of liquid between pairs of vertical cylinders and the respective cross section just below the meniscus on which the equilibrium of forces is written (Princen, 1969a).

In two other papers, Princen studied the capillary phenomena that arise in systems made of multiple parallel cylinders systems with varying spatial arrangements (Princen, 1969b; Princen, 1970). Princen, (1970) is focused on the determination of the shape of liquid columns between horizontal parallel circular cylinders. In Princen, (1969b) the previous approach for pairs of cylinders was extended to predict the capillary rise in periodic cells made of three or four equidistant cylinders (Figure 3.13). The analysis performed by Princen allows predicting the meniscus height as a function of the fibre separation distance, arrangement, and the contact angle. The analysis was also extended to fibres with noncircular cross section. These studies are very interesting since they enable through the knowledge of the meniscus height and shape the determination of the capillary pressure.

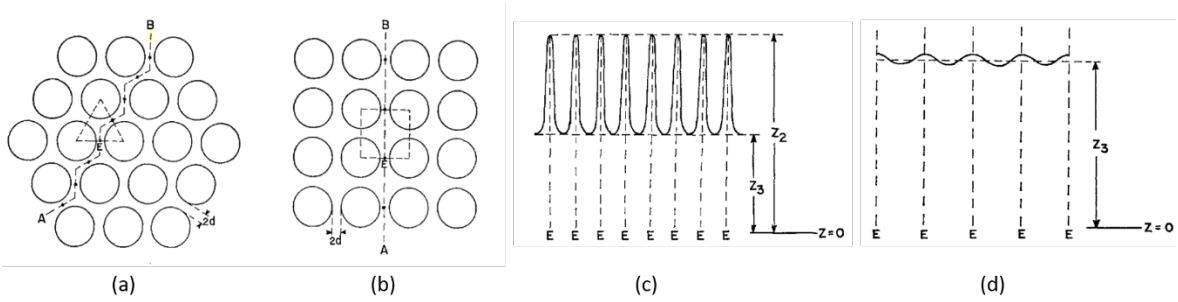

Figure 3.13. Multicylinder systems considered by Princen: (a) hexagonal arrangement, (b) square arrangement. (c) Meniscus profile in the vertical section through AB of the hexagonal arrangement (see drawing a). (d) Same profile in the square arrangement (see drawing b).

In the composite domain, several authors also proposed analytical expressions to compute the average capillary pressure that develops during the impregnation of an array of parallel fibres (Pillai & Advani, 1996; Ahn et al., 1997). These authors proposed the following form for the average capillary pressure:

$$\bar{P}_c = F \frac{\gamma_{lv} \cos\theta}{D_f} \frac{(1-\phi_p)}{\phi_p} \tag{3.33}$$

where D_f is the fibre diameter, ϕ_p the porosity of the fibre network. The parameter F is a form factor that accounts for the flow direction with respect to the main orientation axis of the fibres. The parameter F is equal to 4 for a flow along the fibre direction (longitudinal flow) and equal to 2 for a flow perpendicular to the fibre alignment (transverse flow).

References

Ahn, K., Seferis, J., & Berg, J. C. (1991). Simultaneous Measurements of Permeability and Capillary. *Polymer Composites*, *12*(3), 146-152.

Alratrout, A., Raeini, A. Q., Bijeljic, B., & Blunt, M. J. (2017). Automatic measurement of contact angle in pore-space images. *Advances in Water Resources journal*, *109*, 158-169. https://doi.org/10.1016/j.advwatres.2017.07.018

Andrew, M., Bijeljic, B., & Blunt, M. J. (2014). Pore-scale contact angle measurements at reservoir conditions using X-ray microtomography. *Advances in Water Resources*, *68*, 24-31. https://doi.org/10.1016/j.advwatres.2014.02.014

Andrew, M., Menke, H., Blunt, M. J., & Bijeljic, B. (2015). The Imaging of Dynamic Multiphase Fluid Flow Using Synchrotron-Based X-ray Microtomography at Reservoir Conditions. *Transport in Porous Media*, *110*(1). https://doi.org/10.1007/s11242-015-0553-2

Aris, R. (1962). *Vectors, tensors and the basic equations of fluid mechanics*. Courier Corporation.

Armstrong, R. T., Porter, M. L., & Wildenschild, D. (2012). Linking pore-scale interfacial curvature to column-scale capillary pressure. *Advances in Water Resources*, *46*, 55-62. https://doi.org/10.1016/j.advwatres.2012.05.009

Bear, J., & Braester, C. (1972). On the Flow of Two Immscible Fluids in Fractured Porous Media. In Iahr (Éd.), *Developments in Soil Science* (Vol. 2, p. 177-202). Elsevier. https://doi.org/10.1016/S0166-2481(08)70538-5

Bréard, J., Saouab, A., & Bouquet, G. (1999). Dependence of the Reinforcement Anisotropy on a Three Dimensional Resin Flow Observed by X-Ray Radioscopy. *Journal of Reinforced Plastics and Composites*, *18*(9), 814-826. https://doi.org/10.1177/073168449901800903

Cassie, A. B. D. (1948). Contact angles. *Discussions of the Faraday society*, *3*, 11-16.

Castro, J., Sket, F., & González, C. (2020). S-XCT experimental determination of local contact angle and meniscus shape in liquid moulding of composites. *Composites Science and Technology*, *199*, 108362. https://doi.org/10.1016/j.compscitech.2020.108362

Charpentier, J. B., Brändle de Motta, J. C., & Ménard, T. (2020). Capillary phenomena in assemblies of parallel cylindrical fibers : From statics to dynamics. *International Journal of Multiphase Flow*, *129*, 103304. https://doi.org/10.1016/j.ijmultiphaseflow.2020.103304

Chen, Y. -T, Davis, H. T., & Macosko, C. W. (1995). Wetting of fiber mats for composites manufacturing : I. Visualization experiments. *AIChE Journal*, *41*(10), 2261-2273. https://doi.org/10.1002/aic.690411009

Chevalier, L., Bruchon, J., Moulin, N., Liotier, P. J., & Drapier, S. (2018). Accounting for local capillary effects in two-phase flows with relaxed surface tension formulation in enriched finite elements. *Comptes Rendus - Mecanique*, *346*(8), 617-633. https://doi.org/10.1016/j.crme.2018.06.008

Chwastiak, S. (1973). A Wicking Method for Measuring Wetting Properties of Carbon Yarns. *Journal of Colloid and Interface Science, 42*(2).

Deemer, A. R., & Slattery, J. C. (1978). Balance equations and structural models for phase interfaces. *International Journal of Multiphase Flow*, *4*(2), 171-192. https://doi.org/10.1016/0301-9322(78)90043-5

Dimitrovova, Z., & Advani, S. G. (2002). Analysis and characterization of relative permeability and capillary pressure for free surface flow of a viscous fluid across an array of aligned cylindrical fibers. *Journal of Colloid and Interface Science*, *245*(2), 325-337. https://doi.org/10.1006/jcis.2001.8003

Drelich, J. W. (2019). Contact angles : From past mistakes to new developments through liquid-solid adhesion measurements. *Advances in Colloid and Interface Science*, *267*, 1-14. https://doi.org/10.1016/j.cis.2019.02.002

Endruweit, A., Glover, P., Head, K., & Long, A. C. (2011). Mapping of the fluid distribution in impregnated reinforcement textiles using Magnetic Resonance Imaging : Methods and issues. *Composites Part A: Applied Science and Manufacturing*, *42*(3), 265-273. https://doi.org/10.1016/j.compositesa.2010.11.012

Gennes, P.-G. de, Brochard-Wyart, F., & Quere, D. (2013). *Capillarity and Wetting Phenomena : Drops, Bubbles, Pearls, Waves*. Springer Science & Business Media.

Hamidi, Y. K., Aktas, L., & Altan, M. C. (2004). Formation of microscopic voids in resin transfer molded composites. *Journal of Engineering Materials and Technology, Transactions of the ASME*, *126*(4), 420-426. https://doi.org/10.1115/1.1789958

Hassanizadeh, S. M., & Gray, W. G. (1993a). Thermodynamic basis of capillary pressure in porous media. *Water Resources Research*, *29*(10), 3389-3405. https://doi.org/10.1029/93WR01495

Hassanizadeh, S. M., & Gray, W. G. (1993b). Thermodynamic basis of capillary pressure in porous media. *Water Resources Research*, *29*(10), 3389-3405. https://doi.org/10.1029/93WR01495

Herring, A. L., Middleton, J., Walsh, R., Kingston, A., & Sheppard, A. (2017). Flow rate impacts on capillary pressure and interface curvature of connected and disconnected fluid phases during multiphase flow in sandstone. *Advances in Water Resources*, *107*, 460-469. https://doi.org/10.1016/j.advwatres.2017.05.011

Ibekwe, A., Pokrajac, D., & Tanino, Y. (2020). Computers and Geosciences Automated extraction of in situ contact angles from micro-computed tomography images of porous media. *Computers and Geosciences*, *137*, 104425. https://doi.org/10.1016/j.cageo.2020.104425

James, B. D. F. (1974). The meniscus on the outside of a small circular cylinder. *Journal of Fluid Mechanics 63*, 657-664.

Klise, K. A., Moriarty, D., Yoon, H., & Karpyn, Z. (2016). Advances in Water Resources Automated contact angle estimation for three-dimensional X-ray microtomography data. *Advances in Water Resources*, *95*, 152-160. https://doi.org/10.1016/j.advwatres.2015.11.006

Kuentzer, N., Simacek, P., Advani, S. G., & Walsh, S. (2006). Permeability characterization of dual scale fibrous porous media. *Composites Part A: Applied Science and Manufacturing*, *37*(11), 2057-2068. https://doi.org/10.1016/j.compositesa.2005.12.005

Larson, N. M., Cuellar, C., & Zok, F. W. (2019). X-ray computed tomography of microstructure evolution during matrix impregnation and curing in unidirectional fiber beds. *Composites Part A: Applied Science and Manufacturing*, *117*, 243-259. https://doi.org/10.1016/j.compositesa.2018.11.021

Larson, N. M., & Zok, F. W. (2018). Insights from in-situ X-ray computed tomography during axial impregnation of unidirectional fiber beds. *Composites Part A: Applied Science and Manufacturing*, *107*, 124-134. https://doi.org/10.1016/j.compositesa.2017.12.024

Li, T., Schlüter, S., Dragila, M. I., & Wildenschild, D. (2017). An improved method for estimating capillary pressure from 3D microtomography images and its application to the study of disconnected nonwetting phase. *Advances in Water Resources*, *114*, 249-260. https://doi.org/10.1016/j.advwatres.2018.02.012

Lin, Q., Bijeljic, B., Pini, R., Blunt, M. J., & Krevor, S. (2018). Imaging and Measurement of Pore-Scale Interfacial Curvature to Determine Capillary Pressure Simultaneously With Relative Permeability. *Water Resources Research, 54* 7046-7060. https://doi.org/10.1029/2018WR023214

Marmur, A., Volpe, C. Della, & Siboni, S. (2017). Contact angles and wettability : Towards common and accurate terminology. *Surface Innovations 5*, 3-8.

Michaud, V. (2016). A Review of Non-saturated Resin Flow in Liquid Composite Moulding processes. *Transport in Porous Media*, *115*(3), 581-601. https://doi.org/10.1007/s11242-016-0629-7

Neacsu, V., Abu Obaid, A., & Advani, S. G. (2006). Spontaneous radial capillary impregnation across a bank of aligned micro-cylinders—Part I: Theory and model development. *International Journal of Multiphase Flow*, *32*(6), 661-676. https://doi.org/10.1016/j.ijmultiphaseflow.2006.02.006

Neacsu, V., Leisen, J., Beckham, H. W., & Advani, S. G. (2007). Use of magnetic resonance imaging to visualize impregnation across aligned cylinders due to capillary forces. *Experiments in Fluids*, *42*(3), 425-440. https://doi.org/10.1007/s00348-007-0251-0

Park, C. H., Lebel, A., Saouab, A., Bréard, J., & Lee, W. Il. (2011). Modeling and simulation of voids and saturation in liquid composite molding processes. *Composites Part A: Applied Science and Manufacturing*, *42*(6), 658-668. https://doi.org/10.1016/j.compositesa.2011.02.005

Park, C. H., & Lee, W. (2011). Modeling void formation and unsaturated flow in liquid composite molding processes : A survey and review. *Journal of Reinforced Plastics and Composites*, *30*(11), 957-977. https://doi.org/10.1177/0731684411411338

Patel, N., & Lee, L. J. (1995). Effects of fiber mat architecture on void formation and removal in liquid composite molding. *Polymer Composites*, *16*(5), 386-399. https://doi.org/10.1002/pc.750160507

Patel, N., & Lee, L. J. (1996). Modeling of void formation and removal in liquid composite molding. Part I: wettability analysis. *Polymer Composites, 17*(1). https://doi.org/10.5194/gmdd-8-6669-2015

Pillai, K. M., & Advani, S. G. (1996). Wicking across a Fiber-Bank. *Journal of Colloid and Interface Science*, *110*, 100-110.

Princen, H. M. (1969a). Capillary phenomena in assemblies of parallel cylinders. I. Capillary Rise between Two Cylinders. *Journal of Colloid And Interface Science*, *30*(1), 69-75. https://doi.org/10.1016/0021-9797(69)90379-8

Princen, H. M. (1969b). Capillary phenomena in assemblies of parallel cylinders : II. Capillary rise in systems with more than two cylinders. *Journal of Colloid and Interface Science*, *30*(3), 359-371. https://doi.org/10.1016/0021-9797(69)90403-2

Princen, H. M. (1970). Capillary phenomena in assemblies of parallel cylinders : III. Liquid Columns between Horizontal Parallel Cylinders. *Journal of Colloid and Interface Science*, *34*(2), 171-184. https://doi.org/10.1016/0021-9797(70)90167-0

Pucci, M. F., Liotier, P.-J., & Drapier, S. (2015). Capillary effects on flax fibers – Modification and characterization of the wetting dynamics. *Composites Part A: Applied Science and Manufacturing*, *77*, 257-265. https://doi.org/10.1016/j.compositesa.2015.03.010

Rohatgi, V., Patel, N., & James Lee, L. (1996). Experimental investigation of flow-induced microvoids during impregnation of unidirectional stitched fiberglass mat. *Polymer Composites*, *17*(2), 161-170. https://doi.org/10.1002/pc.10601

Scanziani, A., Singh, K., Blunt, M. J., & Guadagnini, A. (2017). Automatic method for estimation of in situ effective contact angle from X-ray micro tomography images of

two-phase flow in porous media. *Journal of Colloid and Interface Science 496*, 51-59. https://doi.org/10.1016/j.jcis.2017.02.005

Singh, K. (2016). Imaging of oil layers, curvature and contact angle in a mixed- wet and a water-wet carbonate rock. *Water Resources Research*, 1-13. https://doi.org/10.1002/2015WR018072.Received

Starnoni, M., & Pokrajac, D. (2020). On the concept of macroscopic capillary pressure in two-phase porous media flow. *Advances in Water Resources*, *135*, 103487. https://doi.org/10.1016/j.advwatres.2019.103487

Vennat, E., Aubry, D., & Degrange, M. (2010). Collagen Fiber Network Infiltration : Permeability and Capillary Infiltration. *Transport in Porous Media*, *84*(3), 717-733. https://doi.org/10.1007/s11242-010-9537-4

Vilà, J., Sket, F., Wilde, F., Requena, G., González, C., & LLorca, J. (2015). An in situ investigation of microscopic infusion and void transport during vacuum-assisted infiltration by means of X-ray computed tomography. *Composites Science and Technology*, *119*, 12-19. https://doi.org/10.1016/j.compscitech.2015.09.016

Washburn, E. W. (1921). The Dynamics of Capillary Flow. *Physical Review*, *17*(3), 273-283. https://doi.org/10.1103/PhysRev.17.273

Wenzel, R. N. (1936). Resistance of solid surfaces to wetting by water. *Industrial & Engineering Chemistry*, *28*(8), 988-994.

Yeager, M., Simacek, P., & Advani, S. G. (2017). Role of fiber distribution and air evacuation time on capillary driven flow into fiber tows. *Composites Part A: Applied Science and Manufacturing*, *93*, 144-152. https://doi.org/10.1016/j.compositesa.2016.11.016

Young, T. (1805). "III. An essay on the cohesion of fluids". *Philosophical transactions of the royal society of London 95*, 65-87.

Chapter 4

Objectives

The literature review done in the previous chapters have highlighted the complexity of the manufacturing processes for composite materials, more especially those reinforced with natural fibres. It was shown that the impregnation phase is crucial for obtaining composite parts with optimised structural and end-use properties. The heterogeneity and complexity of the fibre reinforcement materials and the poor control of phenomena that occur during their impregnation may be at the origin of several defects such as for instance porosity, uncontrolled spatial and orientation fibre distributions and fibre deformation and damage. To better control the impregnation, **it is crucial to properly estimate the permeability properties of fibre reinforcement materials as a function of their microstructural characteristics and their deformation history**. Unprecise permeability estimates can significantly affect the prediction of the flow patterns and mould filling time. **It is also necessary to better understand the role played by the capillary effects on the impregnation** as they can lead to uncontrolled propagation phenomena of the fluid front, inducing for instance voids entrapment phenomena.

In **Chapter 2** a review of experimental results, numerical estimates and analytical predictions for permeability available in literature was presented. The huge amount of experimental data available in the literature show that the permeability of porous materials exhibit a first-order dependence on the fibre volume fraction, or radius. However, the experimental results also show that some parameters such as the specific surface area, tortuosity, anisotropy of the porous media also govern the flow properties in porous media. **Thus, the dependence of permeability properties on these parameters also need to be precisely established.** This is all the more true for fibrous media made of natural fibres that exhibit complex porous and fibrous microstructures. These experimental results are compared and/or completed with results of numerical studies which aim at estimating the permeability of porous media. This method is commonly applied in the composite domain using numerically generated fibrous networks or 3D images of real fibrous materials as input data for these calculations.
Based on experimental and numerical data several authors proposed theoretical models for permeability predictions, using various upscaling approaches. These models are usually developed for simplified pore or fibre geometries. For instance, fibrous media are often simplified as arrays of parallel cylinders with different arrangements with flow directions that are transverse or longitudinal to the main axis of fibres. **However, there is a lack of**

permeability models for complex fibre arrangements, spatial and orientation distributions, i.e. representative of many fibre reinforcement materials used in the composite domain. In these cases, the permeability properties are usually estimated by adapting classical models for porous materials, such as for instance the so-called capillary permeability model proposed by Kozeny-Carman (1927). However, the identification of the microstructural and flow-microstructure coupling parameters of these models remains difficult. In that case, some rare studies have shown that one possible relevant approach consists in identifying microstructural parameters, using X-ray microtomography images of real fibrous materials.

The propagation of a fluid front through a multiscale fibre reinforcement is complex and can result in severe distortion of its geometry. Fluid propagation typically occurs between fibre bundles/yarns and within fibre bundles/yarns. In the latter case, it was established that the fluid flow is mainly driven by capillary forces between individual fibres of fibre yarns/bundles. Thus, **Chapter 3** is focused on the mechanics of capillary phenomena in porous/fibrous media. At the fluid front three different phases (a fluid, i.e., the polymer matrix, a gas, i.e., usually the air, and a solid, i.e., the fibres) interact. The equilibrium of the fluid-air and the triple line at the junction of the three phases depends on several parameters such as the fluid-gas surface tension, solid surface energy, and contact angle. The resulting capillary pressure that is exerted on the fluid-gas interface can promote or slow down the fluid front propagation in the fibrous reinforcement, leading sometimes to uncontrolled gas entrapment phenomena. Precise description of local contact angles, capillary forces, capillary pressure in fibrous materials are still scarce. **This hinders the development of relevant theoretical and numerical approaches that would allow a precise description of the fluid propagation in fibre reinforcement materials.** Several recent studies have shown that X-ray microtomography is a relevant technique to make fruitful observations of capillary phenomena and fluid propagation in unsaturated complex porous materials.

Within this context, the objectives of this study were:

- (i) to propose a modified Kozeny-Carman model for the permeability of disordered and anisotropic biobased fibrous media, (ii) and a methodology to identify the microstructure parameters of this model, analysing 3D images of real fibrous networks made of flax fibres, and (iii) to check the validity of this model with respect to fibre scale direct CFD calculations. The results are presented in **Chapter 5**: “Permeability of flax fibre mats: numerical and theoretical prediction from 3D X-ray microtomography images”.
- (i) to propose a simple analytical and tensorial model for the estimation of the components of the permeability tensor $\boldsymbol{K}$ for disordered fibrous media with discontinuous fibres that exhibit various orientation states, (ii) to gauge the relevance of the prediction of this model with respect to CFD simulations performed on a wide diversity of virtual fibrous networks that were numerically generated or real fibrous networks made more particularly of natural fibres that were imaged using X-ray microtomography. The results obtained are presented in **Chapter 6**: “A

simple analytical permeability model for fibre networks with disordered architectures".

- (i) to perform original in situ impregnation experiments of model fibrous networks in the form of arrays of parallel tubes mimicking fibre bundles, in order to obtain high-resolution 3D images for the observation of the flow front propagation phenomena that occur in wetting and dewetting situations, (ii) develop or adapt image analysis procedures so as to measure local parameters related to capillarity phenomena, (iii) propose a methodology to determine local capillary forces and pressure, (iv) check the relevance of impregnation models that are used in the composite domain. The results obtained are presented in **Chapter 7**: "In situ 3D observations of the impregnation phenomena occurring in parallel arrangements of rigid fibres".

Finally, **Chapter 8** gives the conclusions of this work and some perspectives.

Chapter 5

Permeability of flax fibre mats: numerical and theoretical prediction from 3D X-ray microtomography images

Abstract

Flax fibre mats are promising and versatile biosourced reinforcements that can be used in composite parts obtained using various processing routes. To optimise their impregnation and the end-use properties of composites, it is still crucial to better understand the process-induced evolution of their microstructure and their permeability. In this study, flax fibre mats were subjected to in situ X-ray microtomography compression experiments. The resulting 3D images enabled the evolution of several key descriptors of their microstructure under compression to be determined, and the evolution of their permeability to be quantified by direct fibre scale CFD simulations. The microstructural data were also used as input parameters of a modified tensorial Kozeny-Carman model, accounting for the anisotropy and heterogeneity of mats. Only one unknown directional parameter was identified by inverse method from permeability calculations performed on numerically generated 3D realistic fibre networks. The predictions of the proposed model were consistent with numerical simulations.

5.1 Introduction

Biosourced composites reinforced with plant-based fibres represent a credible alternative to composites reinforced with glass or other synthetic fibres that are commonly used as structural or semi-structural parts in many industrial applications (Bourmaud et al., 2018; Shah, 2013a; Ramesh et al., 2020; Dixit et al., 2017). Several architectures of plant-based fibres are encountered (Müssig & Haag, 2015; Faruk & Sain, 2014): woven fabrics, knitted fabrics, and non-woven materials such as unidirectional veil of fibres and fibre mats. Fibre mats are versatile fibrous materials that consist of an intricate network of individualised fibrous elements such as discontinuous fibres, or discontinuous fibre bundles or both types of elements. The ease of their manufacturing offers the possibility to obtain various fibrous architectures varying for instance their fibre content, areal density and fibre orientation (Martin et al., 2016; Maity et al., 2014). In addition, they offer a good compromise with respect to other types of reinforcements because of their good processability (e.g. large deformation properties) in several composite manufacturing processes, and their ability to provide good reinforcement effect to polymer matrices (Omrani et al., 2019; Ouagne et al., 2020).

The manufacturing of composites parts with biosourced fibre mats can be done using either wet, e.g. Liquid Composite Moulding (LCM), or dry forming, e.g. compression moulding, processes (Shah, 2013b; Bourmaud et al., 2020; Ho et al., 2012). These processes involve the deformation of these reinforcement materials and their simultaneous or subsequent impregnation by a fluid polymer matrix to obtain either a prepreg material or a composite part with the desired shape. For plant-based reinforcement materials such as flax fibre woven fabrics, a poor control of the deformation mechanisms of these materials in their dry state is known to induce several defects such as wrinkling, buckling or tearing that affect the reinforcement architecture and integrity (Omrani et al., 2017; Ouagne et al., 2013; Baley

et al., 2019). Similarly, the impregnation of the same reinforcements by fluids such as filled thermoset resins or thermoplastics may result in voids inside and between tows (Baley et al., 2019; Binetruy et al., 1998; Kuentzer et al., 2007; Bréard et al., 2003; Mehdikhani et al., 2019; Pantaloni et al., 2020). It has been established that the impregnation of fibrous reinforcements is mainly controlled by their anisotropic permeability properties (Xue et al., 2011; Francucci et al., 2010; May et al., 2019) which are also strongly coupled with their deformation state (Pantaloni et al., 2020; Umer et al., 2011; Francucci et al., 2012). At the flow front, capillary effects also play an important role on the impregnation phenomena. Far from the flow front, in saturated zone, the impregnation phenomena occurring in composite forming processes are usually modelled by assuming the Darcy's law (Nguyen et al., 2015; Masoodi et al., 2012), which is, strictly speaking, valid for the flow of incompressible Newtonian fluids through rigid porous media at negligible Reynolds number. Vast research efforts are still ongoing to reveal the links between the components of the permeability tensor $\boldsymbol{K}$ of the Darcy's law and the deformability of various natural fibrous materials with more or less disordered architectures (Umer et al., 2007; Pantaloni et al., 2020). For biosourced fibre mats, the prediction of the permeability components is all the more difficult to establish as the fibrous microstructure of these materials is strongly disordered and fibres exhibit large morphological variations (Francucci et al., 2012; Lundquist et al., 2004; Delisée et al., 2010).

Several experimental studies dealt with the determination of the out-of-plane and in-plane permeability of biosourced fibre mats (Umer et al., 2011; Delisée et al., 2010; Bizet et al., 2008; Rodriguez et al., 2004). The effect of the compaction was also determined and allowed highlighting the effect of the porosity or conversely the fibre volume fraction on the permeability properties. Some authors reported that the evolution of the permeability components could be empirically fitted using either empirical power-law functions (Pantaloni et al., 2020; Francucci et al., 2010) of the fibre volume fraction $\bar{\phi}_s$ or the Kozeny-Carman model (Kozeny, 1927; Carman, 1956; Schulz et al., 2019). This equation is widely used to estimate the permeability K of isotropic porous media:

$$K = \frac{(1-\bar{\phi}_s)^3}{2cS_v^2\tau^2} \tag{5.1}$$

where S_v is the specific surface area, τ is the tortuosity (defined as the ratio between the mean flow path length and a characteristic length of the porous media). The Kozeny-Carman model assumes that the porous medium was equivalent to an assembly of parallel tortuous capillaries with equal length and diameter and circular cross sections. The assembly of capillaries has the same equivalent fibre volume fraction $\bar{\phi}_s$ and specific surface area S_v as the porous medium. The parameter c can be seen as a phenomenological corrective term to account for flows in cylinders with any cross section geometry (Kozeny, 1927; Carman, 1956; Schulz et al., 2019; Chen & Papathanasiou, 2006; Liu & Hwang, 2012; Ozgumus et al., 2014). The Kozeny-Carman model was used by Bizet et al. (Bizet et al., 2008) to fit the evolution of the out-of-plane permeability component of flax fibre mats by determining the best value for c for fitting the experimental data. The parameter c was shown to depend non-linearly on the fibre volume fraction.

The Kozeny-Carman equation thus relates the permeability to some key microstructure descriptors of the porous media and c, the parameter coupling the fluid flow with the structure. It is thus crucial to determine accurately these descriptors and their evolution with the deformation. Several studies used 3D X-ray microtomography imaging techniques to characterise the porous and fibrous architecture of biosourced mat (Delisée et al., 2010; Lux, Delisée, et al., 2006; Joffre et al., 2015) and paper-like materials (Viguié et al., 2013; Marulier et al., 2015; Rolland du Roscoat et al., 2007a). Thanks to the analysis of 3D images, the authors could measure several crucial descriptors such as the mean porosity $\bar{\phi}_p$, the specific surface area S_v and tortuosity τ. They also used these parameters in the Kozeny-Carman equation and compared the prediction of this model for the out-of-plane permeability of wood-based fibre mats with results obtained experimentally or by numerical simulation performed on 3D X-ray microtomography images (Delisée et al., 2010; Delisée et al., 2007). The chosen value of the parameter c did not allow a good prediction of the out-of-plane permeability of the studied materials (Delisée et al., 2007). Their choice was governed by considering geometry of the pore cross sections (circular or flat cross section of pores) that is presumably far from the real geometry of the pores in the investigated anisotropic fibrous networks. This shows that this parameter is critical and also difficult to estimate using uniquely image analysis of 3D fibrous networks. To circumvent this difficulty, Koponen et al. (Koponen et al., 1998) performed flow simulations through the thickness of numerically generated realistic fibrous networks with planar fibre orientation representative of the structure of paper-like materials. Hence, they determined the out-of-plane permeability of these materials, thereby estimating the value of c by an inverse method for this particular direction. They also proposed an empirical non-linear law for the evolution of c as a function of the fibre volume fraction $\bar{\phi}_s$.

Using high-resolution 3D X-ray microtomography images of fibre networks appear to be a powerful approach to estimate the permeability of fibrous materials with complex architectures (Viguié et al., 2013; Marulier et al., 2015; Rolland du Roscoat et al., 2007a; Caglar et al., 2017; Soltani et al., 2015; Soltani et al., 2014; Soltani et al., 2017; Hamdi et al., 2015; Ali et al., 2019). The current progress made in 3D X-ray microtomography imaging allow acquiring 3D images during in situ and in real time experiments that mimic the real forming conditions the composite fibre reinforcements are subjected (Loix et al., 2008; Laurencin et al., 2016; Sentis et al., 2017).

Hence, the objectives of this work were to investigate the microstructure and its evolution during transverse compression of thermolinked flax fibre mats, mimicking compaction phenomena that occur in many composite forming processes. For that purpose, in situ compression experiments were performed using synchrotron X-ray microtomography. Image analysis allowed quantifying the evolution of several key microstructure descriptors of the mats during their compaction. The components of the permeability tensor were estimated by direct numerical simulations on the 3D images for the various compression stages. Then, the microstructural data were used as input parameters of a modified anisotropic Kozeny-Carman model. To account for the anisotropy of the flax fibre mats, the tortuosity and an equivalent term to the aforementioned c parameter of the Kozeny-

Carman model were seen as directional parameters. Following the approach proposed by Koponen et al. (Koponen et al., 1998), the directional values of c were identified by an inverse method from permeability calculations performed using numerically generated 3D fibre networks. Finally, the relevance of the modified Kozeny-Caman model was discussed and was also tested for another type of biosourced mat.

5.2 Materials and methods

5.2.1 Flax fibre mats

The first type of mat were made of 90 wt% of flax fibres combined with 10 wt% of polypropylene fibres. These mats, denoted M1 in the following sections, were fabricated by the Gemtex laboratory using carding, overlapping and needle punching nonwoven technologies (Gnaba, Wang, et al., 2019; Gnaba, Omrani, et al., 2019). These mats were also consolidated using thermo-linking. During thermo-linking, the polypropylene fibres melted, allowing them to bond flax fibres after cooling. This process is usually used to increase the mechanical strength of mats. Figure 5.1 shows microscopic views of the mats before and after thermo-linking. The areal density of these mats was 241 g m^{-2}.

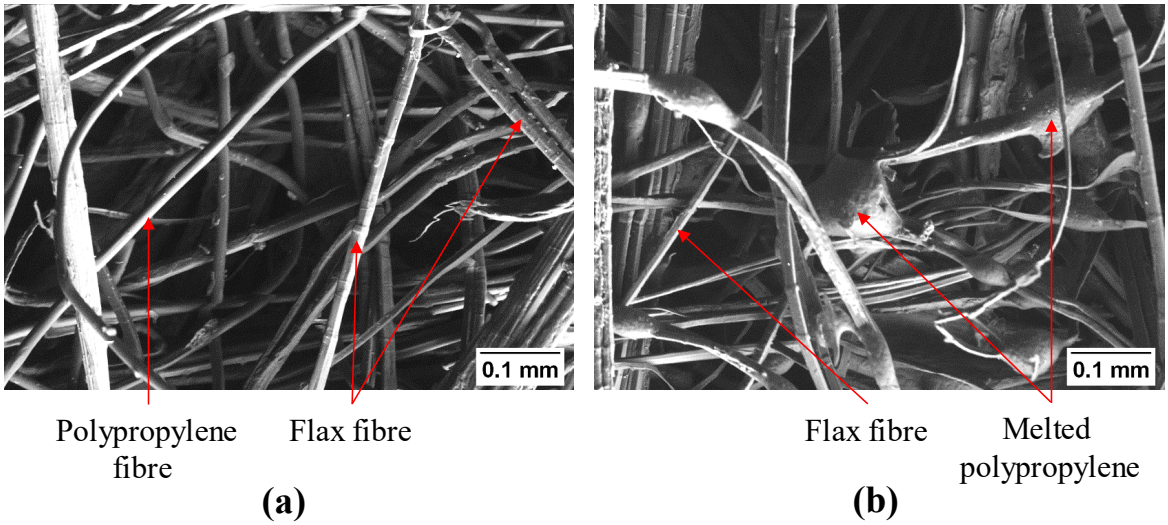

Figure 5.1. SEM micrographs of the mat M1 (a) before thermolinking and (b) after thermolinking.

A second type of flax fibre mat, denoted M2 in the following sections, was also used. This mat denoted Feutralin by the supplier Ecotechnilin (Valliquerville, France) had an areal density G of 540 g m^{-2}. This mat was also fabricated using carding, overlapping and needle punching processing techniques and was only made of flax fibres.

5.2.2 In situ compression experiments and 3D image acquisition

A specimen of mat M1 was subjected to out-of-plane compression tests using a micro-press installed on a synchrotron microtomograph (ID19 beamline, ESRF, Grenoble, France) (Laurencin et al., 2016; Latil et al., 2011; Martoïa et al., 2016). This micro-press was equipped with a load cell with a maximum capacity of 50 N which allowed the compression force F to be measured. The X-ray energy and the number of radiographs were set to 20 keV and 2000, respectively. A voxel size of 2.8^3 µm^3 was chosen to obtain accurate representation of the fibrous microstructure of the mats. Then, 3D images were reconstructed using the so-called Paganin procedure, which is based on the use of the phase contrast in the images, required for so low absorbing materials (Beltran et al., 2010) (Paganin et al., 2002). This technique is used to obtain 3D images that exhibit a good contrast between flax fibre and PP phases with nearly similar X-ray absorption coefficients. The specimen, initially in the form of a cylinder with a diameter of 10 mm, was subjected to a slight pre-compression of 0.06 N to ensure contact with the platens. The thickness h_0 was about 0.8 mm. Once a complete relaxation was reached, a first scanning experiment (Figure 5.2, step A) was performed (scanning time ≈ 1 min). Then, the specimen was sequentially put under compression up to a compression force of 6 N using a low compression velocity (Figure 5.2, step B, the image was taken after a 10-min relaxation). The sample was further loaded to a compression force of 15 N (Figure 5.2, step C, again the image was taken after a 10-min relaxation time). Finally, a fourth scan was carried out after unloading and relaxation (Figure 5.2, step D). Figure 5.2 also shows the stress-strain values as well as the 3D images of the specimen microstructure obtained during the compression test. The compression stress σ_{zz} was calculated as the ratio $|F|/S_0$ with S_0 the initial contact area of the specimen surface with the compression platens. The compression strain was calculated as $\varepsilon_{zz} = |\ln(h/h_0)|$ with h the sample thickness measured on the 3D images.

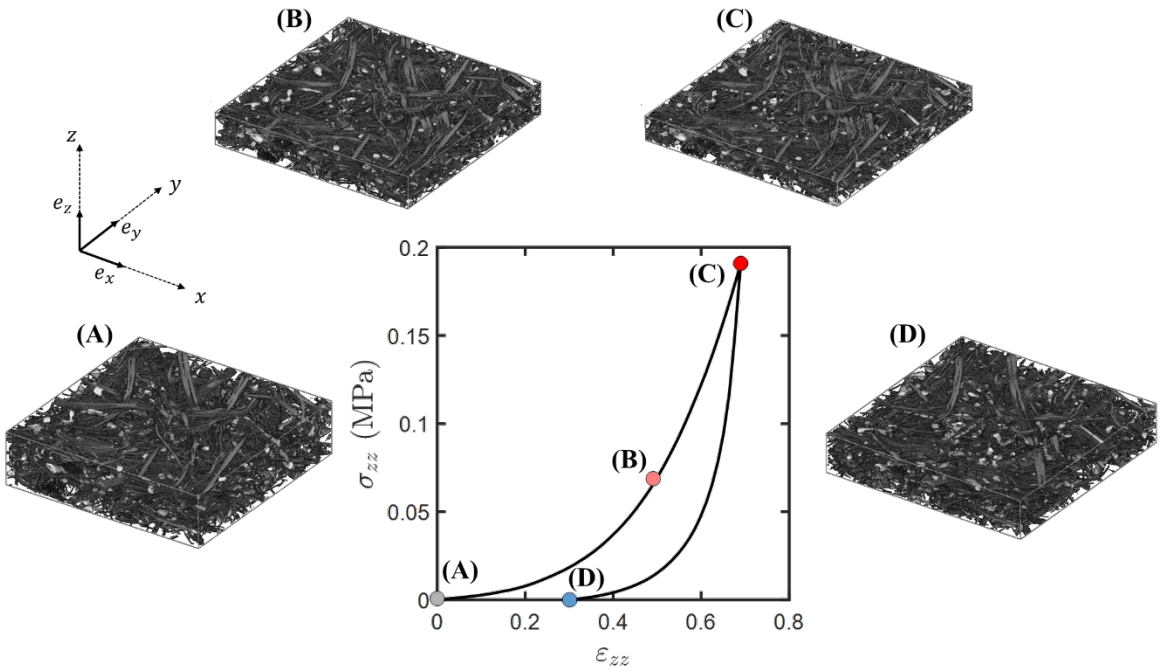

Figure 5.2. A-D: 3D cropped views of the fibrous microstructure of mat M1 during in situ compression. The sizes of the 3D images A, B, C and D are 3.1 x 3.1 x 0.8, 3.1 x 3.1 x 0.5, 3.1 x 3.1 x 0.4 and 3.1 x 3.1 x 0.6 mm^3, respectively. Graph: symbols A, B, C and D correspond to the recorded stress-strain values during the in situ compression test. The curve shows the compression response of another specimen of mat M1 obtained using the micro-press at low compression velocity.

5.2.3 Image analysis and morphological characterization

Thanks to the good contrast between the three imaged phases, i.e. the flax fibres, the polypropylene and pore phases, the 3D reconstructed images could be easily segmented. This operation was done manually using the threshold function implemented in Fiji Software (Schneider et al., 2012). The relevance of the thresholding operation will be discussed in section 5.3.1. Figure 5.3 shows the segmented X-ray microtomography images of mat M1. Figure 5.3d shows the evolution of the volume fraction of pores $\bar{\phi}_p$ as a function of the in-plane dimensions of the region of interest (ROI) chosen in the 3D images. This figure reveals that $\bar{\phi}_p$ was poorly affected by the size of the ROI for $l > 2000$ µm. This tends to show that above this size, the ROI's can be considered to be Representative Elementary Volume (REV) (Rolland du Roscoat et al., 2007a; Lux, Ahmadi, et al., 2006). In the following sections, the image analysis operations were performed for ROI's with $l = 3080$ µm as shown in Figures 5.2A-D.

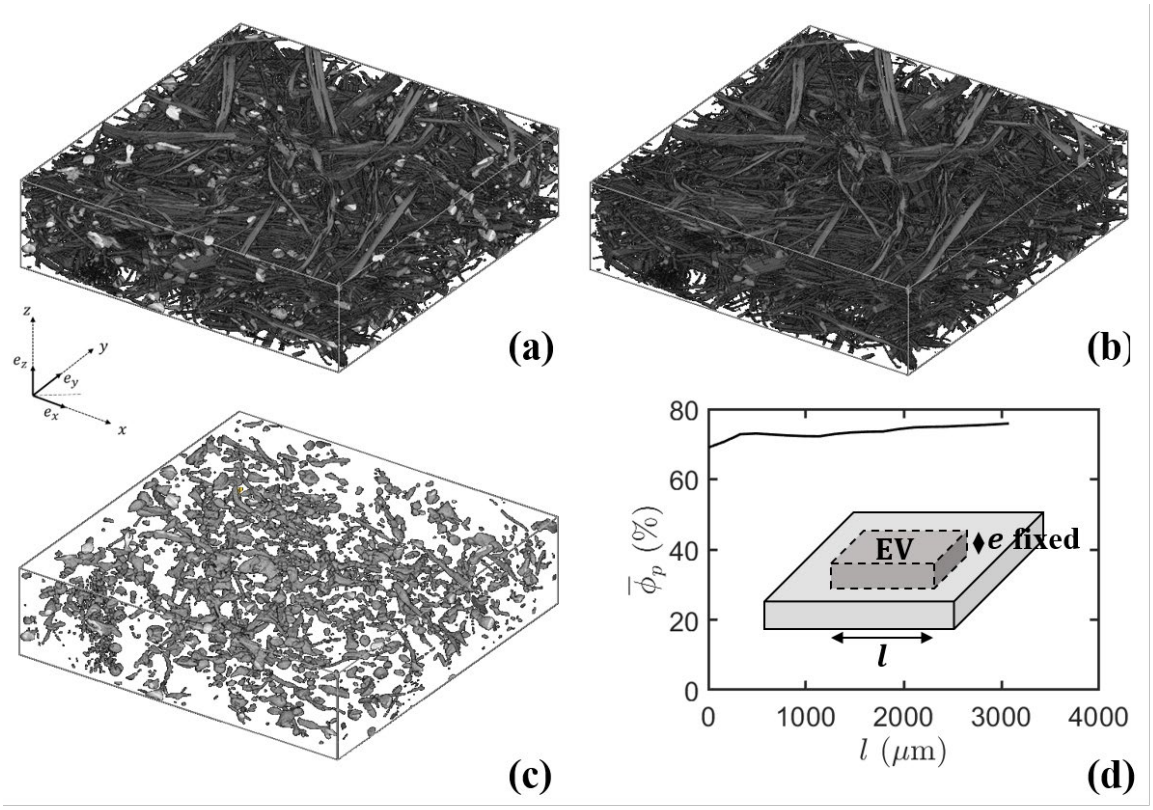

Figure 5.3. (a) Segmented X-ray microtomography image of mat M1 after pre-compression showing in grey levels both the flax fibre phase and the polypropylene phase (size of the 3D images: 3.1 × 3.1 × 0.8 mm^3). (b-c) Same images for the flax fibre and the polypropylene phases only. (d) Evolution of the mean pore volume fraction $\bar{\phi}_p$ as a function of the size of the in-plane length $\boldsymbol{l}$ of the ROI.

5.2.3.1 Volume fraction of pores

The local volume fraction of pores ϕ_p was calculated on each horizontal cross-section of the different 3D images obtained during compression (Figures 5.2A-D) by dividing the number of voxels of this phase by the total number of voxels of the treated image. Similarly, the volume fraction of pores $\bar{\phi}_p$ was calculated on the different 3D images obtained during compression (Figures 5.2A-D) from the number of voxels of this phase divided by the total number of voxels of the treated image. In order to check the relevance of the thresholding operation, $\bar{\phi}_p$ was also estimated theoretically from Eq. 5.2:

$$\bar{\phi}_p = 1 - \chi_f \frac{\rho_{mat}}{\rho_f} - \chi_{pp} \frac{\rho_{mat}}{\rho_{pp}} \tag{5.2}$$

where $\rho_{mat} = G/h$, $\rho_f = 1380$ kg m^{-3} and $\rho_{pp} = 910$ kg m^{-3} (Gurunathan et al., 2015) are the densities of the fibrous mat, flax fibres and polypropylene, respectively. The parameters $\chi_f = 90\%$ and $\chi_{pp} = 10\%$ are the mass ratios of flax fibres and polypropylene in the studied material, respectively.

5.2.3.2 Volumetric size distributions

The volumetric size distributions of the diameters d of flax fibres, solid phase (flax fibres plus melted polypropylene fibres) and pore sizes were estimated using the function 3D granulometry (Serra, 1982; Maire et al., 2007; Lux, Delisée, et al., 2006; Martoïa et al., 2017) implemented in the plugin Analysis 3D in Fiji (Boulos et al., 2012). These measurements were performed using octahedron structural elements (Martoïa et al., 2017).

5.2.3.3 Specific surface area S_v

A stereological technique (Underwood, 1969; Serra, 1982) based on the use of intercept lines was used to estimate the specific surface area S_v of the solid phase, i.e. flax fibre phase plus the polypropylene phase. The specific surface density was calculated as follows (Saltykov, 1958):

$$S_v = 2\overline{P_L} \tag{5.3}$$

where $\overline{P_L}$ is the mean number of intercepts per unit of intercept lines. $\overline{P_L}$ was calculated from the measurements of the number of intersection with the solid phase of 500 intercept lines the directions of which were randomly distributed in the orientation space and crossing at the center of the samples. For this number of intercept lines, the values of S_v was stabilized.

5.2.3.4 Directional tortuosities τ_{ii}

The directional tortuosities τ_{xx}, τ_{yy} and τ_{zz} of the pore phases of the studied mats were calculated along the directions $\boldsymbol{e_x}$, $\boldsymbol{e_y}$ and $\boldsymbol{e_z}$ of the 3D images, using the plugin Tortuosity (Roque & Costa, 2020) implemented in Fiji software. More details are given in Roque & Costa, 2020.

5.2.4 Permeability estimation using 3D images and CFD simulation

The components of the permeability tensor $\boldsymbol{K}$ of the mats M1 and M2 and the virtual fibrous mats that were numerically generated were calculated numerically using the CFD module FlowDict of the Finite Volume software GeoDict and the Explicit Jump-Stokes (EJ-Stokes) solver. Within this numerical package, the localization Stokes flow problems, deduced from the homogenization method with multiple scale asymptotic expansions (Auriault, 1991; Boutin, 2000; Idris et al., 2004), were solved within the pore phase of the 3D X-ray microtomography binarized images of the different fibrous materials (Figure 5.2). The local velocity field as well as the first-order pressure fluctuation field were considered as in-plane periodic. By imposing unit macroscale pressure successively along the directions $\boldsymbol{e}_x$, $\boldsymbol{e}_y$ and $\boldsymbol{e}_z$ and by solving the Stokes-like localization problem on the binarised 3D images and considering no-slip boundary conditions at the interface between the fluid domain and

the solid phases, it was possible to determine the components of the permeability tensor (Caglar et al., 2017; Rolland du Roscoat et al., 2008; Chalencon et al., 2016). More details about the numerical procedure are reported by Chalencon et al. (Chalencon et al., 2016). For illustration purpose, Figure 5.9a shows the norm of the stationary velocity field obtained by numerical simulation for a fluid flow along $\boldsymbol{e}_z$ direction through the mat M1 in its initial state. Using such approach, it can be inferred from the statistical analysis by Jeulin (Jeulin, 2012) that the relative error for the predicted components of the dimensionless permeability tensor (Table 5.1) is about 10% to 15%. The analysis by Jeulin relates the relative error of a property (e.g. the components of the permeability tensor) to the size of the volume used to calculate the property, the number of calculations and the evolution of the variance of the property with the size of the calculation volume. Decain (Decain, 2009) and Marulier (Marulier, 2013) used a similar approach for the predictions of the thermal and mechanical properties of cellule-based fibrous materials and confirmed the relevancy of this approach to estimate the relative error.

5.3 Results

5.3.1 Analysis of the microstructure of mat M1 under compression

5.3.1.1 Evolution of the pore volume fraction

Figure 5.4a shows the variation of the local volume fraction of pores ϕ_p along the thickness of the sample for the different stages of compression shown in Figure 5.2. This figure shows that the volume fraction of pores decreases with the increase in the compression loading and increases after unloading. However, in the initial state and during the deformation of the sample, the volume fraction of pores varies slightly along the thickness. After unloading, the volume fraction of pores is different from that in the initial state. This type of evolution of the microstructure has already been observed for other types of fibre reinforcements (Robitaille & Gauvin, 1999; Abdul Ghafour et al., 2019). Figure 5.4b shows that the mean value of the volume fraction of pores $\bar{\phi}_p$ calculated from the data shown in Figure 5.4a decreases with the increase in the compression strain ε_{zz}. These results also show a good agreement with the predictions of Eq. 5.2. This tends to show that the thresholding of the 3D images was accurate as well as the estimate of the pore volume fractions.

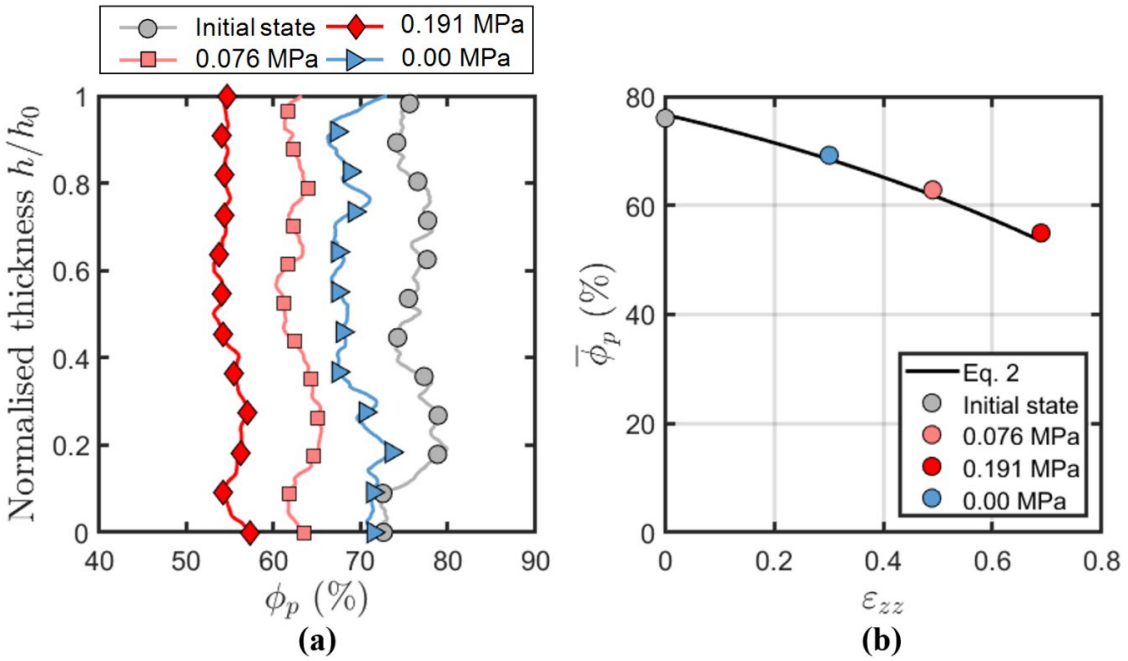

Figure 5.4. Mat M1 - (a) Variation of the local volume fraction of pores ϕ_p along the normalized thickness. (b) Evolution of the mean volume fraction of pores $\bar{\phi}_p$ as a function of the compressive strain ε_{zz}.

5.3.1.2 Evolution of the volumetric distributions of pore, fibre and solid phases

The evolution of the volumetric pore distributions reveals a decrease in the pore sizes and a decrease in the width of the distributions with the increase in the compressive strain ε_{zz}. (Figure 5.5a). This is further confirmed by the evolution of the mean value of the pore sizes, as shown in Figure 5.5d. This shows the densification of the mat M1 with the compression loading. In addition, the volumetric pore size distribution after unloading (stage D) do not superimpose to that of the initial state (stage A). This phenomenon has to be related to the aforementioned evolution of the porosity and is certainly due to rearrangements in the fibre network of mat M1. This is confirmed by the results shown in Figures 5.5b and 5.5d which reveal that both the volumetric fibre diameter distribution and the mean fibre diameter remain almost unchanged during compression. This tends to show that the fibre cross sections did not collapse during compression. Note also the mean value of flax fibre diameter $\bar{d}_f$ was around 28 µm, which is accordance with the observations made from SEM images (Figure 5.1). This value is also in agreement with those reported by several authors for elementary flax fibres (Baley & Bourmaud, 2014; Bourmaud et al., 2013). Similarly, the volumetric distributions that were measured on the solid phase did not vary significantly during the compression test (Figure 5.5c). As expected, the mean thickness of the solid phase (flax fibres plus melted polypropylene fibres) $\bar{d}_s$ was higher than $\bar{d}_f$, i.e. close to 40 µm.

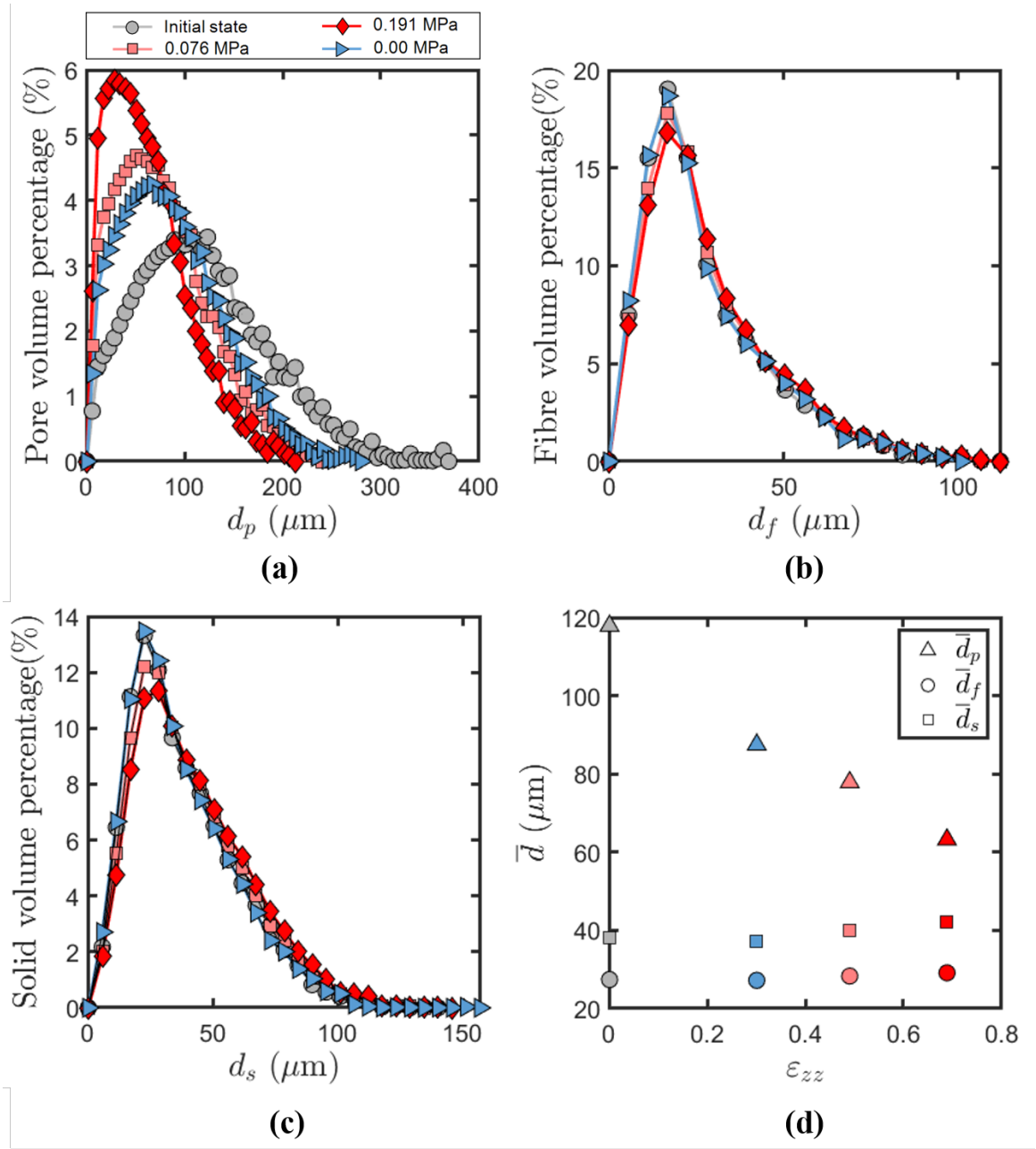

Figure 5.5. Mat 1 – Volumetric distributions of (a) the sizes of the pores d_p , (b) the diameters of flax fibres d_f and (c) the thicknesses of the solid phase (flax fibres plus melted polypropylene fibres) d_s. (d) Evolution of the mean size of pores $\bar{d}_p$, mean diameter of flax fibres $\bar{d}_f$ and mean thickness of the solid phase $\bar{d}_s$ as a function of the compressive strain ε_{zz}.

5.3.1.3 Specific surface area S_v

Figure 5.6 shows that the specific surface area S_v increases non-linearly with the increase in the solid phase volume fraction $\bar{\phi}_s$. The values for S_v are close to those reported for others types of fibrous materials with similar solid volume fractions $\bar{\phi}_s$ such as wood fibre mats (Delisée et al., 2010; Delisée et al., 2007) or papers (Rolland du Roscoat et al., 2007b). The increase of S_v can be explained by the compaction of the sample of mat M1 with the

compression loading. The compaction induces a decrease in the thickness h and in the volume of the sample, which results in a higher specific surface area. The compaction effect can be counterbalanced by the creation of new contacts between the fibres of the mat, thus decreasing the overall surface area of the solid phase. These two opposite effects could be at the origin of the slightly non-linear evolution of S_v with the volume fraction of the solid phase $\bar{\phi}_s$. The effects of possible rearrangement mechanisms is also visible in Figure 5.6 as the value of S_v after unloading (stage D) do not superimpose to that of the initial state (stage A).

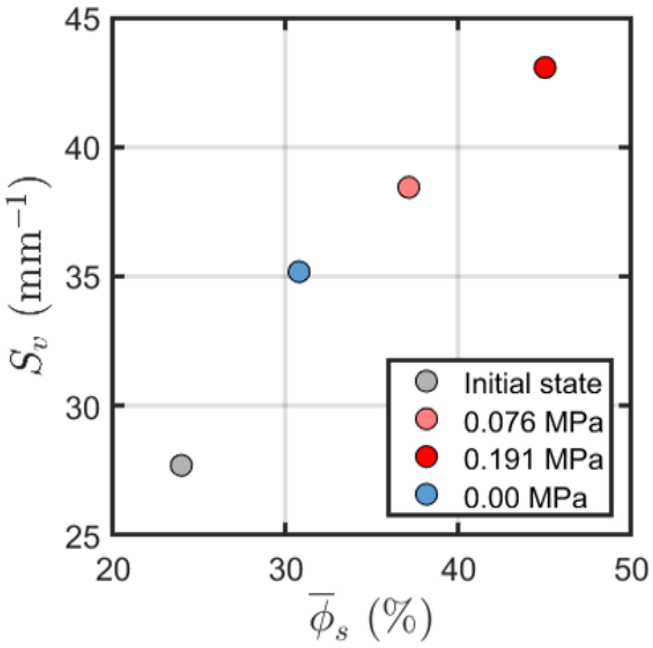

Figure 5.6. Evolution of the specific surface area of mat M1 as a function of the mean volume fraction of the solid phase $\bar{\phi}_s$.

5.3.1.4 Directional tortuosities τ_{xx}, τ_{yy} and τ_{zz}

Figure 5.7 shows that the directional tortuosities τ_{xx}, τ_{yy} *and* τ_{zz} increase with increasing the volume fraction of the solid phase ϕ_s, i.e. the paths followed by a particle in the pore phase from one side to the opposite side of the sample would become longer with the increase in the compaction. The out-of-plane tortuosity τ_{zz} is higher than the in-plane tortuosities τ_{xx} and τ_{yy}, regardless of the solid volume fraction ϕ_s. In addition, as $\tau_{xx} \approx \tau_{yy} \neq \tau_{zz}$, the tortuosity of mat M1 could be considered to exhibit transverse isotropy. Note that the orders of magnitude of the tortuosities τ_{xx}, τ_{yy} *and* τ_{zz} are in accordance with those reported by Peyrega and Jeulin (Peyrega & Jeulin, 2013) for similar fibrous materials with in-plane fibre orientation.

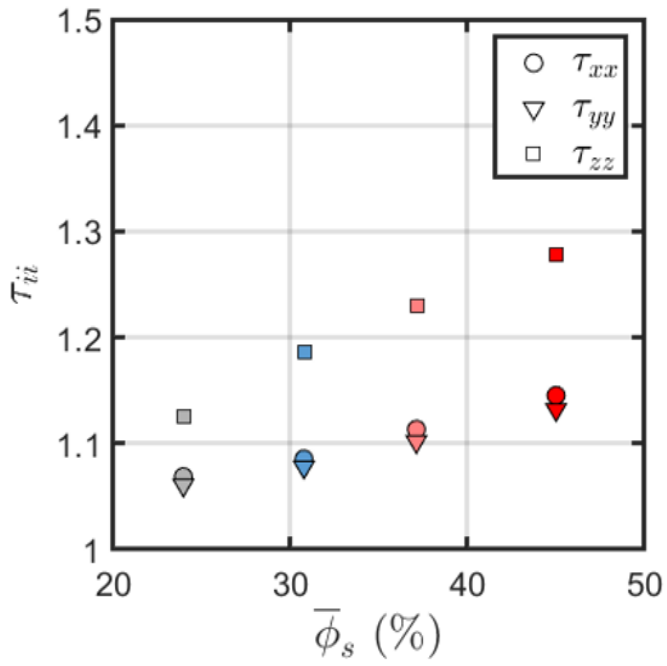

Figure 5.7. Evolution of the directional tortuosities τ_{xx}, τ_{yy} and τ_{zz} of mat M1 as a function of the solid volume fraction $\bar{\phi}_s$.

5.3.2 Numerical permeability estimates

Table 5.1 gives values of the components of the dimensionless permeability tensors ($\boldsymbol{K}^* = \frac{1}{\bar{r}_s^2}\boldsymbol{K}$, with $\bar{r}_s = \bar{d}_s/2 = 20$ µm, see Figure 5.5d) obtained by numerical simulation for the different compression stages of mat M1. The diagonal components of $\boldsymbol{K}^*$, i.e. K_{xx}^*, K_{yy}^* and K_{zz}^*, are greater of at least one order of magnitude than the non-diagonal components. The components K_{xx}^* and K_{yy}^* are also very close to each other regardless of the compression state. This tends to show that mat M1 initially exhibits transverse isotopy for the permeability and that the directions $\boldsymbol{e}_x$, $\boldsymbol{e}_y$ and $\boldsymbol{e}_z$ (Figure 5.2) are the principal directions of the permeability tensor. Note that the permeability components show a decrease with increasing the compression and that they tend to reach the same values for the highest compression level. In this case the permeability tensor is almost isotropic.

Table 5.1. Components of the dimensionless permeability tensor $\boldsymbol{K}^* = \frac{1}{\bar{r}_s^2}\boldsymbol{K}$ obtained for the mat M1 for the different compression stages in the $(\boldsymbol{e}_x, \boldsymbol{e}_y, \boldsymbol{e}_z)$ frame shown in Figure. 5.2.

	Dimensionless permeability tensors
Initial state (Fig. 5.2A)	$[\boldsymbol{K}^*] = \begin{bmatrix} 0.36 & 0.02 & -0.01 \\ 0.02 & 0.41 & 0.00 \\ -0.01 & 0.00 & 0.27 \end{bmatrix}_{(\boldsymbol{e}_x, \boldsymbol{e}_y, \boldsymbol{e}_z)}$
0.076 MPa (Fig. 5.2B)	$[\boldsymbol{K}^*] = \begin{bmatrix} 0.10 & 0.00 & 0.00 \\ 0.00 & 0.11 & 0.00 \\ 0.00 & 0.00 & 0.09 \end{bmatrix}_{(\boldsymbol{e}_x, \boldsymbol{e}_y, \boldsymbol{e}_z)}$
0.191 MPa (Fig. 5.2C)	$[\boldsymbol{K}^*] = \begin{bmatrix} 0.05 & 0.00 & 0.00 \\ 0.00 & 0.05 & 0.00 \\ 0.00 & 0.00 & 0.05 \end{bmatrix}_{(\boldsymbol{e}_x, \boldsymbol{e}_y, \boldsymbol{e}_z)}$
0.00 MPa (Fig. 5.2D)	$[\boldsymbol{K}^*] = \begin{bmatrix} 0.17 & 0.01 & 0.00 \\ 0.01 & 0.18 & 0.00 \\ 0.00 & 0.00 & 0.14 \end{bmatrix}_{(\boldsymbol{e}_x, \boldsymbol{e}_y, \boldsymbol{e}_z)}$

5.4 Discussion

5.4.1 Proposition of an anisotropic Kozeny-Carman permeability model

Based on the previous studies, devoted to the prediction of the permeability properties of fibrous materials with disordered fibrous architectures such as papers (Koponen et al., 1998), boards or reinforcement for composites made of discontinuous fibres (Delisée et al., 2010; Delisée et al., 2007; Soltani et al., 2015; Soltani et al., 2014; Soltani et al., 2017b), we propose the following adaptation of the Kozeny-Carman (KC) model for anisotropic porous materials, where the principal components of the dimensionless permeability tensor K_i^* are written as follows:

$$K_i^* = \frac{(1-\bar{\phi}_s)^3}{2c_i S_v^2 {\tau_i}^2} \frac{1}{\bar{r}_s^2} \tag{5.4}$$

with $i = I, II, III$ (no summation on i). In this expression, the terms c_i represent directional equivalent terms to the scalar parameter c of the classical KC model (cf. Eq. 5.1).

Following the approach proposed by Koponen et al. (Koponen et al., 1998), we propose to identify the components c_i using for that an inverse calculation method. This method consists in (i) generating a set of Representative Elementary Volumes (REV) of fibrous media with random in-plane fibre orientations and various fibre volume fractions $5\% < \bar{\phi}_s < 60\%$, (ii) calculating the principal components of the permeability tensor K_i^* of these REV's as well as (iii) the directional tortuosities τ_i in the anisotropy directions of the

permeability tensor, i.e. along $\boldsymbol{e}_x$, $\boldsymbol{e}_y$, $\boldsymbol{e}_z$ the principal orientation directions of the generated fibrous media (Figure 5.8), and the specific surface area S_v, adopting the same approach to that used for the mat M1. Finally, the directional components c_i were identified as a function of ϕ_s.

Figures 5.8a,b show that the dimensionless specific surface area $S_v^* = S_v\bar{r}_s$ and directional tortuosities τ_i of the numerically generated idealized fibrous mats are close to those measured for the mat M1. The dimensionless permeability components K_i^* (Fig. 5.8c) are in the same order of magnitude as those of the mat M1. These results tend to show that the generated REV's represent quite well the real microstructures of the flax fibre mats. Finally, using the data obtained for the numerically generated REV's, it was possible to identify the evolution of the in-plane and out-of-plane values c_i as a function of $\bar{\phi}_s$ (Figure 5.8d). The following empirical functions were determined by the least squares method to fit the values obtained for these components:

$$\begin{aligned} c_I(\bar{\phi}_s) = c_{II}(\bar{\phi}_s) &= -10\left(1 - e^{-\frac{\bar{\phi}_s}{0.07}}\right) + 11.55 \\ c_{III}(\bar{\phi}_s) &= -11\left(1 - e^{-\frac{\bar{\phi}_s}{0.07}}\right) + 12.9 \end{aligned} \tag{5.5}$$

The values of c_{III} that were calculated are close to that obtained by numerical simulation by Koponen et al. (Koponen et al., 1998) for generated paper networks with a fibre volume fraction $\bar{\phi}_s$ that ranges between 0.2 and 0.5 ($c_{III} \approx 2.8$). The slight difference is presumably due to the rectangular geometry of the cross section of the fibres of the networks considered by Koponen et al. (Koponen et al., 1998). Note also that these authors did not correct the values of c_{III} by accounting for the out-of-plane tortuosity τ_{III} of the networks.

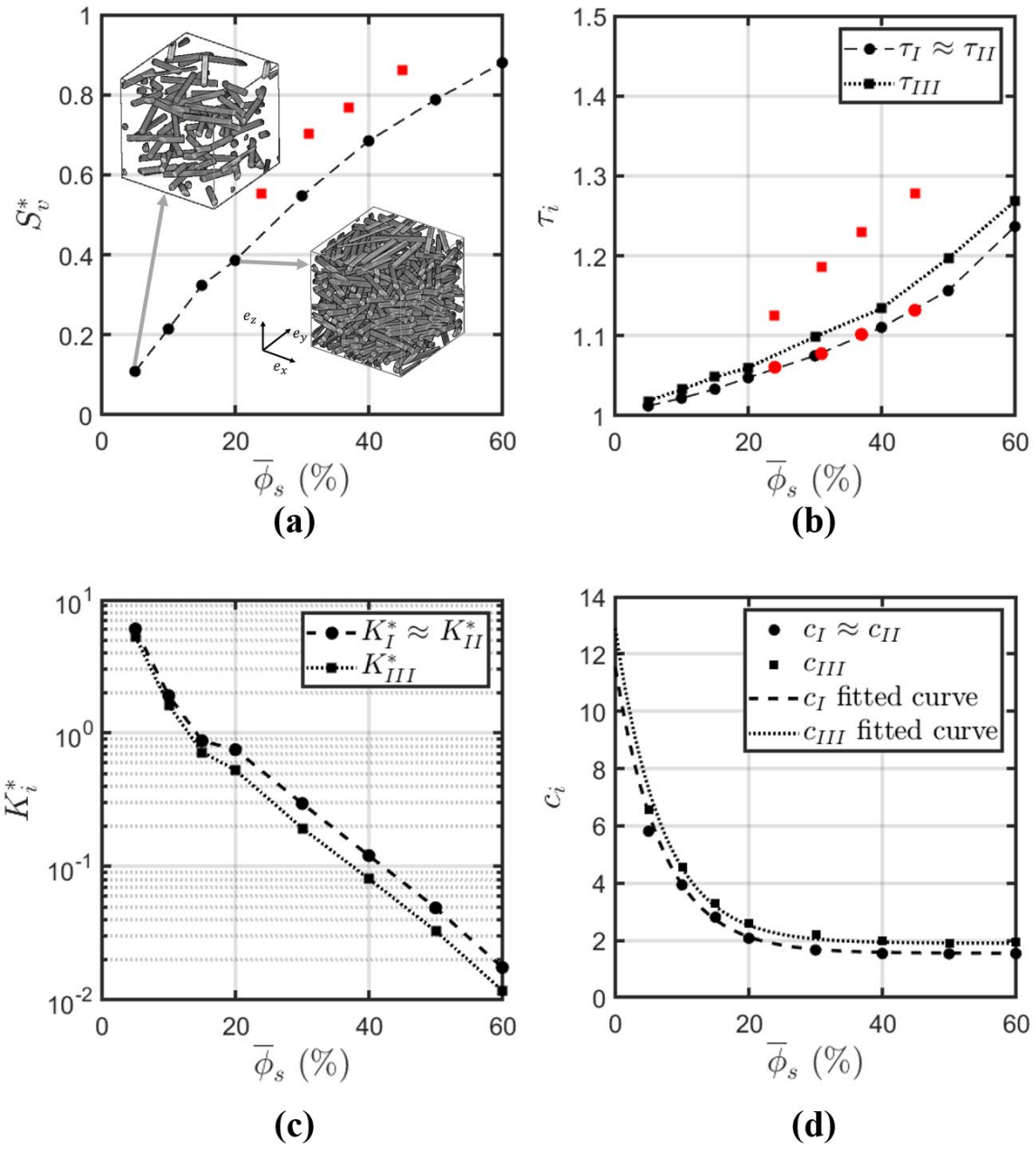

Figure 5.8. (a) Dimensionless specific surface area $S_v^* = S_v \bar{r}_s$, (b) directional tortuosities τ_i,(c) dimensionless permeability components K_i^* and (d) directional values c_i as a function of the solid volume fraction $\bar{\phi}_s$ obtained for the numerically generated REV's of fibrous media. Note that the REV's were generated numerically using the microstructure generator FiberGeo of software GeoDict which is based on a softcore approach. The calculations of the permeability components were performed using the module FlowDict of this software (as explained in section 5.2). For comparison purpose, the coloured symbols correspond to the values obtained for the mat M1.

5.4.2 Model predictions and validation

The principal components of the permeability tensors were estimated for the mat M1 using the modified KC model (Eq. 5.4) and the expressions of c_i obtained for the numerically generated REV's (Eqs. 5.5), whereas the specific surface area, directional tortuosities and the fibre volume fraction were obtained from the analysis carried out in Section 5.3. Figure 5.9b shows the principal components of the dimensionless permeability tensor obtained by the numerical simulation and the prediction of the modified KC model. The relative errors between the numerical values and the KC predictions are below approximately 18% for all the components K_I^*, K_{II}^* and K_{III}^*, (Figure 5.9c), which is fairly reasonable. Thus, both sets of values are in accordance regardless of the fibre volume fractions reached during the compression experiments.

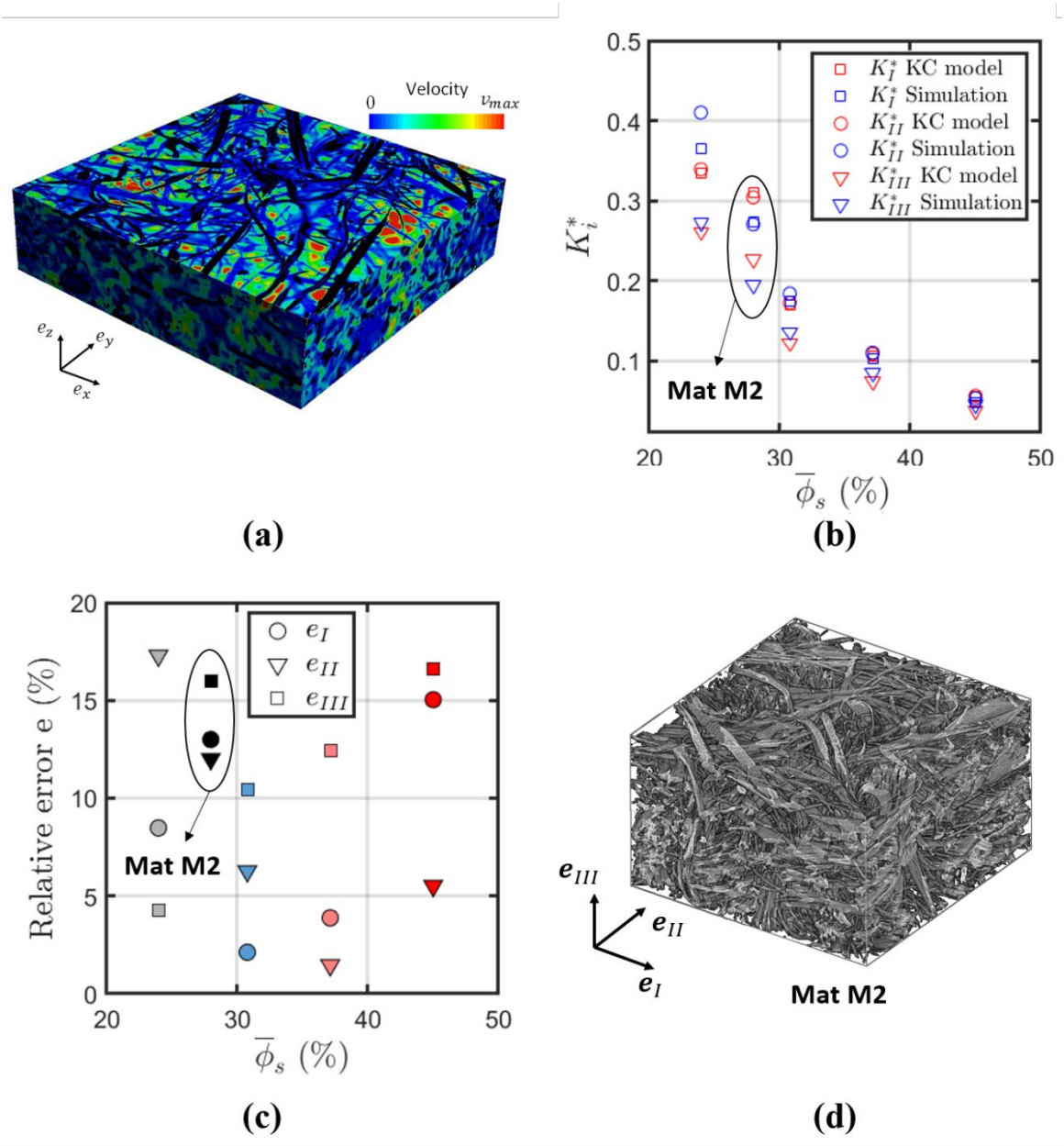

Figure 5.9 (a) Norm of the velocity field corresponding to a transverse fluid flow through the fibrous mat M1 in its initial state. (b) Dimensionless permeability

components: modified KC model and Geodict numerical simulation results. (c) Relative error between the numerical and theoretically estimated permeability components. (d) 3D microtomography images showing the fibrous microstructure of the mat M2(size of the 3D image: 3.3 × 3.3 × 2.0 mm^3).

Furthermore, the prediction of the modified KC model was tested for the mat M2 (Figures. 5.9b,c). This mat is only composed of flax fibres and is not thermolinked (Figure 5.9d). Using again 3D X-ray microtomography images (resolution: 6.5^3 μm^3, Tomcat beamline, Paul Scherrer Institute, Villigen, Switzerland), the following microstructural characteristics were determined: $\bar{\phi}_s = 0.28$, $S_v = 20.4\ mm^{-1}$, $\tau_I = 1.07$, $\tau_{II} = 1.08$, $\tau_{III} = 1.13$ and $\bar{d}_f = \bar{d}_s = 54\ \mu m$. Both the predictions of the modified KC model and the numerical predictions are in good agreement for this other type of flax fibre mat.

5.5 Conclusion

In situ out-of-plane compression tests were performed on a thermolinked flax fibre mat, using a micro-press installed on a synchrotron microtomography beamline. This technique allowed us to show that (i) the porous phase evolved significantly as shown by the measurements of the mean porosity, pore size distribution, and components of the directional tortuosities (ii) the cross sections of the flax fibres remained almost unchanged, (iii) and the specific surface area increased with increasing the compaction. The changes of the porous phase are not totally reversible as shown by the analysis of the unloading stage. The 3D images were also used as input data to numerically calculate the principal components of the permeability tensor of the studied fibrous mats and their evolution during compression. The simulation results showed that the permeability is transversely isotropic with principal axes that did not evolve during compression.

In parallel, a modified Kozeny-Carman model taking into account the transverse anisotropy of the permeability tensor was proposed. This model accounts for parameters such as the fibre volume fraction, specific surface area, directional tortuosities and several directional terms c_i that are related to the heterogeneity and the variations in the porous anisotropic structure that induce fluid flow perturbation. All parameters of this model could be identified from the analysis of 3D images, except the in-plane and out-of-plane values c_i. To identify them a set of fibrous mats were numerically generated for a wide range of fibre volume fractions $\bar{\phi}_s$. Expressions of the in-plane and out-of-plane values c_i were proposed as a function of the fibre volume fraction $\bar{\phi}_s$. The permeability values obtained by this model were consistent with those obtained by numerical simulation for all the investigated compression state of the thermolinked flax fibre mat. This model also allowed a good prediction of the permeability of another type of mat with a different fibrous architecture and only composed of flax fibres using 3D images acquired at lower spatial resolution.

This study shows that using 3D X-ray microtomography images, it is possible to identify nearly all the parameters of a Kozeny-Carman-like permeability model well adapted for

materials that exhibit disordered fibrous microstructure with varying size and shape of the fibre elements and consequently a complex porous architecture for which microstructure models for, e.g. the surface specific area do not exist. It would be interesting to test this model for a larger set of fibrous mats subjected to various deformation modes such as those encountered in composite forming processes.

References

Abdul Ghafour, T., Colmars, J., & Boisse, P. (2019). The importance of taking into account behavior irreversibilities when simulating the forming of textile composite reinforcements. *Composites Part A: Applied Science and Manufacturing*, *127*, 105641. https://doi.org/10.1016/j.compositesa.2019.105641

Ali, M. A., Umer, R., Khan, K. A., & Cantwell, W. J. (2019). Application of X-ray computed tomography for the virtual permeability prediction of fiber reinforcements for liquid composite molding processes : A review. *Composites Science and Technology*, *184*, 107828.

Auriault, J. L. (1991). Heterogeneous medium. Is an equivalent macroscopic description possible? *International Journal of Engineering Science*, *29*(7), 785-795. https://doi.org/10.1016/0020-7225(91)90001-J

Baley, C., & Bourmaud, A. (2014). Average tensile properties of French elementary flax fibers. *Materials Letters*, *122*, 159-161. https://doi.org/10.1016/j.matlet.2014.02.030

Baley, C., Gomina, M., Breard, J., Bourmaud, A., Drapier, S., Ferreira, M., Le Duigou, A., Liotier, P. J., Ouagne, P., Soulat, D., & Davies, P. (2019). Specific features of flax fibres used to manufacture composite materials. *International Journal of Material Forming*, *12*(6), 1023-1052. https://doi.org/10.1007/s12289-018-1455-y

Beltran, M. A., Paganin, D. M., Uesugi, K., & Kitchen, M. J. (2010). 2D and 3D X-ray phase retrieval of multi-material objects using a single defocus distance. *Optics Express*, *18*(7), 6423-6436. https://doi.org/10.1364/OE.18.006423

Binetruy, C., Hilaire, B., & Pabiot, J. (1998). Tow Impregnation Model and Void Formation Mechanisms during RTM. *Journal of Composite Materials*, *32*(3), 223-245. https://doi.org/10.1177/002199839803200302

Bizet, L., Ouagne, P., Bréard, J., Baley, C., Jernot, J.-P., & Gomina, M. (2008). Transverse permeability and kozeny constant in flax fiber mats preforms. *FPCM-9 (2008) The 9th International Conference on Flow Processes in Composite Materials*.

Boulos, V., Fristot, V., Houzet, D., Salvo, L., & Lhuissier, P. (2012). Investigating performance variations of an optimized GPU-ported granulometry algorithm. *Proceedings of the 2012 Conference on Design and Architectures for Signal and Image Processing*, 1-6.

Bourmaud, A., Beaugrand, J., Shah, D. U., Placet, V., & Baley, C. (2018). Towards the design of high-performance plant fibre composites. *Progress in Materials Science*, *97*, 347-408. https://doi.org/10.1016/j.pmatsci.2018.05.005

Bourmaud, A., Morvan, C., Bouali, A., Placet, V., Perré, P., & Baley, C. (2013). Relationships between micro-fibrillar angle, mechanical properties and biochemical

composition of flax fibers. *Industrial Crops and Products*, *44*, 343-351. https://doi.org/10.1016/j.indcrop.2012.11.031

Bourmaud, A., Shah, D. U., Beaugrand, J., & Dhakal, H. N. (2020). Property changes in plant fibres during the processing of bio-based composites. *Industrial Crops and Products*, *154*, 112705. https://doi.org/10.1016/j.indcrop.2020.112705

Boutin, C. (2000). Study of permeability by periodic and self-consistent homogenisation. *European Journal of Mechanics - A/Solids*, *19*(4), 603-632. https://doi.org/10.1016/S0997-7538(00)00174-1

Bréard, J., Henzel, Y., Trochu, F., & Gauvin, R. (2003). Analysis of dynamic flows through porous media. Part I : Comparison between saturated and unsaturated flows in fibrous reinforcements. *Polymer Composites*, *24*(3), 391-408. https://doi.org/10.1002/pc.10038

Caglar, B., Orgéas, L., Rolland du Roscoat, S., Sozer, E. M., & Michaud, V. (2017). Permeability of textile fabrics with spherical inclusions. *Composites Part A: Applied Science and Manufacturing*, *99*, 1-14. https://doi.org/10.1016/j.compositesa.2017.03.031

Carman, P. C. (1956). *Flow of gases through porous media*.

Chalencon, F., Dumont, P. J. J., Orgéas, L., Foray, G., Cavaillé, J.-Y., & Maire, E. (2016). Homogeneous and heterogeneous rheology and flow-induced microstructures of a fresh fiber-reinforced mortar. *Cement and Concrete Research*, *82*, 130-141. https://doi.org/10.1016/j.cemconres.2015.12.012

Chen, X., & Papathanasiou, T. D. (2006). On the variability of the Kozeny constant for saturated flow across unidirectional disordered fiber arrays. *Composites Part A: Applied Science and Manufacturing*, *37*(6), 836-846.

Dumont P.J.J., Orgéas L., Martoïa F., Budtova T., Vincent, M., 5 Mise en œuvre des composites à fibres lignocellulosiques. In: Composites polymères et fibres lignocellulosiques. Ed. Berzin F., Lavoisier, Paris, 20162

Decain, M. (2009). *Contribution à l'étude des relations microstructures : Propriétés thermiques et d'écoulement pour les matériaux fibreux cellulosiques* [PhD Thesis]. Grenoble INPG.

Delisée, C., Lux, J., & Malvestio, J. (2010). 3D Morphology and Permeability of Highly Porous Cellulosic Fibrous Material. *Transport in Porous Media*, *83*(3), 623-636. https://doi.org/10.1007/s11242-009-9464-4

Delisée, C., Malvestio, J., Lux, J., Castéra, P., Chaunier, L., & Chrusciel, L. (2007). Microstructure et propriétés de transport de matériaux isolants à base de fibres cellulosiques. *Annales du Bâtiment et des travaux publics*, *5*, 23.

Dixit, S., Goel, R., Dubey, A., Shivhare, P. R., & Bhalavi, T. (2017). Natural Fibre Reinforced Polymer Composite Materials - A Review. *Polymers from Renewable Resources*, *8*(2), 71-78. https://doi.org/10.1177/204124791700800203

Faruk, O., & Sain, M. (2014). *Biofiber Reinforcements in Composite Materials*. Elsevier.

Francucci, G., Rodríguez, E. S., & Vázquez, A. (2010). Study of saturated and unsaturated permeability in natural fiber fabrics. *Composites Part A: Applied Science and Manufacturing*, *41*(1), 16-21. https://doi.org/10.1016/j.compositesa.2009.07.012

Francucci, G., Rodríguez, E. S., & Vázquez, A. (2012). Experimental study of the compaction response of jute fabrics in liquid composite molding processes. *Journal of Composite Materials*, *46*(2), 155-167. https://doi.org/10.1177/0021998311410484

Gnaba, I., Omrani, F., Wang, P., Soulat, D., Ferreira, M., Vroman, P., & Jaouachi, B. (2019). Mechanical behavior of flax/polypropylene commingled nonwoven at dry scale : Influence of process parameters. *Textile Research Journal*, *89*(5), 791-800. https://doi.org/10.1177/0040517518755789

Gnaba, I., Wang, P., Soulat, D., Omrani, F., Ferreira, M., & Vroman, P. (2019). Investigation about the Effect of Manufacturing Parameters on the Mechanical Behaviour of Natural Fibre Nonwovens Reinforced Thermoplastic Composites. *Materials*, *12*(16), 2560. https://doi.org/10.3390/ma12162560

Gurunathan, T., Mohanty, S., & Nayak, S. K. (2015). A review of the recent developments in biocomposites based on natural fibres and their application perspectives. *Composites Part A: Applied Science and Manufacturing*, *77*, 1-25. https://doi.org/10.1016/j.compositesa.2015.06.007

Hamdi, S. E., Delisée, C., Malvestio, J., Da Silva, N., Le Duc, A., & Beaugrand, J. (2015). X-ray computed microtomography and 2D image analysis for morphological characterization of short lignocellulosic fibers raw materials : A benchmark survey. *Composites Part A: Applied Science and Manufacturing*, *76*, 1-9.

Ho, M., Wang, H., Lee, J.-H., Ho, C., Lau, K., Leng, J., & Hui, D. (2012). Critical factors on manufacturing processes of natural fibre composites. *Composites Part B: Engineering*, *43*(8), 3549-3562. https://doi.org/10.1016/j.compositesb.2011.10.001

Idris, Z., Orgéas, L., Geindreau, C., Bloch, J.-F., & Auriault, J.-L. (2004). Microstructural effects on the flow law of power-law fluids through fibrous media. *Modelling and Simulation in Materials Science and Engineering*, *12*(5), 995-1015. https://doi.org/10.1088/0965-0393/12/5/016

Jeulin, D. (2012). Morphology and effective properties of multi-scale random sets : A review. *Comptes Rendus Mécanique*, *340*(4-5), 219-229.

Joffre, T., Girlanda, O., Forsberg, F., Sahlén, F., Sjödahl, M., & Gamstedt, E. K. (2015). A 3D in-situ investigation of the deformation in compressive loading in the thickness direction of cellulose fiber mats. *Cellulose*, *22*(5), 2993-3001. https://doi.org/10.1007/s10570-015-0727-7

Koponen, A., Kandhai, D., Hellén, E., Alava, M., Hoekstra, A., Kataja, M., Niskanen, K., Sloot, P., & Timonen, J. (1998). Permeability of Three-Dimensional Random Fiber Webs. *Physical Review Letters*, *80*(4), 716-719. https://doi.org/10.1103/PhysRevLett.80.716

Kozeny, J. (1927). Uber kapillare leitung der wasser in boden. *Royal Academy of Science, Vienna, Proc. Class I*, *136*, 271-306.

Kuentzer, N., Simacek, P., Advani, S. G., & Walsh, S. (2007). Correlation of void distribution to VARTM manufacturing techniques. *Composites Part A: Applied Science and Manufacturing*, *38*(3), 802-813. https://doi.org/10.1016/j.compositesa.2006.08.005

Latil, P., Orgéas, L., Geindreau, C., Dumont, P. J. J., & Rolland du Roscoat, S. (2011). Towards the 3D in situ characterisation of deformation micro-mechanisms within a compressed bundle of fibres. *Composites Science and Technology*, *71*(4), 480-488. https://doi.org/10.1016/j.compscitech.2010.12.023

Laurencin, T., Orgéas, L., Dumont, P. J. J., Rolland du Roscoat, S., Laure, P., Le Corre, S., Silva, L., Mokso, R., & Terrien, M. (2016). 3D real-time and in situ characterisation of fibre kinematics in dilute non-Newtonian fibre suspensions during confined and lubricated compression flow. *Composites Science and Technology*, *134*, 258-266. https://doi.org/10.1016/j.compscitech.2016.09.004

Liu, H. L., & Hwang, W. R. (2012). Permeability prediction of fibrous porous media with complex 3D architectures. *Composites Part A: Applied Science and Manufacturing*, *43*(11), 2030-2038.

Loix, F., Badel, P., Orgéas, L., Geindreau, C., & Boisse, P. (2008). Woven fabric permeability : From textile deformation to fluid flow mesoscale simulations. *Composites Science and Technology*, *68*(7), 1624-1630. https://doi.org/10.1016/j.compscitech.2008.02.027

Lundquist, L., Willi, F., Leterrier, Y., & Maanson, J.-A. (2004). Compression behavior of pulp fiber networks. *Polymer Engineering & Science*, *44*(1), 45-55.

Lux, J., Ahmadi, A., Gobbé, C., & Delisée, C. (2006). Macroscopic thermal properties of real fibrous materials : Volume averaging method and 3D image analysis. *International Journal of Heat and Mass Transfer*, *49*(11), 1958-1973. https://doi.org/10.1016/j.ijheatmasstransfer.2005.09.038

Lux, J., Delisée, C., & Thibault, X. (2006). 3d characterization of wood based fibrous materials : an application. *Image Analysis & Stereology*, *25*(1), 25-35. https://doi.org/10.5566/ias.v25.p25-35

Maire, E., Colombo, P., Adrien, J., Babout, L., & Biasetto, L. (2007). Characterization of the morphology of cellular ceramics by 3D image processing of X-ray tomography. *Journal of the European Ceramic Society*, *27*(4), 1973-1981. https://doi.org/10.1016/j.jeurceramsoc.2006.05.097

Maity, S., Gon, D. P., & Paul, P. (2014). A Review of Flax Nonwovens : Manufacturing, Properties, and Applications. *Journal of Natural Fibers*, *11*(4), 365-390. https://doi.org/10.1080/15440478.2013.861781

Martin, N., Davies, P., & Baley, C. (2016). Evaluation of the potential of three non-woven flax fiber reinforcements : Spunlaced, needlepunched and paper process mats. *Industrial Crops and Products*, *83*, 194-205. https://doi.org/10.1016/j.indcrop.2015.10.008

Martoïa, F., Cochereau, T., Dumont, P. J. J., Orgéas, L., Terrien, M., & Belgacem, M. N. (2016). Cellulose nanofibril foams : Links between ice-templating conditions, microstructures and mechanical properties. *Materials & Design*, *104*, 376-391. https://doi.org/10.1016/j.matdes.2016.04.088

Martoïa, F., Orgéas, L., Dumont, P. J. J., Bloch, J.-F., Flin, F., & Viguié, J. (2017). Crumpled paper sheets : Low-cost biobased cellular materials for structural applications. *Materials & Design*, *136*, 150-164. https://doi.org/10.1016/j.matdes.2017.09.031

Marulier, C. (2013). *Etudes multi-échelles des couplages entre les propriétés hygroélastiques des papiers et leur microstructure* [PhD Thesis]. Grenoble.

Marulier, C., Dumont, P. J. J., Orgéas, L., Rolland du Roscoat, S., & Caillerie, D. (2015). 3D analysis of paper microstructures at the scale of fibres and bonds. *Cellulose*, *22*(3), 1517-1539. https://doi.org/10.1007/s10570-015-0610-6

Masoodi, R., Pillai, K. M., Grahl, N., & Tan, H. (2012). Numerical simulation of LCM mold-filling during the manufacture of natural fiber composites. *Journal of Reinforced Plastics and Composites*, *31*(6), 363-378. https://doi.org/10.1177/0731684412438629

May, D., Aktas, A., Advani, S. G., Berg, D. C., Endruweit, A., Fauster, E., Lomov, S. V., Long, A., Mitschang, P., & Abaimov, S. (2019). In-plane permeability characterization of engineering textiles based on radial flow experiments : A benchmark exercise. *Composites Part A: Applied Science and Manufacturing*, *121*, 100-114.

Mehdikhani, M., Gorbatikh, L., Verpoest, I., & Lomov, S. V. (2019). Voids in fiber-reinforced polymer composites : A review on their formation, characteristics, and effects on mechanical performance. *Journal of Composite Materials*, *53*(12), 1579-1669. https://doi.org/10.1177/0021998318772152

Müssig, J., & Haag, K. (2015). The use of flax fibres as reinforcements in composites. In O. Faruk & M. Sain (Éds.), *Biofiber Reinforcements in Composite Materials* (p. 35-85). Woodhead Publishing. https://doi.org/10.1533/9781782421276.1.35

Nguyen, V. H., Deléglise-Lagardère, M., & Park, C. H. (2015). Modeling of resin flow in natural fiber reinforcement for liquid composite molding processes. *Composites Science and Technology*, *113*, 38-45. https://doi.org/10.1016/j.compscitech.2015.03.016

Omrani, F., Soulat, D., Ferreira, M., & Wang, P. (2019). Effects of needle punching process and structural parameters on mechanical behavior of flax nonwovens preforms. *Advances in Aircraft and Spacecraft Science*, *6*(2), 157-168.

Omrani, F., Wang, P., Soulat, D., Ferreira, M., & Ouagne, P. (2017). Analysis of the deformability of flax-fibre nonwoven fabrics during manufacturing. *Composites Part B: Engineering*, *116*, 471-485. https://doi.org/10.1016/j.compositesb.2016.11.003

Ouagne, P., Soulat, D., Evon, P., Renouard, S., Ferreira, M., Labonne, L., Labanieh, A. R., Laine, E., & De Luycker, E. (2020). Use of bast fibres including flax fibres for high challenge technical textile applications. Extraction, preparation and requirements for the manufacturing of composite reinforcement fabrics and for geotextiles. In R. M. Kozłowski & M. Mackiewicz-Talarczyk (Éds.), *Handbook of Natural Fibres (Second Edition)* (p. 169-204). Woodhead Publishing. https://doi.org/10.1016/B978-0-12-818782-1.00005-5

Ouagne, P., Soulat, D., Moothoo, J., Capelle, E., & Gueret, S. (2013). Complex shape forming of a flax woven fabric; analysis of the tow buckling and misalignment defect. *Composites Part A: Applied Science and Manufacturing*, *51*, 1-10. https://doi.org/10.1016/j.compositesa.2013.03.017

Ozgumus, T., Mobedi, M., & Ozkol, U. (2014). Determination of Kozeny constant based on porosity and pore to throat size ratio in porous medium with rectangular rods. *Engineering Applications of Computational Fluid Mechanics*, *8*(2), 308-318.

Paganin, D., Mayo, S. C., Gureyev, T. E., Miller, P. R., & Wilkins, S. W. (2002). Simultaneous phase and amplitude extraction from a single defocused image of a homogeneous object. *Journal of Microscopy*, *206*(1), 33-40. https://doi.org/10.1046/j.1365-2818.2002.01010.x

Pantaloni, D., Bourmaud, A., Baley, C., Clifford, M. J., Ramage, M. H., & Shah, D. U. (2020). A Review of Permeability and Flow Simulation for Liquid Composite

Moulding of Plant Fibre Composites. *Materials*, *13*(21), 4811. https://doi.org/10.3390/ma13214811

Peyrega, C., & Jeulin, D. (2013). Estimation of tortuosity and reconstruction of geodesic paths in 3D. *Image Analysis and Stereology*, *32*(1), 27-43.

Ramesh, M., Deepa, C., Kumar, L. R., Sanjay, M., & Siengchin, S. (2020). Life-cycle and environmental impact assessments on processing of plant fibres and its bio-composites : A critical review. *Journal of Industrial Textiles*, 1528083720924730. https://doi.org/10.1177/1528083720924730

Robitaille, F., & Gauvin, R. (1999). Compaction of textile reinforcements for composites manufacturing. III : Reorganization of the fiber network. *Polymer Composites*, *20*(1), 48-61. https://doi.org/10.1002/pc.10334

Rodriguez, E., Giacomelli, F., & Vazquez, A. (2004). Permeability-porosity relationship in RTM for different fiberglass and natural reinforcements. *Journal of composite materials*, *38*(3), 259-268.

Rolland du Roscoat, S., Decain, M., Geindreau, C., Thibault, X., & Bloch, J.-F. (2008). Microstructural Analysis of Paper Using Synchrotron X-ray Microtomography : Numerical Estimation of the Permeability and Effective Thermal Conductivity. *Appita : Technology, Innovation, Manufacturing, Environment*. https://search.informit.org/doi/abs/10.3316/INFORMIT.187944502104494

Rolland du Roscoat, S., Decain, M., Thibault, X., Geindreau, C., & Bloch, J.-F. (2007a). Estimation of microstructural properties from synchrotron X-ray microtomography and determination of the REV in paper materials. *Acta Materialia*, *55*(8), 2841-2850. https://doi.org/10.1016/j.actamat.2006.11.050

Rolland du Roscoat, S., Decain, M., Thibault, X., Geindreau, C., & Bloch, J.-F. (2007b). Estimation of microstructural properties from synchrotron X-ray microtomography and determination of the REV in paper materials. *Acta Materialia*, *55*(8), 2841-2850. https://doi.org/10.1016/j.actamat.2006.11.050

Roque, W. L., & Costa, R. R. A. (2020). A plugin for computing the pore/grain network tortuosity of a porous medium from 2D/3D MicroCT image. *Applied Computing and Geosciences*, *5*, 100019. https://doi.org/10.1016/j.acags.2020.100019

Saltykov, S. A. (1958). *Stereometric metallography* (Metallurgizdat, Moscow).

Schneider, C. A., Rasband, W. S., & Eliceiri, K. W. (2012). NIH Image to ImageJ : 25 years of image analysis. *Nature Methods*, *9*(7), 671-675. https://doi.org/10.1038/nmeth.2089

Schulz, R., Ray, N., Zech, S., Rupp, A., & Knabner, P. (2019). Beyond Kozeny–Carman : Predicting the permeability in porous media. *Transport in Porous Media*, *130*(2), 487-512.

Sentis, D. F., Orgéas, L., Dumont, P. J., Du Roscoat, S. R., Sager, M., & Latil, P. (2017). 3D in situ observations of the compressibility and pore transport in Sheet Moulding Compounds during the early stages of compression moulding. *Composites Part A: Applied Science and Manufacturing*, *92*, 51-61.

Serra, J. (1982). *Image analysis and mathematical morphology.* (London: Academic Press). Academic press.

Shah, D. U. (2013a). Developing plant fibre composites for structural applications by optimising composite parameters : A critical review. *J Mater Sci*, *48*(18), 6083-6107. https://doi.org/10.1007/s10853-013-7458-7

Shah, D. U. (2013b). Developing plant fibre composites for structural applications by optimising composite parameters : A critical review. *Journal of Materials Science*, *48*(18), 6083-6107. https://doi.org/10.1007/s10853-013-7458-7

Soltani, P., Johari, M. S., & Zarrebini, M. (2014). Effect of 3D fiber orientation on permeability of realistic fibrous porous networks. *Powder Technology*, *254*, 44-56. https://doi.org/10.1016/j.powtec.2014.01.001

Soltani, P., Johari, M. S., & Zarrebini, M. (2015). Tomography-based determination of transverse permeability in fibrous porous media. *Journal of Industrial Textiles*, *44*(5), 738-756. https://doi.org/10.1177/1528083713512357

Soltani, P., Zarrebini, M., Laghaei, R., & Hassanpour, A. (2017a). Prediction of permeability of realistic and virtual layered nonwovens using combined application of X-ray μCT and computer simulation. *Chemical Engineering Research and Design*, *124*, 299-312. https://doi.org/10.1016/j.cherd.2017.06.035

Soltani, P., Zarrebini, M., Laghaei, R., & Hassanpour, A. (2017b). Prediction of permeability of realistic and virtual layered nonwovens using combined application of X-ray μCT and computer simulation. *Chemical Engineering Research and Design*, *124*, 299-312. https://doi.org/10.1016/j.cherd.2017.06.035

Umer, R., Bickerton, S., & Fernyhough, A. (2007). Characterising wood fibre mats as reinforcements for liquid composite moulding processes. *Composites Part A: Applied Science and Manufacturing*, *38*(2), 434-448.

Umer, R., Bickerton, S., & Fernyhough, A. (2011). The effect of yarn length and diameter on permeability and compaction response of flax fibre mats. *Composites Part A: Applied Science and Manufacturing*, *42*(7), 723-732. https://doi.org/10.1016/j.compositesa.2011.02.010

Underwood, E. E. (1969). Stereology, or the quantitative evaluation of microstructures. *Journal of Microscopy*, *89*(2), 161-180. https://doi.org/10.1111/j.1365-2818.1969.tb00663.x

Viguié, J., Latil, P., Orgéas, L., Dumont, P. J. J., Rolland du Roscoat, S., Bloch, J.-F., Marulier, C., & Guiraud, O. (2013). Finding fibres and their contacts within 3D images of disordered fibrous media. *Composites Science and Technology*, *89*, 202-210. https://doi.org/10.1016/j.compscitech.2013.09.023

Xue, D., Miao, M., & Hu, H. (2011). Permeability anisotropy of flax nonwoven mats in vacuum-assisted resin transfer molding. *The Journal of The Textile Institute*, *102*(7), 612-620. https://doi.org/10.1080/00405000.2010.504566

Chapter 6

A simple analytical permeability model for fibre networks with disordered architectures

Abstract

Several fibre reinforcements used in the composite domain can be seen as anisotropic porous and fibrous materials showing a disordered fibre architecture with varying fibre volume fractions, fibre spatial and orientation distributions, geometries of fibres. Several permeability models have been established for specific fibre networks, e.g. ordered fibre arrangements with varying fibre volume fractions. However, simple permeability models that account for the variations in fibre orientation distributions would be crucial to optimise the impregnation phase of fibre reinforcements during their processing. For that purpose, a simple analytical and tensorial model was proposed and identified. Its robustness was assessed with respect to permeability estimates obtained by CFD simulation on a large set of numerically generated virtual fibre networks exhibiting various fibre volume fractions ($0.01 < \phi_s <0.45$), fibre aspect ratios ($2< l/d < 30$), and fibre orientation distributions (unidirectional, 2D planar isotropic, 2D oriented, 3D isotropic orientations) as well as on 3D images of real fibre networks. The model was able to reproduce the overall evolution of the principal components of the permeability tensor with those of the second-order orientation tensor of the virtual and real fibre networks. Some limitations of the model were identified and some enhancements were proposed.

6.1 Introduction

Viscous flow through fibrous media is a problem of long-standing interest in engineering due to its importance in the manufacturing and processing industries. For instance, the study of flow through fibrous media is crucial to optimise the impregnation phase occurring in many composite forming processes such as, for instance, liquid composite molding (LCM), pultrusion, and autoclave processes (Advani & Sozer, 2002; Advani & Hsiao, 2012). The flow of polymer resin through anisotropic fibrous reinforcements is usually modelled using Darcy's law (Darcy, 1856), which is, strictly speaking, valid for the laminar flow of incompressible Newtonian fluids through rigid porous media. In Darcy's law, the fluid velocity is linked to the pressure gradient through the fluid viscosity and the permeability tensor $\boldsymbol{K}$. Theoretical, numerical and experimental works have shown that the components of the permeability tensor $\boldsymbol{K}$ depends on several descriptors of the microstructure of fibrous networks (Jackson & James, 1986; Bergelin, 1952; Kirsch & Fuchs, 1968; Bechtold & Ye, 2003; Idris et al., 2004). Its components are known to be non-linear functions of the fibre volume fraction ϕ_s (Jackson & James, 1986), and the geometry of fibres (shape of cross sections, aspect ratio, fibre curvature) (Nabovati, Llewellin & Sousa, 2009; Wang et al., 2007). The permeability is also known to depend on the fibre spatial (Bechtold and Ye, 2003; Schell et al., 2007) and orientation (Stylianopoulos et al., 2008; Pradhan et al., 2012; Soltani et al., 2014a; Soltani et al., 2017; Tamayol & Bahrami, 2011; Tahir & Vahedi Tafreshi, 2009) distributions.

Several theoretical models were developed for the prediction of the components of the permeability tensor $\boldsymbol{K}$ of porous fibrous networks. For instance, the well-known Kozeny-

Carman (KC) model (Kozeny, 1927; Carman, 1956) originally developed for isotropic porous media was adapted to anisotropic fibre reinforcements (Koponen et al., 1998; Chen and Papathanasiou, 2006; Liu & Hwang, 2012; Bizet et al., 2008). This model (Kozeny, 1927; Carman, 1956) relates the components of the permeability tensor to the porosity, specific surface area, tortuosity of the fibre networks. It also includes a phenomenological parameter usually denoted c. This parameter is associated to the coupling between the fluid flow perturbation and the fibrous microstructure. It was also shown to depend on the fibre volume fraction (Koponen et al., 1998), fibre network architecture on the flow direction with respect to the network anisotropy axes (Ali et al., 2019). Even though the Kozeny-Carman is an efficient permeability model, the determination of microstructure descriptors such as specific surface area, tortuosity and parameter c is difficult to be determined for fibre reinforcement materials. This hinders the use of KC model for this type of anisotropic porous materials that exhibit a wide diversity of structural properties.

Other types of models were developed for the prediction of the permeability of well-controlled arrangements of infinite fibres. In these approaches, the permeability components of arrays of infinite fibres are deduced from the resolution of the Stokes flow problem using, for instance, the lubrication approximation (Batchelor & Batchelor, 2000; Keller, 1964; Gebart, 1992; Bruschke & Advani, 1993) or by estimating the drag force exerted on the fibres in a fluid flow using a cell model idealisation (Happel, 1959; Kuwabara, 1959; Happel & Brenner, 1983). For parallel fibres arrays (or UD) with controlled fibre spatial distributions, e.g. square, triangular, hexagonal, several theoretical analytical expressions for the longitudinal and transverse permeabilities were thus derived (Gebart, 1992; Bruschke & Advani, 1993; Happel, 1959; Drummond & Tahir, 1984; Berdichevsky & Cai, 1993; Tamayol & Bahrami, 2009).

In addition, some of these approaches were extended for the modelling of the out-of-plane permeability of planar (2D) isotropic networks (Davies, 1973; Spielman & Goren, 1968; Tomadakis & Robertson, 2005) as well as the permeability of 3D isotropic networks (Spielman & Goren, 1968; Jackson & James, 1982; Tomadakis & Robertson, 2005). The relevance of these models was assessed experimentally and numerically using CFD results. These results show the predictions of these models are relevant for well-controlled fibre networks such as UD fibre networks with varying fibre volume fractions. However, these models are not able to accurately predict all the components of the permeability tensor for reinforcement materials that exhibit disordered architectures and fibres with complex geometries (Soltani et al., 2014b; Soltani et al.,2015; Delisée et al., 2010; Delisée et al., 2007).

In this context, the objective of this study was to propose an original analytical model for the prediction of the components of the permeability tensor $\boldsymbol{K}$ of fibre networks that exhibit varying fibre orientation distributions, including UD, 2D planar isotropic, 3D isotropic fibre orientation as well as other orientation cases such as UD with slight fibre misalignment and 2D with privileged in-plane fibre orientation. This model was built within the framework of the homogenisation with multiple scale asymptotic expansions (Auriault, 1991). Using simplifying assumptions on the fibre cross section geometry and

on the viscous drag force exerted by the fluid on the fibre, it was possible to derive generic analytical expressions for the permeability tensor as a function of the second-order fibre orientation and cross section orientation tensors weighted by two permeability coefficients. In the case of straight fibres with circular cross sections, these two coefficients that represent the longitudinal and transverse permeabilities of networks made of parallel fibres were identified using literature analytical models. The predictions of the model were compared with some numerical permeability results that were obtained using numerically-generated virtual fibrous media or real fibrous networks exhibiting various fibrous architectures. This approach allowed discussing the relevance of the proposed permeability model and identifying its limitations as well as some enhancement strategies.

6.2 Theoretical background

6.2.1 Homogenisation problem

We consider the flow of a fluid through a fibrous medium of volume V, the domain of which is defined by Ω. This domain contains a solid phase of volume V_s and a porous phase of volume V_p that occupy the domains Ω_s and Ω_p, respectively, such that $\Omega = \Omega_s \cup \Omega_p$. The fluid is assumed to be an incompressible Newtonian fluid with a viscosity μ. The porous domain is assumed to be fully saturated by the fluid. The solid phase is constituted of slender fibres: the length of each fibre i is l_i and the volume of each fibre V_i is large compared to the typical length of its cross section d_i, *i.e.* $\lambda_i = l_i/2r_i$. The interface between the fluid-solid phase is defined by Γ. The volume fractions of pores and fibres are $\phi_p = V_p/V$ and $\phi_s = 1 - \phi_p$, respectively.
The fluid flow through the fibrous medium is governed at the microscale by the Navier-Stokes equations:

$$\begin{cases} \mu\, \boldsymbol{\nabla}^2 \boldsymbol{v} = \boldsymbol{\nabla} p & \text{in } \Omega_p \\ \boldsymbol{\nabla} \cdot \boldsymbol{v} = 0 & \text{in } \Omega_p \\ \boldsymbol{v} = 0 & \text{on } \Gamma \end{cases} \tag{6.1}$$

where $\boldsymbol{v}$ and p are the local velocity and pressure of the fluid, respectively.

Using the homogenisation with multiple scale asymptotic expansions (Auriault, 1991), it was shown that the above boundary value problem yields at the first order to the Darcy's law at the macroscale (Boutin, 2000; Auriault, 2002; Auriault, 2005; Orgéas et al., 2006):

$$\begin{gathered} \boldsymbol{\nabla} \overline{p} = -\mu\, \boldsymbol{K}^{-1} \overline{\boldsymbol{v}} \\ \nabla \cdot \overline{\boldsymbol{v}} = 0 \end{gathered} \tag{6.2}$$

where $\overline{\boldsymbol{v}}$ is the macroscopic velocity:

$$\overline{\boldsymbol{v}} = \frac{1}{V} \int \boldsymbol{v}'\, dV \tag{6.3}$$

and $\overline{p}$ is the mean macroscale pressure:

$$\overline{p} = \frac{1}{V}\int p'\, dV \tag{6.4}$$

and $\boldsymbol{K}$ is the symmetric permeability tensor and $\boldsymbol{v'}$ and p' are the first order terms of the asymptotic expansion of $\boldsymbol{v}$ and p, respectively. Under these conditions, the velocity field $\boldsymbol{v'}$ is a linear function of the given constant macroscale pressure gradient $\boldsymbol{\nabla}\overline{p}$ so:

$$\boldsymbol{v'} = -\frac{1}{\mu}\boldsymbol{k}\cdot\boldsymbol{\nabla}\overline{p} \tag{6.5}$$

where $\boldsymbol{k}$ is the symmetric localisation tensor. Thus, for a given pressure gradient $\boldsymbol{\nabla}\overline{p}$, the localisation problem can be solved numerically or analytically, with a set of simplifying assumptions as described below, to estimate the permeability tensor (Boutin, 2000; Auriault, 2002; Auriault, 2005; Orgéas et al., 2006):

$$\boldsymbol{K} = \frac{1}{V}\int \boldsymbol{k}\, dV \tag{6.6}$$

Based on these assumptions, we propose an analytical solution to estimate the permeability tensor $\boldsymbol{K}$ for fibre networks with disordered architectures.

6.2.2 A simple analytical expression of *K*

The right hand side of Darcy's law (Eq. 6.2) represents an overall volumetric viscous drag force $\boldsymbol{f}_d$ exerted by the fibres, with a drag tensor equal to $\mu\boldsymbol{K}^{-1}$. This drag force is balanced by the sum of elementary forces $\delta\boldsymbol{f}_j^i$ exerted on the elementary segment j ($1 \le j \le N_i$) of length δl_j^i of the fibre i ($1 \le i \le N$) contained in a Representative Elementary Volume of the fibre porous network:

$$\boldsymbol{f}_d = \mu\boldsymbol{K}^{-1}\cdot\overline{\boldsymbol{v}} = \frac{1}{V}\sum_{i=1}^{N}\sum_{j=1}^{N_i}\delta\boldsymbol{f}_j^i \tag{6.7}$$

The properties of the Darcy's law (Eq. 6.2) and the local velocity field (Eq. 6.5) show that the elementary force $\delta\boldsymbol{f}_j^i$ is a linear function of the macroscopic velocity $\overline{\boldsymbol{v}}$:

$$\delta\boldsymbol{f}_j^i = \mu\boldsymbol{\Lambda}_j^i\cdot\overline{\boldsymbol{v}} \tag{6.8}$$

where $\mu\boldsymbol{\Lambda}_j^i$ is the elementary drag tensor of the segment j of the fibre i. Finally, the relation between $\boldsymbol{K}^{-1}$ and $\boldsymbol{\Lambda}_j^i$ writes:

$$\boldsymbol{K^{-1}} = \frac{1}{V}\sum_{i=1}^{N}\sum_{j=1}^{N_i}\boldsymbol{\Lambda}_j^i = \frac{1}{V}\sum_{k=1}^{M}\boldsymbol{\Lambda}_k \tag{6.9}$$

where M is the total number of fibre segments in the REV.

The local resistance tensor $\boldsymbol{\Lambda}_k$ depends on the geometry of the local cross section of the considered fibre segment and on the fibres surrounding the fibre segment δl_j^i, thus the local fibre content, spatial location and orientation.

6.2.3 Analytical estimates of the local resistance tensor

The fluid flow problem is linear, thus the most general form of $\boldsymbol{\Lambda}_k$ can be written as follows:

$$\boldsymbol{\Lambda}_k = \lambda_{Lk}\boldsymbol{t}_k\otimes\boldsymbol{t}_k + \lambda_{T1k}\,\boldsymbol{m}_k\otimes\boldsymbol{m}_k + \lambda_{T2k}\,\boldsymbol{n}_k\otimes\boldsymbol{n}_k \tag{6.10}$$

where $\boldsymbol{t}_k$ is a unit orientation vector of fibre segment k. The vectors $\boldsymbol{m}_k$ and $\boldsymbol{n}_k = \boldsymbol{t}_k \times \boldsymbol{m}_k$ are the two orthogonal orientation unit vectors to the vector $\boldsymbol{t}_k$. The parameters λ_{Lk}, λ_{T1k} and λ_{T2k} are drag resistance coefficients along the longitudinal direction and along the two transverse directions to the fibre segment axis, respectively. Introducing equation 6.10 in 6.9, the general expression of the tensor $\boldsymbol{K^{-1}}$ is written as follows:

$$\boldsymbol{K}^{-1} = \frac{1}{V}\sum_{k=1}^{M}(\lambda_{Lk}\boldsymbol{t}_k\otimes\boldsymbol{t}_k + \lambda_{T1k}\,\boldsymbol{m}_k\otimes\boldsymbol{m}_k + \lambda_{T2k}\,\boldsymbol{n}_k\otimes\boldsymbol{n}_k) \tag{6.11}$$

The aforementioned expressions have been established without any simplifying assumptions. However, theses expressions can be further simplified by accounting for the following assumptions:

i. All fibres and fibre segments exhibit the same transverse geometrical properties;
ii. Fibres are sufficiently slender in order to neglect edge effects on the local fluid flow;
iii. Contacts between fibres are sufficiently small so that they do not alter the local fluid flow;
iv. The resistance coefficients are not altered by the local fibre orientations.

Under these assumptions, the resistance coefficients can be considered as constant parameters: $\lambda_{Lk} = \lambda_L$, $\lambda_{T1k} = \lambda_{T1}$, and $\lambda_{T2k} = \lambda_{T2}$. Hence, the expression 6.11 can be simplified as follows:

$$\boldsymbol{K}^{-1} = \frac{\phi_s}{V_{seg}}(\lambda_L\boldsymbol{A} + \lambda_{T1}\,\boldsymbol{B} + \lambda_{T2}(\boldsymbol{I} - \boldsymbol{A} - \boldsymbol{B})) \tag{6.12}$$

where V_{seg} is the volume of an elementary fibre segment, ϕ_s the volume fraction of fibre segments, $\boldsymbol{A}$ the second order fibre segments orientation tensor, $\boldsymbol{B}$ the cross section orientation tensor, and $\boldsymbol{I}$ the unit tensor. The tensors $\boldsymbol{A}$ and $\boldsymbol{B}$ can be written as:

$$\boldsymbol{A} = \frac{1}{M}\sum_{k=1}^{M}\boldsymbol{t}_k\otimes\boldsymbol{t}_k \tag{6.13}$$

$$\boldsymbol{B} = \frac{1}{M}\sum_{k=1}^{M} \boldsymbol{m}_k \otimes \boldsymbol{m}_k \tag{6.14}$$

Hence, the expression 6.12 can also be written as:

$$\boldsymbol{K}^{-1} = \frac{1}{k_L}\boldsymbol{A} + \frac{1}{k_{T1}}\boldsymbol{B} + \frac{1}{k_{T2}}(\boldsymbol{I} - \boldsymbol{A} - \boldsymbol{B}) \tag{6.15}$$

where $\frac{1}{k_L} = \frac{\phi_s}{V_{seg}}\lambda_L$, $\frac{1}{k_{T1}} = \frac{\phi_s}{V_{seg}}\lambda_{T1}$, $\frac{1}{k_{T2}} = \frac{\phi_s}{V_{seg}}\lambda_{T2}$. The coefficients k_L,k_{T1} and k_{T2} correspond to the longitudinal and transverse components of the permeability tensor $\boldsymbol{K}$ of a network made of fibre segments that are all aligned along one given direction, *e.g.* the $\boldsymbol{e}_1$direction and so $\boldsymbol{t}_k = \boldsymbol{e}_1$.

In addition, if the cross sections of the fibre segments are circular, the local resistance tensor $\boldsymbol{\Lambda}_k$ is transverse isotropic with $\lambda_{T1} = \lambda_{T2} = \lambda_T$ and its expression can be simplified as:

$$\boldsymbol{\Lambda}_k = \lambda_L \boldsymbol{t}_k \otimes \boldsymbol{t}_k + \lambda_T(\boldsymbol{I} - \boldsymbol{t}_k \otimes \boldsymbol{t}_k) \tag{6.16}$$

which leads from equation 6.15 to:

$$\boldsymbol{K}^{-1} = \frac{1}{k_L}\boldsymbol{A} + \frac{1}{k_T}(\boldsymbol{I} - \boldsymbol{A}) \tag{6.17}$$

In this approach, the permeability tensor $\boldsymbol{K}$ of any fibre networks depends on the permeability coefficients k_L, k_T and the overall orientation of fibre segments as represented through the tensors $\boldsymbol{A}$ and $\boldsymbol{B}$. Note that the tensor $\boldsymbol{K}$ also depends on the fibre volume fraction ϕ_s and the fibre geometry since k_L and k_T are functions of these parameters (Gebart, 1992; Bruschke and Advani, 1993; Happel, 1959; Drummond and Tahir, 1984; Berdichevsky and Cai, 1993; Tamayol and Bahrami, 2009).

In the following of this study, we chose to extend the analysis to virtual fibre networks made up of straight fibres with circular cross section. Thus, each fibre of the network can be seen as constituted of a single segment. To obtain a full analytical expression of the transverse isotropic permeability model (Eq. 6.17), the coefficients k_L, k_T were identified as the longitudinal and transversal permeability coefficients of networks made of parallel and straight fibres with infinite length, using analytical expressions from the literature. We chose to consider that fibres were straight cylinders of radius r and were organised in the form of triangular arrays. Consequently, the model proposed by Drummond and Tahir (Drummond and Tahir, 1984) was used for the dimensionless permeability coefficient k_L^* defined as:

$$k_L^* = \frac{k_L}{r^2} = \frac{1}{4\phi_s}\left(-\ln(\phi_s) - 1.498 + 2\phi_s - \frac{{\phi_s}^2}{2} + O({\phi_s}^6)\right) \tag{6.18}$$

The so-called hybrid model of Bruschke and Advani (Bruschke and Advani, 1993) was used for the dimensionless permeability coefficient k_T^*:

$$k_T^* = \frac{k_T}{r^2} = \xi_1 k_{lub}^* + \xi_2 k_{cell}^* \tag{6.19}$$

with

$$k_{lub}^* = \frac{k_{lub}}{r^2} = \frac{1}{3\sqrt{3}} \frac{(1-\Phi)^2}{\Phi^{3/2}} \left(3\sqrt{\Phi} \frac{\tan^{-1}\left(\sqrt{\frac{1+\sqrt{\Phi}}{1-\sqrt{\Phi}}}\right)}{\sqrt{1-\Phi}} + \frac{\Phi}{2} + 1 \right)^{-1} \tag{6.20}$$

and

$$k_{cell}^* = \frac{k_{cell}}{r^2} = \frac{1}{8\phi_s} \left(-\ln \phi_s - \frac{3}{2} + 2\phi_s - \frac{\phi_s^2}{2} \right) \tag{6.21}$$

where $\xi_1 = 1 - e^{\alpha\left(\frac{\Phi}{\Phi-1}\right)}$, $\xi_2 = 1 - e^{\alpha((\Phi-1)/\Phi)}$, $\alpha = 0.528$ and $\Phi = \pi\phi_s/(2\sqrt{3})$. These models are known to give good predictions for a wide range of fibre volume fractions, *i.e.*, $0 < \phi_s \leq 0.8$ (Tamayol and Bahrami, 2011; Jackson and James, 1986).

6.3 Experimental and numerical procedures

The relevance of the aforementioned analytical model (Eq. 6.17) was assessed using different types of numerically generated fibrous networks with various fibre volume fractions, aspect ratios, fibre orientations and spatial arrangements. The relevance of the model was also assessed using real fibrous networks made of various types of fibres (e.g., synthetic and natural fibres) and fibre architectures. The permeability tensor $\boldsymbol{K}$ of the virtual and real fibre networks was obtained through numerical calculations performed on 3D images of the considered fibrous networks.

6.3.1 Numerically generated virtual fibrous networks

The virtual fibrous networks were generated using the FiberGeo module of Geodict software. In the Geodict software, the unit-cells are generated using a voxel-based method. In this approach, each voxel in the domain is assigned to be either "empty" or "filled", thus representing the fluid and fibre domains, respectively. Several types of fibre networks were generated, varying some parameters such as the fibre geometry (aspect ratios $\frac{l}{2r} = 2, 5, 10$ and 30, with l the fibre length and r the fibre radius), volume fractions $\phi_s =$ 0.01 , 0.05, 0.10 and 0.15, overall fibre orientation (unidirectional (UD), planar (2D isotropic and 2D oriented), 3D isotropic fibre orientations) and spatial distributions (triangular arrays of

parallel fibres, random and dispersed fibre spatial distributions). All the fibres are represented as straight cylinders. An isolation distance of 2 voxels between the fibres was systematically imposed to avoid fibre interpenetration, regardless of the architectures of the networks. Besides, an isolation distance between the fibres' centres of gravity was controlled to obtain dispersed or random fibre spatial distributions. Increasing the controlled distance enabled avoiding fibre clusters which are characteristic of random spatial fibre distributions (Sampson, 2008). The overall fibre orientations of the networks were controlled by two anisotropy parameters of the FiberGeo module. These parameters are given in Table 6.1, as well as the types of generated fibrous networks.

Table 6.1. Types of generated virtual fibrous structures.

1st FiberGeo parameter	2nd FiberGeo parameter	Types of structure
1	1	3D isotropic fibre orientation
10^{9}	1	Planar isotropic fibre orientation in plane (x, y)
1	10^{-9}	Planar isotropic fibre orientation in plane (x, z)
10^{-9}	10^{9}	Planar isotropic fibre orientation in plane (y, z)
10^{9}	10^{-9}	UD with fibres aligned in the x direction
1	10^{9}	2D oriented with fibres mainly aligned in the y direction
10^{9}	10^{9}	UD with fibres aligned in the y direction
10^{-9}	1	2D oriented with fibres aligned in the z direction
10^{-9}	10^{-9}	UD with fibres aligned in the z direction

The second-order orientation tensor $\boldsymbol{A}$ was calculated for each network by determining the unit orientation vector $\boldsymbol{n}_i$ of each fibre i of the networks as follows (Advani & Tucker, 1987):

$$\boldsymbol{A} = \frac{1}{N}\sum_{i=1}^{N} \boldsymbol{n}_i \otimes \boldsymbol{n}_i \tag{6.22}$$

where N is the total number of fibres.

Twenty fibre networks were generated for each fibre arrangement. It was chosen to create a large number of networks for a given fibre architecture since the generated fibre networks for a given type of fibre orientation and spatial distributions could vary slightly. Furthermore, the ratios between the fibre radius and the overall dimensions of the disordered fibre networks were large enough to allow a good scale separation, thereby

allowing these networks to be considered as representative elementary volumes (REV's) (Sampson, 2008).

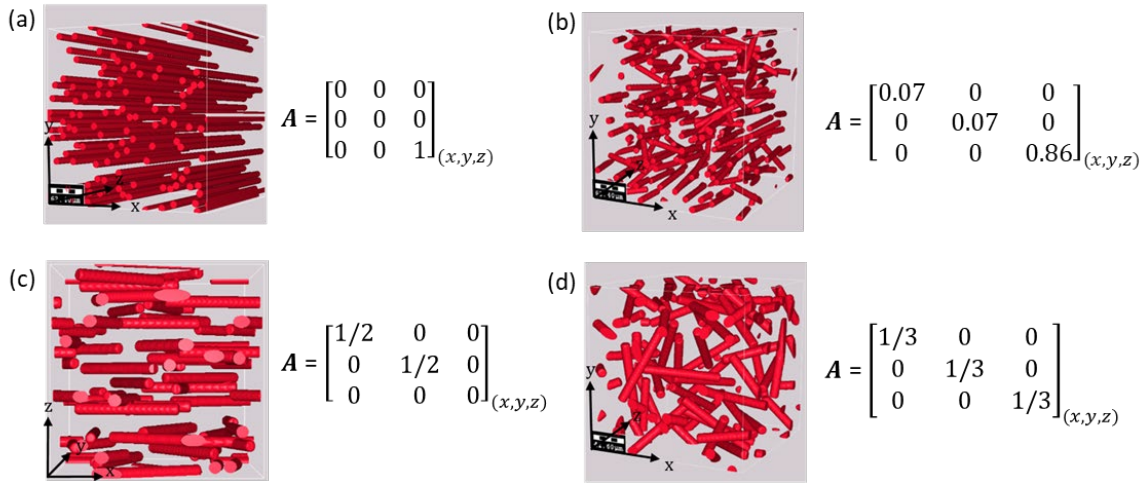

Figure 6.1. Examples of virtual fibrous networks generated numerically. (a) Network of aligned fibres with random spatial fibre distribution. (b) Fibre networks showing a preferential fibre alignment along the z axis. (c) Network with a planar isotropic fibre orientation in the plane(x, y). (d) Network with 3D isotropic fibre orientation.

6.3.2 Real fibrous networks

3D images of different types of real fibrous networks were also studied. These 3D images were obtained using synchrotron X-ray microtomography. These fibrous networks are briefly described below:

- One copper fibre network was studied. It exhibits a preferential in-plane fibre orientation. The fibres of this network are almost perfectly cylindrical and thus allow testing the model for fibres with regular cross section (Figure 6.2a). The imaging conditions used to obtain 3D images of this network are reported by Orgéas et al. (Orgéas et al., 2012).
- One unidirectional flax fibre network (Figure 6.2b). The 3D images of these materials were acquired on a synchrotron microtomograph (Tomcat beamline, Paul Scherrer Institute, Villigen, Switzerland). The X-ray energy and the number of radiographs were set to 30 keV and 2500, respectively. A voxel size of 0.81 µm^3 was used.
- One thermolinked mat made of flax fibres (90%wt) and melted polypropylene (10%wt). This mat was subjected to an out-of-plane compaction (states 1 and 2) during X-ray microtomography imaging experiments (acquisition parameters: 20 keV, 2000 radiographs, voxel size of 2.83 µm^3) performed on the ID19 beamline of the ESRF (Grenoble, France). This mat exhibit nearly planar random fibre orientation (Figure 6.2c).

All these images were segmented manually using the Threshold function of Fiji software (Schneider, Rasband and Eliceiri, 2012) which enabled calculating the fibre/solid volume fraction ϕ_s using a voxel counting method (Doube et al., 2010). The volumetric size distributions of the radii of the solid phase was obtained using the function 3D granulometry of the plugin Analysis 3D (Boulos et al., 2012) implemented in Fiji. These measurements were done with octahedron structural elements. From the obtained size distributions, it was possible to estimate the mean radius r of the solid phase (Martoïa et al., 2017). The second-order fibre orientation tensor $\boldsymbol{A}$ (Advani & Tucker, 1987) was estimated using the specially developed image analysis procedure reported by Bailly et al. (Bailly et al., 2018). The microstructure descriptors obtained for all the aforementioned networks are given in Table 6.2. Note that the size of these 3D images was large enough so that they can be considered as REV's of the studied materials.

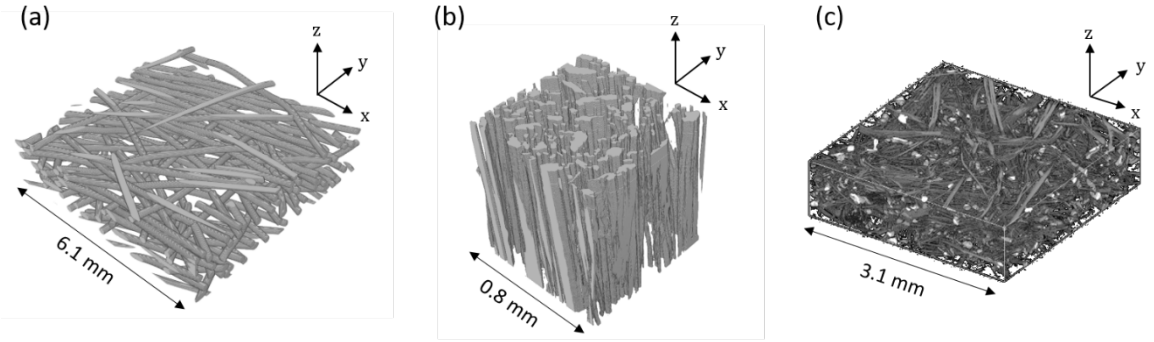

Figure 6.2. Examples of 3D images of the real fibrous materials obtained using X-ray microtomography. (a) 2D copper fibrous network with preferential in-plane fibre orientation (Orgéas et al., 2012). (b) Unidirectional flax fibre network. (c) Thermolinked flax fibre mat in its undeformed state (state 1).

Table 6.2. Microstructure parameters of the real fibrous networks.

	ϕ_s	$2r$ (μm)	$\boldsymbol{A}$
2D copper fibrous network with preferential in-plane fibre orientation	0.17	260	$\begin{bmatrix} 0.28 & 0 & 0 \\ 0 & 0.7 & 0 \\ 0 & 0 & 0.02 \end{bmatrix}_{(x,y,z)}$
Unidirectional flax fibre network	0.28	30	$\begin{bmatrix} 0 & 0 & 0 \\ 0 & 0 & 0 \\ 0 & 0 & \approx 1 \end{bmatrix}_{(x,y,z)}$
Flax fibre mat – State 1	0.24	38	$\begin{bmatrix} 0.48 & 0 & 0 \\ 0 & 0.45 & 0 \\ 0 & 0 & 0.07 \end{bmatrix}_{(x,y,z)}$
Flax fibre mat – State 2	0.37	40	$\begin{bmatrix} 0.48 & 0 & 0 \\ 0 & 0.46 & 0 \\ 0 & 0 & 0.06 \end{bmatrix}_{(x,y,z)}$

6.3.3 Numerical permeability estimation

The permeability of the virtual and real fibrous networks was estimated numerically using the finite volume software GeoDict and the CFD module FlowDict. This code enables solving the localization Stokes flow problems, deduced from the homogenization method with multiple scale asymptotic expansions (Eq. 6.2) within the pore phase of the 3D binarized images of the studied fibrous networks. The local velocity field and the first-order pressure fluctuation field are considered as in-plane periodic and the macroscale pressure-gradient is imposed (Caglar et al., 2017; Chalencon et al., 2016; Rolland du Roscoat et al., 2008). For the virtual fibre networks, a voxel size equal to 0.5^3 µm^3 was chosen to obtain an accurate description of the fibrous networks. The so-called convergence parameter of FlowDict was also chosen to be 0.001, which allowed minimizing the calculation time and the error made on the permeability estimation. This choice was based on a study conducted on networks with cylindrical and parallel fibres with an infinite length and well-ordered fibre arrangements (e.g., triangular, square fibre arrangements) with a low, resp. $\phi_s = 0.05$, and high fibre volume fractions, resp. $\phi_s = 0.35$, for which analytical estimates of the transverse and longitudinal permeability coefficients exist (Drummond & Tahir, 1984; Bruschke & Advani, 1993).

6.4 Results

6.4.1 Model predictions for numerically generated fibrous networks with various fibre orientations

Figure 6.3 shows the evolution of the components K_i^* of the dimensionless permeability tensor $\boldsymbol{K}^* = \boldsymbol{K}/r^2$ as a function of the components A_i of the second-order orientation tensor $\boldsymbol{A}$ of several fibre networks with disordered fibre arrangements and different fibre volume fractions ϕ_s and a fibre aspect ratio $l/(2r) = 10$. This figure reveals that the components K_i^* obtained using numerical simulation are increasing functions of A_i, i.e., the permeability components in the direction of privileged fibre orientation are higher ($A_i \approx 1$) than the permeability components in the transverse direction ($A_i \approx 0$). This result is in accordance with the literature (Stylianopoulos et al., 2008; Pradhan et al., 2012; Soltani, Johari & Zarrebini, 2014a; Soltani et al., 2017; Tamayol & Bahrami, 2011; Tahir & Vahedi Tafreshi, 2009). Note that the scattering of the numerical results exhibits a large decrease with the increase in the fibre volume fraction ϕ_s which might show that the networks exhibit a more homogeneous fibre spatial distribution at higher fibre volume fractions ϕ_s. This point would be further discussed in section 6.5.

Regardless of the fibre volume fraction ϕ_s, Figure 6.3 shows that the analytical model (Eq 6.17 with Eqs. 6.18-6.19) follows a similar trend as the numerical results. However, a difference with the numerical results was observed for $A_i \approx 0$ or $A_i \approx 1$, suggesting that the analytical models used to predict the evolutions of k_L^* and k_T^* (Eqs. 6.18-6.19) are not

sufficiently relevant for the types of investigated fibre networks. Contrary to what is considered in these models, in the numerically generated virtual networks the fibres do not exhibit infinite length and are not ordered in triangular arrays. Such discrepancy between numerical simulation results and the predictions of the model of Drummond and Tahir (Drummond & Tahir, 1984) has already been reported by Tahir and Tafreshi (Tahir & Vahedi Tafreshi, 2009) for disordered arrays of parallel fibres with infinite length.

To better predict the numerical simulation results, the parameters k_L^* and k_T^* were fitted using the least square method. Using such approach, the predictions of the analytical model were clearly enhanced (Figure 6.3). The fitting parameters for k_L^* and k_T^* are given in Table 6.3.The mean and maximum relative differences that exhibit the fitted parameters k_L^* and k_T^* with the parameters of the analytical models (Eqs. 6.18-6.19) are also given in this table, showing a decrease of both differences with the increase in ϕ_s.

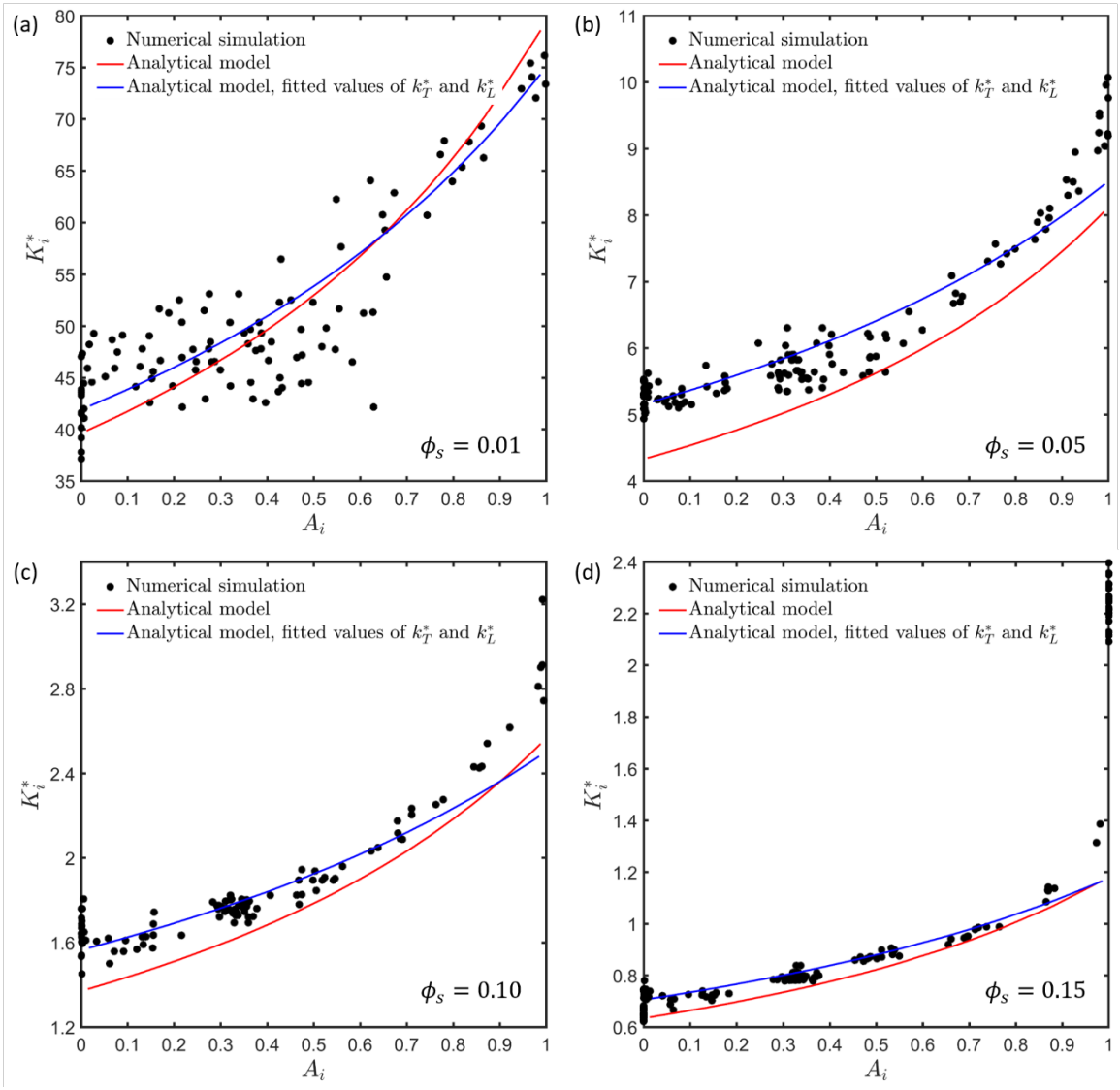

Figure 6.3. Evolution of the dimensionless permeability components K_i^* with the components A_i of second-order orientation tensor obtained by numerical simulation for the virtual fibre networks with a fibre aspect ratio $l/(2r) = 10$. Predictions of the

analytical model (Eq. 6.17) using dimensionless parameters k_L^* and k_T^* from Eqs. 6.18 and 6.19 (red line). Predictions of the analytical model using fitted values of k_L^* and k_T^* parameters (blue line).

6.3. Fitted values of the dimensionless parameters k_L^* and k_T^*. Relative mean and maximum differences with respect to the values of these parameters used in the analytical model given in Eqs. 6.18 and 6.19.

ϕ_s	k_L^*	k_T^*	Mean relative difference	Maximum relative difference
0.01	74.45	42.06	6.70%	27.23%
0.05	8.75	5.08	4.39%	15.14%
0.10	2.61	1.54	3.83%	24.08%
0.15	1.18	0.69	3.39%	23.36%

6.4.2 Influence of the fibre aspect ratio $l/(2r)$

Figure 6.4 shows the evolution of the components K_i^* as a function of the components A_i for several fibre networks with varying fibre aspect ratios $l/(2r)$ and ϕ_s=0.05 and 0.10. Regardless of the aspect ratios $l/(2r)$, the components K_i^* increased with the increase in A_i. However, this increase was less pronounced for the lowest fibre aspect ratios $l/(2r)$. Figure 6.4 shows that the analytical model failed to predict in detail the trends observed for the numerically generated fibre networks because

1. the coefficients k_L^* and k_T^* were obtained from expressions established for well-ordered arrays of parallel fibres with infinite length,
2. the analytical expressions of k_L^* and k_T^* are not dependent on the fibre aspect ratio $l/(2r)$.

In addition, the permeability coefficients K_i^* obtained by numerical simulation for the networks showing the lowest or the highest aspect ratios, i.e. $l/(2r) = 2$ or 30, were the furthest from the predictions of the analytical model. The origin of this discrepancy could be related to the difference between the number of fibres per unit volume expressed as $n = \phi_s/(\pi r^2 l)$. At low aspect ratio $l/(2r) = 2$, n is large, resulting presumably in pronounced edge effects in the fluid flow such as viscous dissipative mechanisms in the vicinity of the numerous extremities of fibres that are not taken into account in the analytical model. At high aspect ratio $l/(2r) = 30$, n is smaller, resulting in less pronounced edge effects and a higher permeability. However, even in these conditions, the analytical model is not able to accurately predict the permeability of the studied fibre networks. This could be associated to the increase in fibre clustering as n decreases and also to the appearance of preferential flow channels within the fibre networks where low viscous dissipative mechanisms occur. This aspect will be further discussed in section 6.5.

As already observed in Figure 6.3, the response of this model is enhanced by using fitted parameters for k_L^* and k_T^*. The fitting parameters for k_L^* and k_T^* are given in Table 6.4.

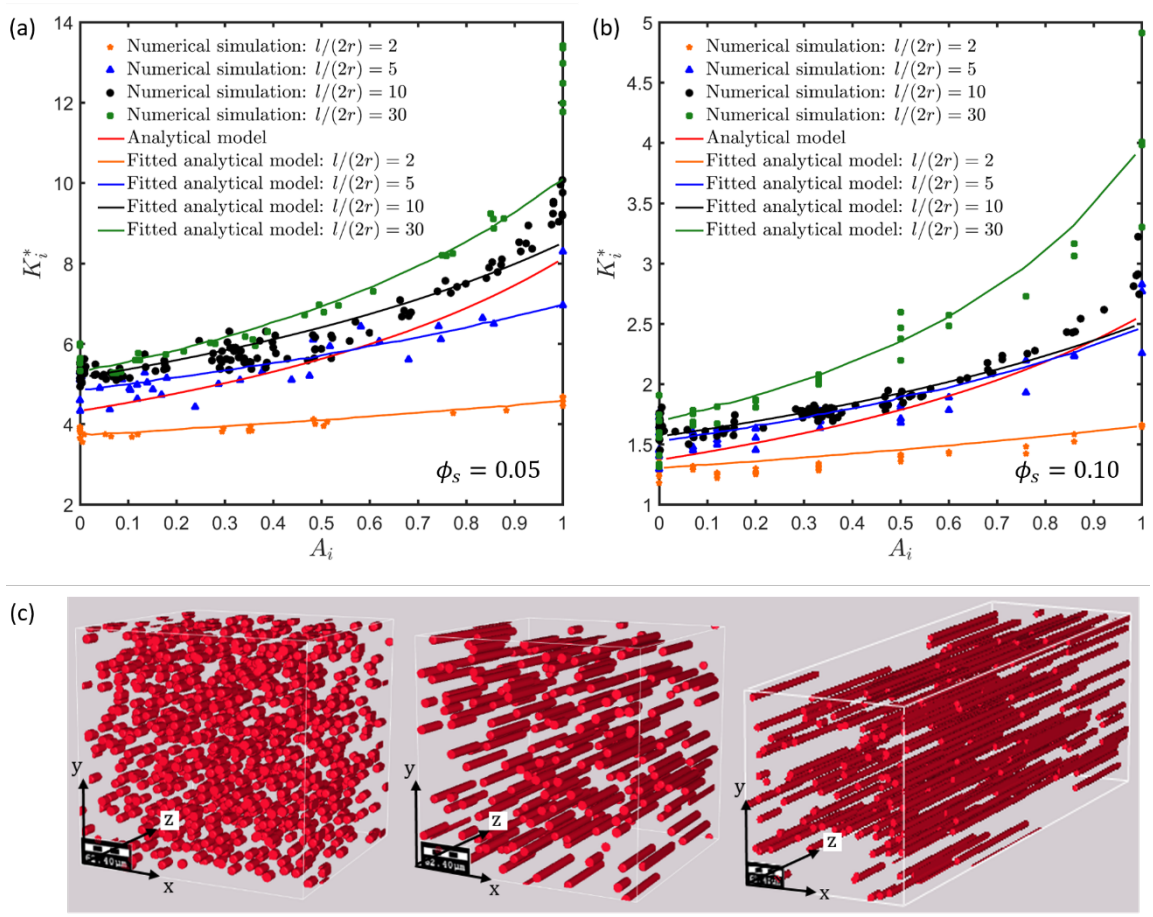

Figure 6.4. (a,b) Evolution of the dimensionless permeability components K_i^* with the components A_i of the second-order orientation tensor obtained by numerical simulation for the virtual fibre networks for various fibre aspect ratios $l/(2r)$. Predictions of the analytical model (red line). Predictions of the analytical model using fitted values of k_L^* and k_T^* parameters as a function of the aspect ratio $l/(2r)$. (c) Illustrations showing various fibre networks made of aligned fibres with $\phi_s = 0.05$ and aspect ratios $l/(2r)$ equal to 2, 10 and 30 (from the left-hand side to the right-hand side of the image).

Table 6.4. Fitted values of the dimensionless parameters k_L^* and k_T^*. Relative mean and maximum differences with respect to the values of these parameters used in the analytical model given in Eqs. 6.18 and 6.19.

ϕ_s	l/d	k_L^*	k_T^*	Mean relative difference	Maximum relative difference
0.05	2	4.53	3.65	2.13%	7.70%
0.05	5	6.97	4.80	5.30%	19.15%
0.05	10	8.50	5.08	4.46%	18.42%
0.05	30	10.15	5.24	6.48%	32.08%
0.10	2	1.59	1.23	2.76%	11.41%
0.10	5	2.44	1.46	5.38%	20.24%
0.10	10	2.49	1.56	3.91%	29.93%
0.10	30	3.71	1.66	5.93%	32.36%

6.4.3 Model predictions for real fibrous networks

Figure 6.5 shows the predictions of the analytical model for the two principal permeability coefficients denoted $K_{\parallel}^{*}$ and $K_{\perp}^{*}$, respectively, of the UD flax fibre network and the flax fibre mat in its undeformed and deformed states (Figure 6.2). Note that $K_{\parallel}^{*}$ corresponds to the permeability components along the x and y directions, i.e. $K_{\parallel}^{*} \approx K_{xx}^{*} \approx K_{yy}^{*}$ for the copper fibre network and the flax fibre mat, whereas it corresponds to the permeability coefficient along the z direction, i.e. $K_{\parallel}^{*} = K_{zz}^{*}$ for the UD flax fibre network. The permeability $K_{\perp}^{*}$ correspond to the permeability along the z direction for the copper fibre networks and the flax fibre mat, Figure 6.5. also shows the principal components K_{i}^{*} $(i = I, II, III)$ obtained numerically for the 2D copper fibrous network with preferential in-plane fibre orientation.

Figure 6.5a,b shows that the analytical model gave reasonable predictions, i.e. the relative error ranged between 5% and 38%, of the permeability coefficients of the flax fibre mat, copper fibre network and of the transverse permeability coefficient $K_{\perp}^{*}$ of the UD flax fibre network. The longitudinal component $K_{\parallel}^{*}$ obtained for the UD flax fibre network showed a higher discrepancy. A possible origin of this discrepancy could be associated to the presence of fibre clusters as well to the complex geometry of the fibre cross sections of this particular fibre network, as shown in the inset of Figure 6.5a. The presence of these heterogeneities could lead to preferential flow channels, leading to higher permeability values than those given by the analytical model.

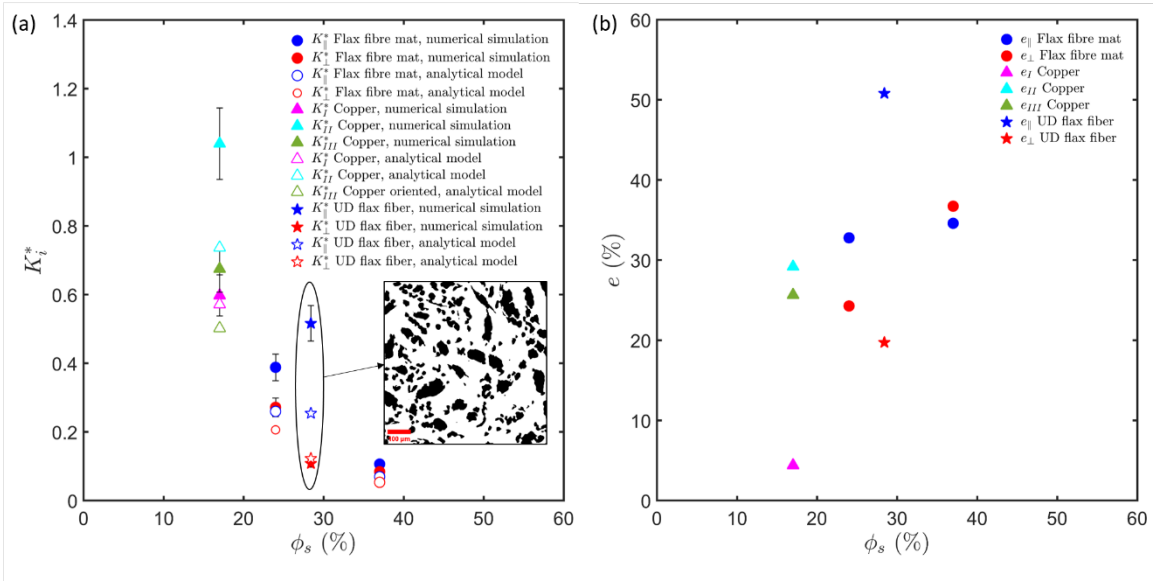

Figure 6.5. (a) Evolution of the dimensionless principal permeability components $K_{\parallel}^{*}$ and $K_{\perp}^{*}$ with the fibre volume fraction ϕ_s obtained by numerical simulation for the real fibrous networks and predictions of the analytical model using dimensionless parameters k_L^* and k_T^* from Eqs. 6.18 and 6.19. Note that it can be inferred from the statistical analysis by Jeulin (Jeulin, 2012) that the relative error for the predicted components of the dimensionless permeability tensor of the real fibre networks is about 15%. Inset image is a transverse cross sectional view of the UD flax fibre network (fibre cross sections are shown in black). (b) Corresponding relative error

between the model and numerical predictions as a function of the fibre volume fraction ϕ_s.

6.5 Discussion

The numerical results gathered in the previous sections were further discussed and compared with various permeability models that are classically used to predict the permeability of isotropic and in-plane oriented fibrous networks. From Figure 6.6, several remarks can be drawn:

- The models of Drummond and Tahir (Drummond & Tahir, 1984) and Bruschke and Advani (Bruschke & Advani, 1993) that consider fibre networks as arrays of parallel infinite fibres with triangular fibre arrangements underpredict the longitudinal ($A_i \approx 1$) and transverse ($A_i \approx 0$) permeabilities of the investigated fibre networks;
- The model of Jackson and James (Jackson & James, 1982) gives a good prediction of the permeability of 3D isotropic fibrous networks ($A_i = 1/3$). Similar observation has already been reported by Tahir and Tafreshi (Tahir & Vahedi Tafreshi, 2009);
- The empirical model of Davies (Davies, 1973) provides a nice prediction of the transverse permeability of planar isotropic fibrous networks ($A_i = 0$);

As shown in Figure 6.6, the previously mentioned models are interesting for the prediction of the permeability properties for some particular cases of fibrous arrangements. However, these models are not able to predict the dependence of all the dimensionless components K_i^* with the fibre orientation variations. On the contrary, the proposed analytical model (Eq. 6.17) was able to predict the increase of the components K_i^* with the increase in A_i. This is highlighted in section 6.3. However, it is interesting to note that the proposed model (Eq. 6.17) predicts that the transverse permeability of planar fibrous networks does not depend on the in-plane fibre orientation. This is in accordance with the theoretical work by Spielman and Goren (Spielman & Goren, 1968) and the numerical results reported by Stylianopoulos et al. (Stylianopoulos et al., 2008) who did not observe any variations of the transverse permeability of planar fibrous networks showing various in-plane fibre orientations.

In addition, the accuracy of the analytical model (Eq. 6.17) increased with increasing the fibre volume fraction ϕ_s. However, discrepancies were also observed. Their origin could be mainly associated to the analytical expressions (Eqs. 6.18 and 6.19) chosen for the coefficients k_L^* and k_T^* and their underlying assumptions. Indeed, these analytical models (Eqs. 6.18 and 6.19) do not take into account the fibre aspect ratio $l/(2r)$ and the heterogeneous spatial distribution of fibres which can lead to fibre clusters.

The effect of the heterogeneity in fibre spatial distributions is further illustrated in Figure 6.6 where the evolution of the permeability components K_i^* with A_i is shown for fibrous

networks with random and dispersed fibre spatial distributions. The permeability of fibre networks with random fibre spatial distributions is larger than those of networks with dispersed fibre spatial distributions. This effect could be ascribed to the presence of large flow channels in networks with random fibre spatial distribution as illustrated in Figure 6.6b. In those channels, weak viscous dissipative mechanisms presumably occur, thus leading to higher permeability. It can be assumed that the viscous dissipative mechanisms are greater in networks with dispersed and ordered fibre spatial distributions (Figure 6.6c). A possible way to enhance the analytical model would consist in choosing analytical models for k_L^* and k_T^* that would account for the heterogeneity of the spatial fibre distributions.

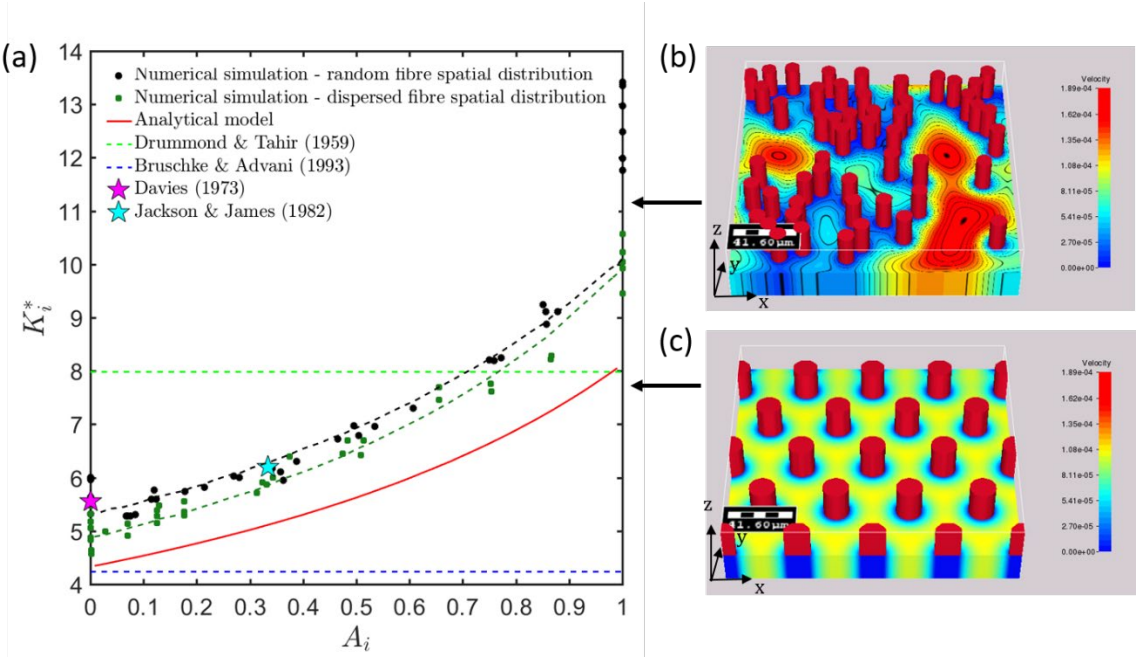

Figure 6.6. (a) Evolution of the dimensionless permeability components K_i^* with the components A_i of the second-order orientation tensor obtained by numerical simulation for the virtual fibre networks with a fibre aspect ratio $\frac{l}{2r} = 30$ and a fibre volume fraction ϕ_s = 0.05. Black, resp. green, dots: numerical results obtained for fibre networks with random, resp. dispersed, fibre spatial distributions. The black, resp. green, line is shown to highlight the numerical tendency. Red line: prediction of the analytical model. (b) Colour map showing the magnitude of the velocity field corresponding to an applied longitudinal pressure gradient in a UD random network. (c) Same illustration for a triangular arrangement of parallel fibres.

6.6 Conclusion

An original analytical model was proposed for the permeability estimation of fibrous networks with varying overall fibre orientations and for fibres with circular cross sections. This model is based on two coefficients k_L^* and k_T^* that are weighted by the second-order orientation tensor $\boldsymbol{A}$ that characterises the overall fibre orientation of the fibrous networks. The coefficients k_L^* and k_T^* represent the longitudinal and transverse permeability of

networks made of parallel fibres. In the proposed model, the dependency of the permeability in microstructure descriptors such as the fibre volume fraction ϕ_s, aspect ratio $l/(2r)$ and fibre spatial distribution is contained in these two coefficients. Therefore, their choice is crucial for the accuracy of the predictions of the model. In this work, to obtain a complete analytical estimate, these coefficients were chosen from literature. For the coefficient k_L^*, the model of Drummond and Tahir (Drummond & Tahir, 1984) for triangular arrangements of circular parallel fibres of infinite length was chosen, whereas the Bruschke and Advani model (Bruschke & Advani, 1993) was chosen for k_T^*.

The permeability predictions of this analytical model were compared with CFD simulations of the fluid flow through various numerically generated fibre networks that reproduce a large set of fibre spatial and orientation distributions. Hence, UD networks, 2D isotropic planar, 2D oriented and 3D isotropic networks with non-overlapping fibres were generated and tested. It was shown that the proposed analytical model was able to predict the increase in the permeability coefficients with the increase in the fibre orientation, as represented by the principal values of the second-order orientation tensor $\boldsymbol{A}$. However, as the analytical models (Drummond & Tahir, 1984; Bruschke & Advani, 1993) chosen for the coefficients k_L^* and k_T^* do not take into account finite aspect ratios nor heterogeneous fibre spatial distributions, some discrepancies with the numerical results were observed. Typically, the analytical model underestimated the permeability of networks showing heterogeneous fibre spatial distributions. In addition, the analytical model was shown to give accurate estimates of the permeability of real fibre networks that exhibited large fibre aspect ratios and homogeneous fibre spatial distributions. Again the model was less accurate for real networks with low fibre volume fraction fraction ϕ_s, irregular fibre arrangements and fibres having cross sections with complex geometries.

This study demonstrated that the accuracy of the model could be enhanced by choosing fitted values for the parameters k_L^* and k_T^*. Hence, it could be interesting to extent this approach to a wide diversity of fibrous networks in order to propose semi-empirical expressions for k_L^* and k_T^* taking into account for instance finite fibre aspect ratios and heterogeneous fibre spatial distributions.

References

Advani, S. G. and Hsiao, K.-T. (2012). *Manufacturing techniques for polymer matrix composites (PMCs)*. Elsevier.

Advani, S. G. and Sozer, E. M. (2002). *Process modeling in composites manufacturing*. CRC press.

Advani, S. G. and Tucker, C. L. (1987). The Use of Tensors to Describe and Predict Fiber Orientation in Short Fiber Composites, *Journal of Rheology*, 31(8), 751–784. doi: 10.1122/1.549945.

Ali, M. A. et al. (2019). XCT-scan assisted flow path analysis and permeability prediction of a 3D woven fabric, *Composites Part B: Engineering*, 176, p. 107320. doi: 10.1016/j.compositesb.2019.107320.

Auriault, J. L. (1991). Heterogeneous medium. Is an equivalent macroscopic description possible?, *International Journal of Engineering Science*, 29(7), pp. 785–795. doi: 10.1016/0020-7225(91)90001-J.

Auriault, J.-L. (2002). Upscaling Heterogeneous Media by Asymptotic Expansions, *Journal of Engineering Mechanics*, 128(8), pp. 817–822. doi: 10.1061/(ASCE)0733-9399(2002)128:8(817).

Auriault, J.-L. (2005). Transport in Porous Media: Upscaling by Multiscale Asymptotic Expansions. *Applied Micromechanics of Porous Materials*. Vienna: Springer (CISM International Centre for Mechanical Sciences), pp. 3–56. doi: 10.1007/3-211-38046-9_1.

Bailly, L. et al. (2018). 3D multiscale imaging of human vocal folds using synchrotron X-ray microtomography in phase retrieval mode, *Scientific Reports*, 8(1), p. 14003. doi: 10.1038/s41598-018-31849-w.

Batchelor, C. K. and Batchelor, G. K. (2000). *An Introduction to Fluid Dynamics*. Cambridge University Press.

Bechtold, G. and Ye, L. (2003). Influence of fibre distribution on the transverse flow permeability in fibre bundles, *Composites Science and Technology*, 63(14), pp. 2069–2079.

Berdichevsky, A. L. and Cai, Z. (1993). Preform permeability predictions by self-consistent method and finite element simulation, *Polymer Composites*, 14(2), 132–143. doi: https://doi.org/10.1002/pc.750140207.

Bergelin, O. P. (1952). Heat Transfer and Fluid Friction During Flow Across Banks of Tubes-IV A study of the Transition Zone Between Viscous and Turbulent Flow, *Trans. ASME*, 74, pp. 953–960.

Bizet, L. et al. (2008). Transverse permeability and Kozeny constant in flax fiber mats preforms, in *FPCM-9 (2008) The 9th International Conference on Flow Processes in Composite Materials*.

Boulos, V. et al. (2012). Investigating performance variations of an optimized GPU-ported granulometry algorithm, in *Proceedings of the 2012 Conference on Design and Architectures for Signal and Image Processing*. IEEE, pp. 1–6.

Boutin, C. (2000). Study of permeability by periodic and self-consistent homogenisation, *European Journal of Mechanics - A/Solids*, 19(4), pp. 603–632. doi: 10.1016/S0997-7538(00)00174-1.

Bruschke, M. V. and Advani, S. G. (1993). Flow of generalized Newtonian fluids across a periodic array of cylinders, *Journal of Rheology*, 37(3), 479–498. doi: 10.1122/1.550455.

Caglar, B. et al. (2017) Permeability of textile fabrics with spherical inclusions, *Composites Part A: Applied Science and Manufacturing*, 99, 1–14. doi: 10.1016/j.compositesa.2017.03.031.

Carman, P. C. (1956). 'Flow of gases through porous media'.

Chalencon, F. et al. (2016). Homogeneous and heterogeneous rheology and flow-induced microstructures of a fresh fiber-reinforced mortar. *Cement and Concrete Research*, 82, pp. 130–141. doi: 10.1016/j.cemconres.2015.12.012.

Chen, X. and Papathanasiou, T. D. (2006). On the variability of the Kozeny constant for saturated flow across unidirectional disordered fiber arrays, *Composites Part A: Applied Science and Manufacturing*, 37(6), 836–846.

Darcy, H. (1856). *Les fontaines publiques de la ville de Dijon: exposition et application des principes à suivre et des formules à employer dans les questions de distribution d'eau*. Victor Dalmont.

Davies, D. C. (1973). Air filtration academic press, *London, New York*.

Delisée, C. et al. (2007). Microstructure et propriétés de transport de matériaux isolants à base de fibres cellulosiques, in *Annales du Bâtiment et des travaux publics*, p. 23.

Delisée, C., Lux, J. and Malvestio, J. (2010). 3D Morphology and Permeability of Highly Porous Cellulosic Fibrous Material, *Transport in Porous Media*, 83(3), 623–636. doi: 10.1007/s11242-009-9464-4.

Doube, M. et al. (2010). BoneJ: free and extensible bone image analysis in ImageJ, *Bone*, 47(6), 1076–1079.

Drummond, J. E. and Tahir, M. I. (1984). Laminar viscous flow through regular arrays of parallel solid cylinders, *International Journal of Multiphase Flow*, 10(5), 515–540. doi: 10.1016/0301-9322(84)90079-X.

Gebart, B. R. (1992) Permeability of Unidirectional Reinforcements for RTM, *Journal of Composite Materials*, 26(8), 1100–1133. doi: 10.1177/002199839202600802.

Happel, J. (1959) Viscous flow relative to arrays of cylinders, *AIChE Journal*, 5(2), 174–177.

Happel, J. and Brenner, H. (1983). The Motion of a Rigid Particle of Arbitrary Shape in an Unbounded Fluid, in Happel, J. and Brenner, H. (eds) *Low Reynolds number hydrodynamics: with special applications to particulate media*. Dordrecht: Springer Netherlands (Mechanics of fluids and transport processes), 159–234. doi: 10.1007/978-94-009-8352-6_5.

Idris, Z. et al. (2004). Microstructural effects on the flow law of power-law fluids through fibrous media, *Modelling and Simulation in Materials Science and Engineering*, 12(5), 995–1015. doi: 10.1088/0965-0393/12/5/016.

Jackson, G. W. and James, D. F. (1982). The hydrodynamic resistance of hyaluronic acid and its contribution to tissue permeability, *Biorheology*, 19(1–2), 317–330.

Jackson, G. W. and James, D. F. (1986). The permeability of fibrous porous media, *The Canadian Journal of Chemical Engineering*, 64(3), 364–374.

Jeulin, D. (2012). Morphology and effective properties of multi-scale random sets: a review, *Comptes Rendus Mécanique*, 340(4–5), 219–229.

Keller, J. B. (1964). Viscous flow through a grating or lattice of cylinders, *Journal of Fluid Mechanics*, 18(1), 94–96. doi: 10.1017/S0022112064000064.

Kirsch, A. A. and Fuchs, N. A. (1968). Studies on fibrous aerosol filters—III Diffusional deposition of aerosols in fibrous filters, *Annals of Occupational Hygiene*, 11(4), 299–304.

Koponen, A. et al. (1998). Permeability of Three-Dimensional Random Fiber Webs, *Physical Review Letters*, 80(4), 716–719. doi: 10.1103/PhysRevLett.80.716.

Kozeny, J. (1927). Uber kapillare leitung der wasser in boden, *Royal Academy of Science, Vienna, Proc. Class I*, 136, 271–306.

Kuwabara, S. (1959). The forces experienced by randomly distributed parallel circular cylinders or spheres in a viscous flow at small Reynolds numbers, *Journal of the physical society of Japan*, 14(4), 527–532.

Liu, H. L. and Hwang, W. R. (2012). Permeability prediction of fibrous porous media with complex 3D architectures, *Composites Part A: Applied Science and Manufacturing*, 43(11), 2030–2038.

Martoïa, F. et al. (2017). Crumpled paper sheets: Low-cost biobased cellular materials for structural applications, *Materials & Design*, 136, 150–164. doi: 10.1016/j.matdes.2017.09.031.

Nabovati, A., Llewellin, E. W. and Sousa, A. C. M. (2009). A general model for the permeability of fibrous porous media based on fluid flow simulations using the lattice Boltzmann method, *Composites Part A: Applied Science and Manufacturing*, 40(6), 860–869. doi: 10.1016/j.compositesa.2009.04.009.

Orgéas, L. et al. (2006). Modelling the flow of power-law fluids through anisotropic porous media at low-pore Reynolds number, *Chemical Engineering Science*, 61(14), 4490–4502. doi: 10.1016/j.ces.2006.01.046.

Orgéas, L. et al. (2012). In-plane conduction of polymer composite plates reinforced with architectured networks of Copper fibres, *Journal of Materials Science*, 47(6), 2932–2942. doi: 10.1007/s10853-011-6126-z.

Pradhan, A. K. et al. (2012). Effect of 3D fiber orientation distribution on transverse air permeability of fibrous porous media, *Powder technology*, 221, 101–104.

Rolland du Roscoat, S. et al. (2008). Microstructural Analysis of Paper Using Synchrotron X-ray Microtomography: Numerical Estimation of the Permeability and Effective Thermal Conductivity, *Appita : Technology, Innovation, Manufacturing, Environment*.https://search.informit.org/doi/abs/10.3316/INFORMIT.187944502104494

Sampson, W. W. (2008). *Modelling Stochastic Fibrous Materials with Mathematica®*. Springer Science & Business Media.

Schell, J. S. U., Siegrist, M. and Ermanni, P. (2007). Experimental determination of the transversal and longitudinal fibre bundle permeability, *Applied Composite Materials*, 14(2), 117–128.

Schneider, C. A., Rasband, W. S. and Eliceiri, K. W. (2012). NIH Image to ImageJ: 25 years of image analysis, *Nature Methods*, 9(7), 671–675. doi: 10.1038/nmeth.2089.

Soltani, P. et al. (2017). Prediction of permeability of realistic and virtual layered nonwovens using combined application of X-ray μCT and computer simulation, *Chemical Engineering Research and Design*, 124, 299–312. doi: 10.1016/j.cherd.2017.06.035.

Soltani, P., Johari, M. S. and Zarrebini, M. (2014a). Effect of 3D fiber orientation on permeability of realistic fibrous porous networks, *Powder Technology*, 254, 44–56.

Soltani, P., Johari, M. S. and Zarrebini, M. (2014b). Effect of 3D fiber orientation on permeability of realistic fibrous porous networks, *Powder Technology*, 254, 44–56. doi: 10.1016/j.powtec.2014.01.001.

Soltani, P., Johari, M. S. and Zarrebini, M. (2015). Tomography-based determination of transverse permeability in fibrous porous media, *Journal of Industrial Textiles*, 44(5), 738–756. doi: 10.1177/1528083713512357.

Spielman, L. and Goren, S. L. (1968). Model for predicting pressure drop and filtration efficiency in fibrous media, *Environmental Science & Technology*, 2(4), 279–287.

Stylianopoulos, T. et al. (2008). Permeability calculations in three-dimensional isotropic and oriented fiber networks, *Physics of Fluids*, 20(12), 123601. doi: 10.1063/1.3021477.

Tahir, M. A. and Vahedi Tafreshi, H. (2009). Influence of fiber orientation on the transverse permeability of fibrous media, *Physics of Fluids*, 21(8), 083604. doi: 10.1063/1.3211192.

Tamayol, A. and Bahrami, M. (2009). Analytical determination of viscous permeability of fibrous porous media, *International Journal of Heat and Mass Transfer*, 52(9), pp. 2407–2414. doi: 10.1016/j.ijheatmasstransfer.2008.09.032.

Tamayol, A. and Bahrami, M. (2011). Transverse permeability of fibrous porous media, *Physical Review E*, 83(4), 046314. doi: 10.1103/PhysRevE.83.046314.

Tomadakis, M. M. and Robertson, T. J. (2005). Viscous Permeability of Random Fiber Structures: Comparison of Electrical and Diffusional Estimates with Experimental and Analytical Results, *Journal of Composite Materials*, 39(2), 163–188. doi: 10.1177/0021998305046438.

Wang, Q. et al. (2007). Simulating through-plane permeability of fibrous materials with different fiber lengths, *Modelling and Simulation in Materials Science and Engineering*, 15(8), 855–868. doi: 10.1088/0965-0393/15/8/003.

Chapter 7

In situ 3D observations of the impregnation phenomena occurring in parallel arrangements of rigid fibres

Abstract

Hypothesis

Capillary-driven impregnation phenomena occurring in 3D anisotropic fibrous networks such as fibre bundles are complex and still not fully understood. However, these phenomena play a central role during the impregnation phase of many composite forming processes. Hence, it is crucial to follow in 3D the propagation and distortion of the fluid front and to measure the capillary pressure and forces at the fibre scale that develop during the impregnation of fibre bundles.

Experiments

High-resolution synchrotron X-ray microtomography was used to investigate the propagation of fluids within a parallel arrangement of glass tubes. The analysis of the obtained 3D images enabled the fluid-air interface curvatures, triple line lengths, and local contact angles to be quantified during wetting and dewetting experiments of the model fibre network, using advanced image analysis procedures.

Findings

Even in quasi-static situations, local contact angles exhibited significant variations along the fibres. These variations also depended on the wetting and/or dewetting state. The transverse capillary forces were shown to be of the same order of magnitude as the longitudinal capillary forces. Local curvatures of the fluid-air interface and the resulting estimate of the average capillary pressure proved the relevance of a mesoscale capillary pressure model adapted for fibre bundles.

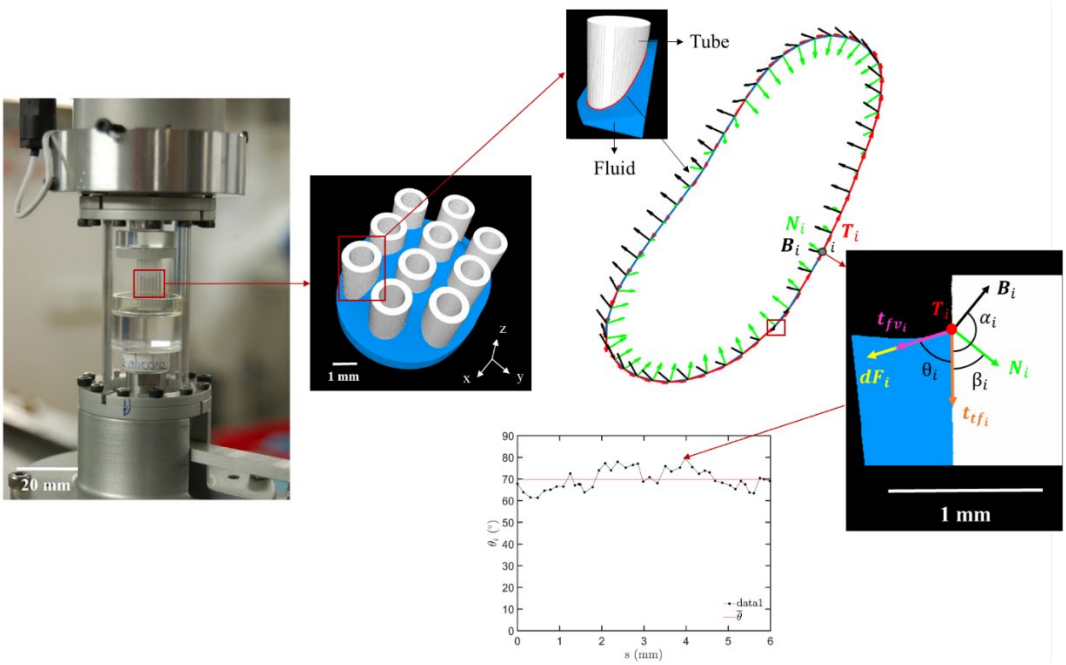

7.1 Introduction

Capillary-driven phenomena in fibrous media are ubiquitous but still not well understood, in particular when they occur in complex 3D fibrous architectures. For example, fibre-reinforced polymer composites are increasingly used to make structural or multi-functional parts for several industrial domains. High-performance composite parts are usually fabricated using liquid composite moulding (LCM) wet-forming processes (Advani & Hsiao, 2012). In these processes, an impregnation phase of the fibrous reinforcements is required (Advani & Hsiao, 2012; Michaud, 2016; Binetruy et al., 1998; Pillai, 2004). Impregnation consists on the flow of a liquid polymer matrix through a fibrous reinforcement, i.e. within an anisotropic, deformable, and multiscale porous medium made of more or less ordered networks of fibre bundles or yarns (Advani & Hsiao, 2012; Michaud, 2016). Impregnation usually involves the displacement of a non-wetting fluid (air) by a wetting fluid (fluid polymer). The flow of the fluid polymer is induced by either a pressure gradient applied by an injection system, or capillary forces or a combination of both (Michaud, 2016).

A poor control of the impregnation phase can lead to the onset of several defects such as porosity that can compromise the mechanical properties of the composite parts (Michaud, 2016; Binetruy et al., 1998; Park & Lee, 2011; Leclerc & Ruiz, 2008; Y. T Chen et al., 1995; Ruiz et al., 2006). Several studies have shown that capillary effects can significantly affect the propagation of the polymer-air interface the geometry of which can become extremely irregular, leading to the formation of pores (Michaud, 2016; Y.T. Chen et al., 1995; Caglar et al., 2019; Verrey et al., 2006; Salvatori et al., 2018; Koubaa et al., 2016). These phenomena depend on several parameters related to the fluid surface tension, fibre wettability properties (surface energy), contact angle, architecture of the fibre reinforcements (fibre volume fraction), as well as the directionality of the fluid flow with respect to their anisotropy axes, and fluid front velocity (interplay between capillary and viscous effects). The capillary effects play an important role in multiscale fibre reinforcements (Binetruy et al., 1998; Park & Lee, 2011; Ruiz et al., 2006; Simacek & Advani, 2003; Chwastiak, 1973; Rohatgi et al., 1996; Kuentzer et al., 2006; S. Amico & Lekakou, 2004; Schell et al., 2007). They can lead to large differences between the fluid propagation velocity within and between fibre bundles that often result in extreme distortion phenomena of the flow front. However, capillary effects can also drastically affect the flow of liquid polymer within fibre bundles, i.e. one-dimension structures with quasi parallel fibres (Amico & Lekakou, 2004; Pillai & Advani, 1996; Lawrence et al., 2009).

The study of the impregnation of fibre bundles was the subject of many research efforts (Princen, 1969b; Bayramli & Powell, 1992; Princen, 1969a; Neacsu et al., 2006; Washburn, 1921; Bayramli & Powell, 1990; Bayramli & Powell, 1991; Yeager et al., 2017). Several experiments based on the Wilhelmy method were performed to study longitudinal and transverse capillary driven flows within fibre bundles (Washburn, 1921; Batch et al., 1996; Neumann & Good, 1979; Amico & Lekakou, 2002). These experiments consisted in immersing fibre bundles in a test fluid to draw the fluid upward by capillary forces.

Measurement of height rise at various times was then related to the fluid surface tension, contact angle and permeability of the fibre bundles. In addition, the fluid propagation in fibre bundles was studied using magnetic resonance imaging (MRI) measurements (Neacsu et al., 2007). This technique enabled detecting variations in fluid concentration and thus the formation of voids/pores during the impregnation of fibre bundles (Endruweit et al., 2011a; Endruweit et al., 2011b). X-ray radiography was also used to track fluid propagation within fibre bundles (Bréard et al., 1999). The 2D information provided by this technique was very useful to better understand how the fluid propagated but did not allow the development of porosity to be finely observed. Recently, several studies used 3D X-ray microtomography images to monitor the infiltration process of industrial fibre bundles (Vilà et al., 2015; Larson & Zok, 2018; Castro et al., 2020). These studies revealed the formation of preferential flow channels and important fibre rearrangements associated to variations in the fibre volume fraction. An estimation of the fluid-fibre contact angle was also given through the analysis of the 3D images. However, this parameter was measured only in particular zones using 2D cross sections of the 3D images (Larson & Zok, 2018; Castro et al., 2020). In addition, several studies that were carried out with granular and porous geomaterials showed that it was possible to measure several interesting local parameters such as local contact angles (Klise et al., 2016; Scanziani et al., 2017; Alratrout et al., 2017; Ibekwe et al., 2020a), local average curvatures (Armstrong et al., 2012; Andrew et al., 2015; Singh, 2016; Lin et al., 2018) of the interfaces between the wetting and non-wetting phases. For that purpose, 3D high-resolution images allowing a good description of the geometry of the solid, fluid phases and interfaces were needed.

In this context, the objective of this study was to follow the fluid front propagation and distortion that occurred during the capillary-driven impregnation of a model fibre network. The model fibre network was made of parallel millimetre glass tubes. This allowed mimicking the structure of a real fibre bundle used in composite materials while enabling high-resolution 3D X-ray synchrotron microtomography images to be acquired. For that purpose several wetting and dewetting stages of the model fibre network were imaged using a specially developed impregnation device that was installed on an X-ray microtomography beamline. Thanks to the good compromise between the tube diameter and the spatial resolution of the 3D images, it was possible using specific image analysis procedures to make quantitative measurements of the variations of the local mean curvatures of the fluid-air interface, local contact angles, and lengths of the triple lines. Then, using this database, it was possible to estimate the local capillary pressure and the local transverse and longitudinal capillary forces exerted by the fluid on each tube of the fibre network. Finally, the relevance of the results and their impact on composite processes were discussed.

7.2 Material and methods

7.2.1 Model fibre networks and impregnation fluids

In this study, several specimens of a model fibre network were fabricated. This fibre network was made of parallel hollow glass tubes (Hirschmann, Eberstadt Germany) with

an external radius r_e= 0.75 mm and an internal radius r_i = 0.50 mm. The tubes had a length L = 16 mm and were sealed at their top extremity with an epoxy glue to prevent the rising of the liquid inside the tubes. The network was composed of ten tubes arranged in a triangular geometry (Figure 7.1a,b). The centrelines of each tube were spaced 2 mm apart from each other to form isosceles triangles. The top extremities of the tubes were fixed in a disk made of a plastic resin. To clean the surface of the tubes, the fabricated fibre networks were plunged for 1 min inside an ultrasonic bath that was filled with acetone (ACS reagent, Sigma Aldrich).

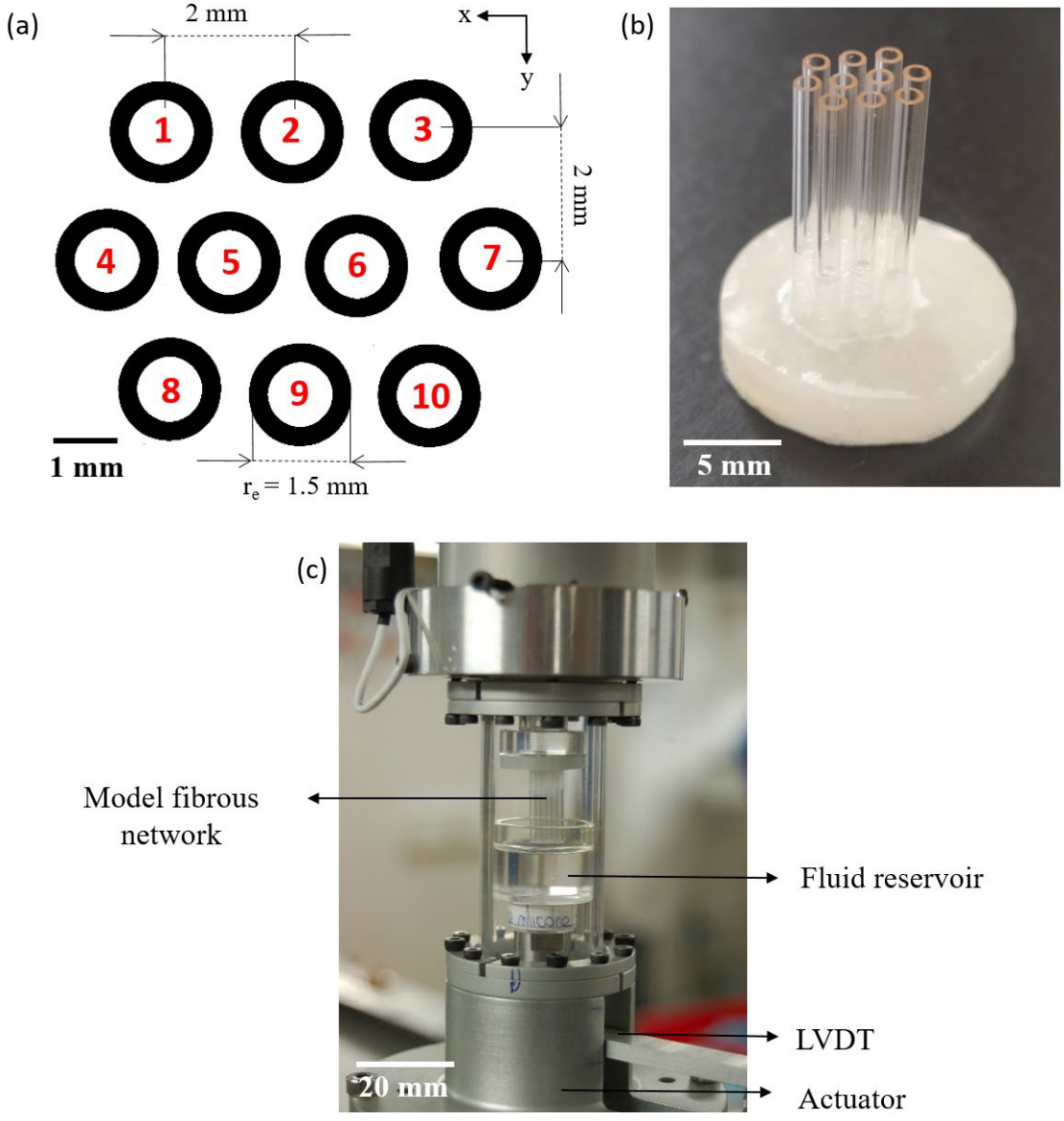

Figure 7.1. (a) Scheme of the geometry of the model fibre network composed of ten tubes arranged with a triangular geometry. A reference number was attributed to each tube of the model fibre network. (b) Photograph of a specimen of model fibre network that shows the tube arrangement fixed in the plastic part. (c) Photograph of the micro impregnation device.

Table 7.1. Properties of the two fluids used for the impregnation experiments. These properties were measured at a temperature $T = 23°C$. The equilibrium contact angle θ_e was measured by plunging a single glass tube in the considered fluid using a Krüss tensiometer and applying a correction for the buoyancy force. The procedure is further detailed in refs. (Qiu et al., 2016; Barraza et al., 2001; Pucci et al., 2017).

Fluid	Surface tension γ_{lv} (mN m^{-1})	Equilibrium tube/fluid contact angle θ_e (°)	Viscosity η (mPa s)	Density ρ (g cm^{-3})
Demineralised water	72.8	47	1	1
Silicone oil	21.1	20	970	0.97

Two Newtonian fluids with controlled rheological and surface tension properties, namely demineralised water and a silicone oil (47V1000 - 80026, Chimie-Plus Laboratoires), were used for the impregnation experiments of the aforementioned model fibre network. The viscosities η, densities ρ and surface tensions γ_{lv} as well as tube/fluid equilibrium contact angles θ_e of these fluids are given in Table 7.1. Regardless of the fluid, the equilibrium contact angle θ_e was less than 90°, showing that the tube surface can be wetted by both types of fluids.

The Bond number B_o was estimated as r_e^2/λ_c^2 (where $\lambda_c = \sqrt{\frac{\gamma_{lv}}{\rho g}}$ is the capillary length) for the impregnation experiments of the model fibre network. $B_o = 0.25$ and $B_o = 0.08$ for the silicone oil and demineralised water, respectively, which shows that the capillary effects were predominant compared to the gravity effects, i.e. fluid menisci are formed around the tubes of the model fibre network. It is also important to note that the mean separation distance $2\bar{d}$ between adjacent tubes of the model fibre network shown in Figure 7.1a, was chosen to have $\bar{d}/\lambda_c$ close to 1 for both types of fluids. This separation distance $2\bar{d}$ enables a capillary-driven rising of the fluids within the model fibre network.

7.2.2 In situ impregnation experiments and X-ray microtomography conditions

In situ impregnation experiments of the model fibre network were performed using a specially designed setup, as shown in Figure 7.1c. The setup was composed of an actuator (Latil et al., 2011; Martoïa et al., 2016; Laurencin et al., 2016) that allowed moving vertically, upwards or downwards, a PMMA reservoir (inner diameter = 18 mm) fixed on it and filled with the impregnation fluid. The vertical position of the reservoir was controlled using a linear variable differential transformer (LVDT). The fibre network was fastened on the upper part of the impregnation device. The fibre network and the reservoir were placed inside a transparent cylindrical part made of PMMA fastened to the frame of the actuator. The impregnation device was installed on the rotation stage of a synchrotron X-ray microtomograph (ID19 beamline, ESRF, Grenoble) to perform in situ impregnation experiments. They consisted in plunging or withdrawing the model fibre network in the

fluid, moving at different heights the level of the fluid reservoir using a translational velocity $v \approx 5$ µm/s, while taking 3D images of the experiments.

Two types of experiments were performed, namely interrupted and sequentially continuous impregnation scanning conditions. The specimen of model fibre network impregnated with the silicone oil was scanned using interrupted conditions, i.e. the vertical displacement of the reservoir was interrupted at certain positions and after a resting time $\Delta t > 5$ min, a 3D image was acquired. Six different positions or impregnation steps were investigated, moving upwards or downwards the fluid reservoir. The specimen of model fibre network impregnated with demineralized water was scanned using sequentially continuous conditions. The scans were done while the fluid reservoir was moving upwards or downwards. Six different impregnation steps were studied. During the motion needed to reach every position, a sequence of ten 3D images, corresponding to a total scanning of approximately 20 s, was taken, thereby allowing in situ 3D observations of the impregnation phenomena occurring within the fibre network.

To acquire 3D X-ray microtomography images of these experiments, the following imaging conditions were used. The X-ray energy and the number of radiographs (1584×1584 pixels) were set to 36.6 keV and 800, respectively. The exposure time of each radiograph was 2 ms and the scan duration less than 2 s. From the radiographs, 3D images with a voxel size of 5.1^3 µm^3 were reconstructed using the so-called Paganin procedure, which is based on the use of the phase contrast in the images (Beltran et al., 2010; Paganin et al., 2002). These ultrafast acquisition conditions and image resolution allowed obtaining an accurate representation of the tubes and the fluid front propagation, while having a sufficiently large field of view.

The capillary number C_a of the impregnation experiments was estimated as $\frac{\eta v}{\gamma_{lv}}$. For the experiments performed with silicone oil (resp. demineralised water) $C_a \approx 2 \times 10^{-4}$ (resp. $C_a \approx 8 \times 10^{-8}$), thus showing that in both cases the surface tension effects were largely predominant compared to the viscous effects. Hence, both imaging conditions can be considered as delivering 3D images of a sequence of quasi-static states of the flow front propagation governed by the capillary effects.

7.3 3D image analysis

7.3.1 Image segmentation

3D image reconstruction gave sequences of 8 bit grey scale images of the horizontal cross sections of the zones scanned, also called regions of interest (ROI). From these sequences, it was possible to obtain horizontal and vertical cross sections of the ROI's, as shown in Figure 7.2a,b. In these images, three phases can be identified: the tubes with a lighter shade of grey, the impregnating liquid between the tubes and the air that corresponds to the darker region. The image segmentation of the three phases was done manually using the Threshold

function implemented in Fiji software (Schneider et al., 2012). Due to the presence of the PMMA reservoir, the 3D images exhibited variations in their mean grey scale values between their lower and upper parts, diminishing more particularly the contrast between the fluid and air phases (Figure 7.2b). Thus, it was necessary to perform thresholding operations into two sub-volumes that corresponded to the lower (resp. upper) parts of the 3D images. Then, both segmented sub-images were recombined. No filters were used prior or after the segmentation operations to not alter the interfaces between the fluid, tubes and air phases. An example of a trinarised 3D image is shown in Figure 7.2c-e.

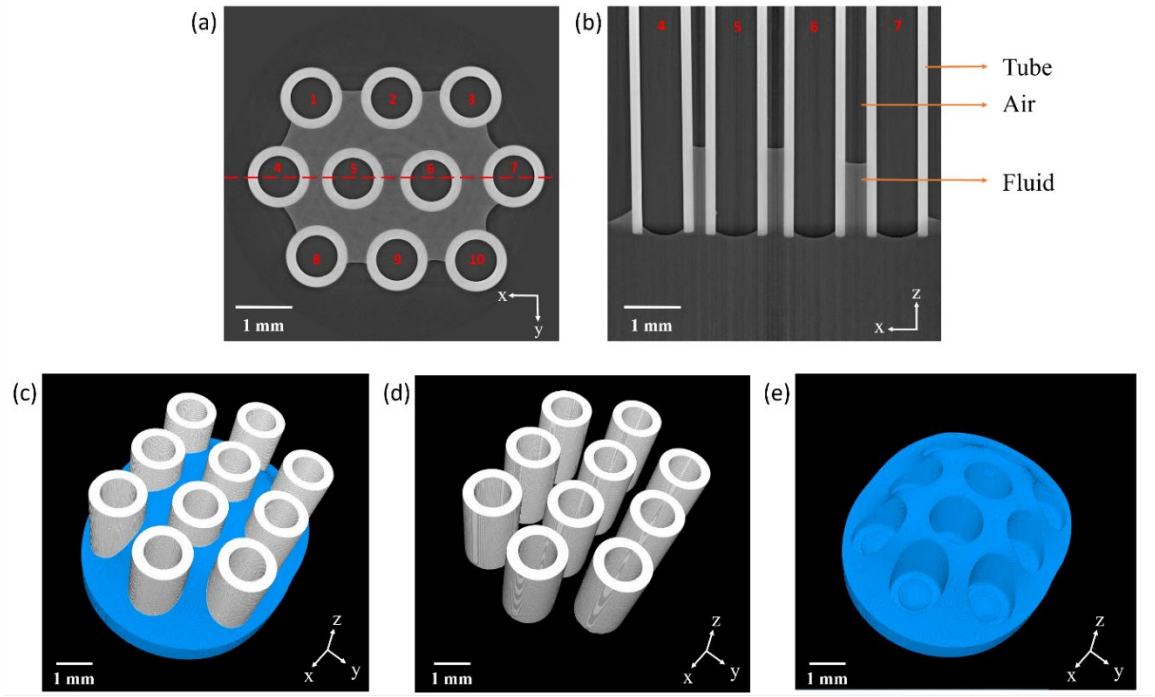

Figure 7.2. (a-b) Examples of horizontal (a) and vertical (b) cross sections of a grey scale X-ray microtomography image of an impregnated model fibre network. The dashed red line shows the trace of the cutting plane that was used to obtain the vertical cross section shown in image b. (c) Corresponding 3D views obtained after segmentation operations (dimensions: 8.1×8.1×8.1 mm^3). (d-e) Corresponding 3D images of the tubes of the model network (d) and the fluid (e).

7.3.2 Identification of the triple lines

A procedure was specially developed to identify the triple lines that formed on the external surface of the tubes between the fluid, tubes and air phases. The identification was applied on each tube of the model fibre network and consisted in several steps. For that purpose a "crop" operation using Fiji software was performed on the 3D images to obtain sub-volumes centred on the tube axes (dimensions of the sub-volumes: 400×400×900 voxels). Then, the inner cavity of each tube was "filled" using the "Fill holes" function implemented in Fiji software (Schneider et al., 2012). The result of this operation is visible in Figure 7.3. 3D dilatation operations were performed for each phase of the sub-volumes using the plugin Analysis 3D. Figure 7.3b illustrates this operation, showing in red the phase that was

subjected to 3D dilation and cross-sections of the resulting 3D images for the three phases. These 3D images were then intersected using the Image calculator function which allowed keeping only the common voxels of the three phases (Figure 7.3c) and then skeletonized to obtain the voxels belonging to the triple line (Figure 7.3d).

7.3.3 Measurement of the triple line length and local contact angles

The measurement of the length of the triple line and the local contact angle along it was performed using a specially developed procedure implemented in Matlab. Smoothed closed linear parametric curves of the triple lines with curvilinear abscissa s were fitted using the set of discrete voxels of coordinates (x, y, z) representing the triple lines in the 3D images that were obtained following the procedure described in the previous section. This parametric curve was then discretized into N_s elementary segments i of lengths ds_i with $1 \leq i \leq N_s$. Depending on the considered tube and on the shape of the triple line, N_s could vary from 35 to 60. The lengths l of the triple lines were computed as $l = \sum_{i=1}^{N_s} ds_i$. It was verified that such discretization gave a good approximation of the lengths of numerically generated circular triple lines. Then, a local Frenet basis was associated to each elementary segment i using the procedure reported by Latil (Latil, 2012). In this local basis, $\boldsymbol{T}_i$ is the tangent unit vector, $\boldsymbol{N}_i$ is the normal unit vector pointing towards to the tube, and $\boldsymbol{B}_i$ the binormal unit vector to the segment i (Figure 7.3e).

For measuring the N_s local contact angles θ_i along the triple lines, the 3D images were cut in the ($\boldsymbol{N}_i$,$\boldsymbol{B}_i$) planes using the image rotation function of the image processing toolbox of Matlab. For that purpose, the 3D images were successively rotated of an angle ω_i around the z axis and of an angle ψ_i around the y axis of the (x, y, z) frame of the 3D images (Figure 7.3e). Then the local contact angles θ_i were measured manually as the angle formed between the vector $\boldsymbol{t}_{tf_i}$ tangent to the tube (marked in orange) and the vector tangent to the fluid surface $\boldsymbol{t}_{fv_i}$ (marked in pink), using a ROI of 50×50 pixels centred on the triple points. This procedure was tested with numerically generated images exhibiting the same spatial resolution of the X-ray microtomography images and a predefined local contact angle varying from 5° to 90°. The error made following this procedure was shown to be ±3°. Figure 7.3g shows an example of the evolution of the local contact angle θ_i and its mean value $\bar{\theta}$ along a triple line. Besides, it is important to mention that the aforementioned procedure was performed for each triple line that formed along all the tubes of the fibre network.

7.3.4 Measurement of the capillary force

Using the cross sections of the rotated 3D images as explained in the previous section, it was possible to estimate for each segment i of a triple line the components in the ($\boldsymbol{N}_i$, $\boldsymbol{B}_i$) basis of the local capillary force $d\boldsymbol{F}_i = \gamma_{lv} ds_i \boldsymbol{t}_{fv_i}$ exerted by the fluid on a portion of tube as follows:

$$dF_{i\ B} = d\boldsymbol{F}_i \cdot \boldsymbol{B}_i = \gamma_{lv} ds_i \cos(\theta_i - \alpha_i) \tag{7.1}$$

$$dF_{i\ N} = d\boldsymbol{F}_i \cdot \boldsymbol{N}_i = \gamma_{lv} ds_i \cos(\theta_i - \beta_i) \tag{7.2}$$

where the angles α_i and β_i are shown in Figure 7.3f. The overall capillary force $\boldsymbol{F}$ exerted by the fluid on a tube of a model fibre network was obtained by summing all the local capillary forces $d\boldsymbol{F}_i$. The capillary force exerted by the fluid was measured for each tube of the fibre bundle.

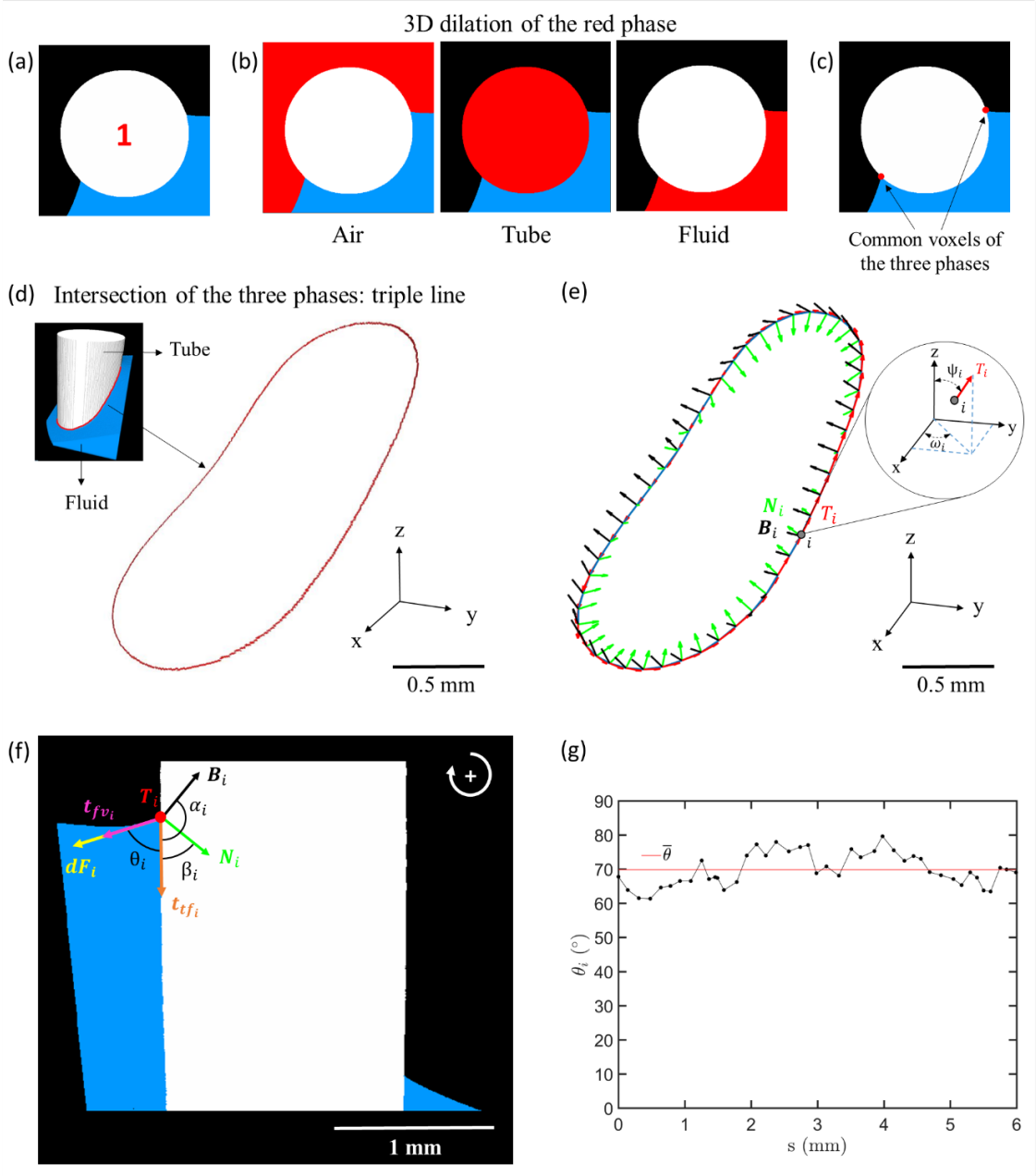

Figure 7.3. Procedure used to identify the triple lines and to compute the local contact angles. (a) View of a horizontal cross section of a trinarised 3D sub-volume centred on the axis tube n°1 of a model fibre network. (b) Same images showing the results

of the 3D dilatation operations that were performed on the air, tube and fluid phases. (c) Same image as (a) showing in red the voxels belonging to the air, tube and fluid phases and corresponding to voxels belonging to the triple line. (d) 3D view of the corresponding triple line. (e) Smoothed linear parametric representation of the triple line with the local Frenet bases ($\boldsymbol{T}_i$, $\boldsymbol{N}_i$,$\boldsymbol{B}_i$) associated to each elementary discretisation segment i. (f) View of a cross section in a ($\boldsymbol{N}_i$,$\boldsymbol{B}_i$) plane of the 3D sub-volume and associated tangent vectors to the tube-fluid and fluid-air interfaces as well as local contact angles θ_i. The arrow shows that a clock-wise positive measurement of angles was chosen by convention. (g) Evolution of the local angle θ_i along the curvilinear abscissa s of the triple line.

7.3.5 Measurement of the surface curvatures

The local mean curvatures of the interface between the fluid and the air phases was estimated using an approach developed by Flin et al. (Flin et al., 2004; Flin et al., 2005). The method is based on the following expression of the mean curvature κ at a point P located at the interface between the fluid and the air which is defined as the divergence of the downward unit normal vector $\boldsymbol{n}(P)$:

$$\kappa(P) = \frac{\boldsymbol{\nabla} \cdot \boldsymbol{n}(P)}{2} \tag{7.3}$$

The algorithm computes the normal vectors $\boldsymbol{n}(P)$ using the volumetric information related to the gradient in the grey levels of the signed distance map of a binarised 3D image of the fluid phase (Figure 7.4a). An example of a 3D map of the mean curvature of the fluid-air interface is shown in Figure 7.4b. A corresponding 2D map of the mean curvature is shown in Figure 7.4c and was obtained by projecting the 3D map on the (x, y) plane. This 2D map was then smoothed with a coarse graining approach (Molnár et al., 2016). To check the relevance of the measurements, the algorithm was tested using binarised 3D images of the tubes whose curvature is known. From the mean curvature map, it was then possible to estimate the local capillary pressure P_c using the Laplace-Young equation:

$$P_c = P_v - P_l = 2\,\gamma_{lv}\kappa \tag{7.4}$$

where $P_v - P_l$ is the pressure difference across the air-fluid interface.

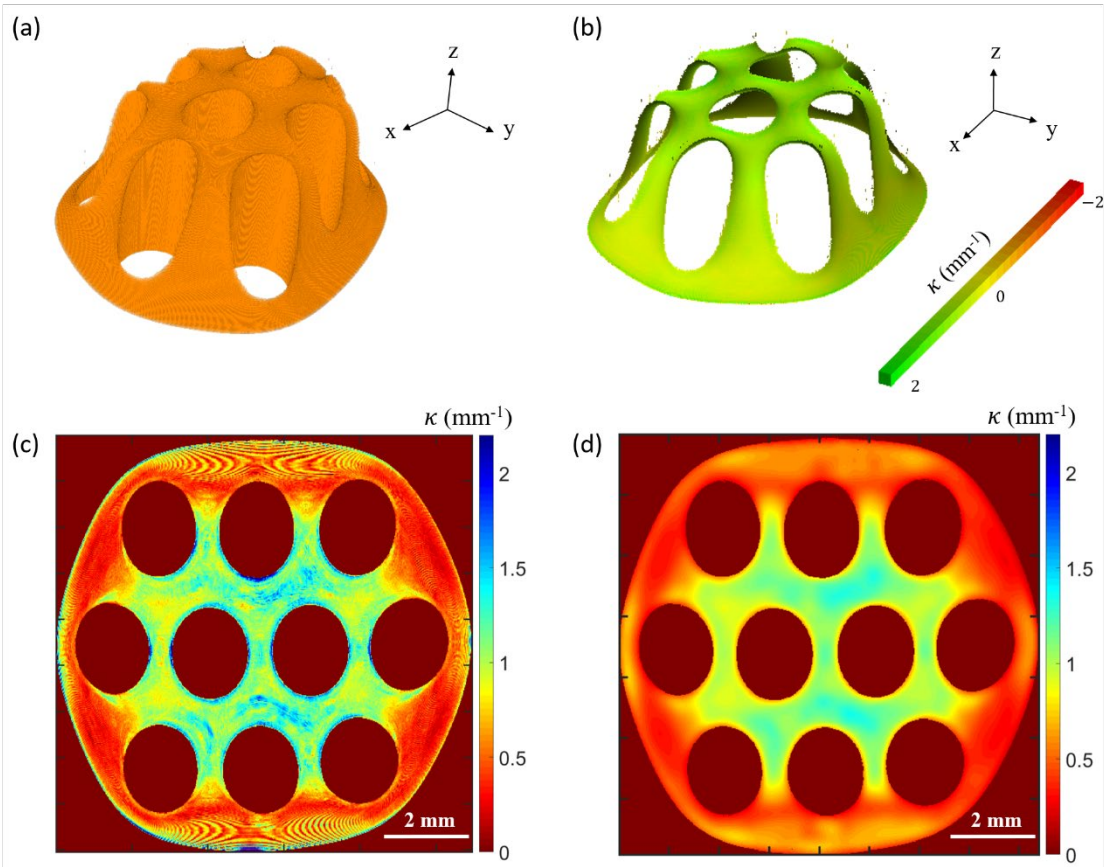

Figure 7.4. (a) Example of a 3D view of a binarised image of the fluid phase obtained during an impregnation experiment with the silicone oil. (b) 3D view of the mean curvature κ of the fluid-air interface. (c) Corresponding 2D map obtained by projecting the 3D map on the (x-y) plane. (d) Smoothed 2D map of the mean curvature κ obtained using a coarse graining approach (Molnár et al., 2016).

7.4 Results

7.4.1 Analysis of the in situ impregnation experiments

Figure 7.5 shows vertical cross sections of the 3D images acquired during the impregnation of the model fibre network with silicone oil or demineralised water.

7.4.1.1 Impregnation sequence using interrupted scanning conditions

The impregnation experiment that was performed using the silicone oil consisted in a sequence of six impregnation stages. They are denoted A–F in Figure 7.5a. In image A, the silicone oil was not in contact with the model fibre network. The bottom extremities of the tubes were located at a vertical distance of approximately 2 mm of the fluid-air interface, as shown in the position-time graph in the inset of Figure 7.5a. This image revealed that the fluid-air interface was nearly planar in spite of the rotation of the platen of the X-microtomograph stage during scanning. The slight distortion of the fluid-air interface

observed on the edges of image A was presumably due to the presence of a meniscus that formed on the wall of the cylindrical reservoir. In stage B, the model fibre network was immersed in the silicone oil. The extremities of the tubes reached a depth of approximately -0.3 mm measured with respect to the initial position of the fluid-air interface of stage A. In stage C, this depth was -4.2 mm. Then the fluid reservoir was moved downwards in stages D and E until the fluid meniscus that formed between the tubes and the fluid was broken (stage F). Images obtained for stages B and C showed that the fluid rose between the tubes of the model fibre network. The fluid reached its maximum height in the centre of the network and the fluid-air interface formed a dome-like shape (see also Figure 7.4a). Note that the image spatial resolution allows observing the shape of the menisci that formed where the tubes crossed the fluid-air interface. Besides, as the tubes were sealed at their top extremities, the fluid could not rise inside the tubes. Only a slight meniscus formed at their lower extremities. Images B and C did not reveal any significant changes between the overall shape of the dome that formed within the model fibre network apart from its left-hand and right-hand side borders (close to tubes 4 and 7) where a slight difference in the shape of the menisci was noticed. Similar observations could be done for the outer tubes of the model fibre network. For the tubes 5 and 6, these observations revealed that the fluid tended to slide on the tube surfaces when the reservoir was lifted up. When the reservoir was pulled down (stages D and E), again the fluid tended to slide on the tube surfaces which induced that the dome-like shape of the fluid-air interface was mostly preserved. However, the shape of the menisci of the outer tubes was affected. These phenomena will be further analysed and quantified in next sections by quantifying the local contact angles θ_i and the lengths of the triple lines l along all the tubes for stages B and E. In stage F, the reservoir was further pulled down, which resulted in the breakage of the capillary bridge. Finally, a volume of liquid was trapped within the model fibre network.

7.4.1.2 Impregnation sequence using sequentially continuous scanning conditions

The impregnation experiment described in this section was performed using demineralised water in a sequence of six impregnation stages (A-F) of the model fibre network. For each of this stage a sequence of ten images (A_i, B_i, C_i… with $i = 1, 2 \ldots 10$) was obtained (1 image every 2 s). Starting from the initial position (stage A_1), where the extremities of the tubes were above the fluid surface, the fluid reservoir was moved upwards and the extremities of the tubes entered in contact with the fluid (stage A_{10}), as shown in Figure 7.5b. Then, the reservoir was further moved upwards (stage B) before being gradually withdrawn (stages C-F). Similarly to the previously described impregnation experiment performed using silicone oil, a dome-like shape of the fluid-air interface was obtained. However, the height of the "dome" reached at the centre of the model fibre network was lower (2 < 3.70 mm). Slight height variations of the fluid-air interface were visible in the vertical cross section in Figure 7.5b. These variations were due to slight vertical misalignments of the tubes of the model fibre network used in this experiment. Contrary to what was observed with silicone oil, it is visible from Figure 7.5b of stage F that the capillary bridge was not broken for a similar withdrawing position of approximately 2 mm.

In Figure 7.5b, the zones of the fluid phase highlighted with a lighter blue were obtained by subtracting the volume of fluid of image 1 (resp. image 10) to image 10 (resp. image 1) for the sequences $A_{1\text{-}10}$ and $B_{1\text{-}10}$ ($C_{1\text{-}10}$, $D_{1\text{-}10}$, $E_{1\text{-}10}$ and $F_{1\text{-}10}$). This allows the evolution of the geometry of the fluid front to be followed live for 20 s. For each stage (from B to F), the vertical cross sections show that the fluid that was trapped in the centre of the model fibre network (around tubes 5 and 6) did not move significantly. On the contrary, the fluid motion could be clearly observed on the edges of the model fibre network (tubes 4 and 7 in the vertical cross section of Figure 7.5b). The vertical cross section of stage B shows that the menisci that formed on the inner tubes 5 and 6 did not exhibit significant geometric changes between images B_1 and B_{10}. In addition, the menisci that formed on the outer tubes of the model fibre networks showed slight changes. Thus, the fluid tended to slide on the surfaces of the tubes of the model fibre network. The evolution of the menisci will be discussed in detail in the next sections. Stages C-F reveal that the menisci that formed on the inner tubes 5 and 6 were apparently not affected by the withdrawing motion of the reservoir. On the contrary, the menisci that formed on the outer tubes were distorted. The triple line was like anchored on the outer tubes. The positions of the triple points on tubes 4 and 7 in Figure 7.5b did not change and the local contact angles exhibited a decrease (the values of the local contact angles θ_i will be given in next sections).

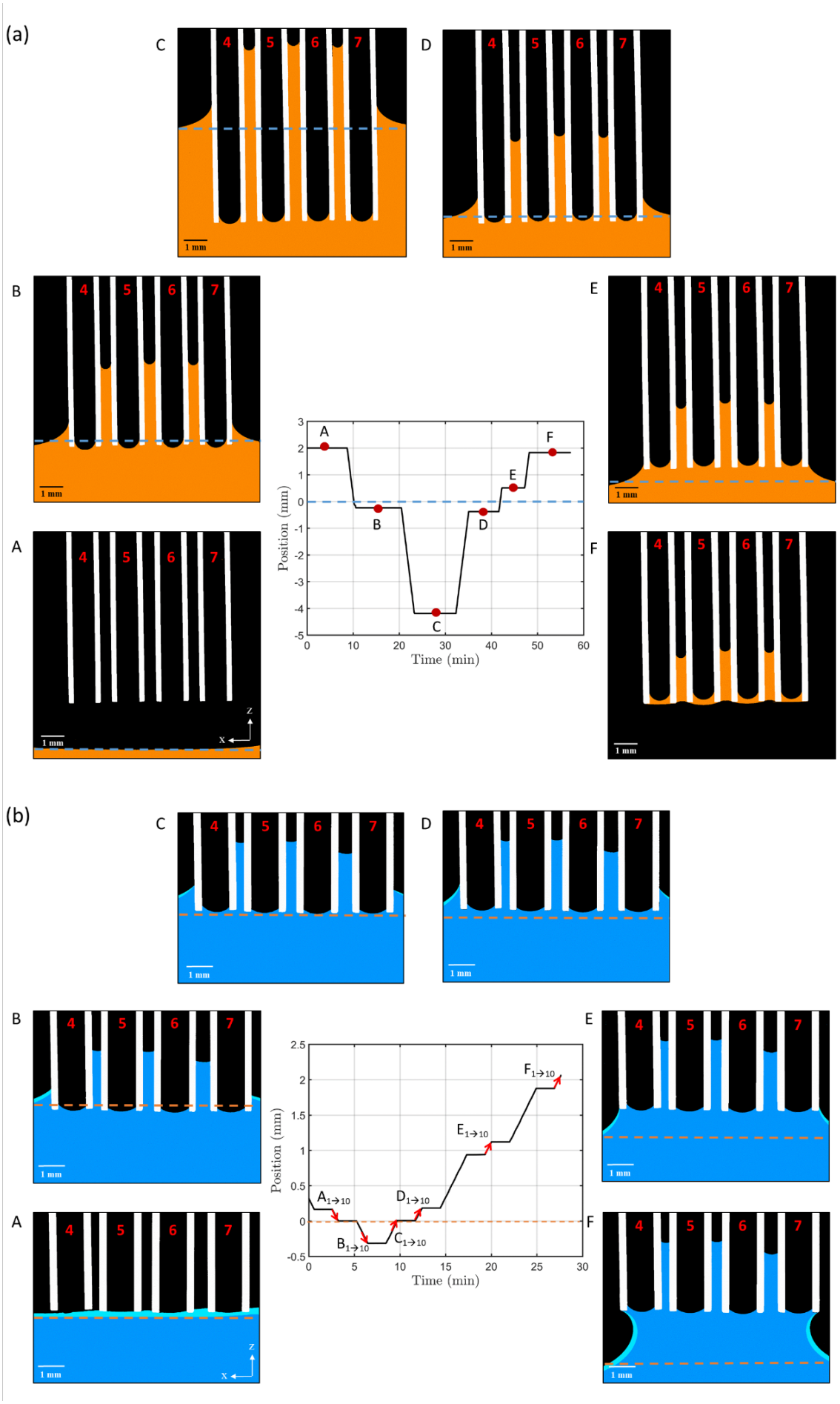

Figure 7.5. Vertical cross sections of the 3D images acquired during the impregnation of the model fibre network with silicone oil (a) and demineralised water (b). The dashed lines show the initial position of the fluid surface. The tubes are represented in white, the air in black, the silicone oil in orange and the demineralised water in blue. The graphs represent the position of the bottom extremities of the tubes with respect to the initial position of the fluid surface as a function of time. The red arrows in the graph indicate the time intervals when the sequences of 3D images were acquired.

7.4.2 Contact angles and triple line lengths

7.4.2.1 Interrupted conditions

Figure 7.6a,b show the measurements of the local contact angles θ_i along the triple lines that formed along all the tubes of the model fibre network for stages B and E for the experiments performed with the silicone oil. For these two stages, these figures show that the local contact angles θ_i exhibit a great variation along the triple lines, regardless of the tube. The difference between the maximum and the minimum values was almost 15° for each tube. The dispersion of the values of the local contact angles was higher for the outer tubes whose triple lines were more distorted than for the tubes located at the centre of the model fibre network (tubes 5 and 6). A further analysis of the evolution of the local contact angles along the triple lines of all the outer tubes showed that the lowest values of the contact angles θ_i were obtained for regions of the triple lines that were not located in the vicinity of other tubes.

Figure 7.6c shows the mean values $\bar{\theta}$ of the local contact angles for all the tubes of stages B and E, as well as the standard deviation of θ_i. The mean contact angle $\bar{\theta}$ varied for all the tubes. However, it is interesting to notice that the mean contact angles $\bar{\theta}$ of the tubes in symmetry positions (tubes 1,3,8,10 or tubes 2,9 or tubes 5,6) were almost equal. The mean value $\bar{\theta}$ of the tubes 5 and 6 at the centre of the model fibre network were also slightly higher than those measured for the outer tubes. In stage B, the mean value was 35° for tubes 5 and 6, whereas it was 29° for the outer tubes. In stage E, this difference decreased: the mean value $\bar{\theta}$ of the tubes 5 and 6 was 32°, whereas it was 27° for the outer tubes. This difference shows that the mean contact angles $\bar{\theta}$ tended to decrease with the withdrawing of the reservoir.

Figure 7.6d shows the lengths of the triple lines for stages B and E. For the tubes 5 and 6, the lengths of the triple lines were almost similar to that of the perimeter of the tube (~4.8 mm). The triple lines of the outer tubes were strongly distorted (see also Figure 7.3d) and their lengths were much greater (~8 mm). However, there were no significant changes between the lengths measured in stages B and E.

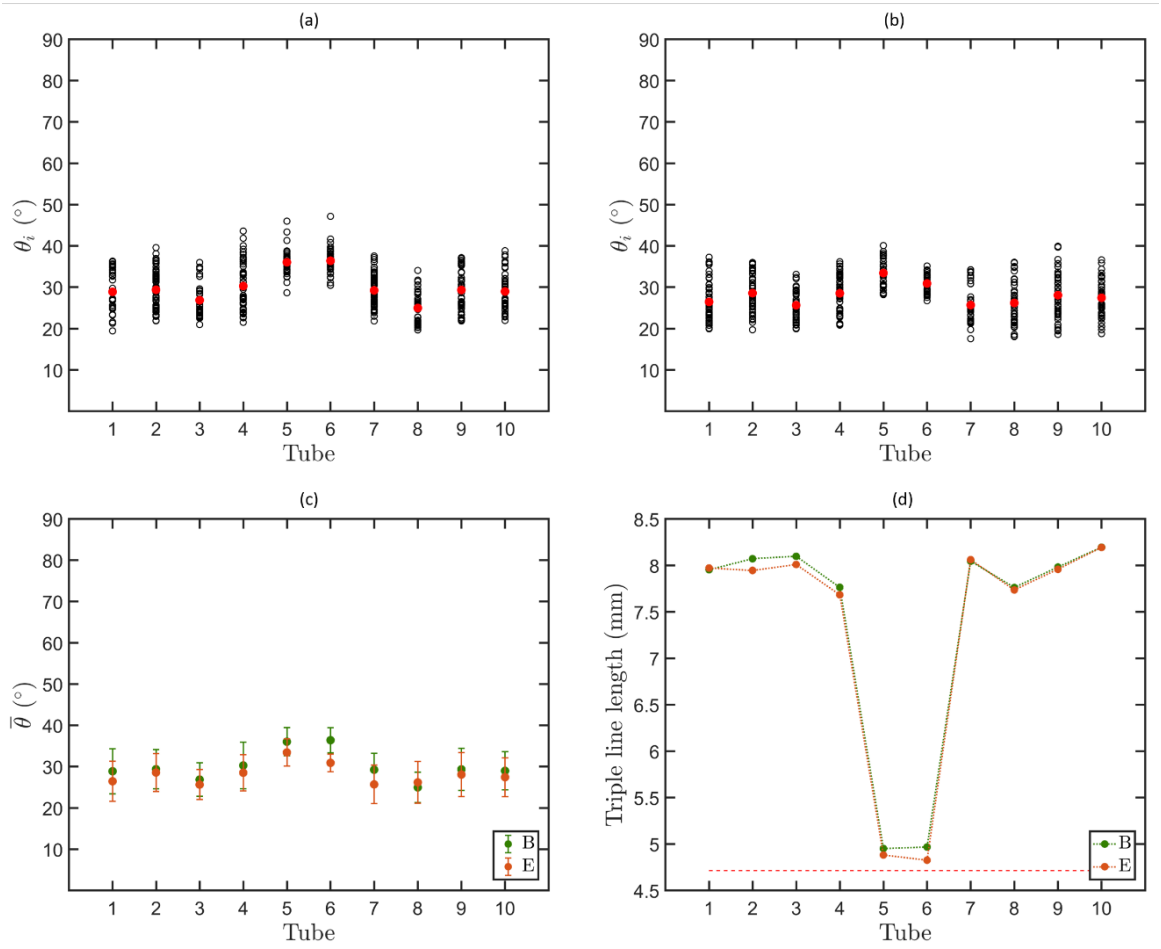

Figure 7.6. Values of local contact angles θ_i measured along the triple lines of all the tubes of the model fibre network for stages B (a) and E (b) of the impregnation experiment performed using silicone oil. (c) Corresponding mean values $\bar{\theta}$ and standard deviations for stages B and E. (d) Lengths of the triple line for all the tubes of the model fibre network for stages B and E. The red dashed line represents the length of the perimeter of the circular tubes used to build the model fibre network.

7.4.2.2 Sequentially continuous conditions

Figure 7.7a shows the mean contact angles $\bar{\theta}$ measured for stages B_1 and B_{10}, D_1 and D_{10} and their standard deviations for the impregnation experiments performed using demineralised water. As observed previously, the mean contact angle $\bar{\theta}$ also varied for all the tubes. In addition, the mean contact angles $\bar{\theta}$ for stage B_1 were slightly lower than for stage B_{10}. The mean contact angles for stages B_1 and B_{10} were $\bar{\theta}_{B_1}$ =72° and 73°, respectively. A more pronounced difference could be observed for the outer tubes than the inner ones (5 and 6). The origin of this slight increase might be due to the flattening of the menisci that formed around the tubes when the reservoir was lifted up (or conversely when the model fibre network was plunged into the demineralised water).

On the contrary, when the reservoir was withdrawn, the mean contact angle tended to decrease between stages D_1 and D_{10} in a more pronounced manner as $\bar{\theta}_{D_1} = 63°$ and

$\bar{\theta}_{D_{10}} = 58°$. It was also apparent that the standard deviation values were larger for stages D than B, i.e. during the withdrawing of the reservoir. This result is confirmed by the difference between the maximum and the minimum values of the local contact angles that was equal to 15° (resp. 45°) for stage B (resp. D).

Figure 7.7b shows the variation of the lengths of the triple lines for the same stages. For the inner tubes (5 and 6), no clear differences in the lengths of the triple lines could be observed. This is in accordance with the observations made in section 7.4.1.2: the positions of the fluid-air interface and triple lines at the centre of the model fibre network did not vary significantly when the reservoir was moved upwards or downwards. The lengths of the triple lines along the outer tubes tended to decrease when the reservoir was lifted up, as shown for stages B_1 and B_{10}. This could be related to the increase in the position of the fluid-air interface around the model fibre network. In contrast, the lengths of the triple lines between stages D_1 and D_{10} increased slightly. In parallel, the mean contact angles $\bar{\theta}$ showed a large decrease, thus confirming the observations made on the vertical cross sections shown in Figure 7.5b, i.e. the triple lines were like anchored on the tube surface during the withdrawing of the reservoir.

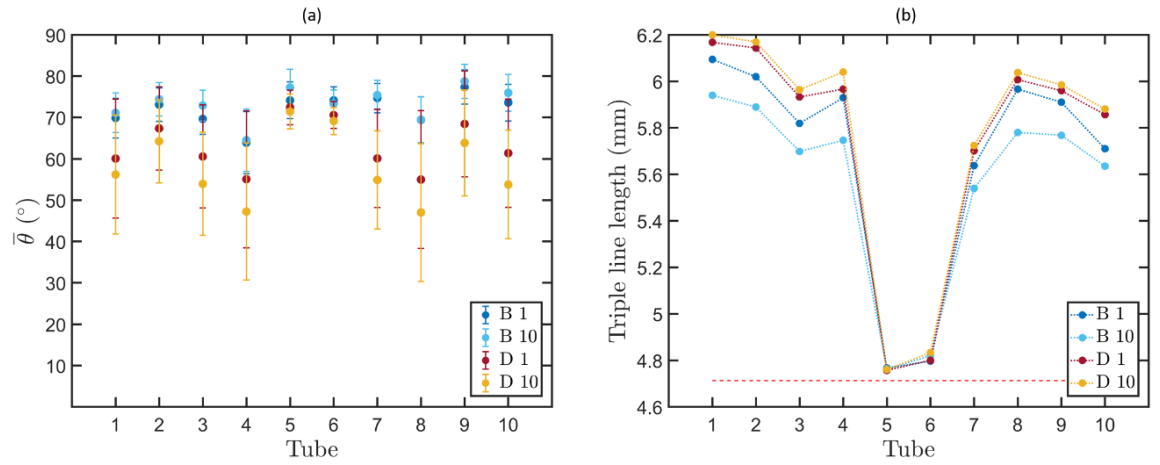

Figure 7.7 (a) Mean contact angles $\bar{\theta}$ for all the tubes of the model fibre network and stages B_1, B_{10}, D_1 and D_{10} of the impregnation experiment performed using demineralised water. (b) Corresponding lengths of the triple lines.

7.4.3 Capillary forces

Using the values of the local contact angles and the lengths of the triple lines, the components F_x, F_y and F_z of the capillary forces exerted by the fluids on each tube of the model fibre network were calculated. The direction and intensity of the transverse capillary force $F_\perp = \sqrt{F_x^2 + F_y^2}$ exerted on each tube by the fluid are shown in Figure 7.8a-c and Figure 7.9a-c for the sample impregnated with the oil for stages B and E, and demineralised water for stages B_1, B_{10}, D_1 and D_{10}, respectively. The normalised intensities of the transverse $F_\perp^* = F_\perp/(2\pi r_e \gamma_{lv} cos\theta_e)$ and longitudinal $F_\parallel^* = |F_z|/(2\pi r_e \gamma_{lv} cos\theta_e)$ capillary

forces measured for each tube are reported in Figure 7.8b,c and Figure 7.9d,e for the two impregnation experiments.

Figure 7.8a and Figure 7.9a-b show that the transverse forces $F_{\perp}$ exerted on the inner tubes were negligible. On the contrary, the transverse forces $F_{\perp}$ exerted on the outer tubes tend to point towards the centre of the fibre network, regardless of the impregnation stages for both experiments. Slight variations in the directions of $F_{\perp}$ could be observed between the various impregnation stages. These results were in accordance with the aforementioned variations of the local contact angles and lengths of the triple lines (Figures 7.6 and 7.7).

In addition, Figures 7.8b,c and 7.9c-f show the dimensionless transverse $F_{\perp}^{*}$ and longitudinal $F_{\parallel}^{*}$ capillary forces exerted by the fluid on each tube. For the inner tubes (5 and 6), the transverse forces were negligible which is due to the symmetries of the model fibre networks, whereas for some of the outer tubes (tubes 1, 3, 4, 7, 8 and 10), both forces were of the same order of magnitude. For tubes 2 and 9, the transverse capillary forces were approximately one half or more lower than the longitudinal forces. Figures 7.8b,c show that the dimensionless longitudinal capillary forces were approximately equal to 1 (except for tubes 2 and 9). This tends to show that the longitudinal capillary exerted by the fluid on each tube of the fibre model network is close to that obtained for a single tube plunged in the silicone oil with a meniscus that would form a constant contact angle equal to θ_e. As already noticed for the measurements of the mean contact angles, the forces obtained for the experiments performed with the demineralised water showed a higher discrepancy than those measured for the silicone oil. A possible origin of this discrepancy might be a poorer precision in the placement of tubes (e.g. slight inclination or misalignment) in the model fibre network used for the experiments performed with the demineralised water. This discrepancy could also be related to a wider diversity of physicochemical interactions between water and the surfaces of the tubes.

For the experiments performed using the silicone oil, the comparison of Figures 7.8b and 7.8c show that the withdrawing of the fluid reservoir tended to slightly increase the dimensionless longitudinal capillary forces $F_{\parallel}^{*}$. This effect was less clear for the dimensionless transverse capillary forces $F_{\perp}^{*}$. This increase could be associated to the slight decrease in the mean contact angles as shown in Figure 7.6c. A similar but more pronounced tendency to the increase in both capillary forces is revealed by comparing Figures 7.9c,d with Figures 7.9e,f. More interestingly, the comparison of stages B_1 (resp. D_1) with B_{10} (resp. D_{10}) shows a decrease (resp. an increase) in both capillary forces when the reservoir was moved upwards (resp. downwards). Again, these tendencies have to be related to the aforementioned evolutions of the contact angles and lengths of the triple lines, as shown in Figures 7.7a,b.

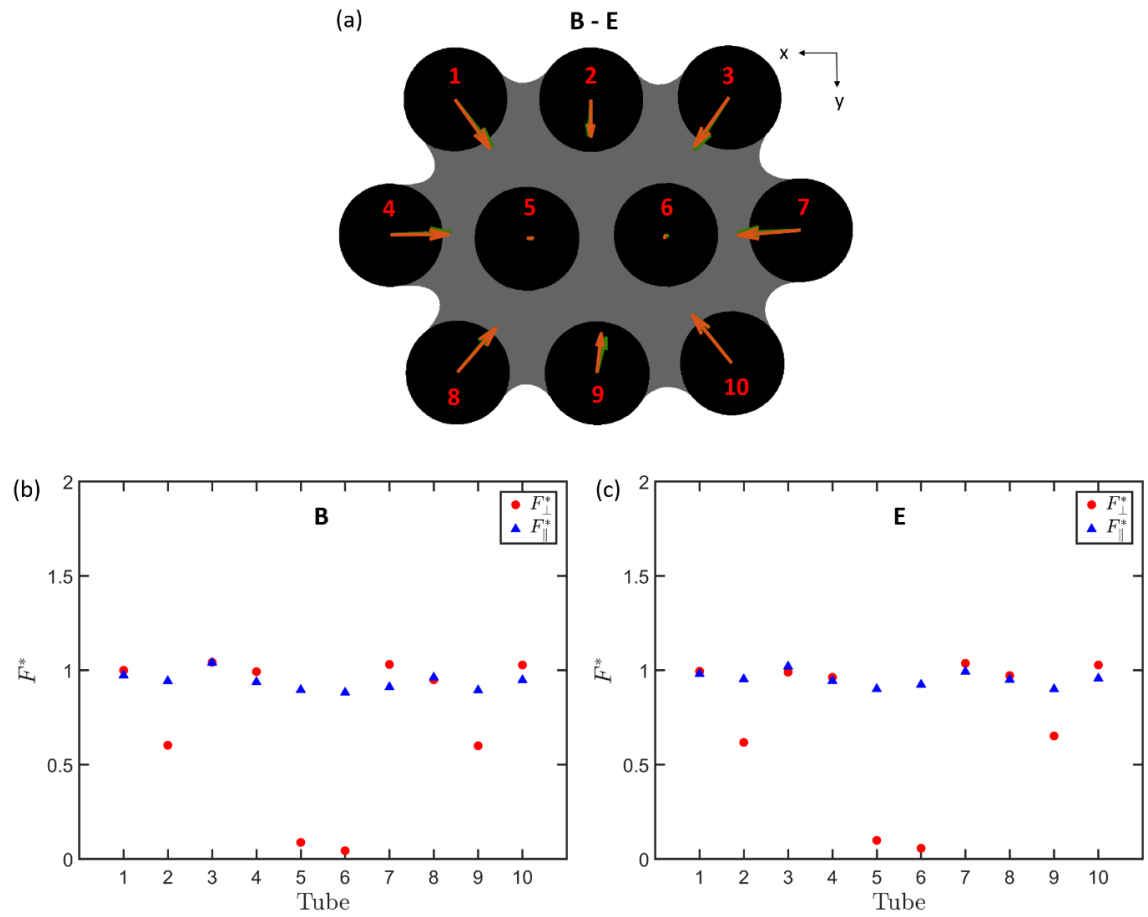

Figure 7.8. (a) Cross section of the model fibre network showing the transverse capillary force $F_\perp$ exerted by the fluid on each tube (in black) for stages B (green arrows) and E (orange arrows) of the impregnation experiment carried out with the silicone oil. The application points of the forces were placed arbitrary on the axes of the tubes. The cross section of the model fibre network was also chosen arbitrary (the fluid is grey in the cross section). (b-c) Graphs showing the dimensionless transverse $F^*_\perp$ and longitudinal $F^*_\parallel$ capillary forces exerted by the fluid on each tube for stages B (b) and E (c).

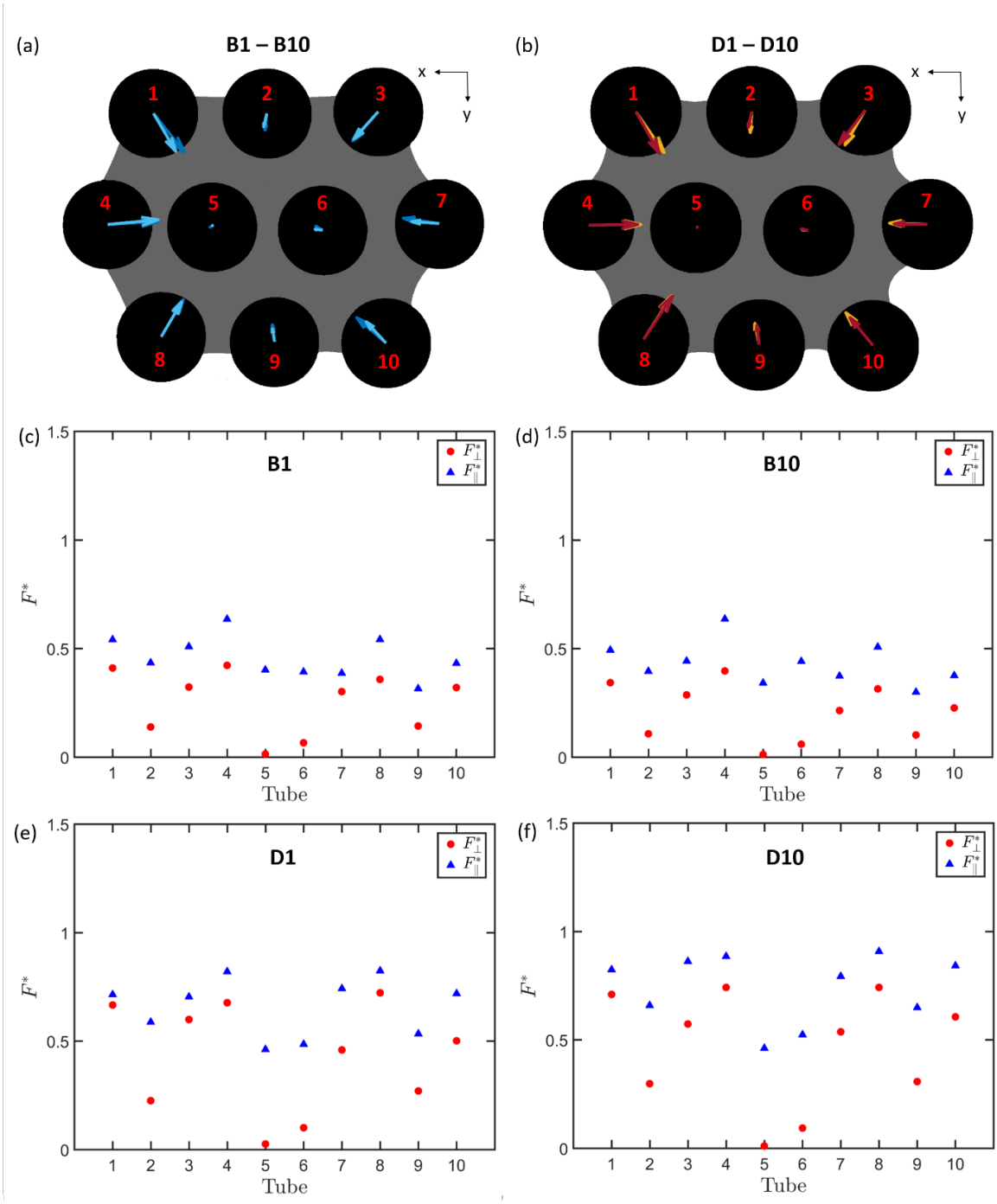

Figure 7.9. (a,b) Cross sections of the model fibre network showing the transverse capillary force $F_\perp$ exerted by the fluid on each tube (in black) for stages B_1 (dark blue arrows) and B_{10} (pale blue arrows) and D_1 (red arrows) and D_{10} (yellow arrows) of the impregnation experiment carried out with the demineralised water. The application points of the forces were placed arbitrary on the axes of the tubes. The cross section of the model fibre network was also chosen arbitrary (the fluid is grey in the cross section). Graphs showing the dimensionless transverse $F^*_\perp$ and longitudinal $F^*_\parallel$ capillary forces exerted by the fluid on each tube for stages B_1 (c), B_{10} (d), D_1 (e) and D_{10} (f).

7.4.4 Fluid front curvatures and capillary pressure

Figure 7.10a shows 2D maps of the mean curvature κ for stages B of the impregnation experiment performed using silicone oil. The mean curvature κ measured in the centre of the model fibre network ranged between 0.80 mm^{-1} and 1.20 mm^{-1} (Figure 7.10a). Consequently, the local capillary pressure P_c in the centre of the model fibre network ranged between approx. 35 and 55 Pa (Figure 7.10b). In addition, Figure 7.10c shows that the average capillary pressure $\bar{P}_c$ measured in the centre of the model fibre network did not show large variations, regardless of the impregnation stages. This is in accordance with the previous observations related to Figure 7.5a since the geometry of the dome-like shape of the fluid-air interface did not exhibit significant changes. On the outer edge of the fibre network, the mean curvature κ was lower and ranged between 0.36 mm^{-1} and 0.50 mm^{-1} (Figure 7.10a).This corresponds to a local capillary pressure P_c that was comprised between 15 Pa and 21 Pa (Figure 7.10b).

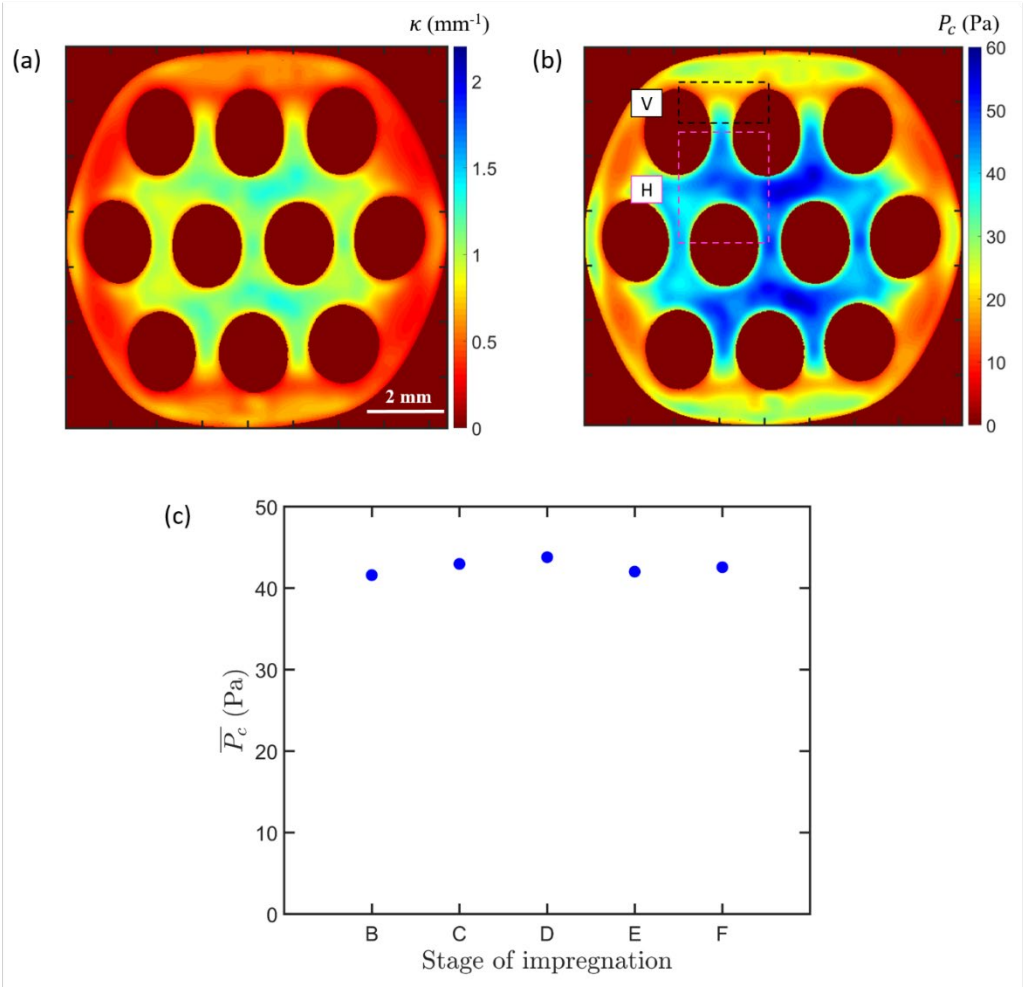

Figure 7.10. (a) 2D map of the mean curvature κ of the fluid-air interface for stage B of the impregnation experiment performed using silicone oil. (b) Corresponding 2D map of the capillary pressure P_c. The traces of the tubes are not perfectly circular in the 2D maps because of their possible slight vertical misalignement. (c) Average capillary pressure $\bar{P}_c$ in the centre of the model fibre network as a function of the impregnation stage.

7.5 Discussion

7.5.1 Variations in the local contact angles

For both investigated fluids this study revealed that during the impregnation experiments, the local contact angles exhibited large variations along the triple lines formed onto the surfaces of the tubes of the model fibre network. These observations were done during the wetting (upward motion of the fluid reservoir) or dewetting (downward motion of the fluid reservoir) of the model fibre network with both fluids. This phenomenon was pronounced for the outer tubes of the network (Figures 7.6 and 7.7).

Using 3D images similar observations have already been made for geomaterials and granular materials with complex porous structure (Andrew et al., 2015; Andrew et al., 2014; Alhosani et al., 2021; Ibekwe et al., 2020b) impregnated with a wetting fluid. If the wetting fluid is at rest (in "static" conditions), these variations can be associated to several factors such as the local roughness and heterogeneities in the physicochemical properties of the surface of solid, or the topology of pores (Dalton et al., 2020; AlRatrout et al., 2018). A relaxation phenomenon of the local contact angles towards an equilibrium contact can also be a possible origin of these variations. Indeed, the authors observed that relaxation can occur at different rates along the contact lines and thus also leads to contact angle distributions.

Several authors (Andrew et al., 2015; Andrew et al., 2014) have also reported that imbibition or drainage (fluid in "dynamic conditions) of a granular porous media by a wetting phase can induce localised small pressure perturbations in the wetting phase and variations in the contact angles. During imbibition, the authors observed motions of the contact lines once the contact angles approached (or exceeded) a maximal contact angle (denoted as the advancing contact angle). During drainage, they observed motions of the contact lines once the contact angles approached a minimum angle (denoted as the receding contact angle). Similar scenarios are expected to occur in our experiments.

7.5.2 Comparison of capillary pressure measurements and theoretical predictions

From the local capillary pressure maps, it was possible to identify two characteristics zones (denoted H and V in Figure 7.10a,b). These zones were located in the centre and on the side of the model fibre network, respectively. They corresponded to fluid-air interface zones that were nearly perpendicular or parallel to the tubes' axes. As mentioned previously in section 7.3.5, the algorithm proposed by Flin et al. (Flin et al., 2004; Flin et al., 2005) enables the unit normal vector $\boldsymbol{n}$ to the fluid-air interface to be computed. The components of the unit average normal vector $\overline{\boldsymbol{n}}$ were (0.05, -0.13, -0.99) in zone H and (-0.01, -0.94, -0.34) in zone V, showing that these vectors were nearly aligned with the tube axes or perpendicular to the tube axes, respectively. Then, the average capillary pressure $\bar{P}_c$ was

estimated in the fluid domain of zones H and V. In zone H (resp. V), the pressure $\bar{P}_c$ was equal to 45 Pa (resp. 21 Pa). The pressure measured in zone H is in accordance with that given by the fluid statics that can be estimated from the relative height $\bar{z}$ of the fluid-air interface and the gravity force g, i.e., $\bar{P} = \rho g \bar{z} \approx 39$ Pa. This shows once again that the mean curvature of the fluid-air interface is relevant. These values can be compared to the predictions of the model proposed by Ahn et al. (Ahn et al., 1991) for the prediction of the average capillary pressure within porous media consisting of arrays of parallel fibres:

$$\bar{P}_c = F \frac{\gamma_{lv} \cos\theta \, (1 - \phi_p)}{2\phi_p r_e} \tag{7.5}$$

with θ the contact angle of the fluid on the fibre, ϕ_p the porosity, and F is a form factor that depends on the flow direction and fibre network geometry. For flow parallel or transverse to fibres, F is equal to 4 and 2, respectively. To estimate the capillary pressure $\bar{P}_c$ from Eq. 7.5, the average of the local contact angles θ_i was calculated along the portions of the triple lines formed along the tubes comprised in zones H or V (Figure 7.6a). For zone H, this average value was equal to 35°, whereas, for zone V, it was equal to 27.5°. Furthermore, the porosity ϕ_p=0.55 corresponds to the porosity of a period of the triangular tube arrangements that constitute the model fibre network. Then, the model prediction for the capillary pressure was 38 Pa for zone H and 20 Pa for zone V, showing a good agreement with the experimental measurements.

7.5.3 Interest of measurements of capillary forces

The measurements of the capillary forces exerted by the fluid on the tubes performed in this study are original. They showed that in this network of parallel fibres the transverse capillary forces $F_{\perp}^{*}$ measured on the outer tubes are important and of the same order of magnitude as the longitudinal capillary forces $F_{\parallel}^{*}$. In networks with similar geometry made of deformable fibres (e.g. bundles of glass or carbon filaments), these forces would severely deform each fibre and probably pull them closer to each other in the form of an aggregate (Duprat et al., 2012; Bico et al., 2004; Py et al., 2007). The knowledge of such forces in real fibre bundles used for instance in composite processing routes such as pultrusion would help in properly controlling the fibrous microstructure of the obtained composite parts.

7.6 Conclusion

We carried out an analysis of the capillary phenomena that occur during the impregnation at low capillary number of a fibre network made of arrays of parallel glass tubes. This network mimics the structure of fibre bundles that are classically used in composite reinforcement materials. For that purpose, a specific device was especially developed and allowed the acquisition of 3D X-ray microtomography images of several wetting and dewetting stages of the fibre network. Two types of wetting fluids, namely demineralised

water and silicone oil, were used. Specific image analysis procedures were adapted or developed to measure the triple line lengths, local contact angles, fluid-air interface mean curvature. This original database allowed calculating the local capillary forces exerted on each tube of the fibre network by the fluid as well as the local capillary pressure. The results showed that the transverse forces are of the same order of magnitude as the longitudinal capillary forces. To the best of our knowledge, the measurements of the local transverse component of the capillary forces exerted on the individual elements that constitute a fibre network are original. This is an important result for a better understanding and control of the impregnation phase of fibrous reinforcements used in composite materials because the propagation of a polymer matrix within fibre bundles is partially governed by capillary forces that can often lead to complex deformation phenomena of fibre bundles made of compliant fibres (Duprat et al., 2012; Bico et al., 2004; Py et al., 2007). The induced perturbation on the propagation of the flow front of the matrix and the deformation of the fibre bundles can lead to several microstructural defects such as the formation of voids because of air entrapment phenomena (Michaud, 2016; Binetruy et al., 1998; Park & Lee, 2011; Leclerc & Ruiz, 2008; Y. T Chen et al., 1995; Ruiz et al., 2006). Understanding and controlling the flow front propagation would allow reducing composite defects which are detrimental for their mechanical performances.

Our results confirmed that large variations in the local contact angles can occur in quasi static impregnation situations as it has already been reported in several studies dealing with the impregnation of geomaterials (Andrew et al., 2015; Andrew et al., 2014; Alhosani et al., 2021; Ibekwe et al., 2020b). Our results also enabled testing the relevance of the theoretical predictions of an average capillary pressure model proposed by Ahn et al. (Ahn et al., 1991). The predictions for the average capillary pressure appearing during longitudinal and transverse flow situations were in accordance with our experimental measurements.

Finally, this study shows that a fine description of the geometry of the fluid-air interfaces, contact lines and local contact angles in fibre networks is accessible through the analysis of 3D images obtained using synchrotron X-ray microtomography. It also shows that the local capillary pressure and forces can be finely estimated. This experimental approach could be extended to natural or synthetic materials with deformable fibres when subject to capillary forces (Duprat et al., 2012; Bico et al., 2004; Py et al., 2007). It is also important to note that the numerical modelling of the presented results would certainly constitute a challenging task. Indeed, impregnation experiments performed at low capillary numbers are usually modelled using a unique “equilibrium” contact angle (Charpentier et al., 2020; Vennat et al., 2010; Chevalier et al., 2018) which is not in line with the experimental evidence.

References

Advani, S. G., & Hsiao, K.-T. (2012). *Manufacturing techniques for polymer matrix composites (PMCs)*. Elsevier.

Ahn, K. J., Seferis, J. C., & Berg, J. C. (1991). Simultaneous measurements of permeability and capillary pressure of thermosetting matrices in woven fabric reinforcements. *Polymer Composites*, *12*(3), 146-152. https://doi.org/10.1002/pc.750120303

Alhosani, A., Lin, Q., Scanziani, A., Andrews, E., Zhang, K., Bijeljic, B., & Blunt, M. J. (2021). Pore-scale characterization of carbon dioxide storage at immiscible and near-miscible conditions in altered-wettability reservoir rocks. *International Journal of Greenhouse Gas Control*, *105*, 103232. https://doi.org/10.1016/j.ijggc.2020.103232

AlRatrout, A., Blunt, M. J., & Bijeljic, B. (2018). Spatial Correlation of Contact Angle and Curvature in Pore-Space Images. *Water Resources Research*, *54*(9), 6133-6152. https://doi.org/10.1029/2017WR022124

Alratrout, A., Raeini, A. Q., Bijeljic, B., & Blunt, M. J. (2017). Automatic measurement of contact angle in pore-space images. *Advances in Water Resources journal*, *109*, 158-169. https://doi.org/10.1016/j.advwatres.2017.07.018

Amico, S. C., & Lekakou, C. (2002). Axial impregnation of a fiber bundle. Part 1 : Capillary experiments. *Polymer Composites*, *23*(2), 249-263. https://doi.org/10.1002/pc.10429

Amico, S., & Lekakou, C. (2004). Flow Through a Two-Scale Porosity, Oriented Fibre Porous Medium. *Transport in Porous Media, 54,* 35-53.

Andrew, M., Bijeljic, B., & Blunt, M. J. (2014). Pore-scale contact angle measurements at reservoir conditions using X-ray microtomography. *Advances in Water Resources*, *68*, 24-31. https://doi.org/10.1016/j.advwatres.2014.02.014

Andrew, M., Menke, H., Blunt, M. J., & Bijeljic, B. (2015). The Imaging of Dynamic Multiphase Fluid Flow Using Synchrotron-Based X-ray Microtomography at Reservoir Conditions. *Transport in Porous Media*, *110*(1). https://doi.org/10.1007/s11242-015-0553-2

Armstrong, R. T., Porter, M. L., & Wildenschild, D. (2012). Linking pore-scale interfacial curvature to column-scale capillary pressure. *Advances in Water Resources*, *46*, 55-62. https://doi.org/10.1016/j.advwatres.2012.05.009

Barraza, H. J., Hwa, M. J., Blakley, K., O'Rear, E. A., & Grady, B. P. (2001). Wetting Behavior of Elastomer-Modified Glass Fibers. *Langmuir*, *17*(17), 5288-5296. https://doi.org/10.1021/la0102071

Batch, G. L., Chen, Y.-T., & Macoskot, C. W. (1996). Capillary Impregnation of Aligned Fibrous Beds : Experiments and Model. *Journal of Reinforced Plastics and Composites*, *15*(10), 1027-1051. https://doi.org/10.1177/073168449601501004

Bayramli, E., & Powell, R. L. (1990). The normal (transverse) impregnation of liquids into axially oriented fiber bundles. *Journal of Colloid and Interface Science*, *138*(2), 346-353. https://doi.org/10.1016/0021-9797(90)90217-C

Bayramli, E., & Powell, R. L. (1991). Experimental investigation of the axial impregnation of oriented fiber bundles by capillary forces. *Colloids and Surfaces*, *56*, 83-100. https://doi.org/10.1016/0166-6622(91)80115-5

Bayramli, E., & Powell, R. L. (1992). Impregnation Dynamics of Carbon Fiber Tows. *Journal of Composite Materials*, *26*(10), 1427-1442. https://doi.org/10.1177/002199839202601002

Beltran, M. A., Paganin, D. M., Uesugi, K., & Kitchen, M. J. (2010). 2D and 3D X-ray phase retrieval of multi-material objects using a single defocus distance. *Optics Express*, *18*(7), 6423-6436. https://doi.org/10.1364/OE.18.006423

Bico, J., Roman, B., Moulin, L., & Boudaoud, A. (2004). Elastocapillary coalescence in wet hair. *Nature*, *432*(7018), 690-690. https://doi.org/10.1038/432690a

Binetruy, C., Hilaire, B., & Pabiot, J. (1998). Tow Impregnation Model and Void Formation Mechanisms during RTM. *Journal of Composite Materials*, *32*(3), 223-245. https://doi.org/10.1177/002199839803200302

Bréard, J., Saouab, A., & Bouquet, G. (1999). Dependence of the Reinforcement Anisotropy on a Three Dimensional Resin Flow Observed by X-Ray Radioscopy. *Journal of Reinforced Plastics and Composites*, *18*(9), 814-826. https://doi.org/10.1177/073168449901800903

Caglar, B., Tekin, C., Karasu, F., & Michaud, V. (2019). Assessment of capillary phenomena in liquid composite molding. *Composites Part A: Applied Science and Manufacturing*, *120*, 73-83. https://doi.org/10.1016/j.compositesa.2019.02.018

Castro, J., Sket, F., & González, C. (2020). S-XCT experimental determination of local contact angle and meniscus shape in liquid moulding of composites. *Composites Science and Technology*, *199*, 108362. https://doi.org/10.1016/j.compscitech.2020.108362

Charpentier, J.-B., Brändle de Motta, J. C., & Ménard, T. (2020). Capillary phenomena in assemblies of parallel cylindrical fibers : From statics to dynamics. *International Journal of Multiphase Flow*, *129*, 103304. https://doi.org/10.1016/j.ijmultiphaseflow.2020.103304

Chen, Y.T, Davis, H. T., & Macosko, C. W. (1995). Wetting of fiber mats for composites manufacturing : I. Visualization experiments. *AIChE Journal*, *41*(10), 2261-2273. https://doi.org/10.1002/aic.690411009

Chen, Y.T., Davis, H. T., & Macosko, C. W. (1995). Wetting of fiber mats for composites manufacturing : I. Visualization experiments. *AIChE Journal*, *41*(10), 2261-2273. https://doi.org/10.1002/aic.690411009

Chevalier, L., Bruchon, J., Moulin, N., Liotier, P.-J., & Drapier, S. (2018). Accounting for local capillary effects in two-phase flows with relaxed surface tension formulation in enriched finite elements. *Comptes Rendus Mécanique*, *346*(8), 617-633. https://doi.org/10.1016/j.crme.2018.06.008

Chwastiak, S. (1973). A Wicking Method for Measuring Wetting Properties of Carbon Yarns. *Journal of Colloid and Interface Science*, *42*(2). 298-309.

Dalton, L. E., Tapriyal, D., Crandall, D., Goodman, A., Shi, F., & Haeri, F. (2020). Contact Angle Measurements Using Sessile Drop and Micro-CT Data from Six Sandstones. *Transport in Porous Media*, *133*(1). https://doi.org/10.1007/s11242-020-01415-y

Duprat, C., Protière, S., Beebe, A. Y., & Stone, H. A. (2012). Wetting of flexible fibre arrays. *Nature*, *482*(7386), 510-513. https://doi.org/10.1038/nature10779

Endruweit, A., Glover, P., Head, K., & Long, A. C. (2011a). Mapping of the fluid distribution in impregnated reinforcement textiles using Magnetic Resonance Imaging : Methods and issues. *Composites Part A: Applied Science and Manufacturing*, *42*(3), 265-273. https://doi.org/10.1016/j.compositesa.2010.11.012

Endruweit, A., Glover, P., Head, K., & Long, A. C. (2011b). Mapping of the fluid distribution in impregnated reinforcement textiles using Magnetic Resonance Imaging : Application and discussion. *Composites Part A: Applied Science and Manufacturing*, *42*(10), 1369-1379. https://doi.org/10.1016/j.compositesa.2011.05.020

Flin, F., Brzoska, J. B., Coeurjolly, D., Pieritz, R. A., Lesaffre, B., Coléou, C., Lamboley, P., Teytaud, O., Vignoles, G. L., & Delesse, J. F. (2005). Adaptive estimation of normals and surface area for discrete 3-D objects : Application to snow binary data from X-ray tomography. *IEEE Transactions on Image Processing*, *14*(5), 585-596. https://doi.org/10.1109/TIP.2005.846021

Flin, F., Brzoska, J. B., Lesaffre, B., Coléou, C., & Pieritz, R. A. (2004). Three-dimensional geometric measurements of snow microstructural evolution under isothermal conditions. *Annals of Glaciology*, *38*, 39-44. https://doi.org/10.3189/172756404781814942

Ibekwe, A., Pokrajac, D., & Tanino, Y. (2020a). Automated extraction of in situ contact angles from micro-computed tomography images of porous media. *Computers and Geosciences*, *137*, 104425. https://doi.org/10.1016/j.cageo.2020.104425

Ibekwe, A., Pokrajac, D., & Tanino, Y. (2020b). Automated extraction of in situ contact angles from micro-computed tomography images of porous media. *Computers & Geosciences*, *137*, 104425. https://doi.org/10.1016/j.cageo.2020.104425

Klise, K. A., Moriarty, D., Yoon, H., & Karpyn, Z. (2016). Automated contact angle estimation for three-dimensional X-ray microtomography data. *Advances in Water Resources*, *95*, 152-160. https://doi.org/10.1016/j.advwatres.2015.11.006

Koubaa, S., Burtin, C., & Le Corre, S. (2016). Investigation of capillary impregnation for permeability prediction of fibrous reinforcements. *Journal of Composite Materials*, *50*(11), 1417-1429. https://doi.org/10.1177/0021998315593797

Kuentzer, N., Simacek, P., Advani, S. G., & Walsh, S. (2006). Permeability characterization of dual scale fibrous porous media. *Composites Part A: Applied Science and Manufacturing 37*, 2057-2068. https://doi.org/10.1016/j.compositesa.2005.12.005

Larson, N. M., & Zok, F. W. (2018). Insights from in-situ X-ray computed tomography during axial impregnation of unidirectional fiber beds. *Composites Part A: Applied Science and Manufacturing*, *107*, 124-134. https://doi.org/10.1016/j.compositesa.2017.12.024

Latil, P. (2012). *Micro-mécanismes de deformation des mèches de fibres saturées.* [PhD Thesis]. Univ. Grenoble Alpes.

Latil, P., Orgéas, L., Geindreau, C., Dumont, P. J. J., & Rolland du Roscoat, S. (2011). Towards the 3D in situ characterisation of deformation micro-mechanisms within a compressed bundle of fibres. *Composites Science and Technology*, *71*(4), 480-488. https://doi.org/10.1016/j.compscitech.2010.12.023

Laurencin, T., Orgéas, L., Dumont, P. J. J., Rolland du Roscoat, S., Laure, P., Le Corre, S., Silva, L., Mokso, R., & Terrien, M. (2016). 3D real-time and in situ characterisation of fibre kinematics in dilute non-Newtonian fibre suspensions during confined and lubricated compression flow. *Composites Science and Technology*, *134*, 258-266. https://doi.org/10.1016/j.compscitech.2016.09.004

Lawrence, J. M., Neacsu, V., & Advani, S. G. (2009). Modeling the impact of capillary pressure and air entrapment on fiber tow saturation during resin infusion in LCM. *Composites Part A: Applied Science and Manufacturing*, *40*(8), 1053-1064. https://doi.org/10.1016/j.compositesa.2009.04.013

Leclerc, J. S., & Ruiz, E. (2008). Porosity reduction using optimized flow velocity in Resin Transfer Molding. *Composites Part A: Applied Science and Manufacturing*, *39*(12), 1859-1868. https://doi.org/10.1016/j.compositesa.2008.09.008

Lin, Q., Bijeljic, B., Pini, R., Blunt, M. J., & Krevor, S. (2018). Imaging and Measurement of Pore-Scale Interfacial Curvature to Determine Capillary Pressure Simultaneously With Relative Permeability. *Water Resources Research, 54.9* 7046-7060. https://doi.org/10.1029/2018WR023214

Martoïa, F., Cochereau, T., Dumont, P. J. J., Orgéas, L., Terrien, M., & Belgacem, M. N. (2016). Cellulose nanofibril foams : Links between ice-templating conditions, microstructures and mechanical properties. *Materials & Design*, *104*, 376-391. https://doi.org/10.1016/j.matdes.2016.04.088

Michaud, V. (2016). A Review of Non-saturated Resin Flow in Liquid Composite Moulding processes. *Transport in Porous Media*, *115*(3), 581-601. https://doi.org/10.1007/s11242-016-0629-7

Molnár, G., Ganster, P., Török, J., & Tanguy, A. (2016). Sodium effect on static mechanical behavior of MD-modeled sodium silicate glasses. *Journal of Non-Crystalline Solids*, *440*, 12-25. https://doi.org/10.1016/j.jnoncrysol.2016.02.024

Neacsu, V., Leisen, J., Beckham, H. W., & Advani, S. G. (2007). Use of magnetic resonance imaging to visualize impregnation across aligned cylinders due to capillary forces. *Experiments in Fluids*, *42*(3), 425-440. https://doi.org/10.1007/s00348-007-0251-0

Neacsu, V., Obaid, A. A., & Advani, S. G. (2006). Spontaneous radial capillary impregnation across a bank of aligned micro-cylinders. Part II : Experimental investigations. *International Journal of Multiphase Flow*, *32*(6), 677-691. https://doi.org/10.1016/j.ijmultiphaseflow.2006.02.015

Neumann, A. W., & Good, R. J. (1979). Techniques of Measuring Contact Angles. In R. J. Good & R. R. Stromberg (Éds.), *Surface and Colloid Science : Volume 11 : Experimental Methods* (p. 31-91). Springer US. https://doi.org/10.1007/978-1-4615-7969-4_2

Paganin, D., Mayo, S. C., Gureyev, T. E., Miller, P. R., & Wilkins, S. W. (2002). Simultaneous phase and amplitude extraction from a single defocused image of a homogeneous object. *Journal of Microscopy*, *206*(1), 33-40. https://doi.org/10.1046/j.1365-2818.2002.01010.x

Park, C. H., & Lee, W. (2011). Modeling void formation and unsaturated flow in liquid composite molding processes : A survey and review. *Journal of Reinforced Plastics and Composites*, *30*(11), 957-977. https://doi.org/10.1177/0731684411411338

Pillai, K. M. (2004). Modeling the Unsaturated Flow in Liquid Composite Molding Processes : A Review and Some Thoughts. *Journal of Composite Materials*, *38*(23), 2097-2118. https://doi.org/10.1177/0021998304045585

Pillai, K. M., & Advani, S. G. (1996). Wicking across a Fiber-Bank. *Journal of Colloid and Interface Science*, *110*, 100-110.

Princen, H. M. (1969a). Capillary phenomena in assemblies of parallel cylinders : I. Capillary rise between two cylinders. *Journal of Colloid and Interface Science*, *30*(1), 69-75. https://doi.org/10.1016/0021-9797(69)90379-8

Princen, H. M. (1969b). Capillary phenomena in assemblies of parallel cylinders : II. Capillary rise in systems with more than two cylinders. *Journal of Colloid and Interface Science*, *30*(3), 359-371. https://doi.org/10.1016/0021-9797(69)90403-2

Pucci, M. F., Liotier, P.-J., Seveno, D., Fuentes, C., Van Vuure, A., & Drapier, S. (2017). Wetting and swelling property modifications of elementary flax fibres and their effects on the Liquid Composite Molding process. *Composites Part A: Applied Science and Manufacturing*, *97*, 31-40. https://doi.org/10.1016/j.compositesa.2017.02.028

Py, C., Bastien, R., Bico, J., Roman, B., & Boudaoud, A. (2007). 3D aggregation of wet fibers. *Europhysics Letters (EPL)*, *77*(4), 44005. https://doi.org/10.1209/0295-5075/77/44005

Qiu, S., Fuentes, C. A., Zhang, D., Van Vuure, A. W., & Seveno, D. (2016). Wettability of a Single Carbon Fiber. *Langmuir*, *32*(38), 9697-9705. https://doi.org/10.1021/acs.langmuir.6b02072

Rohatgi, V., Patel, N., & James Lee, L. (1996). Experimental investigation of flow-induced microvoids during impregnation of unidirectional stitched fiberglass mat. *Polymer Composites*, *17*(2), 161-170. https://doi.org/10.1002/pc.10601

Ruiz, E., Achim, V., Soukane, S., Trochu, F., & Bréard, J. (2006). Optimization of injection flow rate to minimize micro/macro-voids formation in resin transfer molded composites. *Composites Science and Technology*, *66*(3), 475-486. https://doi.org/10.1016/j.compscitech.2005.06.013

Salvatori, D., Caglar, B., Teixidó, H., & Michaud, V. (2018). Permeability and capillary effects in a channel-wise non-crimp fabric. *Composites Part A: Applied Science and Manufacturing*, *108*, 41-52. https://doi.org/10.1016/j.compositesa.2018.02.015

Scanziani, A., Singh, K., Blunt, M. J., & Guadagnini, A. (2017). Automatic method for estimation of in situ effective contact angle from X-ray micro tomography images of two-phase flow in porous media. *Journal of Colloid and Interface Science 496*, 51-59. https://doi.org/10.1016/j.jcis.2017.02.005

Schell, J. S. U., Siegrist, M., & Ermanni, P. (2007). Experimental determination of the transversal and longitudinal fibre bundle permeability. *Applied Composite Materials*, *14*(2), 117-128.

Schneider, C. A., Rasband, W. S., & Eliceiri, K. W. (2012). NIH Image to ImageJ : 25 years of image analysis. *Nature Methods*, *9*(7), 671-675. https://doi.org/10.1038/nmeth.2089

Simacek, P., & Advani, S. G. (2003). A numerical model to predict fiber tow saturation during liquid composite molding. *Composites Science and Technology*, *63*(12), 1725-1736. https://doi.org/10.1016/S0266-3538(03)00155-6

Singh, K. (2016). Imaging of oil layers, curvature and contact angle in a mixed- wet and a water-wet carbonate rock. *Water Resources Research*, 1-13. https://doi.org/10.1002/2015WR018072.Received

Vennat, E., Aubry, D., & Degrange, M. (2010). Collagen Fiber Network Infiltration : Permeability and Capillary Infiltration. *Transport in Porous Media*, *84*(3), 717-733. https://doi.org/10.1007/s11242-010-9537-4

Verrey, J., Michaud, V., & Månson, J.-A. E. (2006). Dynamic capillary effects in liquid composite moulding with non-crimp fabrics. *Composites Part A: Applied Science and Manufacturing*, *37*(1), 92-102. https://doi.org/10.1016/j.compositesa.2005.04.011

Vilà, J., Sket, F., Wilde, F., Requena, G., González, C., & LLorca, J. (2015). An in situ investigation of microscopic infusion and void transport during vacuum-assisted infiltration by means of X-ray computed tomography. *Composites Science and Technology*, *119*, 12-19. https://doi.org/10.1016/j.compscitech.2015.09.016

Washburn, E. W. (1921). The Dynamics of Capillary Flow. *Physical Review*, *17*(3), 273-283. https://doi.org/10.1103/PhysRev.17.273

Yeager, M., Simacek, P., & Advani, S. G. (2017). Role of fiber distribution and air evacuation time on capillary driven flow into fiber tows. *Composites Part A: Applied Science and Manufacturing*, *93*, 144-152. https://doi.org/10.1016/j.compositesa.2016.11.016

Chapter 8

General conclusion and perspectives

In Chapter 5, the objectives were to study the evolution of the microstructure and the permeability properties of a thermolinked flax fibre mat subjected to an out-of-plane compression. For that purpose, in situ compression experiments were performed with a micro-press installed on a synchrotron X-ray microtomography beamline, enabling the acquisition of 3D images of the flax fibre mat. Relevant microstructural descriptors, i.e., porosity, fibre diameter, specific surface area and directional tortuosity, were quantified analysing the 3D images using dedicated image analysis procedures. The 3D images were also used to perform fibre scale CFD simulations to estimate the components of the permeability tensor of the flax fibre mat for various compression stages. The numerical results showed that the permeability of the mats exhibited a transverse isotropic behaviour and decreased significantly with compaction. These results were then compared to predictions given by a modified Kozeny-Carman anisotropic model that allows estimating the principal components of the permeability tensor. Microstructural parameters measured on 3D images were used to feed the model. The only parameter that could not be measured from 3D images was a coupling flow-microstructure parameter c_i. The latter was identified by inverse method using a numerical database for the permeability properties of numerically generated fibrous networks with planar random fibre orientation. Using this set of parameters, the model predictions for the permeability were shown to be consistent with those obtained using CFD simulation performed on 3D X-ray microtomography images.

It would be interesting to further test the modified Kozeny-Carman model for a larger set of transverse isotropic fibrous materials subjected to various thermo-hygromechanical deformation modes such as in-plane shear, uniaxial or biaxial tensile modes under varying environmental conditions. To extend this model to other types of fibrous materials with different fibre arrangements or fibre types, it would be necessary to specifically determine the parameter c_i using an inverse method similar to that proposed in Chapter 5. Furthermore, as the walls of natural fibres are prone to absorb liquid, it would be interesting to adopt the same approach using 3D images of dry, partially saturated and fully saturated flax fibre mats (see for instance Figure 8.1).

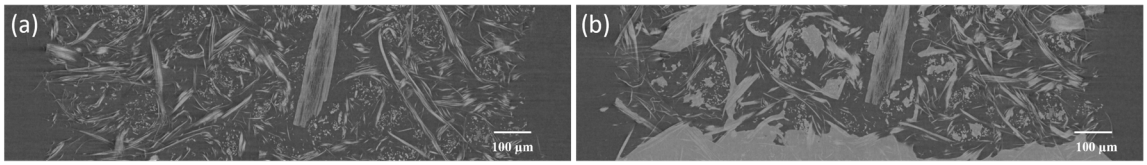

Figure 8.1. (a) Vertical cross section of a 3D X-ray microtomography image of a dry sample of flax fibre mat. (b) Same cross section of the same material impregnated with demineralised water illustrating the complexity of the flow front propagation in this kind of fibre network. Pores are black, fibres in light grey and water in shade grey. Voxel size of 6.5 μm^3.

The Kozeny-Carman model is an efficient permeability model that can be adapted to porous materials that exhibit an anisotropic microstructure. However, this model requires several microstructure descriptors such as the fibre volume fraction, fibre specific surface area, or tortuosity. It has been shown that relevant estimates of the aforementioned descriptors can be obtained, analysing 3D images of the studied materials acquired using advanced imaging techniques. In addition, the fluid-microstructure coupling parameter c_i cannot be easily identified without the use of direct CFD simulations on 3D images of the materials.

Thus, it can be useful to propose a full analytical model for the prediction of the permeability of fibrous networks with disordered microstructures. To this end, a tensorial permeability model was presented in Chapter 6. The model was developed in the framework of the homogenisation with multiple scale asymptotic expansions, using a simplified description of the viscous drag force exerted by the fluid on the fibres. The model was further simplified to fibres with circular cross sections and networks with transverse isotropic fibre orientation. With this approach, the permeability tensor $\boldsymbol{K}$ depends on two permeability coefficients weighted by the second order orientation tensor. The two permeability coefficients were obtained from literature models so as to formulate a full analytical version of the permeability model. The prediction of the model were compared with numerical permeability results that were performed on numerically generated virtual and 3D-imaged real fibre networks with various fibre contents and fibre slenderness and fibre orientation states. Contrary to most of current permeability models that are available in the literature, the proposed model can well reproduce the evolution of the permeability tensor components with those of the second-order orientation tensor. The prediction is all the more accurate as the fibre volume fraction increases. We also highlighted some limitations of the model. For instance, these limitations are related to heterogeneities in the spatial distribution of fibres and to fibre networks with low fibre aspect ratios.

To overcome these limitations, it is necessary to have better estimates for the two permeability coefficients of the model. These coefficients should account for the fibre volume fractions, the spatial fibre distribution as well as the fibre aspect ratio. This could be achieved using inverse method from a large numerical database obtained using fibre scale CFD simulations on virtual or real fibrous networks.

Finally, we investigated the capillary effects that occur during the impregnation of a model fibre network in the form of a bundle made of an assembly of rigid parallel tubes. In situ

wetting and dewetting impregnation experiments were performed using high resolution synchrotron X-ray microtomography and a specially developed device. An image analysis procedure was also specially developed to extract from the as-obtained 3D images several local descriptors related to capillary phenomena such the lengths of the triple lines, contact angles along the triple lines, fluid-air interface curvatures. From these measurements, it was possible to estimate the local capillary pressure as well as the transverse and longitudinal capillary forces exerted by the fluid on each fibre of the model fibre network. We observed that the contact angles vary significantly along the triple lines, also in quasi static situations. Noticeable variations were also observed during wetting and dewetting experiments. Depending on the location of the tubes in the model fibre network, it was shown that transverse capillary forces can have the same order of magnitude as the longitudinal capillary forces. The measurements of capillary pressure enabled testing the relevance of an impregnation model that is commonly used in the composite domain to predict capillary pressure in fibre bundles of reinforcement materials.

This approach could be extended to investigate the capillary-driven phenomena that occur during the impregnation of more complex/realistic fibre networks made, for instance, of deformable fibres. It could be also interesting to investigate coupling between impregnation and swelling in bundles made of natural fibres. Results of preliminary experiments are illustrated in Figures 8.1 and 8.2.

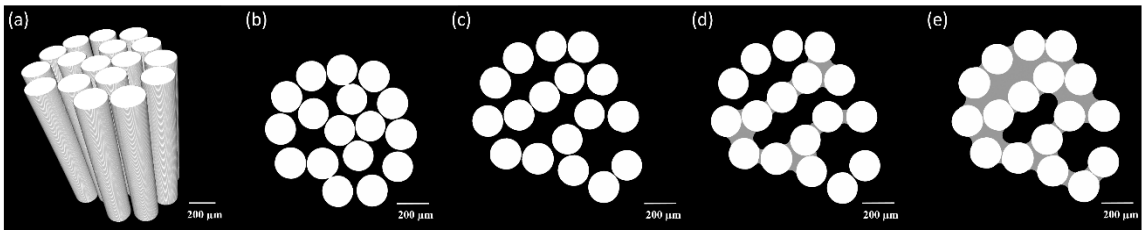

Figure 8.2. (a) 3D partial view of a dry bundle made of PVDF fibres. (b-e) Horizontal cross sections of the same fibre bundles that illustrate the rearrangement of individual fibres within the fibre bundle with the propagation of the impregnating fluid. The capillary forces that act within the bundle tend to pull apart the fibres in cross sections located above the fluid front (image c). Images d and e show the preferential flow channels that develop during the impregnation process. Fibres are white. Pores are black. Fluid is grey. Voxel size of 0.81 μm^3.